Ultracold Ytterbium Atoms in a Tunable Non-Primitive Optical Lattice

A dissertation submitted to the
Department of Physics of the Kyoto University

presented by
Hideki Ozawa

for the degree of
Doctor of Science

February 6, 2018

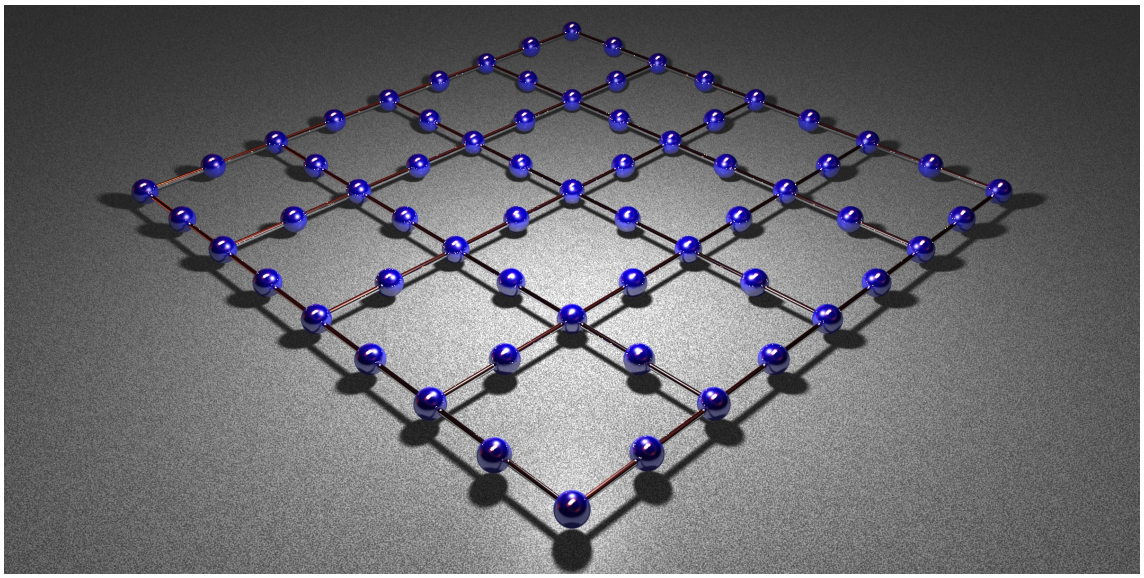

Abstract

Ultracold atoms trapped in optical lattices offer a clean and highly flexible experimental platform to investigate exotic phases of condensed matter. Recently, nonprimitive optical lattices with multiple lattice sites per unit cell have been realized, revealing nontrivial ordering and dynamics arising from the orbital degree of freedom. In this thesis, we present a series of experiments with ultracold ytterbium (Yb) atoms in a Lieb lattice and dimerized cubic lattice geometry, which are realized by optical means.

In a Lieb lattice, a flat band appears due to destructive interference of the tunneling. It is a fascinating question whether a Bose-Einstein condensate (BEC) is stable in a flat band. Experimental study for this question is hampered by the fact that a flat band is in an excited state in the case of Lieb lattice. We have developed a method to coherently transfer a BEC of ^{174}Yb into the flat band of Lieb lattice, and studied the stability of the BEC loaded in the flat band. We also investigate the inter-sublattice dynamics of the system by projecting the sublattice population onto the band population. This measurement shows the formation of the localized state in the flat band. Furthermore, we measure the lowest three bands of an optical Lieb lattice for a BEC in a momentum-resolved manner. A BEC, which initially prepared around zero quasimomentum in the lattice, is transported to a desired quasimomentum by applying a constant force. The energy dispersion of the lowest band is reproduced by integrating measured group velocities. The excited band energy is reconstructed by measuring the gap from the lowest band with the same quasimomentum, which can be extracted by from the oscillation of the sublattice populations after preparing a superposition of the band eigenstates. It is revealed that the second band, which should be flat in a single-particle description, is shifted and distorted around the Brillouin zone edge as the interaction strength increases.

A Lieb lattice system has a mathematical analogy to a three-level system with Λ-type transition. Most interestingly, a localized state in a flat band of the Lieb lattice corresponds to the dark state in the three-level system. By adiabatically changing the tunneling amplitudes in an counter-intuitive order, we coherently transfer atoms from one sublattice to another without populating the intermediate sublattice, which can be regarded as a spatial analogue of stimulated Raman adiabatic passage. We also successfully observe a matter-wave analogue of Autler-Townes doublet effect using the optical Lieb lattice.

^{173}Yb is characterized by SU($\mathcal{N} = 2I + 1$) symmetric repulsive interaction for nuclear spin $I = 5/2$. For this large-spin system, Pomeranchuk cooling is enhanced; large-spin degrees of freedom can effectively cool down the system by absorbing the entropy from motional degrees of freedom. The precise control of the spin degree of freedom provided by optical pumping technique enables us a straightforward comparison between SU(2) and SU(4). Our main finding is that larger singlet-triplet imbalance is observed in a

dimerized cubic lattice for SU(4) spin system compared with SU(2) as a consequence of Pomeranchuk cooling effect. This is an important step towards the realization of novel SU($\mathcal{N} > 2$) quantum magnetism.

Contents

1 Introduction **1**

2 Basic theory for an optical superlattice **6**
2.1 Tight-binding model . . . 6
2.1.1 Dimerized lattice . . . 6
2.1.2 Lieb lattice . . . 6
2.2 Optical lattice potential . . . 8
2.2.1 Monochromatic lattice . . . 8
2.2.2 1D superlattice . . . 8
2.2.3 Lieb lattice . . . 9
2.3 Band structure by optical lattice . . . 9
2.3.1 Monochromatic lattice . . . 10
2.3.2 1D superlattice . . . 12
2.3.3 Lieb lattice . . . 13
2.4 Hubbard parameters in optical lattice . . . 17
2.4.1 Simple cubic lattice . . . 17
2.4.2 Dimerized lattice . . . 18
2.4.3 Lieb lattice . . . 22
2.5 Bogoliubov theory . . . 27
2.5.1 Gross-Pitaevskii equation . . . 27
2.5.2 Bogoliubov-de Genne equation . . . 29
2.5.3 Density distribution in lattice . . . 30
2.6 Atomic limit calculation of the Fermi-Hubbard model . . . 33
2.6.1 SU(2) Fermi-Hubbard model . . . 33
2.6.2 The harmonic trap and local density approximation . . . 38
2.6.3 Extension to the SU($\mathcal{N} > 2$) system . . . 38

3 Experimental setup **41**
3.1 Properties of Ytterbium (Yb) . . . 41
3.1.1 Isotopes and s-wave scattering lengths . . . 41
3.1.2 Energy level . . . 41
3.2 Cooling processes . . . 44
3.2.1 Zeeman slower . . . 44
3.2.2 Magneto-Optical Trap (MOT) . . . 44
3.2.3 Far-Off Resonance Trap (FORT) . . . 44
3.3 Imaging system . . . 45

3.3.1 Absorption imaging . . . 45
3.4 Thermometry for trapped atoms . . . 46
3.4.1 Thermal gas . . . 48
3.4.2 Degenerate Fermi gas . . . 48
3.4.3 Bose-Einstein condensation . . . 50
3.5 Optical lattice . . . 51
3.5.1 Monochromatic lattice . . . 51
3.5.2 Optical superlattice . . . 57
3.5.3 Optical Lieb lattice . . . 60

4 Coherent driving and freezing of bosonic matter wave in an optical Lieb lattice 66
4.1 Loading a BEC into a flat band by phase imprinting . . . 66
4.2 Relaxation dynamics from a flat band . . . 68
4.3 Observation of a localized state in a flat band . . . 69
4.4 Conclusion and outlook . . . 71

5 Interaction-Driven Shift and Distortion of a Flat Band in an Optical Lieb Lattice 72
5.1 Group-velocity measurement . . . 72
5.2 Band-gap measurement . . . 74
5.2.1 Dependence on the mean-field interaction strength . . . 77
5.3 Conclusion and outlook . . . 77

6 Spatial Adiabatic Passage of Massive Quantum Particles 80
6.1 Introduction . . . 80
6.1.1 Three-level system with Λ-type transition . . . 80
6.1.2 Correspondence between a three-level system and Lieb lattice . . . 81
6.2 Spatial adiabatic passage (SAP) . . . 81
6.3 Autler-Townes doublet . . . 84
6.4 Conclusion and outlook . . . 84

7 Antiferromagnetic spin correlation of SU($\mathcal{N}$) Fermi gas in an optical dimerized lattice 86
7.1 Introduction . . . 86
7.2 Spin manipulation by the optical pumping . . . 87
7.2.1 Numerical simulation of the spin relaxation . . . 87
7.2.2 Loss spectroscopy of transition used for optical pumping . . . 88
7.2.3 Optical Stern-Gerlach Experiment . . . 90
7.2.4 Creation of balanced 4-spin mixture . . . 93
7.3 Photoassociation Experiment . . . 98
7.3.1 Creation of arbitrary 2-spin mixture . . . 99
7.4 Singlet-triplet oscillation in dimer . . . 104
7.5 Conclusion and outlook . . . 110

8 Conclusion & Outlook 113

A Trap geometry **116**
A.1 Dipole force trap . . . 116
A.2 Trap frequency . . . 117
A.2.1 FORT . . . 118
A.2.2 Optical lattice . . . 120
A.2.3 Trap frequency for a combined optical trap . . . 122

B Mean velocity in a periodic potential **124**
B.1 The case without external field . . . 124
B.2 The case with external field . . . 125
B.2.1 Adiabatic evolution [1] . . . 125
B.2.2 The case where the momentum is adiabatically changing [2] . . . 128

C Berry curvature in an optical lattice **131**
C.1 Chern number and Berry curvature . . . 131
C.2 Calculation method without specifying any gauge . . . 131

Bibliography **134**

Acknowledgements **144**

Chapter 1

Introduction

In solid state physics, the combination of huge number of particles and Coulomb interactions makes a detailed understanding of the many-body phenomena very difficult. For some materials, a band theory description in non-interaction regime is effective, which explains the distinction between metallic, semi-conducting and insulating states, but it is particularly in the complex material with strong interactions where novel physical phenomena appear. Examples range from frustrated spin systems [3] to high-temperature superconductivity [4]. A problem toward understanding these phenomena is the associated many-body state emerging at low temperatures, where the strong correlations between the microscopic particles give rise to novel quantum phases.

Typical approach in condensed-matter physics is to introduce simplified model systems for the complex many-body problem: one attempts to formulate minimal models which include few crucial degrees of freedom necessary to reproduce the observed physical behavior. Yet, such models are the result of several assumptions and approximation. For several materials, the formulation of a simplified model system is difficult due to non-negligible contributions of the long-range interactions, higher lattice orbital effects, coupling between electron and phonon modes in the crystal, and so on. In addition, understanding even the apparently-simple model systems is exceedingly difficult in the low-temperature regime, as they have found to be numerically intractable due to the exponentially growing number of quantum states. Therefore, the model's ability to provide a correct description of the system's key properties needs to be verified.

One of the minimal models for interacting fermionic particles in a crystal is the Fermi-Hubbard model [5]. In the model, we simplify the crystalline structure by periodic lattice sites, which are filled with spin 1/2 particles that tunnel between the neighbouring sites and feel an interaction energy when occupying the same site. In spite of the simplicity, the Fermi-Hubbard model includes many of the diverse phenomena driven by the interplay between charge and spin degrees of freedom. For a three-dimensional cubic lattice, the Fermi-Hubbard model predicts a cross-over from a metallic to Mott-insulating state at half filling, and a phase transition to an antiferromagnetically ordered state at low temperature. Despite intense study using this model by the theoretical solid state community, the exact ground-state for the repulsively-interacting two-compoent ferimons in the simple cubic lattice is still not clear except at half filling [6]. Furthermore, the case of more complex lattice structures, which have multiple sites per unit cell, is equally little understood.

Ultracold quantum gases in optical lattices [7, 8] emerged as a promising experimental platform toward further understanding of solid state systems. The basic idea is to cool a dilute atomic gas down to quantum degeneracy and introduce the gas into an optical lattice, which is created by interference of counter-propagating laser beams. Due to the atom-light interaction, the atoms feel a periodical potential. The role of the electrons moving in a crystal is then taken by the atoms, while the crystalline structure is formed by the optical lattice. This *artificial solid* is a defect-free environment and has high controllability of parameters in the system. The concept to study a quantum system by choosing a physically different, but fully controllable system with the same properties originates from Richard P. Feynman; *quantum simulation* [9].

In real solids, the temperature required to reach degeneracy regime is typically on the order of the room temperature. In an optical lattice, that is not the case, as the lattice spacing is on the order of 1 μm, which is a factor of 10^4 larger than in solids. Due to such a very low density of dilute atoms in an optical lattice, extremely low temperatures close to a few nK are required to uncover the quantum nature of the system. A key technique to reach these temperature scale was brought by the laser cooling and evaporative cooling [10]. A breakthrough came with the first realization of Bose-Einstein condensation of ^{87}Rb and ^{23}Na [11, 12], where a macroscopic number of atoms occupies the same quantum state. Shortly after, the degenerate Fermi gas was first realized with ^{40}K [13]. Such breakthroughs marked the advent of the prosperous era of ultracold atom physics. Cold atom research aimed initially at revealing the single-particle coherence effects induced by quantum statics, but the research field rapidly expanded and developed towards the investigation of inter-atomic interactions. A lot of experiments succeeded in observing quantum effects induced by strong interactions, as represented by a detailed understanding of the BEC-BCS crossover in Fermi gases [14, 15, 16].

After the possibility was pointed out in 1998 that ultracold atoms trapped in an optical lattice accurately implement the Hubbard model, the first experimental demonstration was made in 2001 with the observation of the superfluid to Mott-insulator transition for bosonic atoms [17]. This experiment ensures the capability of ultracold atoms to simulate and study quantum phases within the Bose-Hubbard model, and promoted a series of further experimental studies with interacting bosonic atoms [18, 19, 20, 21]. Particularly, the realization of quantum gas microscope for bosonic atoms enables spatial observation of Mott-insulating shell structure on the single-site level [22, 23, 24].

Starting from the observation of the Fermi surface of non-interacting Fermi gas, many experiments with ultracold fermionic atoms in an optical lattice have been performed, such as mixtures with bosonic atoms [25, 26, 27, 28], noise-correlation measurement [29], Anderson localization [30], and transport properties [31]. The unique control of inter-atomic interaction by Feshbach resonances allowed the study of strongly interacting fermionic gases in optical lattices, which lead to the first realization of a fermionic Mott-insulating state for repulsive interactions [32, 33].

These experiments were important milestones toward the major goal to realize *quantum simulator* with optical lattice system, and the next milestone was to observe Néel ordered states in optical lattices. Yet, further progress had been hampered by the extremely low temperature required, where the relevant energy scale is given by the exchange energy. This scale is typically much lower than the already very small tunneling and interaction energy in cold atom systems, and therefore leads to the temperature requirements

in the lattice on the order of 1 nK. A key for quantum magnetism in optical lattices was the local entropy redistribution scheme, proposed in [34, 35, 36]. The basic idea is to make the entropy reservoir around the outer region within the trap by manipulating the trap confinement or lattice geometry. Even though the entire entropy in an optical lattice conserves, the reservoir absorbs entropy, which leads to low entropy at central region of the trap. This concept was first demonstrated with an anisotropic and dimerized lattice, and succeeded in realizing a short-range quantum magnetism in the lattices [37]. By using a compensated optical lattice, in which the confinement of each lattice beam is compensated by a blue-detuned laser beam, short-range antiferromagnetic correlations were observed even in a three dimensional cubic lattice [38]. Most surprisingly, the antiferromagnetic long-range order with ^{6}Li atoms in two dimensional square lattice was realized very recently [39]. They use the combined potential of the optical lattice and the anti-confinement that is generated by the digital micromirror device (DMD). Thus, development in experimental technique for manipulating and detecting fermionic atoms in optical lattices enables us to explore the Fermi-Hubbard phase diagram in theoretically challenging regimes.

Taking advantage of atoms internal degrees of freedom also permits to expand the possibilities for quantum simulation, and stimulated a growing interest in several atomic species, instead of the widely used alkali elements (^{40}K and ^{6}Li). Among others, the atomic species belonging to the category of alkaline-earth-like atoms got special attention, such as calcium, strontium and ytterbium. Alkaline-earth-like elements have been primarily used in the recent past as powerful frequency standards: their atomic structure includes low-lying metastable electronic levels and the associated ultra-narrow optical transitions provides a remarkable intrinsic precision. Since the first realization of the optical lattice clock with alkaline-earth-like atoms [40], many lattice clock systems around the world were assembled, and currently provide the most precise frequency standards at the level of 10^{-18} [41, 42], superior to the performance of the atomic clocks. Along with use of alkaline-earth-like atoms in quantum metrology, their potential for quantum simulation arose when the first bosonic isotope of ytterbium was cooled to degeneracy regime [43]. Since then, various isotopes of alkaline-earth-like species have been brought to quantum degeneracy [44, 45, 46, 46, 47, 48, 49], and even a fermionic Mott insulating state has already been realized [50]. Among them, the fermionic ^{87}Sr and ^{173}Yb are promising candidates for the quantum simulation of strongly-correlated phases, owing to their strong interactions and nuclear spin properties. Their positive scattering lengths $a = 10.55$ nm for ^{173}Yb [51] and $a = 5.09$ nm for ^{87}Sr [52] correspond to repulsive interactions, which is the case of interest in the context of most theoretical studies. In addition, these fermionic isotopes possess high nuclear spins $I = 5/2$ for ^{173}Yb and $I = 9/2$ for ^{87}Sr, which are strongly decoupled from the electron degree of freedom due to the absence of electronic angular momentum, and permits the emergence of a high, unique symmetry of interactions. This SU($\mathcal{N} = 2I + 1$) symmetry attracts theoretical interests, as it is predicted to have drastic effect on the properties of interacting fermionic many-body state [52], and have the possibility of emergence of novel quantum phases, for example, SU($\mathcal{N} > 2$) quantum magnetism [53, 54]. Ultracold alkaline-earth-like atoms in optical lattices are suitable tool to verify such theoretical predictions, as there are (yet) no known analogue in nature.

Apart from atoms internal degrees for freedom, complex lattice geometries also provide

unique physics, owing to their special band structure and orbital degrees of freedom. By superimposing optical lattices with different lattice constant, or interfering more than three laser beams at different angles, a lot of non-standard optical lattices are realized for ultracold atoms, and fascinating experiments are performed. One dimensional optical superlattice is the simplest example, where the superexchange energy is directly measured [55]. As for two dimensional lattice system, an optical honeycomb lattice [56], optical triangular lattice [57], optical checker board lattice [58], optical kagome lattice [59] are so far realized. In the optical honeycomb lattice, manipulation of Dirac points is reported. A large variety of magnetic phases is simulated in the optical triangular lattice. In the optical checker board lattice, a superfluid in higher bands is realized. Kagome lattice has a flat band, where it is predicted that a bosonic gas in the band shows novel supersolidity, meaning the counter-intuitive coexistence of superfluid and crystalline order [60]. Yet, experimental access is hampered by the fact that the flat band exists in an excited state.

In this thesis, we present the experimental realization of an optical Lieb lattice for ultracold ytterbium atoms [61]. The Lieb lattice geometry [62] is a square lattice with additional sites at each bond center, and therefore is also called decorated square lattice. Such a structure is identical to the three-band d-p model, which describes the CuO_2 plane of high-T_c superconductors [63, 64, 65]. The Lieb lattice has a flat band and Dirac cones in the energy spectrum. Emergence of flat-band ferromagnetism in the lattice at sufficiently low temperature was rigorously proved [66]. Ultracold Fermi gases in an optical Lieb lattice is a promising experimental platform to study such ordered state. The Lieb lattice or its one-dimensional analog (sawtooth lattice) was realized in a photonic lattice [67, 68, 69] and polaritonic systems [70]. However, optical lattice realization has definite advantages in terms of simple and strong interactions, dynamical controllability of system parameters, and availability of both bosonic and fermionic systems.

Our first work during the course of this thesis was to demonstrate novel manipulation and detection of a BEC in a flat band by developing a dynamically tunable optical Lieb lattice [61]. We invent a method to engineer the population and phase on each sublattice site, which enables us to coherently transfer atoms into the flat band and to observe frozen motion of atoms on a specific sublattice. In addition, almost arbitrary superposition of band eigenstates can be prepared, which drives coherent oscillation modes in the Lieb lattice and enables mapping out the band structure. This high controllability inspired our second work [71], where we measured the lowest three bands of an optical Lieb lattice for a BEC in a momentum-resolved manner. This work systematically investigated the interaction effect on the band structure, in particular a flat band. Our third work shed light on a mathematical analogy of a Lieb lattice to a three-level system with Λ-type transition [72]. A key is the existence of dark eigenstates forming a flat band in an optical Lieb lattice. This analogy allows us to coherently transfer atoms from a sublattice to another without populating the intermediate sublattice in the lattice, which can be regarded as a spatial version of stimulated Raman adiabatic passage in the three-level system [73, 74, 75]. Our fourth work was to investigate high-spin symmetry effects on a short-range quantum magnetism of ultracold fermionic atoms in a dimerized cubic lattice. The spin number of ^{173}Yb is precisely manipulated by optical pumping technique, which allows a straightforward comparison between SU(2) and SU(4) spins in a dimer. This work is an important milestone toward future realization of novel SU($\mathcal{N} > 2$) quantum magnetism.

Outline of this thesis

This thesis is organized as follows.

- Chapter2 introduces theoretical background for optical superlattices, including a Lieb lattice.
- Chapter3 gives the details of our experimental apparatus and procedures used for optical Lieb lattice experiments with ytterbium atoms.
- Chapter4 describes a series of experiments with a bosonic matter-wave of ^{174}Yb in an optical Lieb lattice.
- Chapter5 is devoted to the momentum-resolved measurement of the Bloch bands for a BEC of ^{174}Yb in an optical Lieb lattice.
- Chapter6 presents demonstration of spatial adiabatic passage of ultracold fermionic atoms of ^{171}Yb in a Lieb lattice geometry.
- Chapter7 reports the creation of the SU(4)-spin system of ^{173}Yb by optical pumping and the result of comparison with the cases of SU(2) and SU(4) in a dimerized lattice.
- Chapter8 briefly summarizes the works in this thesis and gives future prospects in these experimental systems.

Chapter 2

Basic theory for an optical superlattice

In this chapter, we introduce the theoretical backgrounds for optical superlattices. First, we begin with the tight-binding model, where the on-site interaction is neglected.

In this chapter, basic properties of an optical Lieb lattice are described. First, the Hubbard model of a Lieb lattice is introduced. After optical lattice potentials in our system is given in the section 2.2, we present a single-particle band structure calculated from the potential in 2.3. In section 2.4, the Hubbard parameters of the tunneling amplitudes and on-site interactions in the lattices are calculated. Using the Hubbard parameters, the mean-field theory and the atomic limit calculation of the SU($\mathcal{N}$) Fermi-Hubbard model are presented in the sections 2.5, 2.6, respectively.

2.1 Tight-binding model

2.1.1 Dimerized lattice

The tight-binding Hamiltonian in the dimerized lattice is given in

$$H = \begin{pmatrix} \Delta & -t\mathrm{e}^{-iq_x d/2} - t_d \mathrm{e}^{iq_x d/2} \\ -t\mathrm{e}^{iq_x d/2} - t_d \mathrm{e}^{-iq_x d/2} & -\Delta \end{pmatrix}, \tag{2.1.1}$$

where t_d is the intra-dimer tunneling, t is the inter-dimer tunneling, and 2Δ corresponds to the energy difference between the sublattices.

2.1.2 Lieb lattice

A Lieb lattice is schematically illustrated in Fig.2.1.2. It is the square lattice decorated with the additional site at each bond center. For a single particle regime, the nearest-neighbor tight-binding Hamiltonian in the Lieb lattice is given by

$$H = -J \sum_{\langle i,j \rangle} c_i^\dagger c_j + \sum_i \epsilon_i c_i^\dagger c_i, \tag{2.1.2}$$

where $\langle i, j\rangle$ denotes the nearest-neighboring sites and J is the tunneling amplitude. We set the site offset energy as $\epsilon_B = \epsilon_C = -\epsilon_A = \Delta$, and write the Hamiltonian in the bases of the Bloch sums $|\boldsymbol{q}, X\rangle = \frac{1}{\sqrt{N}} \sum_{i\in X} \mathrm{e}^{i\boldsymbol{q}\cdot\boldsymbol{k}_i} c_i^\dagger |0\rangle$ as

$$H = \begin{pmatrix} \Delta & -2J\cos(q_x d/2) & 0 \\ -2J\cos(q_x d/2) & -\Delta & -2J\cos(q_y d/2) \\ 0 & -2J\cos(q_y d/2) & \Delta \end{pmatrix}, \tag{2.1.3}$$

where d is the lattice constant. By diagonalizing this Hamiltonian, we obtain the eigenvalues:

$$E = \Delta, \pm\sqrt{\Delta^2 + 4J^2\left[\cos(q_x d/2)^2 + \cos(q_y d/2)^2\right]}. \tag{2.1.4}$$

The energy dispersion is plotted in the Fig.2.1.2 for $\Delta = 0$. The Lieb lattice has a dispersionless band (flat band, in other words) at zero energy, and at $\boldsymbol{q} = (\pm\pi/d, \pm\pi/d)$ the 1st band and 3rd band touch the 2nd band.

For $\Delta = 0$, the eigenstate of each band can be written as

$$|1\mathrm{st}, \boldsymbol{q}\rangle \propto \cos(q_x d/2)\,|\boldsymbol{q}, B\rangle + \sqrt{\cos^2(q_x d/2) + \cos^2(q_y d/2)}\,|\boldsymbol{q}, A\rangle + \cos(q_y d/2)\,|\boldsymbol{q}, C\rangle\,, \tag{2.1.5}$$

$$|2\mathrm{nd}, \boldsymbol{q}\rangle \propto \cos(q_y d/2)\,|\boldsymbol{q}, B\rangle - \cos(q_x d/2)\,|\boldsymbol{q}, C\rangle\,, \tag{2.1.6}$$

$$|3\mathrm{rd}, \boldsymbol{q}\rangle \propto \cos(q_x d/2)\,|\boldsymbol{q}, B\rangle - \sqrt{\cos^2(q_x d/2) + \cos^2(q_y d/2)}\,|\boldsymbol{q}, A\rangle + \cos(q_y d/2)\,|\boldsymbol{q}, C\rangle\,. \tag{2.1.7}$$

The 2nd line means that a particle in 2nd band localizes at B-site and C-site regardless of $\boldsymbol{q}$. This is because the tunneling amplitudes from B, C-site to A-site destructively interfere each other. Such localized states construct a flat band. This flat band is intrinsically different from a narrow band in a square lattice with deep potential. While a small hopping in the square lattice results in the narrow band, a flat band appears even if particles in a Lieb lattice are moving around.

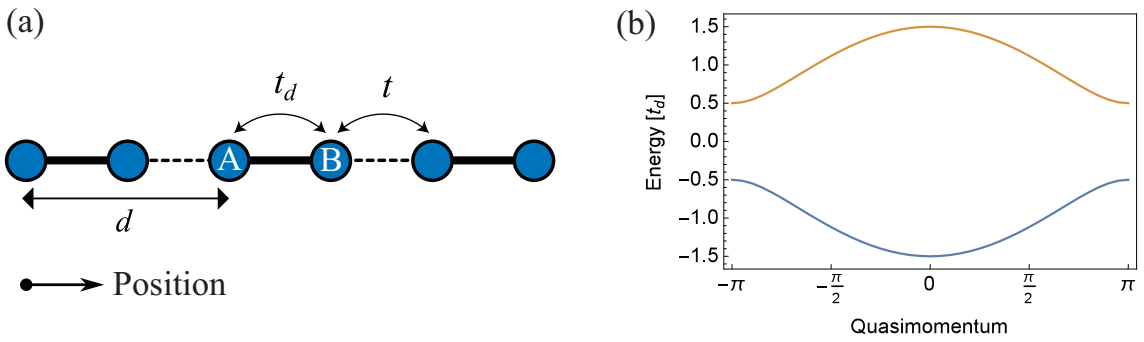

Figure 2.1.1: (a)Dimmerized lattice configuration and (b) the band structure in the tight-binding model with $\Delta = 0$, $t = 0.5t_d$.

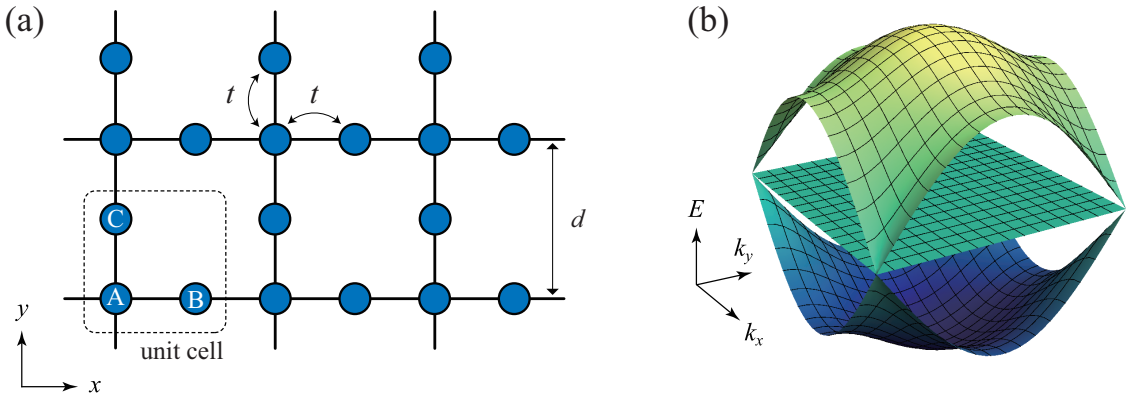

Figure 2.1.2: (a)Lieb lattice configuration and (b) the band structure in the tight-binding model with $\Delta = 0$.

2.2 Optical lattice potential

Ultracold atoms in an optical lattice are expected to be able to simulate the quantum many-body problems. Since the optical lattice is created by the interference of the counter-propagating lasers, it is free from the impurities, defects, and distortions. This feature ensures that a experiment in the optical lattice has good agreement with the theoretical models. In addition, the optical lattice system has high-controllability of the parameters appearing in the Hubbard model. In this section, we introduce the form of the optical lattice potential used in this thesis.

2.2.1 Monochromatic lattice

One-dimentional monochromatic lattice is the simplest optical lattice, which is produced by interference of the two counter-propagating lasers. The potential can be written as

$$V(x) = -V_0 \cos^2(k_L x), \tag{2.2.1}$$

where $k_L = 2\pi/\lambda$ is the wave number of the laser, V_0 is the potential depth. For convenience, we introduce the scaled lattice depth s such as

$$s = \frac{V_0}{E_{\mathrm{R}}}, \quad E_{\mathrm{R}} = \frac{\hbar^2 k^2}{2m}, \tag{2.2.2}$$

where m is the atomic mass, and E_{R} is called recoil energy.

2.2.2 1D superlattice

Optical superlattice can be realized by superimposing the optical lattices with difference lattice constants. Optical superlattice consisting of the monochromatic lattices with lattice spacings of $\lambda/2$ (short lattice) and λ (long lattice) is given in

$$V(x) = -V_{\mathrm{long}} \cos^2(k_L x) - V_{\mathrm{short}} \cos^2(2k_L x + \phi), \tag{2.2.3}$$

where $V_{\mathrm{long}}, V_{\mathrm{short}}$ is the depth of the short lattice and long lattice, respectively. ϕ is the relative phase between the short lattice and long lattice.

2.2.3 Lieb lattice

Our optical Lieb lattice consists of the square lattice with lattice spacing 532nm, more square lattice with spacing 266nm, and one-dimensional diagonal lattice with spacing $\sqrt{2} \times 266$nm. For convenience, we call them long-square lattice, short-square lattice, and diagonal-lattice, respectively. The potential is written as.

$$\begin{aligned} V(x,y) \quad &= -V_{\text{long}}(\cos^2(k_L x) + \cos^2(k_L y)) \\ &\quad -V_{\text{short}}(\cos^2(2k_L x) + \cos^2(2k_L y)) \\ &\quad -V_{\text{diag}}\cos^2(k_L(x-y) + \pi/2) \end{aligned} \tag{2.2.4}$$

where $k_L = 2\pi/(1064\text{ nm}) = \pi/(532\text{ nm})$. The first, second, and third terms denote the long-square lattice, short-square lattice, and diagonal lattice, respectively.

2.3 Band structure by optical lattice

The band structure is a key to understand the behavior of a particle in a periodic potential. In this section, we introduce the numerical calculation method of the single-particle band structure in an optical lattice. Single-particle Hamiltonian in a 1D periodic potential (periodicity: d) is written as

$$H = H_0 + V(\hat{x}) = \frac{\hbar^2 \hat{k}^2}{2M} + V(\hat{x}), \;\; V(\hat{x}+a) = V(\hat{x}). \tag{2.3.1}$$

The problem is to solve Schrödinger equation for this Hamiltonian. The idea is to display the matrix elements in terms of plane-wave and to diagonalize it. We set the system size as $L = N_{\text{site}}d$ (N_{site}: the number of sites) and impose a periodic boundary condition. The eigenstate of free particle Hamiltonian H_0 is the plane-wave such as,

$$\begin{aligned} |k\rangle\,,\; \psi_k(x) \;\; &= \;\; \langle x|k\rangle = \frac{1}{\sqrt{L}}\mathrm{e}^{ikx}, \\ k \;\; &= \;\; \frac{2\pi}{L}l,\; l = 0, \pm 1, \pm 2, \cdots . \end{aligned} \tag{2.3.2}$$

On the other hand, due to the periodicity, the potential V can be expanded in terms of the plane-wave (Fourier components, in other words) whose wave-number coincides with the reciprocal lattice vector K.

$$V(\hat{x}) = \sum_{m=0,\pm 1,\cdots} V_m \mathrm{e}^{imK\hat{x}}, \;\; K = \frac{2\pi}{d} \tag{2.3.3}$$

It is only when $k - k'$ is the integer multiple of K that a matrix element $V_{kk'} = \langle k| V |k'\rangle$ has non-zero value (Remember $\mathrm{e}^{imK}|k\rangle = |k + mK\rangle$):

$$V_{kk'} = \sum_{m=0,\pm 1,\cdots} V_m \delta_{k,k'+mK}. \tag{2.3.4}$$

The matrix $(V_{kk'})$ has block diagonal form, and the number of submatrices is equal to N_{site} because momentum k is quantized and the equation $\frac{2\pi}{L} \times N_{\text{site}} = K$ determines the

number of submatrices. Below we assume the number of sites is even $N_{\rm site} = 2N'_{\rm site}$. We can take a series of momentum inside the 1st Brillouin zone $[-K, K)$ as a label for the submatrices, where

$$q = \frac{2\pi}{L} l, \;\; l = -N'_{\rm site}, -N'_{\rm site}+1, \cdots, N'_{\rm site}-1. \tag{2.3.5}$$

This q is so called quasi-momentum.

The eigenenergies and eigenstates can be obtained by digonalizing the submatrix $H^{(q)} = H_0^{(q)} + V^{(q)}$ for each quasi-momentum. The eigenstates for $H^{(q)}$ labeled by band index n should be superposition fo plane-wave:

$$|q, n\rangle = \sum_{m=0,\pm1,\cdots} A_m^{(q,n)} |q + mK\rangle , \tag{2.3.6}$$

$$\psi_q^{(n)}(x) = \langle x|q, n\rangle = \frac{1}{\sqrt{L}} \sum_{m=0,\pm1,\cdots} A_m^{(q,n)} \mathrm{e}^{i(q+mK)x}. \tag{2.3.7}$$

For translational motion by the lattice constant d, $\psi_q^{(n)}(x)$ is transformed as

$$\psi_q^{(n)}(x+d) = \mathrm{e}^{iqd} \psi_q^{(n)}(x). \tag{2.3.8}$$

This is well-known Bloch theorem.

2.3.1 Monochromatic lattice

The one-dimensional monochromatic lattice induces a sinusoidal potential for atoms:

$$V(x) = V_0 \sin^2(k_L x) = \frac{V_0}{2}\left(1 - \frac{\mathrm{e}^{2ik_L x} + \mathrm{e}^{-2ik_L x}}{2}\right). \tag{2.3.9}$$

Here, V_0 is the lattice potential depth, and k_L is the wave number of a laser beam. The reciprocal lattice vector is $K = 2k_L$. In this case, there are only two Fourier components $\pm K$. Therefore, the submatrix $H^{(q)}$ has the form such as

$$\begin{aligned} H_{ll'}^{(q)} &= \langle q + lK| \left(\frac{\hbar^2 \hat{k}^2}{2M} + V(\hat{x})\right) |q + l'K\rangle \\ &= E_{\rm R} \times \begin{cases} \left(\frac{q}{k_L} + 2l\right)^2 + \frac{s}{2} & l = l' \\ -\frac{s}{4} & |l - l'| = 1 \\ 0 & \text{otherwise} \end{cases} \end{aligned} \tag{2.3.10}$$

with $l, l' = 0, \pm1, \pm2, \cdots$. $s = V_0/E_{\rm R}$ is lattice potential depth scaled by recoil energy $E_{\rm R} = \frac{\hbar^2 {k_L}^2}{2M}$. This matrix has infinite dimension. In actual numerical calculation, we have to truncate it like setting maximum $|l|, |l'|$ as $l = l_{\max}$, and make it $2l_{\max} + 1$ dimensional matrix. The maximum value should be large enough so that the calculation result becomes the same for the larger matrix. As for the number of sites $N_{\rm site}$, we set it large enough

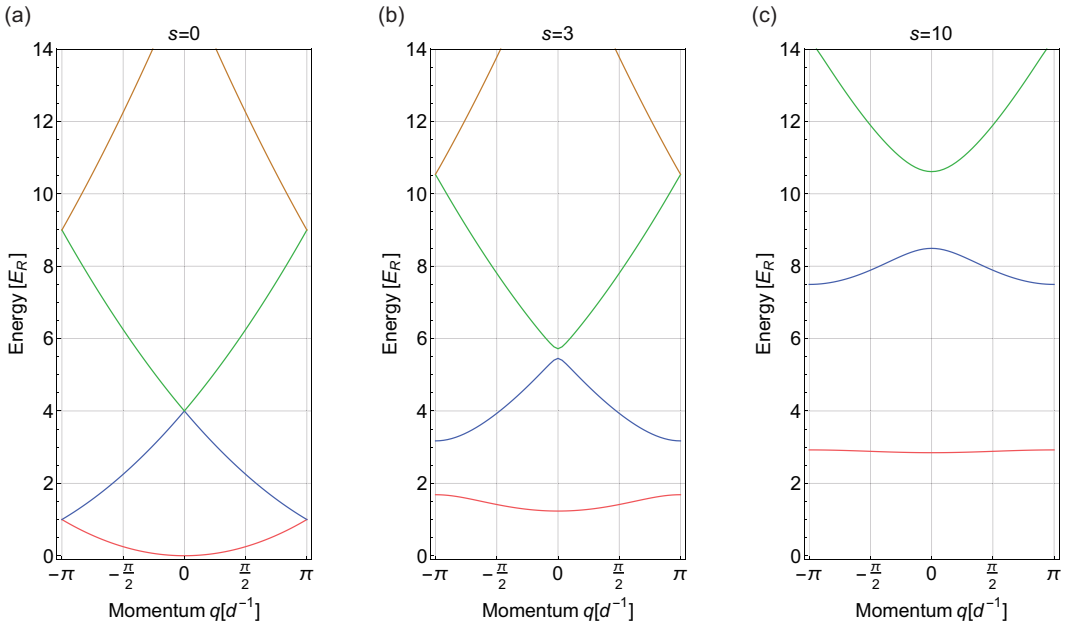

Figure 2.3.1: Band structure of monochromatic lattices. s denotes the potential depth scaled by the recoil energy E_{R}. The deeper the lattice potential is, the larger the band gap is, and the smaller the band width is, which means the suppressed tunneling.

so as to obtain smooth band structure since it determines step size of quasi-momentum q. To show the band dispersion $\epsilon_q^{(n)}$, we diagonalize N_{site} pieces of submatrices $H^{(q)}$ and plot the eigenvalues as a function of q (See Fig.2.3.1).

Using the eigenvector after diagonalization, we can calculate Bloch functions according to Eq.2.3.7 and momentum distributions

$$|\langle k|q,n\rangle|^2 = \sum_{m=0,\pm1,\cdots} \left|A_m^{(q,n)}\right|^2 \delta_{k,q+mK}. \tag{2.3.11}$$

Figure 2.3.2 shows the amplitude of the Bloch functions and the momentum distributions for some band indices and quasimomenta.

Extension to 3D monochromatic lattice

Since the 3D monochromatic lattice can be separated into 1D case ($H = H_x + H_y + H_z$), 3D dispersion is given by the sum of 1D dispersions, and its eigenvector becomes multiple of that of the 1D case:

$$\epsilon_{\boldsymbol{q}}^{(n_x,n_y,n_z)} = \epsilon_{q_x}^{(n_x)} + \epsilon_{q_y}^{(n_y)} + \epsilon_{q_z}^{(n_z)}, \tag{2.3.12}$$

$$\psi_{\boldsymbol{q}}^{(n_x,n_y,n_z)}(\boldsymbol{x}) = \psi_{q_x}^{(n_x)}(x)\psi_{q_y}^{(n_y)}(y)\psi_{q_z}^{(n_z)}(z). \tag{2.3.13}$$

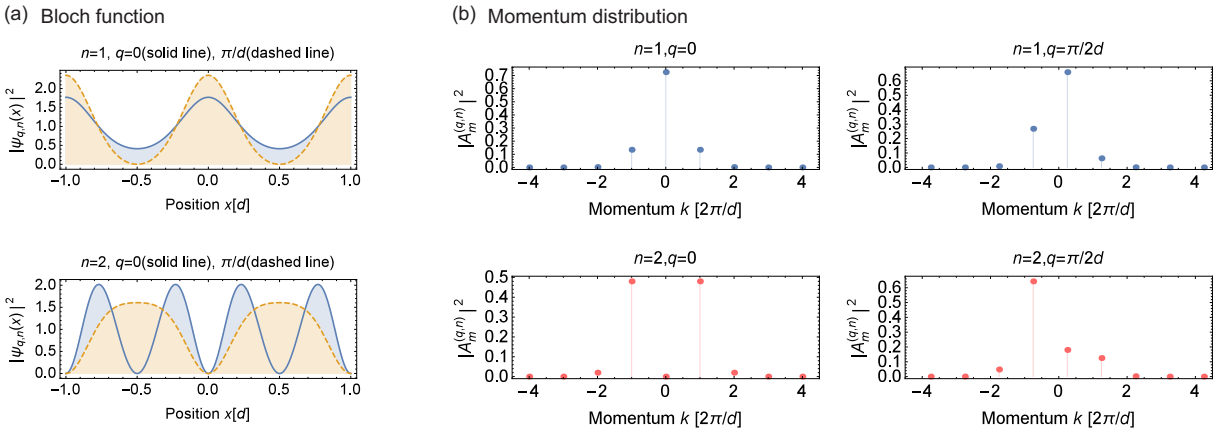

Figure 2.3.2: (a)Bloch functions and (b) momentum distributions in the monochromatic lattices. The lattice depth is set to $s = 3$ for (a) and $s = 10$ for (b).

2.3.2 1D superlattice

Band structure of 1-dimensional optical superlattice can be calculated in the same way for a monochromatic lattice. We represent the optical potential in Fourier components:

$$\begin{aligned} V(x) &= -V_{\text{long}}\cos^2(k_L x) - V_{\text{short}}\cos^2(2k_L x + \phi) \\ &= -\frac{V_{\text{long}} + V_{\text{short}}}{2} - \frac{V_{\text{long}}}{4}\left(e^{i2k_L x} + e^{-i2k_L x}\right) - \frac{V_{\text{short}}}{4}\left(e^{i(4k_L x+\phi)} + e^{-i(4k_L x+\phi)}\right). \end{aligned} \tag{2.3.14}$$

Then, the submatrix is

$$H_{ll'}^{(q)} = E_{\text{R}}^{\text{long}} \times \begin{cases} \left(\frac{q}{k_L} + 2l\right)^2 - \frac{s_{\text{long}}+s_{\text{long}}}{2} & l = l' \\ -\frac{s_{\text{long}}}{4} & |l - l'| = 1 \\ -\frac{s_{\text{short}}e^{i\phi}}{4} & l - l' = 2 \\ -\frac{s_{\text{short}}e^{-i\phi}}{4} & l - l' = -2 \\ 0 & \text{otherwise,} \end{cases} \tag{2.3.15}$$

where

$$E_{\text{R}}^{\text{long}} = \frac{\hbar^2 k_{\text{L}}^{\text{long}\,2}}{2M}, \quad k_{\text{L}}^{\text{long}} = \frac{2\pi}{\lambda_{\text{long}}}, \quad K = 2k_{\text{L}}^{\text{long}} \tag{2.3.16}$$

$$s_{\text{i}} = V_{\text{i}}/E_{\text{R}}^{\text{long}} \quad (\text{i} = \text{short, long}). \tag{2.3.17}$$

Figure 2.3.3 summarizes typical numerical calculation results in 1D superlattice with two characteristic relative phases $\phi = \pi/2, 0$.

2.3.3 Lieb lattice

When calculating the band structure of an optical Leib lattice, we can not separately consider the Hamiltonians of x and y due to existence of the diagonal lattice as in the Eq.2.2.4. To represent the Hamiltonian in a matrix form, the momentum bases $\{(k_x, k_y)\}$ should be nested such as

$$\begin{aligned}\{(k_x,k_y)\} &= \frac{2\pi}{L}\{(-N_{\text{site}},-N_{\text{site}}),(-(N_{\text{site}}-1),-N_{\text{site}}),\cdots,((N_{\text{site}}-1),-N_{\text{site}})| \\ &\quad (-N_{\text{site}},-(N_{\text{site}}-1)),\cdots,((N_{\text{site}}-1),-(N_{\text{site}}-1))| \\ &\quad\quad\vdots \\ &\quad (-N_{\text{site}},(N_{\text{site}}-1)),\cdots,((N_{\text{site}}-1),(N_{\text{site}}-1))\}. \end{aligned} \tag{2.3.18}$$

For the Lieb lattice potential in the Eq.2.2.4, the submatrix $H^{(\boldsymbol{q})}$ has the form such as

$$\begin{aligned} H^{(\boldsymbol{q})}_{\boldsymbol{l}\boldsymbol{l}'} &= \langle q_x + l_x K, q_y + l_y K| \left(\frac{\hbar^2 \hat{\boldsymbol{k}}^2}{2M} + V(\hat{\boldsymbol{x}})\right) |q_x + l'_x, q_y + l'_y\rangle \\ &= E^{\text{long}}_{\text{R}} \times \begin{cases} \left(\frac{q_x}{k_L} + 2l_x\right)^2 + \left(\frac{q_y}{k_L} + 2l_y\right)^2 + s_{\text{short}} + s_{\text{long}} + s_{\text{diag}}/2 & \boldsymbol{l} = \boldsymbol{l}' \\ -s_{\text{long}}/4 & \boldsymbol{l} - \boldsymbol{l}' = \pm\boldsymbol{e}_x \text{or} \pm \boldsymbol{e}_{\text{y}} \\ -s_{\text{short}}/4 & \boldsymbol{l} - \boldsymbol{l}' = \pm 2\boldsymbol{e}_x \text{or} \pm 2\boldsymbol{e}_{\text{y}} \\ -s_{\text{diag}}/4 \times \mathrm{e}^{i\pi/2} & \boldsymbol{l} - \boldsymbol{l}' = \boldsymbol{e}_x - \boldsymbol{e}_y \\ -s_{\text{diag}}/4 \times \mathrm{e}^{-i\pi/2} & \boldsymbol{l} - \boldsymbol{l}' = -(\boldsymbol{e}_x - \boldsymbol{e}_y) \\ 0 & \text{otherwise.} \end{cases} \end{aligned} \tag{2.3.19}$$

Here,

$$s_{\text{i}} = V_{\text{i}}/E^{\text{long}}_{\text{R}} \quad (\text{i} = \text{short, long, diag}). \tag{2.3.20}$$

To show the band dispersion $\epsilon^{(n)}_{\boldsymbol{q}}$, we diagonalize $(N_{\text{site}} \times N_{\text{site}})$ pieces of $(2l_{\max}+1)^2$ dimensional submatrices $H^{(\boldsymbol{q})}$ and plot the eigenenergy as a function of $\boldsymbol{q}$ (See Fig.2.3.4). We have to take special care for lattice potential depth $(V_{\text{short}}, V_{\text{long}}, V_{\text{diagonal}})$ in order to produce a flat band and Dirac cones. Recalling the section 2.1, the tight-binding model of a Lieb lattice includes only the nearest-neighbor hopping, which results in the energy spectrum in Fig.2.1.2. If there are residual hoppings like the next-nearest-neighbor hopping in addition to the nearest-neighbor hopping, the actual band structure is distorted from that of the Hubbard model. For example, a shallow lattice allows such residual hoppings. Conversely, the deeper a lattice potential is, the better the system well approximates the Hubbard model as can be seen in Tab.2.3.1.
The potential depth ratio between V_{diagonal} and V_{long} is important as well. If $V_{\text{diagonal}} = V_{\text{long}}$, the potential depth of A-site is equal to that of B, C-site, but numerically calculated band structure could not produce a flat-band and Dirac cones. If V_{diagonal} is slightly larger than V_{long}, a flat-band and Dirac cones appear like Fig.2.3.4. Inferring from the fact, we need to make V_{diagonal} deeper in order to suppress the next-nearest-neighbor hopping between B-site and C-site.

Table 2.3.1: Band width of optical Lieb lattice. Left end column shows lattice depths used in Fig.2.3.4. ΔE_{i} (i = 1st, 2nd, 3rd) means the width of each band, and $\Delta E_{\mathrm{total}}$ the band width from top of 3rd band to bottom of 1st band, which is proportional to the nearest neighbor tunneling as can be seen from Eq.2.1.4. $\Delta E_{\mathrm{2nd}}/\Delta E_{\mathrm{total}}$ indicates the ratio of the residual tunnelings between next nearest neighbors and the nearest neighbor tunneling.

$(s_{\mathrm{short}}, s_{\mathrm{long}}, s_{\mathrm{diag}})$	ΔE_{1st} $[E_{\mathrm{R}}]$	ΔE_{2nd} $[E_{\mathrm{R}}]$	ΔE_{3rd} $[E_{\mathrm{R}}]$	$\Delta E_{\mathrm{total}}$ $[E_{\mathrm{R}}]$	$\Delta E_{\mathrm{2nd}}/\Delta E_{\mathrm{total}}$
$(13, 13, 15.5)$	0.925	0.310	1.37	2.53	0.122
$(20, 20, 23)$	0.636	0.104	0.862	1.63	0.0638
$(34, 34, 37.4)$	0.350	0.0446	0.317	0.723	0.0616

In the Fig.2.3.5, we plot the Bloch functions

$$\psi^{(n)}_{q_x,q_z}(x,z) = \langle x,z|q_x,q_z,n\rangle = \frac{1}{\sqrt{L_x L_z}} \sum_{m_x,m_z=0,\pm1,\cdots} A^{n,(q_x,q_z)}_{(m_x,m_z)} e^{i(q_x+m_x K)x} e^{i(q_z+m_z K)z} \tag{2.3.21}$$

and the momentum distributions

$$|\langle k_x,k_z|q_x,q_z,n\rangle|^2 = \sum_{m_x,m_z=0,\pm1,\cdots} \left|A^{n,(q_x,q_z)}_{(m_x,m_z)}\right|^2 \delta_{k_x,q_x+m_x K}\delta_{k_z,q_z+m_z K}. \tag{2.3.22}$$

In 1st band and 3rd band, the Bloch functions spread over all the sublattices, while A-sublattice is not occupied in the 2nd band due to destructive interference of tunnelings from B, C-sublattice. Momentum distribution in 2nd band has no amplitude at $(k_x, k_z) = (0, 0)$.

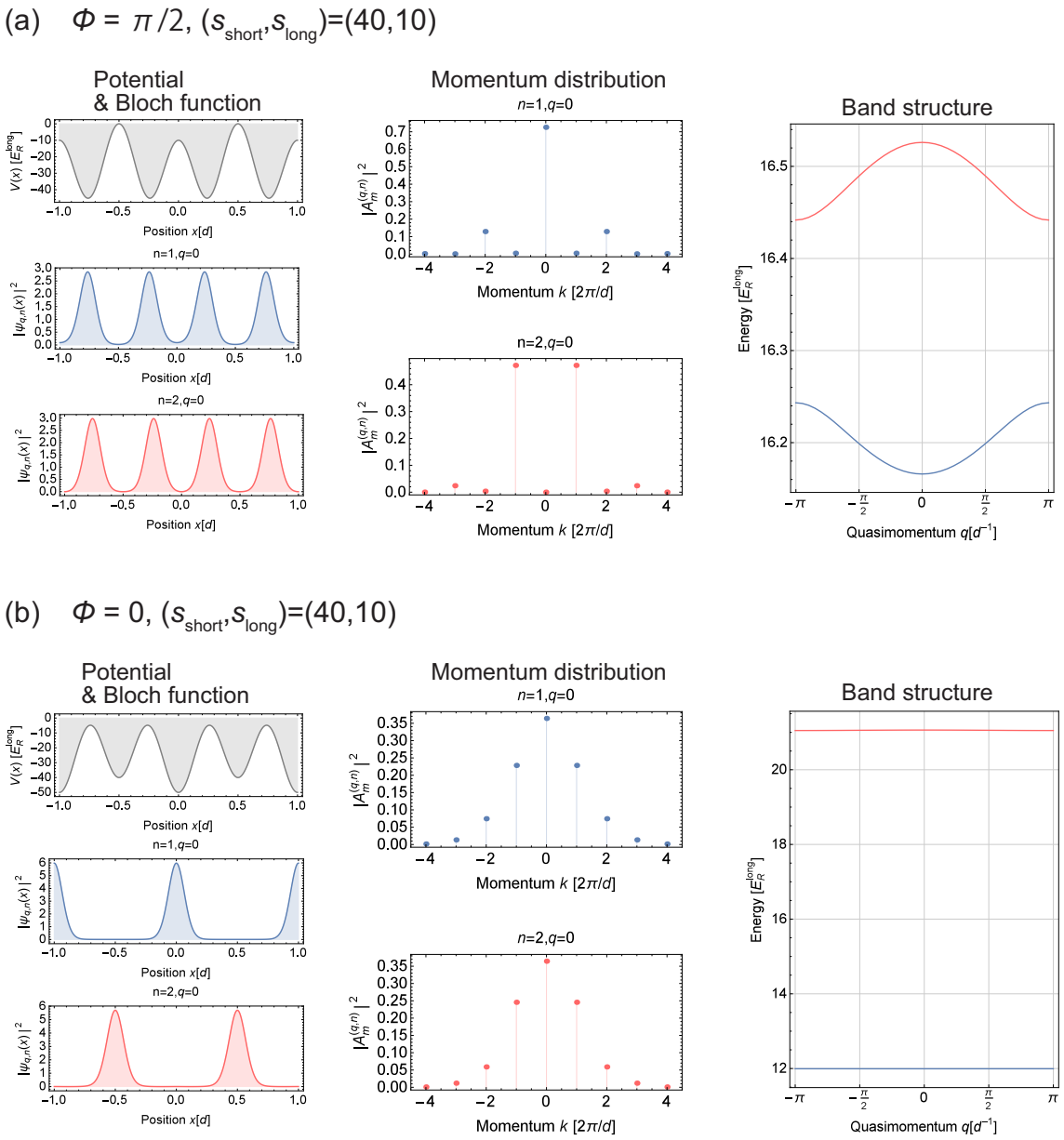

Figure 2.3.3: Typical numerical calculation results in the 1D superlattice. We show the optical potential and Bloch wave function (left column), momentum distributions (center column), and band structure (right column) up to 2nd band. (a) With the relative phase of $\phi = \pi/2$, the potential is dimerized. Bloch functions of 1st and 2nd band consist of superposition of wave-packets localized at each sublattice. Since the periodicity of the wave function is the same for the short lattice, the separation of the momentum peaks becomes $4\pi/d$. In dimerized lattice. The 1st-2nd band gap represents the intra-dimer tunneling. Therefore, the deeper the short lattice is, the smaller the 1st-2nd band gap becomes. (b)With relative phase of $\phi = 0$, the staggered potential is created. Bloch functions of 1st and 2nd band localize at each sublattice. Since the periodicity of the wave function is the same for the long lattice, the separation of the momentum peaks becomes $2\pi/d$. In the staggered lattice, the 1st-2nd band gap represents the energy difference between sublattices.

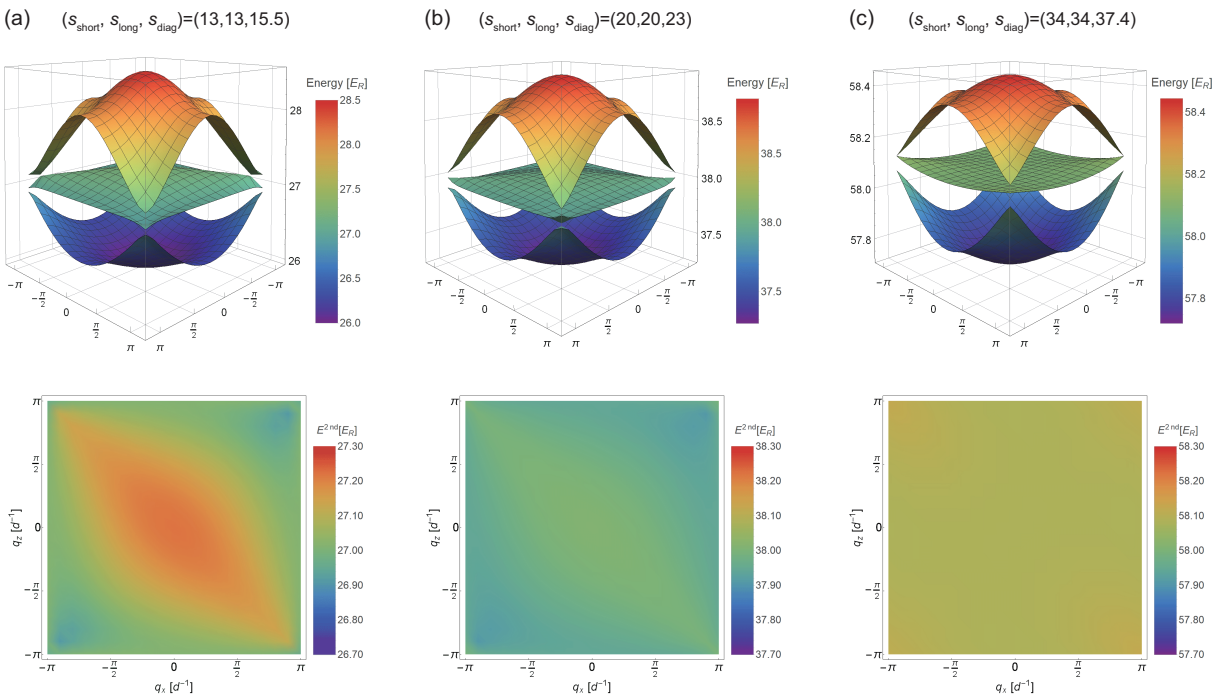

Figure 2.3.4: Band structure of optical Lieb lattice. $\{(s_{\mathrm{short}}, s_{\mathrm{long}}, s_{\mathrm{diag}})\}$ denotes the potential depths scaled by recoil energy E_{R}. Upper figures show the band structure up to 3rd band. Lower figures show density plot of 2nd band.

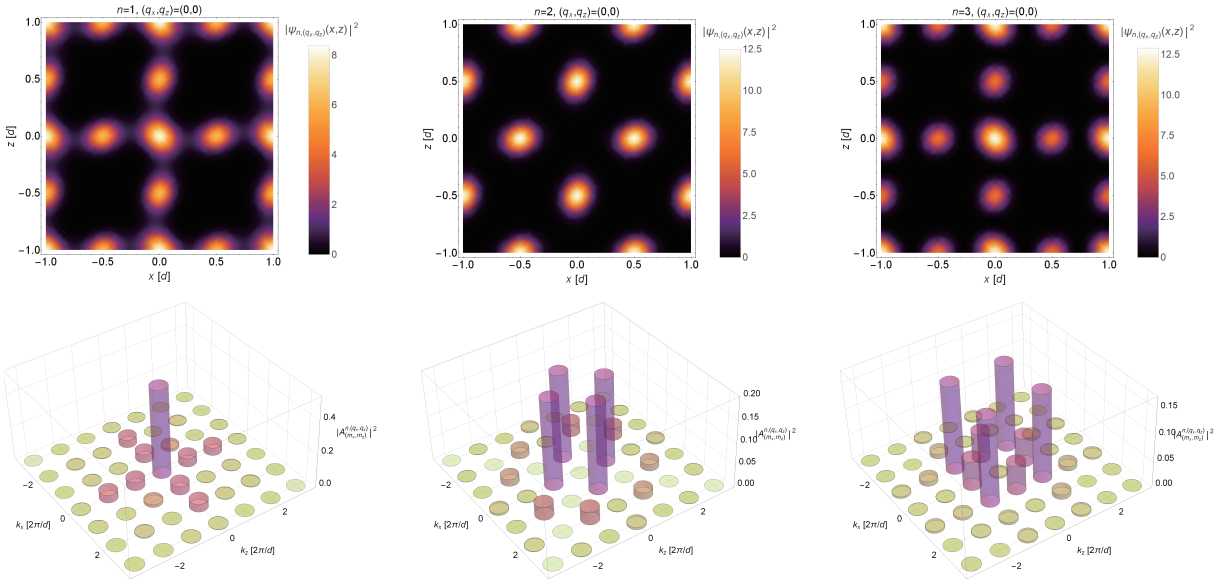

Figure 2.3.5: Bloch function (upper row) and momentum distribution (lower row) in an optical Lieb lattice of $(s_{\mathrm{short}}, s_{\mathrm{long}}, s_{\mathrm{diag}}) = (20, 20, 23)$. The band index differs in each column.

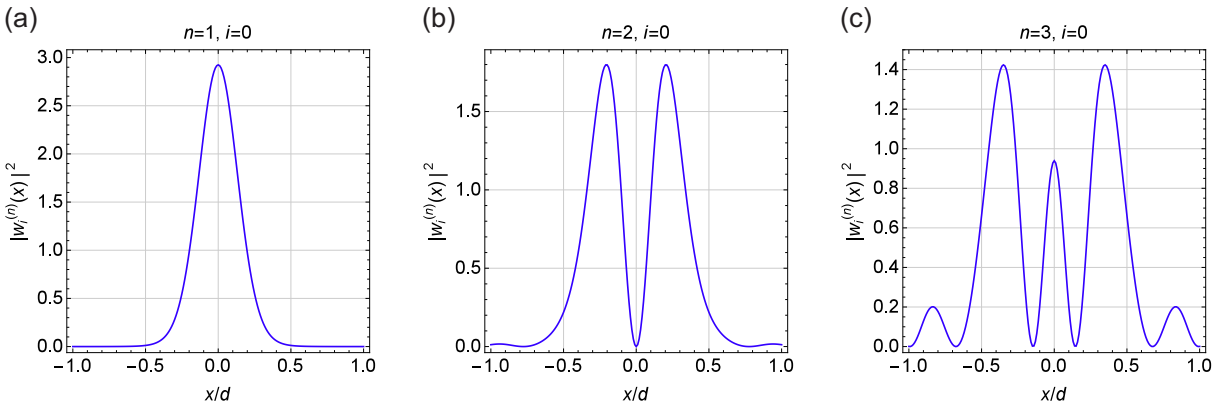

Figure 2.4.1: Wannier functions $|w_i^{(n)}(x)|^2$ for the lowest three energy bands at the lattice depth of $s = 10$.

2.4 Hubbard parameters in optical lattice

2.4.1 Simple cubic lattice

Wannier state

The eigenstate obtained by diagonalizing $H^{(q)}$ is Bloch state, which spreads all over the lattice. By superimposing the Bloch states, the Wannier state can be constructed:

$$|i, n\rangle = \frac{1}{\sqrt{N}} \sum_q \mathrm{e}^{-iqx_i} |q, n\rangle \tag{2.4.1}$$

which localizes at a certain site x_i with exponential decay. Figure 2.4.1 shows square of Wannier functions $|w_i^{(n)}(x)|^2 = |\langle x|i, n\rangle|^2$ with $n = 1, 2, 3$ and $i = 0$. Wannier state is defined as superposition of Bloch states. Since Bloch state has phase degree of freedom, Wannier state is not uniquely determined. We usually optimize the phase of Bloch states so that the resulting Wannier function $w_i^{(n)}(x)$ is maximally localized at a site i. In the following, the method to get such a Wannier function is described especially for a monochromatic lattice. Bloch vectors are given as eigenvectors of Hamiltonian $H^{(q)}$. Since the element of eigenvector is real number, the phase degree of freedom is only plus or minus. After numerical diagonalization of Hamiltonian for each quasimomentum q, the sign in front of the eigenvector is random. Then, we choose the sign so that the eigenvector smoothly changes according to q. For example, starting from $q = -\pi$, we calculate $||\boldsymbol{v}_q^{(n)} + \boldsymbol{v}_{q+\Delta q}^{(n)}||$ and $||\boldsymbol{v}_q^{(n)} - \boldsymbol{v}_{q+\Delta q}^{(n)}||$ using the eigenvectors $\boldsymbol{v}_q^{(n)}, \boldsymbol{v}_{q+\Delta q}^{(n)}$, and change the sign of $\boldsymbol{v}_{q+\Delta q}^{(n)}$ according to the magnitude relation:

$$\boldsymbol{v}_{q+\Delta q}^{(n)} = \begin{cases} \boldsymbol{v}_{q+\Delta q}^{(n)} & \text{if } ||\boldsymbol{v}_q^{(n)} + \boldsymbol{v}_{q+\Delta q}^{(n)}|| > ||\boldsymbol{v}_q^{(n)} - \boldsymbol{v}_{q+\Delta q}^{(n)}|| \\ -\boldsymbol{v}_{q+\Delta q}^{(n)} & \text{if } ||\boldsymbol{v}_q^{(n)} + \boldsymbol{v}_{q+\Delta q}^{(n)}|| \leq ||\boldsymbol{v}_q^{(n)} - \boldsymbol{v}_{q+\Delta q}^{(n)}||. \end{cases} \tag{2.4.2}$$

We repeat the above operation to determine the phase for all the quasimomenta. Figure 2.4.2 shows the norm of the normalized Bloch vectors and the resulting Wannier functions

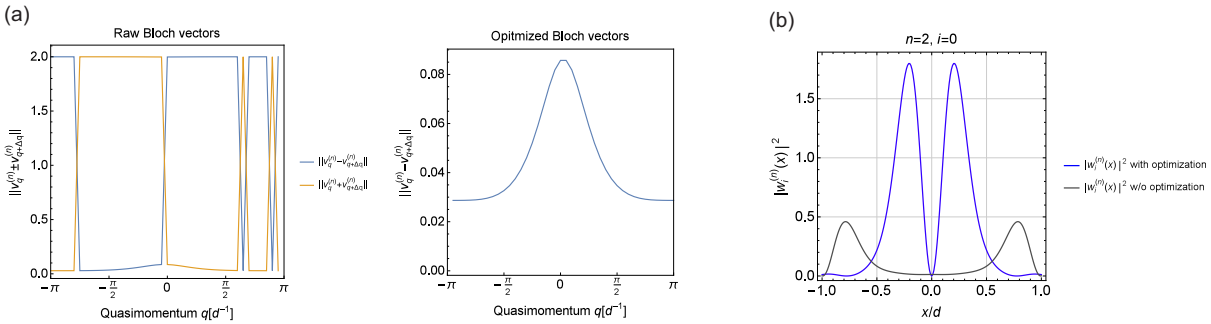

Figure 2.4.2: (a) Norm of the normalized Bloch vector of 2nd band (left) without optimization and (right) with optimization of the phase degree of freedom. After the optimization, the norm is smoothed. (b) Wannier functions of 2nd band at lattice depth of $s = 10$ with and without the optimization.

of 2nd band at the lattice depth $s = 10$. After the above optimization, a well-localized Wannier function is achieved.

Hubbard parameters: tunneling amplitude and on-site interaction

The tunneling between lattice sites $t_{\mathrm{ij}}^{(n)}$ is defined as a matrix element of the Hamiltonian in Wannier basis. With the Eq.2.4.1

$$\begin{aligned} t_{ij}^{(n)} &= \langle i,n|\, H\, |j,n\rangle = \frac{1}{N}\sum_q\sum_p \mathrm{e}^{iqx_i}\mathrm{e}^{-ipx_j}\,\langle q,n|\, H\, |p,n\rangle \\ &= \frac{1}{N}\sum_q \mathrm{e}^{iq(x_i-x_j)}\epsilon_q^{(n)}, \end{aligned} \tag{2.4.3}$$

The last line in Eq.2.4.3 means that the hopping matrix element is Fourier transformation of the energy dispersion. Figure 2.4.3 shows the calculated tunneling matrix elements for $(n, x_i - x_j) = (1, d), (1, 2d), (2, d)$.

The on-site interaction (extended to 3D lattice case) is also defined by the Wannier function such as

$$U = \frac{4\pi\hbar^2 a_s}{m}\int d^3x\, |\langle \boldsymbol{x}|\boldsymbol{i}, 1\rangle|^4 \tag{2.4.4}$$

where a_s is s-wave scattering length. In the Fig.2.4.4, we plot the on-site interaction in 3D monochromatic lattice with $d = 266$nm, $a_s = 10.55$nm.

2.4.2 Dimerized lattice

As mentioned in the section 2.4.1, since Wannier state is defined by superposition of Bloch states and depends on the phase of Bloch state like $|q,n\rangle \to e^{i\phi(q,n)}|q,n\rangle$, the Wannier state is not determined uniquely. It is appropriate to select the phase and band mixing so that the resulting Wannier state is well localized at a site. In this section, we describe the determination method especially for 1D dimerized lattice.

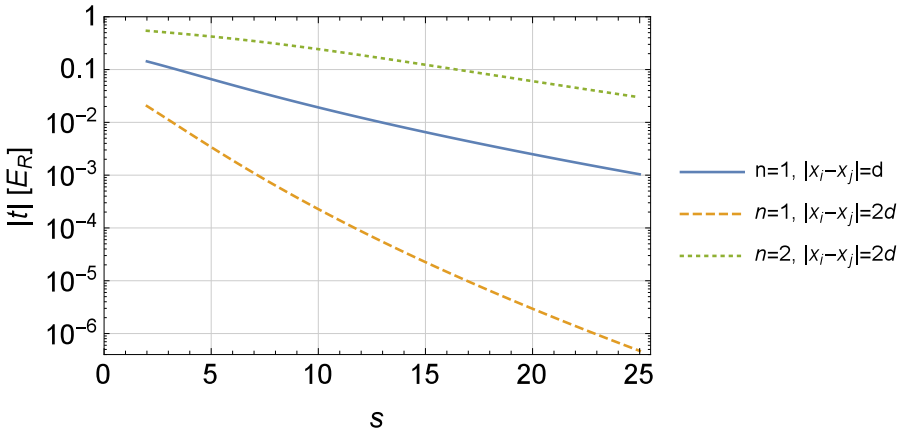

Figure 2.4.3: Tunneling matrix elements versus lattice depth. Tunneling to the nearest neighbors in the lowest band (solid line), to the next nearest neighbors in the lowest band (dashed line), and to the nearest neighbors in the 1st-excited band (dotted line) are shown.

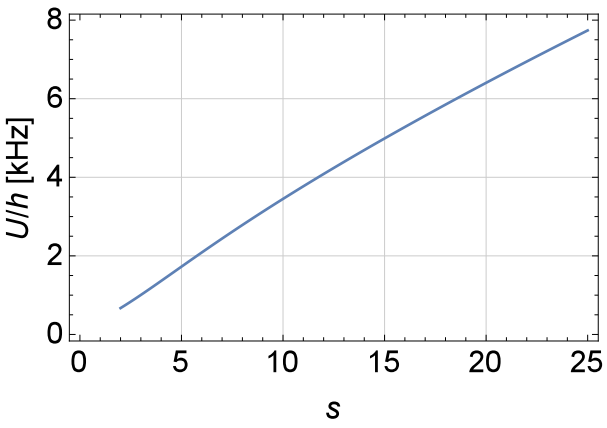

Figure 2.4.4: On-site interaction in 3D monochromatic lattice versus lattice depth. Here, lattice constant is $d = 266$nm, and s-wave scattering length is $a_s = 10.55$nm.

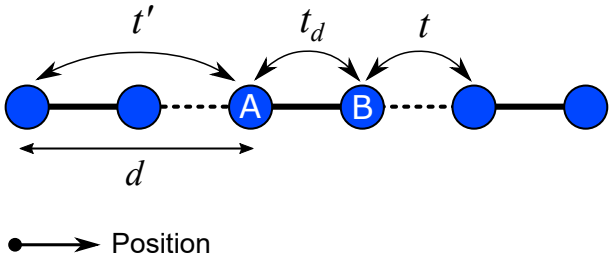

Figure 2.4.5: Extended tight-binding model in 1D dimerized lattice. We consider up to the next-nearest-neighbor tunneling.

Extended tight-binding model

We start with the tight-binding model in 1D dimerized lattice. Since there exists not only the nearest-neighbor tunneling but also the next-nearest-neighbor tunneling in the realistic system, we consider the extended tight-binding model as

$$H_{\mathrm{ETB}} = H_{\mathrm{TB}} + H_{\mathrm{S}} \tag{2.4.5}$$

$$H_{\mathrm{TB}} = -t_d \sum_i \left(a_i^\dagger b_i + \mathrm{H.c.} \right) - t \sum_i \left(a_i^\dagger b_{i-1} + \mathrm{H.c.} \right) \tag{2.4.6}$$

$$H_{\mathrm{S}} = \sum_{s=a,b} \sum_i \left[-t' \left(s_i^\dagger s_{i-1} + \mathrm{H.c.} \right) + \epsilon s_i^\dagger s_i \right], \tag{2.4.7}$$

where ϵ is offset energy, and t' the next-nearest-neighbor tunneling as can be seen in Fig.2.4.5. Substitute Fourier transformation for the creation and annihilation operators

$$c_i = \frac{1}{\sqrt{N}} \sum_k e^{ikx_{i,S}} c_k \quad c = \{a, b\}\,,\ S = \{A, B\}\,, \tag{2.4.8}$$

where N represents the site number, i the index of unit cell, S the index of sublattice within unit cell. For instance, the 1st term in Eq.2.4.6 becomes

$$\sum_i a_i^\dagger b_i = \sum_i \left(\frac{1}{\sqrt{N}} \sum_k e^{-ikx_{i,A}} a_k^\dagger \right) \left(\frac{1}{\sqrt{N}} \sum_{k'} e^{ik'x_{i,B}} b_{k'} \right) \tag{2.4.9}$$

$$= \frac{1}{N} \sum_{k,k'} \sum_i e^{ik'd/2} e^{-i(k-k')x_{i,A}} a_k^\dagger b_{k'} \tag{2.4.10}$$

$$= \sum_k e^{ikd/2} a_k^\dagger b_k. \tag{2.4.11}$$

We used the $x_{i,B} = x_{i,A} + d/2$ from 1st line to 2nd line, and $\sum_i e^{-i(k-k')x_{i,A}} = \delta_{k,k'}$ from 2nd line to 3rd line. Similarly calculating the other terms, Hamiltonian is diagonalized in terms of quasimomentum k:

$$H_{\mathrm{ETB}} = \sum_k \begin{pmatrix} a_k^\dagger & b_k^\dagger \end{pmatrix} \mathcal{T} \begin{pmatrix} a_k \\ b_k \end{pmatrix} \tag{2.4.12}$$

$$\mathcal{T} = \begin{pmatrix} \epsilon - t'\cos(kd) & -t_d e^{ikd/2} - te^{ikd/2} \\ -t_d e^{-ikd/2} - te^{ikd/2} & \epsilon - t'\cos(kd) \end{pmatrix}. \tag{2.4.13}$$

Determination method of Hubbard parameters

By diagonalizing the matrix $\mathcal{T}$ for every quasimomentum, we get the energy spectrum $\epsilon_k^{(n)}$ and eigenvectors $u_k^{(n)} =^t \left(u_{k,A}^{(n)} \;\; u_{k,B}^{(n)}\right)$. Parameters in $\mathcal{T}$ should be numerically optimized so that the resulting energy spectrum would reproduce that calculated from optical potential. Thus, tunneling parameters and energy offset can be determined. In addition, appropriate band-mixing is also settled at the same time.
Eigenvectors have the phase degree of freedom: an eigenvector multiplied by undecided phase $\phi(k,n)$ returns the same eigenvalue for the former eigenstate. Remaining problem is to decide the phase $\phi(k,n)$ so that correct Wannier function is obtained. There are several determination methods [76, 77]. Here, we adopt the method in [77]. The basic idea is as follows. Each Bloch wave needs to be summed up in-phase at each site $x_{i,S}$ $(S = A, B)$ so that Wannier state could be well localized at the site. First, we choose the phase such as

$$\phi(k,n) = \arg\left[e^{-ikx_{i,S}} u_{k,S}^{(n)} \psi_k^{(n)}\left(x_{i,S}\right)\right]. \tag{2.4.14}$$

Then, the resulting Wannier function

$$w_{i,S}(x) = \sum_k e^{-ikx_{i,S}} \sum_{n=1}^{2} u_{k,S}^{(n)} e^{-i\phi(k,n)} \psi_k^{(n)}(x_{i,S}) \tag{2.4.15}$$

would be well localized at the site $x_{i,S}$. When calculating $\phi(k,n)$ at each k, n, we have to choose a sublattice S. We calculate the amplitude

$$A_{k,n}^{(i,S)} = \left| e^{ikx_{i,S}} u_{k,S}^{(n)} \psi_k^{(n)}(x_{i,S}) \right| \tag{2.4.16}$$

for all the sublattices (A, B), and decide the phase $\phi(k,n)$ base on the sublattice which maximizes $A_{k,n}^{(i,S)}$:

$$\phi(k,n) = \arg\left[e^{-ikx_{i,S_{\max}}} u_{k,S_{\max}}^{(n)} \psi_k^{(n)}(x_{i,S_{\max}})\right], \tag{2.4.17}$$

where $S_{\max}$ is a sublattice (A or B) which maximizes the amplitude $A_{k,n}^{(i,S)}$.

Calculation result

Matrix $\mathcal{T}$ in Eq.2.4.13 is diagonalized with the same grid for band calculation from optical potential, and we numerically optimize tunneling parameters and energy offset so that summation of the square error of band-dispersion difference

$$E = \sum_{k,n} \left(\epsilon_k^{(n)}(\text{Real band}) - \epsilon_k^{(n)}(\text{TB model})\right)^2 \tag{2.4.18}$$

is minimized.
Figure 2.4.6 compares the band structure of dimerized lattice calculated from the optical potential and extended tight-binding model. We can see that the band structure is well reproduced. For the lattice depth of $(s_{\text{short}}, s_{\text{long}}) = (20, 15)$, the tunneling parameters and energy offset become

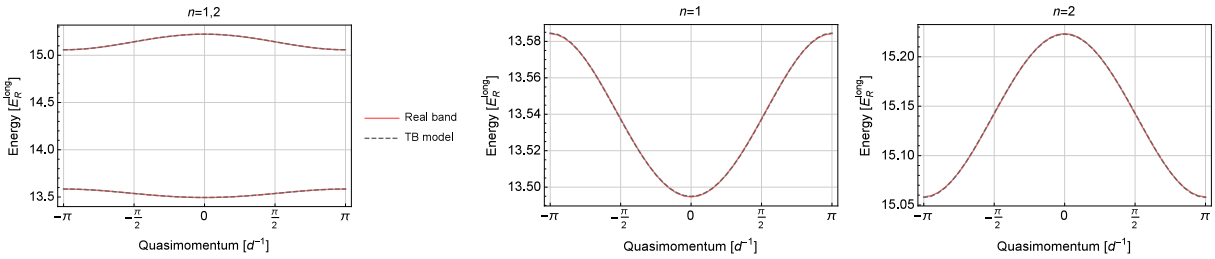

Figure 2.4.6: Band structure in dimerized lattice of $(s_{\text{short}}, s_{\text{long}}) = (20, 15)$ (solid line) and the extended tight-binding model after fitting (dashed line).

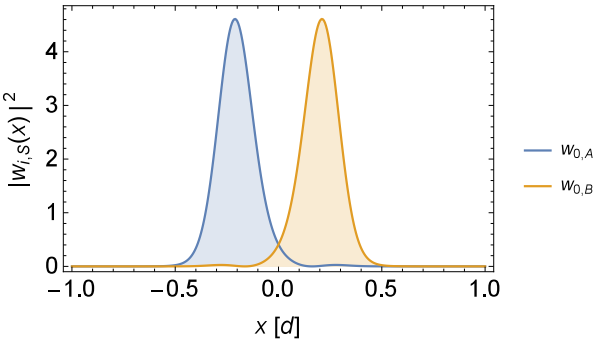

Figure 2.4.7: Wannier function in dimerized lattice of $(s_{\text{short}}, s_{\text{long}}) = (20, 15)$.

- $t_d = 0.8003\ E_{\text{R}}^{\text{long}}$
- $t = 0.06369\ E_{\text{R}}^{\text{long}}$
- $t' = -0.009444\ E_{\text{R}}^{\text{long}}$
- $\epsilon = 14.34\ E_{\text{R}}^{\text{long}}$.

Figure 2.4.7 shows the Wannier function in dimerized lattice. Wannier functions obtained through above procedures seem to be well localized at each sublattice.

Finally, we can calculate the on-site interaction. Our optical superlattice with $d =$ 532nm is created along x-axis, while optical square lattice with $d = 266$ nm exists in yz plane. Since these optical lattice are independent, on-site interaction can be obtained by separately calculating the Wannier functions and multiplying them:

$$U = \frac{4\pi\hbar^2 a_s}{m} \int dx\, |w_{\text{dimer}}(x)|^4 \int dy\, |w_{\text{1D}}(y)|^4 \int dz\, |w_{\text{1D}}(z)|^4 . \tag{2.4.19}$$

2.4.3 Lieb lattice

In this section, we introduce the Hubbard parameters for an optical Lieb lattice. Basically, the method is the same for dimerized lattice which is described in the section 2.4.2.

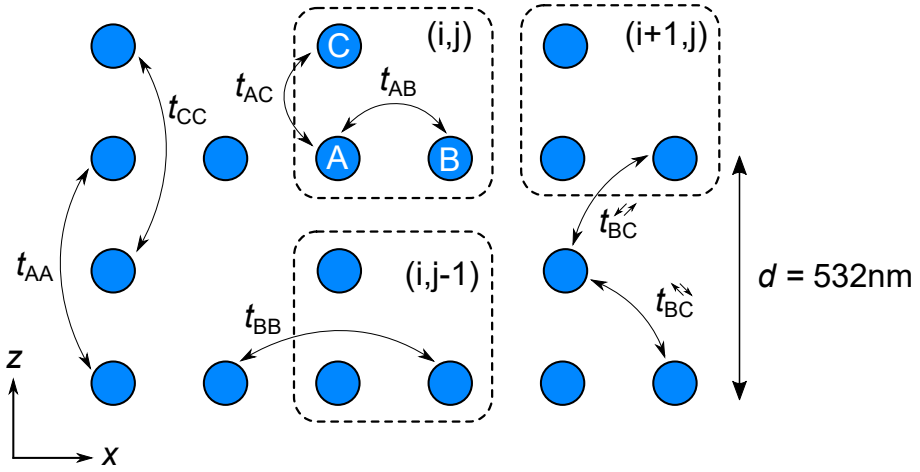

Figure 2.4.8: Extended tight-binding model in Lieb lattice.

As illustrated in the Fig. 2.4.8, the extended tight-binding model in our optical Lieb lattice is

$$
\begin{aligned}
H_{\mathrm{ETB}} &= H_{\mathrm{TB}} + H_{\mathrm{BC}} + H_{\mathrm{S}} && (2.4.20)\\
H_{\mathrm{TB}} &= \sum_{(i,j)} \Big[-t_{\mathrm{AB}} \left(a^{\dagger}_{(i,j)} b_{(i,j)} + a^{\dagger}_{(i,j)} b^{\dagger}_{(i-1,j)} \right) \\
&\qquad -t_{\mathrm{AC}} \left(a^{\dagger}_{(i,j)} c_{(i,j)} + a^{\dagger}_{(i,j)} c_{(i+1,j-1)} \right) \Big] + \mathrm{H.c.} && (2.4.21)\\
H_{\mathrm{BC}} &= \sum_{(i,j)} \Big[-t^{\searrow}_{\mathrm{BC}} \left(b^{\dagger}_{(i,j)} c_{(i,j)} + b^{\dagger}_{(i,j)} c_{(i+1,j-1)} \right) \\
&\qquad -t^{\nearrow}_{\mathrm{BC}} \left(b^{\dagger}_{(i,j)} c_{(i+1,j)} + b^{\dagger}_{(i,j)} c_{(i,j-1)} \right) \Big] + \mathrm{H.c.} && (2.4.22)\\
H_{\mathrm{S}} &= \sum_{(i,j)} \Big[-t_{\mathrm{AA}} \left(a^{\dagger}_{(i,j)} a_{(i+1,j)} + a^{\dagger}_{(i,j)} a_{(i,j+1)} + \mathrm{H.c.} \right) + \epsilon_{\mathrm{A}} a^{\dagger}_{(i,j)} a_{(i,j)} \\
&\qquad -t_{\mathrm{BB}} \left(b^{\dagger}_{(i,j)} b_{(i+1,j)} + \mathrm{H.c.} \right) + \epsilon_{\mathrm{B}} b^{\dagger}_{(i,j)} b_{(i,j)} \\
&\qquad -t_{\mathrm{CC}} \left(c^{\dagger}_{(i,j)} c_{(i,j-1)} + \mathrm{H.c.} \right) + \epsilon_{\mathrm{C}} b^{\dagger}_{(i,j)} c_{(i,j)} \Big], && (2.4.23)
\end{aligned}
$$

where (i,j) denotes the index of unit cell, $s^{\dagger}, s$ $(s = a, b, c)$ creation and annihilation operator at each sublattice, ϵ_{S} $(\mathrm{S} = \mathrm{A}, \mathrm{B}, \mathrm{C})$ energy offset. After Fourier transformation

$$
s_{(i,j)} = \frac{1}{\sqrt{N}} \sum_{\boldsymbol{k}} e^{i\boldsymbol{k}\cdot\boldsymbol{x}_{(i,j),S}} s_{\boldsymbol{k}}, \qquad (2.4.24)
$$

Hamiltonian is diagonalized for quasimomentum $\boldsymbol{k} = (k_x, k_z)$:

$$H_{\mathrm{ETB}} = \sum_{\boldsymbol{k}} \begin{pmatrix} a_{\boldsymbol{k}}^\dagger & b_{\boldsymbol{k}}^\dagger & c_{\boldsymbol{k}}^\dagger \end{pmatrix} \mathcal{T} \begin{pmatrix} a_{\boldsymbol{k}} \\ b_{\boldsymbol{k}} \\ c_{\boldsymbol{k}} \end{pmatrix}, \quad \mathcal{T} = \mathcal{T}_{\mathrm{TB}} + \mathcal{T}_{\mathrm{BC}} + \mathcal{T}_{\mathrm{S}} \tag{2.4.25}$$

$$\mathcal{T}_{\mathrm{TB}} = \begin{pmatrix} 0 & -2t_{\mathrm{AB}}\cos\left(k_x d/2\right) & -2t_{\mathrm{AC}}\cos\left(k_z d/2\right) \\ -2t_{\mathrm{AB}}\cos\left(k_x d/2\right) & 0 & 0 \\ -2t_{\mathrm{AC}}\cos\left(k_z d/2\right) & 0 & 0 \end{pmatrix} \tag{2.4.26}$$

$$\mathcal{T}_{\mathrm{BC}} = \sum_{D=\nwarrow\!\!\searrow(-),\swarrow\!\!\nearrow(+)} \begin{pmatrix} 0 & 0 & 0 \\ 0 & 0 & -2t_{\mathrm{BC}}^D\cos\left(k_x d/2 \pm k_z d/2\right) \\ 0 & -2t_{\mathrm{BC}}^D\cos\left(k_x d/2 \pm k_z d/2\right) & 0 \end{pmatrix} \tag{2.4.27}$$

$$\mathcal{T}_{\mathrm{S}} = \begin{pmatrix} \epsilon_{\mathrm{A}} - t_{\mathrm{AA}}\left[\cos\left(k_x d\right) + \cos\left(k_z d\right)\right] & 0 & 0 \\ 0 & \epsilon_{\mathrm{B}} - t_{\mathrm{BB}}\cos\left(k_x d\right) & 0 \\ 0 & 0 & \epsilon_{\mathrm{C}} - t_{\mathrm{CC}}\cos\left(k_z d\right) \end{pmatrix}. \tag{2.4.28}$$

We diagonalize the matrix $\mathcal{T}$ for every quasimomentum, and numerically optimize each parameter so that the resulting eigenvalues reproduce the band structure by optical potential. When fitting, we assume $t_{\mathrm{AB}} = t_{\mathrm{AC}}, t_{\mathrm{BB}} = t_{\mathrm{CC}}, \epsilon_{\mathrm{B}} = \epsilon_{\mathrm{C}}$ for isotropic Lieb lattice, and neglect the diagonal tunneling along the diagonal lattice $t_{\mathrm{BC}}^{\nwarrow\!\!\searrow}$ since it must be much smaller than others. Figure 2.4.9 shows the fitted tight-binding model for the optical Lieb lattice of $(s_{\mathrm{short}}, s_{\mathrm{long}}, s_{\mathrm{diag}}) = (20, 20, 23)$. The fitted parameters are

- $t_{\mathrm{AB}} = 0.2823 E_{\mathrm{R}}^{\mathrm{long}}$
- $t_{\mathrm{BC}}^{\swarrow\!\!\nearrow} = 0.0223 E_{\mathrm{R}}^{\mathrm{long}}$
- $t_{\mathrm{AA}} = -0.0256 E_{\mathrm{R}}^{\mathrm{long}}$
- $t_{\mathrm{BB}} = -0.0056 E_{\mathrm{R}}^{\mathrm{long}}$
- $\epsilon_{\mathrm{A}} = 38.14 E_{\mathrm{R}}^{\mathrm{long}}$
- $\epsilon_{\mathrm{B}} = 37.95 E_{\mathrm{R}}^{\mathrm{long}}$.

Then, using the eigenvectors $u_{\boldsymbol{k},S}^{(n)}$ and the phase such as

$$\phi(\boldsymbol{k}, n) = \arg\left[e^{-i\boldsymbol{k}\cdot\boldsymbol{x}_{(i,j),S_{\max}}} u_{\boldsymbol{k},S_{\max}}^{(n)} \psi_{\boldsymbol{k}}^{(n)}(\boldsymbol{x}_{(i,j),S_{\max}})\right], \tag{2.4.29}$$

we calculate the Wannier function

$$w_{(i,j),S}(\boldsymbol{x}) = \sum_{\boldsymbol{k}} e^{-i\boldsymbol{k}\cdot\boldsymbol{x}_{(i,j),S}} \sum_{n=1}^{3} u_{\boldsymbol{k},S}^{(n)} e^{-i\phi(\boldsymbol{k},n)} \psi_{\boldsymbol{k}}^{(n)}\left(\boldsymbol{x}_{(i,j),S}\right). \tag{2.4.30}$$

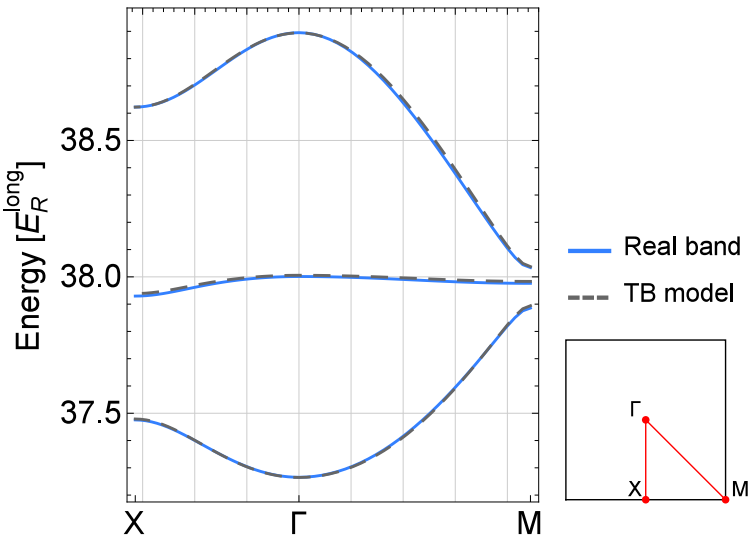

Figure 2.4.9: Band structure in the optical Lieb lattice of $(s_{\text{short}}, s_{\text{long}}, s_{\text{diag}}) = (20, 20, 23)$ (solid lines) and the extended tight-binding model after fitting (dashed lines).

In the Fig.2.4.10, we plot the Wannier functions. As can be seen from Fig.2.4.10(b), Wannier function of B-sublattice is more localized than that of A-sublattice even though there is no large difference of energy offsets. This is because the harmonic confinement for B-sublattice is tighter than for A-sublattice: B-sublattice consists of V^z_{long} and V_{diag}, while A-sublattice consists of V^x_{long} and V^z_{long}. Since the lattice spacing of diagonal lattice is shorter than that of long lattice, diagonal lattice creates tighter confinement than long lattice at the same lattice depth.
At last, we calculate the on-site interaction. Our Lieb lattice is created in x-z plane, while the confinement potential along y axis is made by monochromatic lattice with lattice spacing $d = 266$ nm. Since these Wannier functions are independent on each other, on-site interaction can be written as

$$U_S = \frac{4\pi\hbar^2 a_s}{m} \int dxdz \left| w_S^{\text{Lieb}}(x,z) \right|^4 \int dy \left| w_{\text{1D}}(y) \right|^4, \tag{2.4.31}$$

where $S = A, B, C$.
Figure 2.4.11 shows the on-site interactions in an optical Lieb lattice. B-sublattice has larger on-site interaction than A-sublattice due to difference of the Wannier functions.

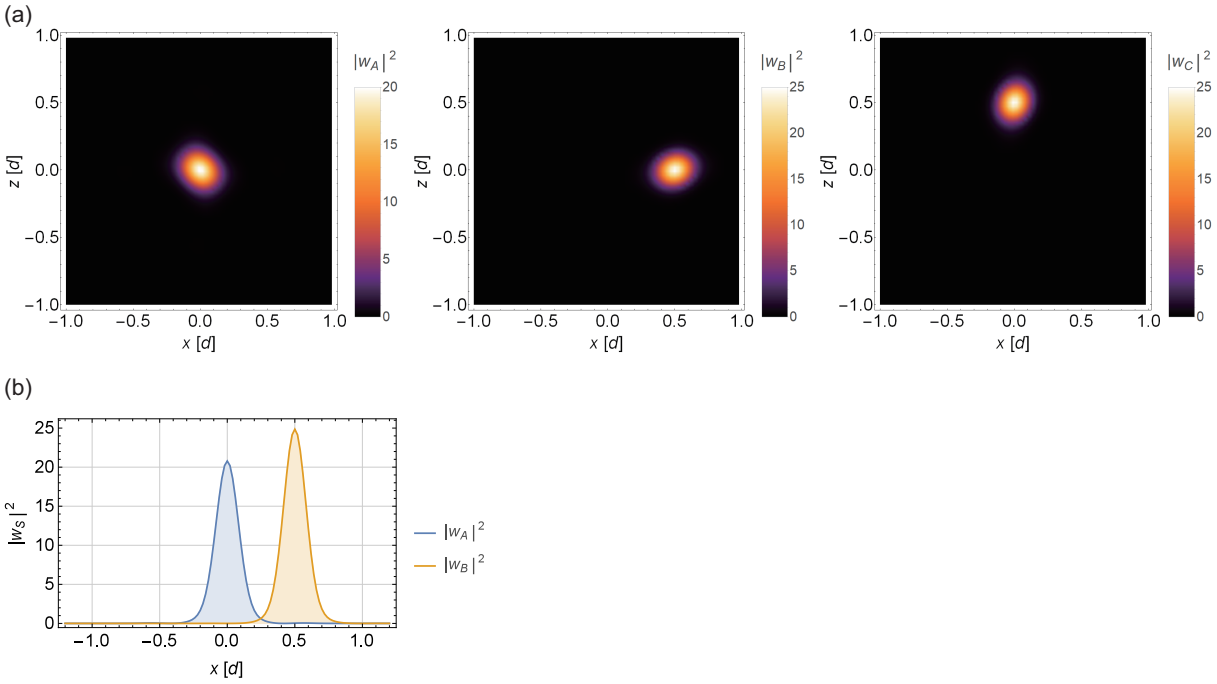

Figure 2.4.10: (a) Wannier Functions of each sublattice in an optical Lieb lattice of $(s_{\text{short}}, s_{\text{long}}, s_{\text{diag}}) = (20, 20, 23)$. (b) Cross section of the Wannier functions along the x axis at $z = 0$.

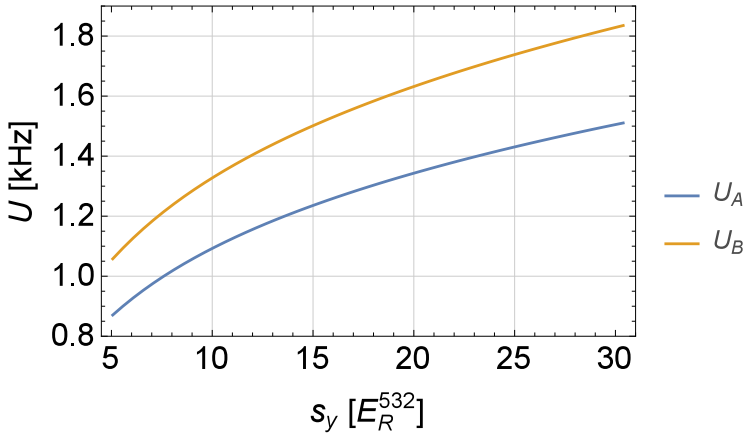

Figure 2.4.11: On-site interaction in an optical Lieb lattice of $(s_{\text{short}}, s_{\text{long}}, s_{\text{diag}}) = (20, 20, 23)$ versus lattice depth of confinement potential along the y axis. The s-wave scattering length is set to $a_s = 5.6$nm.

2.5 Bogoliubov theory

2.5.1 Gross-Pitaevskii equation

The properties of a BEC are described by the Gross-Pitaevskii equation (GPE) [78]:

$$i\hbar\frac{\partial\Psi(\boldsymbol{x},t)}{\partial t}=\left(-\frac{\hbar^2}{2m}\nabla^2+V(\boldsymbol{x})+g|\Psi(\boldsymbol{x},t)|^2\right)\Psi(\boldsymbol{x},t) \tag{2.5.1}$$

where $V(\boldsymbol{x})$ is the external potential, $g=4\pi\hbar^2a/m$, $a(=5.53\text{ nm})$ is the s-wave scattering length between the ${}^1S_0$ ground states of ^{174}Yb atoms, and m is the mass of ^{174}Yb atom. We consider the solution $\Psi(\boldsymbol{x},t)=e^{-i\mu t/\hbar}\psi(\boldsymbol{x})$ where μ is the chemical potential and $\psi(\boldsymbol{x})$ satisfies

$$\left(-\frac{\hbar^2}{2m}\nabla^2+V(\boldsymbol{x})+g|\psi(\boldsymbol{x})|^2\right)\psi(\boldsymbol{x})=\mu\psi(\boldsymbol{x}). \tag{2.5.2}$$

To apply the GPE to an optical lattice system, we consider the periodic optical lattice potential for the external potential $V(\boldsymbol{x})$. Here, we simplify the calculation by starting with the tight-binding approximation [79]. We expand the wave-function of a BEC $\psi(\boldsymbol{x})$ in terms of the Wannier function $w_i(\boldsymbol{x})$:

$$\psi(\boldsymbol{x})=\sum_i\psi_i w_i(\boldsymbol{x}) \tag{2.5.3}$$

where i is the index of lattice sites. Substitute the ansatz(2.5.3) for the GPE(2.5.2) and leave the overlap integral between the neighboring sites, the discrete GPE

$$\mu\psi_i=-\sum_{j\neq i}J_{ij}\psi_j+\epsilon_i\psi_i+U_i|\psi_i|^2\psi_i \tag{2.5.4}$$

is obtained. Each parameter is defined as

$$J_{ij} = -\int \mathrm{d}^3x\; w_i^*(\boldsymbol{x})\left(-\frac{\hbar^2}{2m}\nabla^2+V(\boldsymbol{x})\right)w_j(\boldsymbol{x}) \tag{2.5.5}$$

$$\epsilon_i = \int \mathrm{d}^3x\; w_i^*(\boldsymbol{x})\left(-\frac{\hbar^2}{2m}\nabla^2+V(\boldsymbol{x})\right)w_i(\boldsymbol{x}) \tag{2.5.6}$$

$$U_i = g\int \mathrm{d}^3x\;|w_i(\boldsymbol{x})|^4, \tag{2.5.7}$$

where J_{ij} is the tunneling amplitude, ϵ_i is the enegy offset, and U_i is the on-site interaction, which can be calculated from the optical lattice potential.

To apply the Eq.(2.5.4) to a Lieb lattice, we split the amplitude of the wave function into three sublattices. In the case of an ideal Lieb lattice, the time-independent GPE is written as

$$\begin{cases} -J(\psi_{(i-1,j),B}+\psi_{(i,j),B}+\psi_{(i,j),C}+\psi_{(i,j-1),C})+U|\psi_{(i,j),A}|^2\psi_{(i,j),A}=\mu\psi_{(i,j),A} \\ -J(\psi_{(i,j),A}+\psi_{(i+1,j),A})+U|\psi_{(i,j),B}|^2\psi_{(i,j),B}=\mu\psi_{(i,j),B} \\ -J(\psi_{(i,j),A}+\psi_{(i,j+1),A})+U|\psi_{(i,j),C}|^2\psi_{(i,j),C}=\mu\psi_{(i,j),C}. \end{cases} \tag{2.5.8}$$

where (i, j) is the index of unit cells, and A, B, C are the index of sublattices in a unit cell. The energy offset terms are omitted for simplicity. Since the GPE(2.5.8) has a lot of solutions, we should choose the Bloch solutions:

$$\psi_{(i,j),S} = \sqrt{n} e^{i\boldsymbol{k}\cdot\boldsymbol{x}_{i,S}} \phi_{k,S} \tag{2.5.9}$$

where $n = N/N_{\text{cell}}$ is the particle number in a unit cell, and $S = A, B, C$. Due to normalization condition for the wave function of a BEC, $\phi_{k,S}$ should satisfy

$$\sum_S |\phi_{k,S}|^2 = 1. \tag{2.5.10}$$

The GPE in the tight-binding approximation is given as

$$H(nU, \phi_k)\phi_k = \mu\phi_k, \tag{2.5.11}$$

where

$$\phi_k = (\phi_{k,A}, \phi_{k,B}, \phi_{k,C})^{\mathrm{T}}, \tag{2.5.12}$$

$$H(nU, \phi_k) = \begin{pmatrix} nU|\phi_{k,A}|^2 & -2J\cos(k_x d/2) & -2J\cos(k_z d/2) \\ -2J\cos(k_x d/2) & nU|\phi_{k,B}|^2 & 0 \\ -2J\cos(k_z d/2) & 0 & nU|\phi_{k,C}|^2 \end{pmatrix}. \tag{2.5.13}$$

$\phi_{k,S}$ and μ are determined by numerically solving the Eq.(2.5.10) and Eq.(2.5.13) simultaneously. Though $\phi_{k,S}$ could be complex number in general, we may consider only solutions of the real number except for uncertainty of the whole phase: at least for the lowest band, the wave functions at each sublattice must be summed up in-phase.

The energy per particle is given as

$$\frac{E}{N} = \phi_k^\dagger H\left(\frac{1}{2}nU, \phi_k\right)\phi_k. \tag{2.5.14}$$

We can easily extend this model to a realistic Lieb lattice by taking into account the following terms.

- Tunneling between B-sublattice and C-sublattice: $-2J_{BC}\cos(k_x d/2 + k_z d/2)$
- Inter-unit-cell tunneling: $-2J_{AA}[\cos(k_x d)+\cos(k_z d)], -2J_{BB}\cos(k_x d), -2J_{CC}\cos(k_z d)$
- Sublattice-dependent on-site interaction: $U \to U_A, U_B, U_C$
- Energy offset: $\epsilon_A, \epsilon_B, \epsilon_C$

For the lattice depth of $(s_{\text{long}}, s_{\text{short}}, s_{\text{diag}}) = (13, 13, 15.5)$ in the Lieb lattice configuration, the tunneling, on-site interaction, and energy offset are $J = 0.433, J_{BC} = 0.0590, J_{AA} = -0.0674, J_{BB} = J_{CC} = -0.0218, U_A = 0.198, U_B = U_C = 0.246, \epsilon_A = 27.2, \epsilon_B = \epsilon_C = 27.1$ in unit of E_{R}.

2.5.2 Bogoliubov-de Genne equation

The energy spectrum of the GPE corresponds to the case where the whole BEC occupies a single band at a single wave number k. To calculate the excitation spectrum when the BEC experiences a perturbation, we should solve the Bogoliubov-de Gennes equation (BdGE). Here, the perturbation is taken into account in the time-dependent GPE [78].

We start with a general theory. We consider a wave function such that the wave function of the GPE is perturbed by $u(\boldsymbol{x}), v(\boldsymbol{x})$:

$$\mathrm{e}^{-i\mu t/\hbar}\left[\psi(\boldsymbol{x}) + u(\boldsymbol{x})\mathrm{e}^{-i\omega t} + v^*(\boldsymbol{x})\mathrm{e}^{i\omega t}\right]. \tag{2.5.15}$$

Substituting Eq.(2.5.15) for $\Psi(\boldsymbol{x}, t)$ in the time-dependent GPE(2.5.1), and taking the 1st order of $u(\boldsymbol{x}), v(\boldsymbol{x})$, we obtain the BdGE:

$$\begin{cases} \left(-\frac{\hbar^2}{2m}\nabla^2 + V(\boldsymbol{x}) - \mu + 2g|\psi(\boldsymbol{x})|^2\right) u(\boldsymbol{x}) + g\psi(\boldsymbol{x})^2 v(\boldsymbol{x}) = \hbar\omega u(\boldsymbol{x}) \\ \left(-\frac{\hbar^2}{2m}\nabla^2 + V(\boldsymbol{x}) - \mu + 2g|\psi(\boldsymbol{x})|^2\right) v(\boldsymbol{x}) + g\psi^*(\boldsymbol{x})^2 u(\boldsymbol{x}) = -\hbar\omega v(\boldsymbol{x}). \end{cases} \tag{2.5.16}$$

The eigenvalue $\hbar\omega$ gives the Bogoliubov excitation spectrum.

The BdGE has twice as large dimensions as the original GPE. Therefore, half of the solutions do not have physical meanings. We select the eigenvalues so that the corresponding eigenvectors have a positive norm, which is defined as

$$\int \mathrm{d}^3x\ (|u(\boldsymbol{x})|^2 - |v(\boldsymbol{x})|^2). \tag{2.5.17}$$

In the same way as the GPE, we expand $u(\boldsymbol{x}), v(\boldsymbol{x})$ in terms of plane waves to apply the BdGE to a lattice system. First, we consider the solution of the time-independent GPE with a quasimomentum $\boldsymbol{k}$:

$$\psi_k(\boldsymbol{x}) = \sqrt{n}\sum_S \phi_{k,S} \sum_{(i,j)} \mathrm{e}^{i\boldsymbol{k}\cdot\boldsymbol{x}_{(i,j)}} w_{(i,j),S}(\boldsymbol{x}). \tag{2.5.18}$$

$u(\boldsymbol{x}), v(\boldsymbol{x})$ have a quasimomentum shifted by $\boldsymbol{q}$:

$$u(\boldsymbol{x}) = \sqrt{n}\sum_S u_{q,S} \sum_{(i,j)} \mathrm{e}^{i(\boldsymbol{k}+\boldsymbol{q})\cdot\boldsymbol{x}_{(i,j),S}} w_{(i,j),S}(\boldsymbol{x}) \tag{2.5.19}$$

$$v^*(\boldsymbol{x}) = \sqrt{n}\sum_S v^*_{q,S} \sum_{(i,j)} \mathrm{e}^{i(\boldsymbol{k}-\boldsymbol{q})\cdot\boldsymbol{k}-\boldsymbol{q}_{(i,j),S}} w_{(i,j),S}(\boldsymbol{x}). \tag{2.5.20}$$

Substituting Eq.(2.5.18), (2.5.19), (2.5.20) for the BdGE(2.5.16), we obtain the matrix form such as

$$\begin{pmatrix} H_{k+q}(2nU, \phi_k) - \mu I & G(nU, \phi_k) \\ -G^*(nU, \phi_k) & -H_{k-q}(2nU, \phi_k) + \mu I \end{pmatrix} \begin{pmatrix} u_q \\ v_q \end{pmatrix} = \hbar\omega_q \begin{pmatrix} u_q \\ v_q \end{pmatrix} \tag{2.5.21}$$

where $u_q = (u_{q,A}, u_{q,B}, u_{q,C})^{\mathrm{T}}$, $v_q = (v_{q,A}, v_{q,B}, v_{q,C})^{\mathrm{T}}$, I is the identity matrix and

$$H_{k\pm q}(2nU, \phi_k) = \begin{pmatrix} 2nU|\phi_{k,A}|^2 & -2J\cos\left((k_x \pm q_x)d/2\right) & -2J\cos\left((k_z \pm q_z)d/2\right) \\ -2J\cos\left((k_x \pm q_x)d/2\right) & 2nU|\phi_{k,B}|^2 & 0 \\ -2J\cos\left((k_z \pm q_z)d/2\right) & 0 & 2nU|\phi_{k,C}|^2 \end{pmatrix}, \tag{2.5.22}$$

$$G(nU, \phi_k) = \begin{pmatrix} nU\phi_{k,A}^2 & 0 & 0 \\ 0 & nU\phi_{k,B}^2 & 0 \\ 0 & 0 & nU\phi_{k,C}^2 \end{pmatrix}. \tag{2.5.23}$$

After numerically solving the Hamiltonian, we select the solution in which the norm

$$\sum_S \left(|u_{q,S}|^2 - |v_{q,S}|^2\right) \tag{2.5.24}$$

is positive.

Figure 2.5.1 (a) shows the numerical calculation result of GPE(2.5.11) and BdGE(2.5.21) with $(nU_A/J, nU_B/J) = (1.5, 1.86)$ and $(0, 0)$ in the realistic Lieb lattice of $(s_{\mathrm{long}}, s_{\mathrm{short}}, s_{\mathrm{diag}}) = (13, 13, 15.5)$. We use the GPE for the lowest band, and the BdGE with $\boldsymbol{q} = \boldsymbol{0}$ for the higher bands. Around X point, the 2nd band is strongly distorted by the mean-field interaction. Once the interaction strength exceeds the band gap, the excitation energy to the 2nd band gets zero (Fig. 2.5.1 (b)) and the wave function of the ground state at X point starts to spread over C-sublattice (Fig. 2.5.1 (c)).

2.5.3 Density distribution in lattice

Using the GPE(Eq.2.5.11), we can know one-to-one correspondence between μ and n. Assuming a local density approximation, the density distribution is written as

$$n(\mu_0, \boldsymbol{x}) = n(\mu_0 - V_{\mathrm{ext}}(\boldsymbol{x})) \tag{2.5.25}$$

where μ_0 is the chemical potential at the trap center, and $V_{\mathrm{ext}}(\boldsymbol{x})$ is the external potential. $V_{\mathrm{ext}}(\boldsymbol{x})$ has a quadratic form such as $V(\boldsymbol{x}) = v|\boldsymbol{x}|^2 = \frac{1}{2}m\bar{\omega}^2 d^2|\boldsymbol{x}|^2$, where $\bar{\omega} = \sqrt[3]{\omega_x\omega_y\omega_z}$ is the geometric mean of the trap frequencies and d is the lattice constant. μ_0 is determined so as to reproduce the total atom number N_{tot}, which is given as $N_{\mathrm{tot}} = \int \mathrm{d}\boldsymbol{x}\; n(\mu_0, \boldsymbol{x})$. Since the atoms are distributed in a 2D array of 1D tubes in our experiments described in the main text, we assume that the density distribution is nearly uniform along the y direction perpendicular to the Lieb lattice plane (x-z) and gets to zero where $\mu_0 = V_{\mathrm{ext}}(\boldsymbol{x})$ is satisfied. We take the volume element of the integral as a thin cylinder with the radius $r = \sqrt{x^2 + z^2}$ in the x-z plane and height $2\sqrt{\mu_0/v - r^2}$ along the y direction:

$$N_{\mathrm{tot}} = \int_0^{\sqrt{\mu_0/v}} \mathrm{d}r\; 4\pi r\sqrt{\frac{\mu_0}{v} - r^2}\; n(\mu_0 - vr^2). \tag{2.5.26}$$

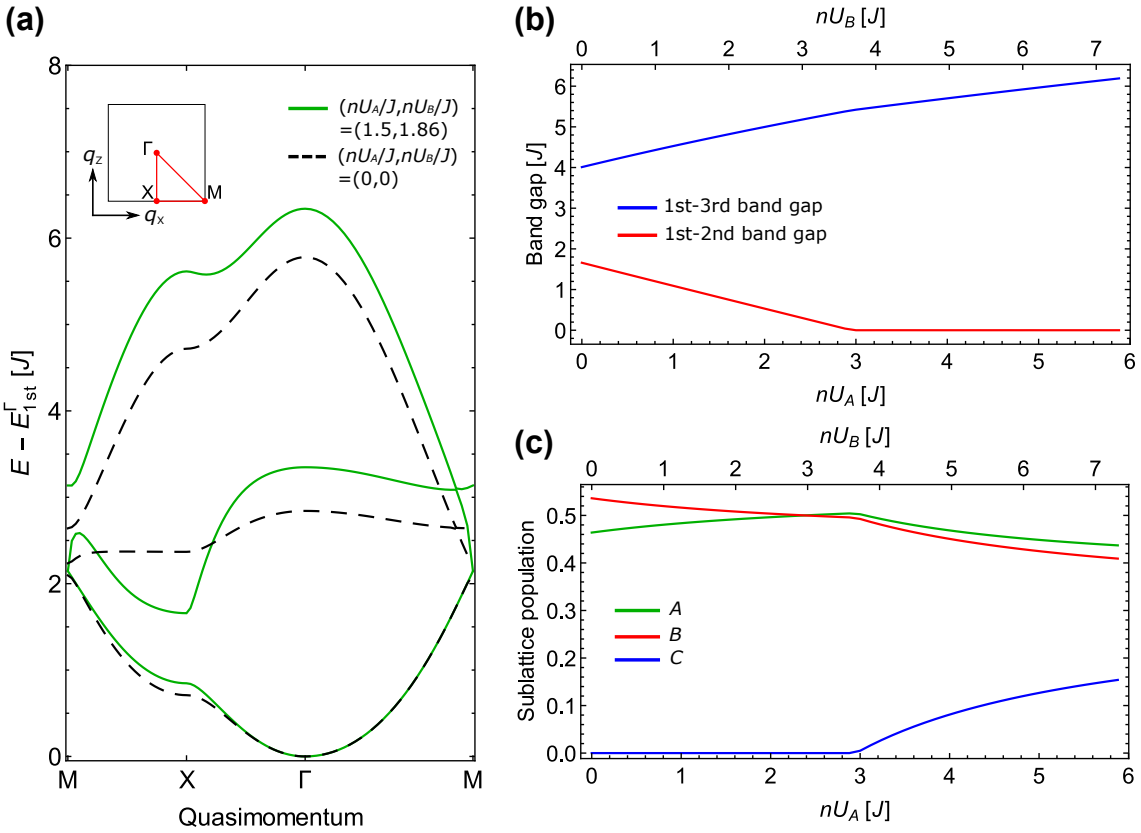

Figure 2.5.1: (a) Numerical calculation for the band energies of the realistic Lieb lattice for $(nU_A/J, nU_B/J) = (0, 0)$ (black dashed line) and $(1.5, 1.86)$ (green solid line). The inset shows the first BZ. (b) Interaction dependence of the gap at X point. Red line and blue line show the 1st-3rd band gap and 1st-2nd band gap, respectively. (c) Interaction dependence of the sublattice population at X point of the lowest band. Green, red, and blue line show the A-, B-, and C-sublattice, respectively.

In the optical Lieb lattice of $(s_{\mathrm{long}}, s_{\mathrm{short}}, s_{\mathrm{diag}}) = (13, 13, 15.5)$ with $N_{\mathrm{tot}} = 2.1 \times 10^4$ and $\bar{\omega} = 2\pi \times 96$ Hz, the resulting chemical potential is $\mu_0 = 65.0$ nK, the Thomas-Fermi radii are $(r_x, r_y, r_z) = (3.07, 8.58, 2.62)$ μm, and the mean-field interaction (nU_A, nU_B) amounts to $(3.48, 4.33)$ kHz at the trap center.

2.6 Atomic limit calculation of the Fermi-Hubbard model

Series expansions are a possible approach for evaluating the thermodynamics and observables for generic lattice models. Depending on the lattice system and parameter regime of interest, a various methods exist. In this section, we introduce the partition function and grand potential for a Fermi-Hubbard model on a dimerized lattice in a high-temperature series expansion up to 0-th order, that is, an atomic limit.

2.6.1 SU(2) Fermi-Hubbard model

We start with the 2-spin Fermions. Hamiltonian of the Fermi-Hubbard model for 2-spin Fermions in a dimerized lattice is given by

$$\hat{H}_{\mathrm{FH}} = \hat{H}_0 + \hat{H}_t, \tag{2.6.1}$$

$$\hat{H}_0 = -t_d \sum_{\langle i,j\rangle_-} \sum_{\sigma=\uparrow,\downarrow} \left(\hat{c}^\dagger_{i,\sigma}\hat{c}_{j,\sigma} + \mathrm{H.c.}\right) + U\sum_i \hat{n}_{i\uparrow}\hat{n}_{i\downarrow} - \mu\sum_i \left(\hat{n}_{i\uparrow} + \hat{n}_{i\downarrow}\right), \tag{2.6.2}$$

$$\hat{H}_t = -t_{yz} \sum_{\langle i,j\rangle_-} \sum_{\sigma=\uparrow,\downarrow} \left(\hat{c}^\dagger_{i,\sigma}\hat{c}_{j,\sigma} + \mathrm{H.c.}\right) - t_w \sum_{\langle i,j\rangle_{\cdots}} \sum_{\sigma=\uparrow,\downarrow} \left(\hat{c}^\dagger_{i,\sigma}\hat{c}_{j,\sigma} + \mathrm{H.c.}\right), \tag{2.6.3}$$

where t_d, t_{yz}, t_w mean the tunneling amplitude between nearest neighbors $\langle i,j\rangle_-$, $\langle i,j\rangle_-$, and $\langle i,j\rangle_{\cdots}$, respectively (see Fig.2.6.1). The on-site interaction energy is given by U,

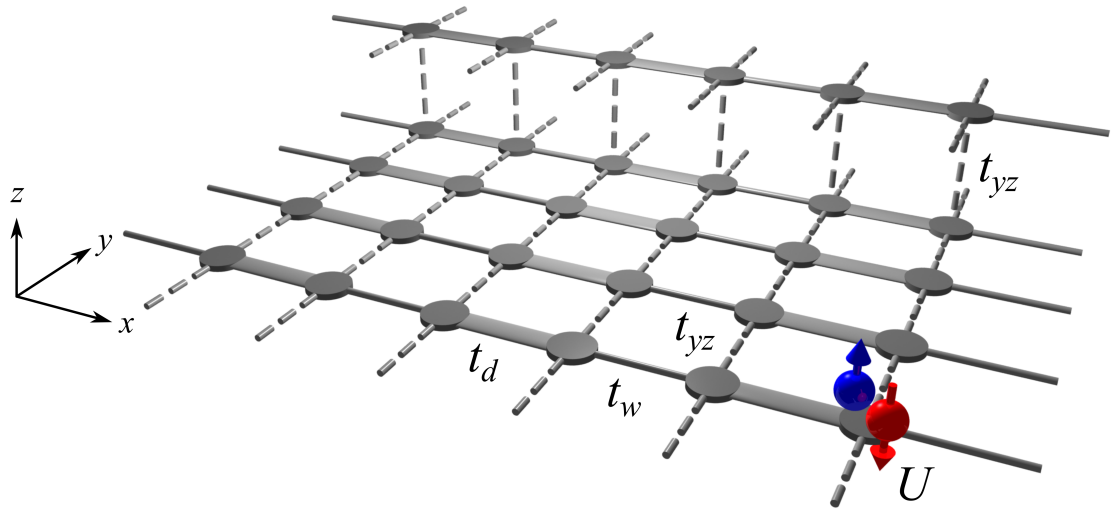

Figure 2.6.1: Fermi-Hubbard model for SU(2) spins on a dimerized lattice. The tunnelings along the x-axis are dimerized with a strong tunneling t_d and a much weaker coupling t_w. The tunneling matrix elements along y- and z-axes are denoted with t_{yz}. Two particles with opposite spins feel an on-site interaction U, while two particles with the same spin can never occupy the same site due to Pauli's principle.

and the chemical potential is denoted with μ. For most parameter regimes considered in this paper, the intra-dimer tunneling t_d is much stronger than all other tunnelings: $t_d \gg t_{yz}, t_w$. Therefore, the coupling between neighboring dimers can be treated as a perturbation. The series expansion is expected to converge in the parameter regime

$$t_{yz}, t_w \ll k_{\mathrm{B}}T \ll U, t_d. \tag{2.6.4}$$

Thermodynamic quantities

Thermodynamic quantities are obtained by evaluating the grand canonical potential $-\beta\Omega = \log\mathcal{Z}$ from the partition function

$$\begin{aligned}\mathcal{Z} &= \mathrm{Tr}\left\{e^{-\beta\hat{H}}\right\} \\ &= \mathcal{Z}_0 + \mathcal{Z}_0 \sum_{n=1}^{\infty} (-1)^n \int_0^{\beta} d\tau_1 \int_0^{\tau_1} d\tau_2 \cdots \int_0^{\tau_n - 1} d\tau_n \left\langle \hat{H}'_c(\tau_1)\hat{H}'_c(\tau_2)\cdots\hat{H}'_c(\tau_n)\right\rangle_0 .\end{aligned} \tag{2.6.5}$$

Here $\mathcal{Z}_0$ denotes the unperturbed function and we express the inter-dimer tunneling operators in the interaction representation:

$$\mathcal{Z}_0 = \mathrm{Tr}\left\{e^{-\beta\hat{H}_0}\right\}, \tag{2.6.6}$$

$$\hat{H}'_t(\tau) = e^{\tau\hat{H}_0}\hat{H}_t e^{\tau\hat{H}_0}. \tag{2.6.7}$$

The average $\langle\cdots\rangle_0$ means evaluation in the unperturbed Hamiltonian

$$\left\langle \hat{H}'_t(\tau_1)\hat{H}'_t(\tau_2)\cdots\hat{H}'_t(\tau_n)\right\rangle_0 = \mathrm{Tr}\left\{e^{-\beta\hat{H}_0}\hat{H}'_t(\tau_1)\hat{H}'_t(\tau_2)\cdots\hat{H}'_t(\tau_n)\right\}/\mathcal{Z}_0. \tag{2.6.8}$$

Several thermodynamic quantities such as the density n, entropy per site s and double occupancy d can be obtained from derivatives of the grand canonical potential per site $\Omega^s = \Omega/l$, where l is the number of sites in the system:

$$n = -\frac{\partial\Omega^s}{\partial\mu}, \tag{2.6.9}$$

$$s = -\frac{\partial\Omega^s}{\partial T}, \tag{2.6.10}$$

$$d = \frac{\partial\Omega^s}{\partial U}. \tag{2.6.11}$$

The sum in Eq.2.6.5 is evaluated by determining the contribution of every order n separately.

Lowest order: atomic limit

The evaluation of the grand potential per dimer Ω^d to lowest order (atomic limit) merely requires the calculation of the isolated dimer Hamiltonian $\hat{H}_d$ defined on two sites

$$-\beta\Omega^d = \log z_0^d, \tag{2.6.12}$$

$$z_0^d = \mathrm{Tr}\left\{e^{-\beta(\hat{H}^d - \mu\hat{N}^d)}\right\}, \tag{2.6.13}$$

$$\hat{H}^d = -t_d \sum_{\sigma}\left(\hat{c}^{\dagger}_{l,\sigma}\hat{c}_{r,\sigma} + \mathrm{H.c.}\right) + U\sum_{i=l,r}\sum_{\sigma\neq\sigma'}\hat{n}_{i,\sigma}\hat{n}_{i,\sigma'}. \tag{2.6.14}$$

For SU(2) case, the trace is evaluated in the eigenenergy basis containing 16 states

$$\begin{aligned}\mathrm{Tr}\left\{e^{-\beta(\hat{H}^d-\mu\hat{N}^d)}\right\} &= \sum_{i=1}^{16}\langle\Psi_i^d|e^{-\beta(\hat{H}^d-\mu\hat{N}^d)}|\Psi_i^d\rangle \\ &= \sum_{i=1}^{16}e^{-\beta(E_i^d-\mu N_i^d)} \end{aligned} \tag{2.6.15}$$

The corresponding eigenstates $|\Psi_i^d\rangle$, eigenvalues E_i^d and particle number N_i^d obtained after diagonalization are given in Tab.2.6.1, where $|\Psi_{\text{singlet}}\rangle$ and $|\Psi_{\text{doublon mix}}\rangle$ are given as

$$|\Psi_{\text{singlet}}\rangle = \frac{\left(u+\sqrt{1+u^2}\right)\left(|\uparrow,\downarrow\rangle-|\downarrow,\uparrow\rangle\right)+|\uparrow\downarrow,0\rangle+|0,\uparrow\downarrow\rangle}{2\sqrt{u^2+1+u\sqrt{1+u^2}}}, \tag{2.6.16}$$

$$|\Psi_{\text{doublon mix}}\rangle = \frac{\left(u-\sqrt{1+u^2}\right)\left(|\uparrow,\downarrow\rangle-|\downarrow,\uparrow\rangle\right)-|\uparrow\downarrow,0\rangle-|0,\uparrow\downarrow\rangle}{2\sqrt{u^2+1-u\sqrt{1+u^2}}}. \tag{2.6.17}$$

Observable evaluation

The evaluation of observables $\hat{\mathcal{O}}$ on a dimer such as the singlet and triplet probabilities or the double occupancy per site is done by determining the expression

$$\left\langle\hat{\mathcal{O}}\right\rangle = \frac{\mathrm{Tr}\left\{\hat{\mathcal{O}}e^{-\beta(\hat{H}^d-\mu\hat{N}^d)}\right\}}{\mathrm{Tr}\left\{e^{-\beta(\hat{H}^d-\mu\hat{N}^d)}\right\}}. \tag{2.6.18}$$

If the observable $\hat{\mathcal{O}}$ commutes with the dimer Hamiltonian $\hat{H}^d$ and $\hat{N}^d$, the evaluation becomes particularly simple since only the relevant eigenstates $|\Psi_i^d\rangle$ have to be counted and weighted with the value of the observable. This is the case for the singlet and triplet probabilities. The evaluation of the double occupancy is a little more complicated because the measurement operator $\hat{n}_{i,\sigma}\hat{n}_{i,\sigma'}$ on site i does not commute with the Hamiltonian $\hat{H}^d$ and $\hat{N}^d$. In this case, we diagonalize the observable $\hat{\mathcal{O}}$ with the localized-spin basis $\left\{|\Phi_i^d\rangle\right\}$ which is defined as

$$\begin{aligned}|\Phi_i^d\rangle &= |\Phi_m^l\rangle\otimes|\Phi_n^r\rangle \\ &\quad m,n=1,2,3,4 \quad i=4(m-1)+n \\ &\quad \left\{\Phi_m^{l(r)}\right\}=\left\{|0\rangle,|\uparrow\rangle,|\downarrow\rangle,|\uparrow\downarrow\rangle\right\}.\end{aligned} \tag{2.6.19}$$

In this notation, $|\Phi_8\rangle = |\uparrow\rangle\otimes|\uparrow\downarrow\rangle = |\uparrow,\uparrow\downarrow\rangle$ for example. Projection of the observable onto $\left\{|\Phi_i^d\rangle\right\}$ can be formally written as

$$\begin{aligned}\mathrm{Tr}\left\{\hat{\mathcal{O}}e^{-\beta\hat{H}^d}\right\} &= \sum_{i=1}^{16}\langle\Psi_i^d|\hat{\mathcal{O}}e^{-\beta(\hat{H}^d-\mu\hat{N}^d)}|\Psi_i^d\rangle \\ &= \sum_{i=1}^{16}\sum_{j=1}^{16}\sum_{k=1}^{16}\langle\Psi_i^d|\Phi_j^d\rangle\langle\Phi_j^d|\hat{\mathcal{O}}|\Phi_k^d\rangle\langle\Phi_k^d|\Psi_i^d\rangle \end{aligned} \tag{2.6.20}$$

Table 2.6.1: Eigenvalues and eigenstates of the Hamiltonian for SU(2) spins in dimer. Here, $u = U/4t_d$, and $|\Psi_{\text{singlet}}\rangle, |\Psi_{\text{doublon mix}}\rangle$ are defined in Eq.2.6.16 and 2.6.17, respectively.

Eigenvalue E_i^d $[t_d]$	Eigenstate $\|\Psi_i^d\rangle$	Spin number N_i^d
0	$\|0,0\rangle$	0
-1	$(\|\uparrow,0\rangle + \|0,\uparrow\rangle)/\sqrt{2}$	1
-1	$(\|\downarrow,0\rangle + \|0,\downarrow\rangle)/\sqrt{2}$	1
1	$(\|\uparrow,0\rangle - \|0,\uparrow\rangle)/\sqrt{2}$	1
1	$(\|\downarrow,0\rangle - \|0,\downarrow\rangle)/\sqrt{2}$	1
0	$\|\uparrow,\uparrow\rangle$	2
0	$\|\downarrow,\downarrow\rangle$	2
$2\left(u - \sqrt{u^2+1}\right)$	$\|\Psi_{\text{singlet}}\rangle$	2
0	$(\|\uparrow,\downarrow\rangle + \|\downarrow,\uparrow\rangle)/\sqrt{2}$	2
$4u$	$(\|\uparrow\downarrow,0\rangle - \|0,\uparrow\downarrow\rangle)/\sqrt{2}$	2
$2\left(u + \sqrt{u^2+1}\right)$	$\|\Psi_{\text{doublon mix}}\rangle$	2
$4u-1$	$(\|\uparrow\downarrow,\uparrow\rangle - \|\uparrow,\uparrow\downarrow\rangle)/\sqrt{2}$	3
$4u+1$	$(\|\uparrow\downarrow,\uparrow\rangle + \|\uparrow,\uparrow\downarrow\rangle)/\sqrt{2}$	3
$4u-1$	$(\|\uparrow\downarrow,\downarrow\rangle - \|\downarrow,\uparrow\downarrow\rangle)/\sqrt{2}$	3
$4u+1$	$(\|\uparrow\downarrow,\downarrow\rangle + \|\downarrow,\uparrow\downarrow\rangle)/\sqrt{2}$	3
$8u$	$\|\uparrow\downarrow,\uparrow\downarrow\rangle$	4

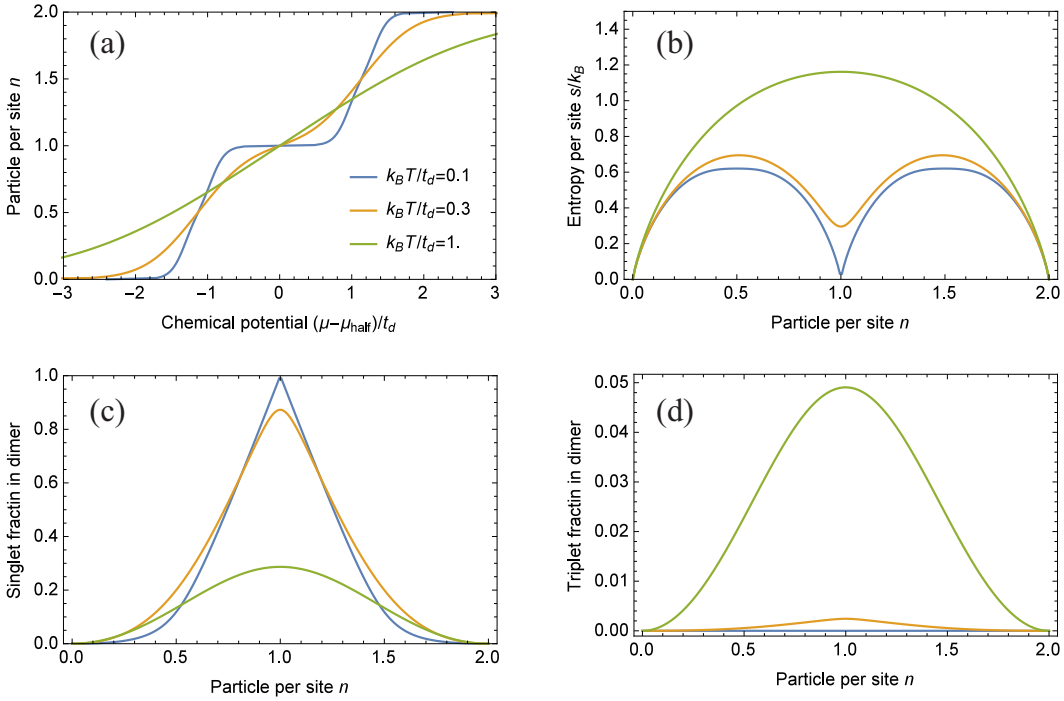

Figure 2.6.2: Atomic limit calculation in the homogeneous dimerized lattice for three different temperatures. (a) Density as a function of chemical potential. The chemical potential at half filling is denoted with μ_{half}. (b), (c), (d) show entropy per site, singlet probability, and triplet probability versus density, respectively. The interaction energy is set to $U/t_d = 0.5$, and $k_{\text{B}} = 1$.

If the observable is double occupancy, the measurement operator $\hat{\mathcal{O}} = \sum_{i,\sigma\neq\sigma'} \hat{n}_{i,\sigma}\hat{n}_{i,\sigma'}$ works as

$$\hat{\mathcal{O}}\left|\Phi_j^d\right\rangle = \begin{cases} \left|\Phi_j^d\right\rangle & \text{for } j = 4, 8, 12, 13, 14, 15 \\ 2\left|\Phi_j^d\right\rangle & \text{for } j = 16 \\ 0 & \text{otherwise} \end{cases} \tag{2.6.21}$$

for example.

Figure 2.6.2 shows the result of atomic limit calculation in the homogeneous dimerized lattice. At low temperature compared with intra-dimer tunneling t_d, the half-filled system forms a Mott-plateau with one particle per site, as can be seen from Fig.2.6.2(a). As the energy splitting between the singlet state and triplet state becomes larger than the temperature, the number of available states reduces from initial four, say $|\uparrow,\uparrow\rangle, |\downarrow,\downarrow\rangle, (|\uparrow,\downarrow\rangle + |\downarrow,\uparrow\rangle)/\sqrt{2}, |\Psi_{\text{singlet}}\rangle$, to only the singlet configuration at half filling, accompanied by a strong reduction of the entropy per site (See Fig.2.6.2(b),(c),(d)). Away from half-filling, the entropy increases again since more configurations become available.

2.6.2 The harmonic trap and local density approximation

The effect of the harmonic trap can be included in a local density approximation, where we assume that the density of the atoms in an optical lattice smoothly changes. The harmonic confinement leads to a quadratically varying chemical potential

$$\mu \to \mu(r) = \mu_0 - \frac{1}{2} m \bar{\omega}^2 \left(\frac{\lambda}{2}\right)^2 r^2, \tag{2.6.22}$$

where $\bar{\omega}$ is the geometric mean of the trapping frequencies, μ_0 is the chemical potential in the center of the trap and r is the normalized distance from the trap center to a site. The trap frequencies in our experimental setup are summarized in the appendix A.
Averaged observable $\mathcal{O}^{\mathrm{trap}}$ can be obtained by integrating the contributions per site $\mathcal{O}^{\mathrm{LDA}}(\mu(r))$:

$$\mathcal{O}^{\mathrm{trap}} = \int_0^\infty 4\pi r^2 \mathcal{O}^{\mathrm{LDA}}(\mu(r)) \mathrm{d}r. \tag{2.6.23}$$

In the experiment, the atom number N and entropy per particle s/N in the entire trapped system are accessible quantities. From these numbers, we can determine the system temperature T and chemical potential at the trap center μ_0 by numerically solving the following simultaneous equations:

$$N = \int_0^\infty 4\pi r^2 n(\mu(r), T) \mathrm{d}r \tag{2.6.24}$$

$$S = \int_0^\infty 4\pi r^2 s(\mu(r), T) \mathrm{d}r. \tag{2.6.25}$$

Figure 2.6.3 shows the distribution of the density (a), entropy (b), and singlet probability (c) for the dimerized lattice with harmonic confinement. The harmonic confinement leads to a coexistence of serveral different phases within the trap (for example, metallic, Mott-insulating, and band-insulating phase). Those phases are located at different radial distances from the trap center, and determine the entropy distribution over the density distribution. For a given fixed total entropy per particle S/N in the entire system, the entropy is stored in the outer region of the density distribution, while very low entropies are achieved around the trap center, where almost all of the particle reduces to the singlet state.

2.6.3 Extension to the SU($\mathcal{N} > 2$) system

We begin with the SU(N) Fermi-Hubbard Hamiltonian in the dimerized lattice such as

$$\hat{H}_{\mathrm{FH}} = \hat{H}_0 + \hat{H}_t, \tag{2.6.26}$$

$$\hat{H}_0 = -t_d \sum_{\langle i,j \rangle_-} \sum_\sigma \left(\hat{c}^\dagger_{i,\sigma} \hat{c}_{j,\sigma} + \mathrm{H.c.}\right) + \frac{U}{2} \sum_i \sum_{\sigma \neq \sigma'} \hat{n}_{i,\sigma} \hat{n}_{i,\sigma'} - \mu \sum_i \sum_\sigma \hat{n}_{i,\sigma} \tag{2.6.27}$$

$$\hat{H}_t = -t_{yz} \sum_{\langle i,j \rangle_-} \sum_\sigma \left(\hat{c}^\dagger_{i,\sigma} \hat{c}_{j,\sigma} + \mathrm{H.c.}\right) - t_w \sum_{\langle i,j \rangle_\cdots} \sum_\sigma \left(\hat{c}^\dagger_{i,\sigma} \hat{c}_{j,\sigma} + \mathrm{H.c.}\right). \tag{2.6.28}$$

For SU($N > 2$) system, the calculation is in principle analogous to the strategy in SU(2) case, with one important differences: the number of relevant states is explosively increased

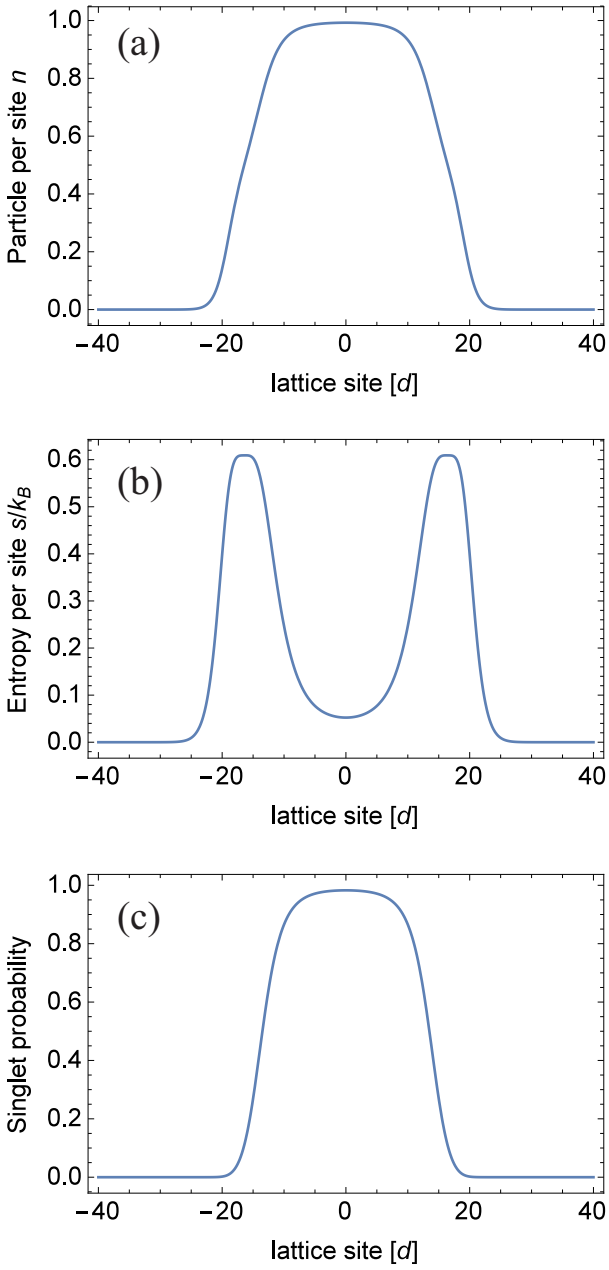

Figure 2.6.3: Atomic limit calculation with the harmonic trap and local density approximation. The horizontal axis is the lattice site in the unit of $d = 266$ nm. Total atom number and entropy are set to $N = 2 \times 10^4$, $S/Nk_{\mathrm{B}} = 1$ with a geometric mean of trap frequency $\bar{\omega} = 2\pi \times 80$ Hz, which gives one particle per site around the trap center. We assume the atomic mass of Yb, and the lattice parameters for the dimerized lattice are $U/h = 1 \times 10^3$, $t_d/h = 1 \times 10^3$ Hz.

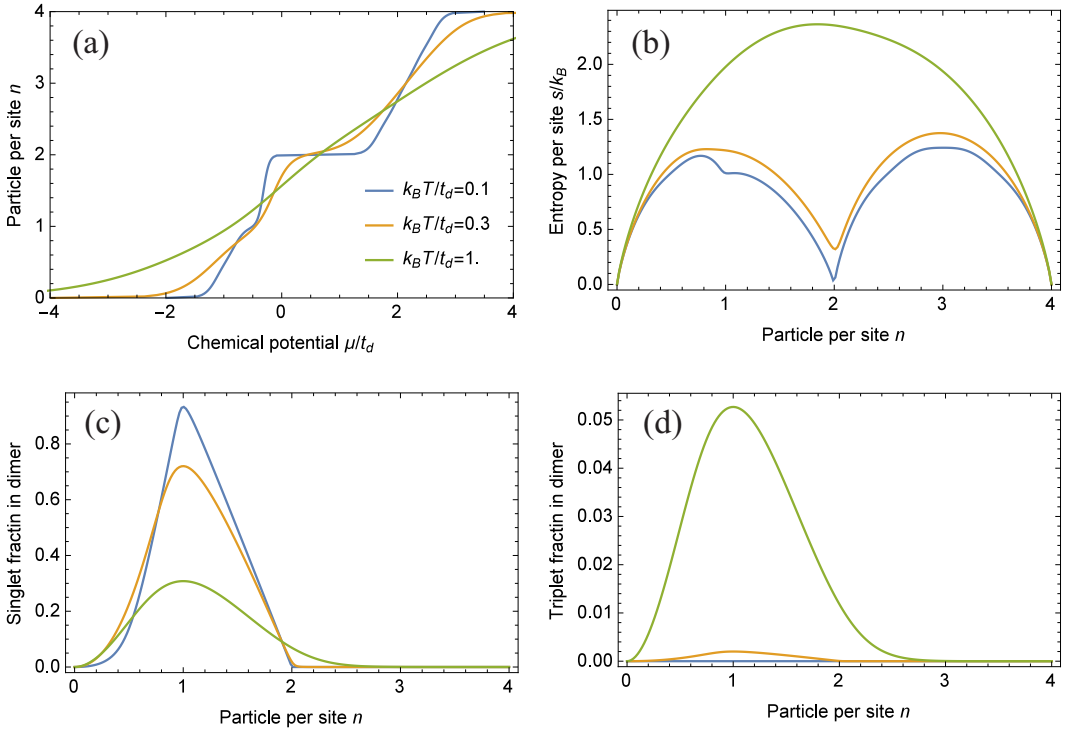

Figure 2.6.4: Atomic limit calculation for SU(4) Fermi-Hubbard model in the homogeneous dimerized lattice. The interaction energy is set to $U/t_d = 1$, and $k_{\mathrm{B}} = 1$.

from 16 per dimer to 2^{2N} per dimer. Due to this difference, it take much more time to numerically diagonalize the Hamiltonian and to evaluate the thermodynamic quantities and observables.

Figure 2.6.4 shows the result of atomic limit calculation for the SU(4) Fermi-Hubbard model in a homogeneous dimerized lattice. Due to the Pauli's principle, the particle number per site is allowed to increase up to 4. At the filling of $n = 1$, the lowest-lying singlet state in dimer get more occupied as the temperature decreases, while the entropy does not decrease so much compared with the case of SU(2) in Fig.2.6.2(b). This is due to larger spin degree of freedom; in the SU(4) Fermi-Hubbard model, the number of singlet configuration is increased from ${}_2\mathrm{C}_2 = 1$ to ${}_4\mathrm{C}_2 = 6$, compared with the SU(2) case.

Chapter 3

Experimental setup

In this chapter, we describe the experimental setup and procedure for producing quantum degenerate gases of ytterbium in optical lattices. First, general properties of Yb atoms are introduced, followed by cooling processes. As for probing, we use the absorption imaging as described in section 3.3. Theory of thermometry is explained in section 3.4. In section 3.5, details of optical lattices including an optical Lieb lattice are presented.

3.1 Properties of Ytterbium (Yb)

3.1.1 Isotopes and s-wave scattering lengths

There are seven stable isotopes of Yb: five bosons (^{168}Yb,^{170} Yb,^{172} Yb,^{174} Yb,^{176} Yb) and two fermions (^{171}Yb,^{173} Yb). In the electronic ground state, all the boson are spinless and fermions have nuclear spin degree of freedom ($I = 1/2$ for ^{171}Yb and ($I = 5/2$ for ^{173}Yb). So far, quantum degeneracy has been achieved for all the isotope of Yb ([44, 49, 43, 80, 81]) except for ^{172}Yb. In addition, various kinds of quantum gas mixtures of Yb isotopes have been realized [45, 28], which open up new quantum phases.

In ultracold regime, interaction between the neutral atoms is characterized by s-wave scattering length. Table 3.1.2 shows experimentally determined s-wave scattering lengths of Yb [51]. Yb has different s-wave scattering lengths between the isotopes. This fact is important for experiments using Yb because magnetic Feshbach resonances are not available for the electronic ground state of Yb.

3.1.2 Energy level

Because Yb has two valence electrons, the structure of energy levels is similar to that of alkaline-earth metals. Fig 3.1.1 is a diagram of low-lying energy levels of Yb used for experiments in this thesis. The electronic ground state of Yb is spin singlet $(6s^2)^1S_0$. The $^1S_0 \leftrightarrow ^1P_1$ transition has natural linewidth of 29 MHz, which enables high photon scattering rate. This is used for Zeeman slowing (section 3.2.1), absorption imaging (section 3.3). Transitions to the triplet states have much narrower linewidth. The $^1S_0 \leftrightarrow ^3P_1$ is used for a magneto-optical trap (MOT) in section 3.2.2 , optical gradient in section 4, and photo-association in section 7.3.

Table 3.1.1: Stable isotope of Yb atom

Isotope	Mass [a.u.]	Abundance ratio [%]	Nuclear spin [$\hbar$]	Boson or Fermion
^{168}Yb	167.933894	0.13	0	Boson
^{170}Yb	169.934759	3.05	0	Boson
^{171}Yb	170.936323	14.3	1/2	Fermion
^{172}Yb	171.936378	21.9	0	Boson
^{173}Yb	172.938208	16.1	5/2	Fermion
^{174}Yb	173.938859	31.8	0	Boson
^{176}Yb	175.942564	12.7	0	Boson

Table 3.1.2: s-wave scattering lengths for combination of Yb isotopes in [nm] unit [51]

	^{168}Yb	^{170}Yb	^{171}Yb	^{172}Yb	^{173}Yb	^{174}Yb	^{176}Yb
^{168}Yb	**13.33**	6.19	4.72	3.44	2.04	0.13	-19.0
^{170}Yb		**3.38**	1.93	-0.11	-4.30	-27.4	11.08
^{171}Yb			**−0.15**	-4.46	-30.6	22.7	7.49
^{172}Yb				**−31.7**	22.1	10.61	5.62
^{173}Yb					**10.55**	7.34	4.22
^{174}Yb						**5.55**	2.88
^{176}Yb							**−1.28**

Table 3.1.3 shows isotope shifts of two cooling transitions, $^1S_0 \leftrightarrow {}^1P_1$ and $^1S_0 \leftrightarrow {}^3P_1$.

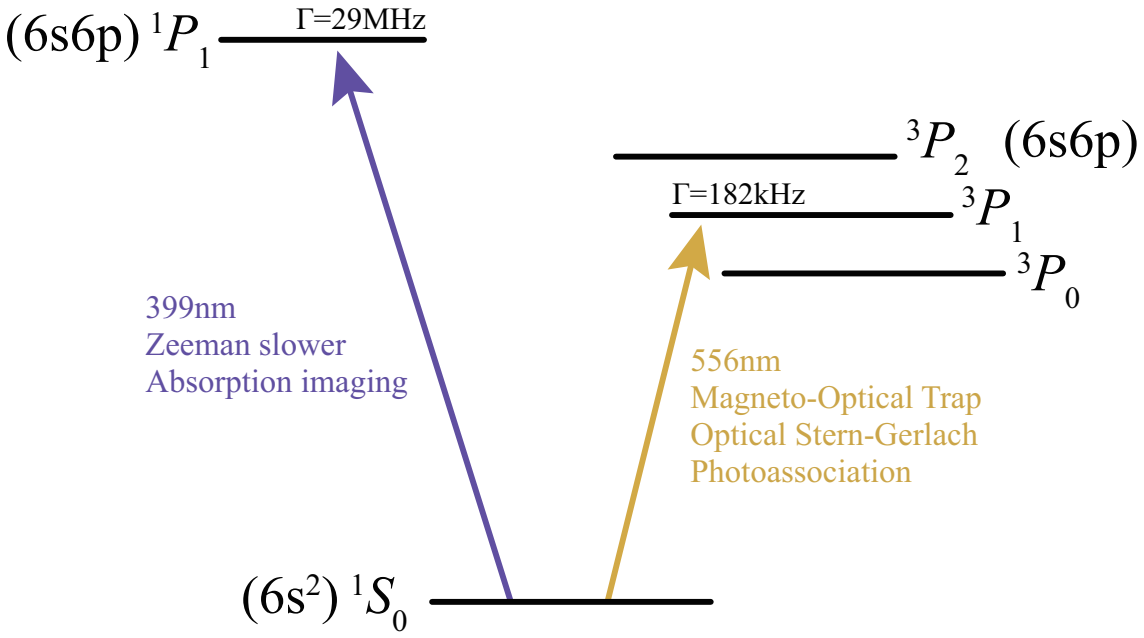

Figure 3.1.1: Low-lying energy level of Yb and its major aaplications

Table 3.1.3: Isotope shifts of the $^1S_0 \leftrightarrow {}^1P_1$ transition [82] and the $^1S_0 \leftrightarrow {}^3P_1$ transition [83]

$^1S_0 \leftrightarrow {}^1P_1$	Shift [MHz]
^{176}Yb	-509.3
^{173}Yb($F' = 5/2$)	-253.4
^{174}Yb	0
^{173}Yb($F' = 3/2$)	516.0
^{172}Yb	533.3
^{173}Yb($F' = 7/2$)	588.0
^{171}Yb($F' = 3/2$)	832.4
^{171}Yb($F' = 1/2$)	1153.7
^{170}Yb	1192.4
^{168}Yb	1887.4

$^1S_0 \leftrightarrow {}^3P_1$	Shift [MHz]
^{173}Yb($F' = 7/2$)	-2386.7
^{171}Yb($F' = 1/2$)	-2132.1
^{176}Yb	-954.8
^{174}Yb	0
^{172}Yb	1000.0
^{170}Yb	2286.4
^{173}Yb($F' = 5/2$)	2311.4
^{168}Yb	3655.1
^{171}Yb($F' = 3/2$)	3804.6
^{173}Yb($F' = 3/2$)	3807.3

3.2 Cooling processes

At room temperature, Yb is solid and very stable. We heat the Yb oven up to about 400 °C to vaporize Yb during experiments. To achieve quantum degeneracy of atomic gases, Yb atoms should be cooled down to a few tens of nK. This is achieved by the all-optical method as explained below.

3.2.1 Zeeman slower

To slow down atoms emitted from the Yb oven at about 400 °C, Zeeman slower is used. Basically, the resonance frequency of atoms in an atomic beam is shifted due to the Doppler effect depending on the atomic velocity. In a Zeeman slower system, such frequency shifts are compensated by gradually varied external magnetic field. We adopted a so called "increasing field type" Zeeman slower in which the magnetic field becomes stronger as the deceleration proceeds. The ${}^1S_0 \leftrightarrow {}^1P_1$ transition is used with wavelength of 399 nm for the Zeeman slowing. The slowing laser is obtained by frequency doubling of a Tisappire laser of 798 nm(MBR-110, Coherent Inc). A ring cavity with a BBO crystal is used for the second harmonic generation with an output power of 100 $\sim$ 150 mW. The laser frequency is locked to a transfer cavity (RG-91T, Burleigh Instruments Inc) stabilized by 556 nm light which is locked to a stable ULE cavity.

3.2.2 Magneto-Optical Trap (MOT)

Atoms slowed by the Zeeman slower system are trapped in a magneto-optical trap (MOT). The MOT consists of three pairs of two circularly polarized counterpropagating lasers and the quadrupole magnetic field. We use the narrow ${}^1S_0 \leftrightarrow {}^3P_1$ transition for a MOT with wavelength of 556 nm, whose Doppler cooling limit is $T_D = 4.4\ \mu$K. There are two laser systems for a MOT. Each system has a fiber laser at 1111 nm (Boostik Y10-PM, Koheras or Orange one, Menlosystem), a ULE cavity for frequency stabilization and a ring cavity with a LBO crystal for frequency doubling. In order to load atoms into a far-off resonant trap, the atomic density is increased by a compressed MOT scheme, where the B-field gradient is ramped up. Subsequently, the intensity and the detuning of the laser light is decreased for cooling. Typically, 4×10^6 of ^{174}Yb are captured at the loading time of 8 s, for example.

3.2.3 Far-Off Resonance Trap (FORT)

For further cooling to quantum denegeracy, atoms are transferred to a far-off resonant trap (FORT). This is formed by crossing two laser beams with the wavelength of 532 nm (Veri-V18/V10, Coherent Inc) at their focusing points. Polarization of the electric fields are the same for two laser beams.

Evaporative cooling is performed by gradually decreasing the intensity of two laser beams. This method enables to selectively evacuate high velocity atoms, which results in achieving lower temperature of the remaining atoms. Through above processes, we obtain quantum degenerate gases of Yb.

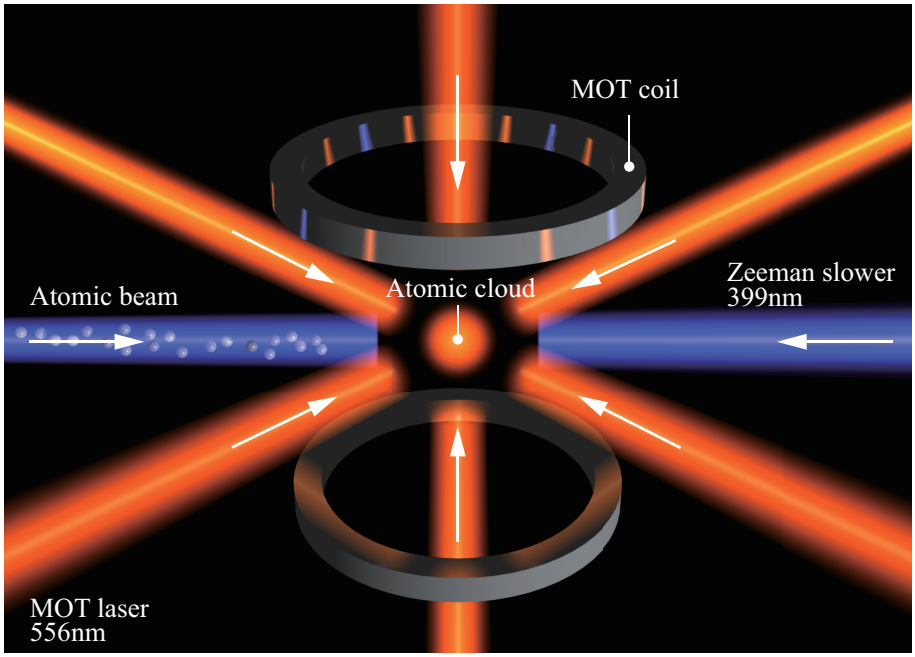

Figure 3.2.1: Schematic view of the laser configuration for the MOT and Zeeman slowing.

3.3 Imaging system

3.3.1 Absorption imaging

Absorption imaging is the most important detection technique in cold atom experiments. Figure 3.3.1 shows schematic of the absorption imaging after a ballistic expansion from a trap. We irradiate a resonant laser light onto an atomic cloud. The cloud absorbs the laser light and its shadow is projected onto a CCD camera. The intensity distribution of a probe laser immediately after passing through the cloud is given by

$$I(x,y) = I_0(x,y)\,\exp\left[-\sigma_{\rm res} n(x,y)\right] \tag{3.3.1}$$

where I_0 is the intensity distribution without atoms, $\sigma_{\rm res} = 3\lambda_{\rm probe}/(2\pi)$ is the resonant cross section for scattering between atoms and probe laser light, and $n(x,y) = \int {\rm d}z n(\boldsymbol{x})$ is the column density of the cloud accumulated along the direction of the probe laser. This intensity distribution is projected on the CCD surface with a certain magnification ratio A:

$$\tilde{I}(x,y) = A^{-2} I_0\left(\frac{x}{A},\frac{y}{A}\right)\,\exp\left[-\sigma_{\rm res} n(\frac{x}{A},\frac{y}{A})\right] \tag{3.3.2}$$

The effect of I_0 can be removed by measuring the intensity $\tilde{I}_0 = A^{-2} I_0\left(\frac{x}{A},\frac{y}{A}\right)$ without atoms, and dividing $\tilde{I}$ by $\tilde{I}_0$. Therefore, $n(x,y)$ is given by

$$\frac{\tilde{I}(x,y)}{\tilde{I}_0(x,y)} = \exp\left[-\sigma_{\rm res} n\left(\frac{x}{A},\frac{y}{A}\right)\right] \implies n\left(\frac{x}{A},\frac{y}{A}\right) = \frac{1}{\sigma_{\rm res}}{\rm In}\left(\frac{\tilde{I}(x,y)}{\tilde{I}_0(x,y)}\right) \tag{3.3.3}$$

In actual images, the obtained position (x,y) is discretized by CCD pixels like (x_i, y_j), where (i,j) is the index to label a CCD pixel. In addition, we take three kinds of images:

One is the image P_{x_i,y_j} with an atomic cloud and a probe light, other is the flat field F_{x_i,y_j} with the probe light but the atomic cloud, and the other is the dark frame D_{x_i,y_j} without both of the atomic cloud and probe light. Generally speaking, D_{x_i,y_j} is not zero due to a stray light, dark current from a CCD pixel, thermal noise, and so on. For each CCD pixel, $n\left(\frac{x_i}{A}, \frac{y_j}{A}\right)$ is given by

$$\begin{aligned} n\left(\frac{x_i}{A}, \frac{y_j}{A}\right) &= \frac{1}{\sigma_{\mathrm{res}}} \mathrm{In}\left(\frac{\tilde{I}_0(x_i, y_j)}{\tilde{I}(x_i, y_j)}\right) \\ &= \frac{1}{\sigma_{\mathrm{res}}} \mathrm{In}\left(\frac{P_{x_i,y_j} - D_{x_i,y_j}}{T_{x_i,y_j} - D_{x_i,y_j}}\right) \end{aligned} \tag{3.3.4}$$

In experiment, this density distribution is used for thermometry of an atomic cloud as described in section 3.4.

The total atom number N can be calculated out by accumulating $n\left(\frac{x_i}{A}, \frac{y_j}{A}\right)$ all over the CCD pixel:

$$N = -\frac{\Delta s}{A^2 \sigma_{\mathrm{res}}} \sum_{i=1}^{m} \sum_{j=1}^{n} \mathrm{In}\left(\frac{P_{x_i,y_j} - D_{x_i,y_j}}{T_{x_i,y_j} - D_{x_i,y_j}}\right) \tag{3.3.5}$$

Here, (m, n) is the number of CCD pixels in horizontal and vertical direction respectively, Δs is the CCD pixel size.

We use an external cavity laser diode (ECLD) with a wavelength $\lambda = 798$ nm as a laser source for absorption imaging. The output is amplified by a tapered amplifier, followed by a wave-guide SHG. The imaging systems are constructed on each axis of optical lattices as can be seen in Fig.3.5.2 and 3.5.3.

3.4 Thermometry for trapped atoms

Temperature of an atomic gas can be derived from measurement of the density distribution of a gas after a ballistic expansion from a trap. In this section, the thermometric techniques for thermal and degenerate gases are briefly described.

We assume that the initial density distribution can approximate a delta function. The ballistic expansion with the time duration of t transfers atoms with a position $\boldsymbol{r}_0$ and momentum $\hbar \boldsymbol{k}_0$ to the position $\boldsymbol{r} = \boldsymbol{r}_0 + \hbar \boldsymbol{k}_0 t/m$. The density distribution after the expansion is thus given by

$$n(\boldsymbol{r}, t) = \int \mathrm{d}^3 r_0 \int \frac{\mathrm{d}^3 k_0}{(2\pi)^3} F(\boldsymbol{r}_0, \boldsymbol{k}_0) \delta\left(\boldsymbol{r} - \boldsymbol{r}_0 - \frac{\hbar \boldsymbol{k}_0}{m} t\right), \tag{3.4.1}$$

where F is the phase space distribution function at $t = 0$.

Scaling law

Now, we derive a scaling law for the time evolution of the density distribution in a ballistic expansion. For simplicity, we consider the case of one-dimension. Maxwell-Bolzmann and

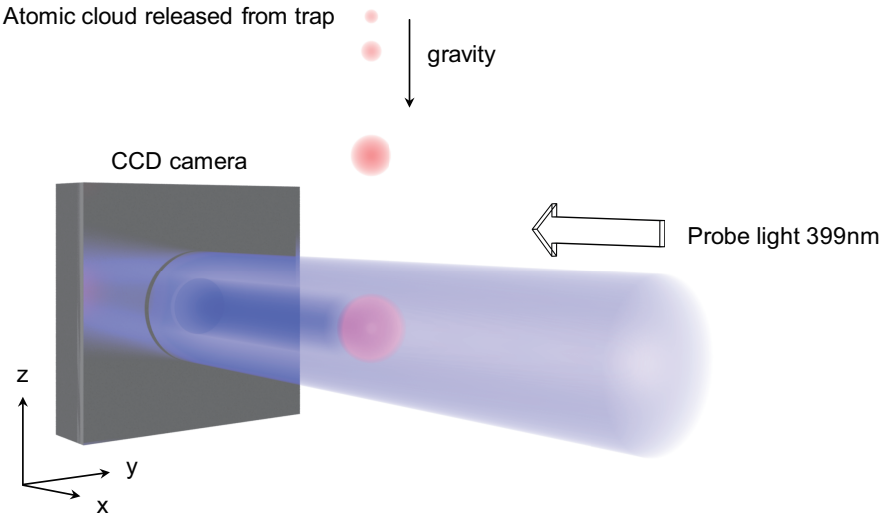

Figure 3.3.1: Schematic of time-of-flight and absorption imaging. After we immediately turn off the trap potential, the atomic cloud released from the trap starts to fall according to the gravitational force, and expands according to the momentum distribution in trap. Then, we shine the probe light, whose wavelength is 399 nm in our experiment, and take an image of the absorbed probe light (the shadow of atomic cloud) by a CCD camera.

Thomas-Fermi distributions for a gas in a harmonic trap have the form

$$F(x,k) = F\left(\frac{\hbar^2 k^2}{2m} + \frac{1}{2}m\omega^2 x^2\right). \tag{3.4.2}$$

Substituting Eq.3.4.2 for Eq.3.4.1, the time evolution of the density distribution can be calculated as

$$\begin{aligned} n(x,t) &= \int_{-\infty}^{\infty} \mathrm{d}x_0 \int_{-\infty}^{\infty} \frac{\mathrm{d}k_0}{2\pi} F(x_0,k_0)\delta\left(x - x_0 - \frac{\hbar k_0}{m}t\right) \\ &= \int_{-\infty}^{\infty} \frac{\mathrm{d}k_0}{2\pi} F\left(\frac{\hbar^2}{2m}(1+\omega^2 t)\left(k_0 - \frac{m\omega^2 x t}{\hbar(1+\omega^2 t^2)}\right)^2 \right. \\ &\qquad \left. + \frac{1}{2}m\frac{\omega^2}{1+\omega^2 t^2}x^2\right). \end{aligned} \tag{3.4.3}$$

Since any translation in k_0-space does not change the integral, we have a scaling law (extended to three-dimensional case)

$$n(\boldsymbol{r},t) = \frac{1}{\lambda_x(t)\lambda_y(t)\lambda_z(t)}\, n\left[\left(\frac{x}{\lambda_x(t)}, \frac{y}{\lambda_y(t)}, \frac{z}{\lambda_z(t)}\right), t=0\right] \tag{3.4.4}$$

with the scaling factor

$$\lambda_i(t) = \sqrt{1+\omega_i^2 t^2} \quad (i = x, y, z). \tag{3.4.5}$$

3.4.1 Thermal gas

Far above the Fermi temperature or the critical temperature for Bose-Einstein condensation, atomic gases obey the Maxwell-Boltzmann distribution:

$$f_{\mathrm{MB}}(\boldsymbol{r},\boldsymbol{k}) = N\left(\frac{\hbar\bar{\omega}}{k_{\mathrm{B}}T}\right)^3 \exp\left[-\beta\sum_i\left(\frac{\hbar k_i^2}{2m}+\frac{1}{2}m\omega_i^2 x_i^2\right)\right]. \tag{3.4.6}$$

Applying the scaling law Eq.3.4.4 to this distribution, the time evolution is given by

$$n_{\mathrm{MB}}(\boldsymbol{r},t) = \frac{N}{\lambda_1(t)\lambda_2(t)\lambda_3(t)}\left(\frac{m\bar{\omega}^2}{2\pi k_{\mathrm{B}}T}\right)^{3/2}\exp\left(-\beta\sum_{i=1}^{3}\frac{1}{2}m\omega_i^2\frac{x_i^2}{\lambda_i(t)^2}\right). \tag{3.4.7}$$

The density distribution obtained from absorption images is the column density which is integrated along the imaging axis. Integrating the Eq.3.4.7 along the z axis, we can get

$$n_{\mathrm{MB}}(x,y,t) = \frac{N}{2\pi\sigma_x(t)\sigma_y(t)}\exp\left(-\sum_{i=1}^{2}\frac{x_i^2}{\sigma_i(t)^2}\right), \tag{3.4.8}$$

where

$$\sigma_i(t) = \sqrt{\frac{k_{\mathrm{B}}T}{m\omega_i^2}}\lambda_i(t) \tag{3.4.9}$$

is the width of the atomic cloud. Therefore, the temperature of the gas can be determined by fitting with the Eq.3.4.8 to the density profile measured by time-of-flight(TOF). If the TOF time is sufficiently long ($\omega_i{}^2t^2 \gg 1$), the temperature can be determined by simpler relation $k_{\mathrm{B}}T = m\sigma^2/t^2$. Twice-integrated density distribution is also used for thermometry:

$$n_{\mathrm{MB}}(x,t) = \frac{N}{\sqrt{2\pi}\sigma_x(t)}\exp\left(-\frac{x^2}{2\sigma_x(t)^2}\right). \tag{3.4.10}$$

3.4.2 Degenerate Fermi gas

Trapped Fermi gases in the degenerate regime is well described by the Thomas-Fermi distribution function, which obeys the same scaling law in Eq.3.4.4:

$$n(\boldsymbol{r},t) = -\frac{1}{\lambda_x(t)\lambda_y(t)\lambda_z(t)}\frac{\mathcal{N}}{\lambda_{\mathrm{th}}^3}\mathrm{Li}_{3/2}\left[-z\exp\left(-\beta\sum_{i=1}^{3}\frac{1}{2}m\omega_i^2\frac{x_i^2}{\lambda_i(t)^2}\right)\right]. \tag{3.4.11}$$

Integrating by using the formula $\int_{-\infty}^{\infty}\mathrm{d}x\ \mathrm{Li}_\alpha(z\mathrm{e}^{-x^2}) = \sqrt{\pi}\mathrm{Li}_{\alpha+1/2}(z)$, we obtain the following 2D and 1D densities:

$$n(x,y,t) = \frac{n_2}{\mathrm{Li}_2(-z)}\mathrm{Li}_2\left[-z\exp\left(-\sum_{i=1}^{2}\frac{x_i^2}{2\sigma_i(t)^2}\right)\right], \tag{3.4.12}$$

$$n(x,t) = \frac{n_1}{\mathrm{Li}_{5/2}(-z)}\mathrm{Li}_{5/2}\left[-z\exp\left(-\frac{x^2}{2\sigma_x(t)^2}\right)\right], \tag{3.4.13}$$

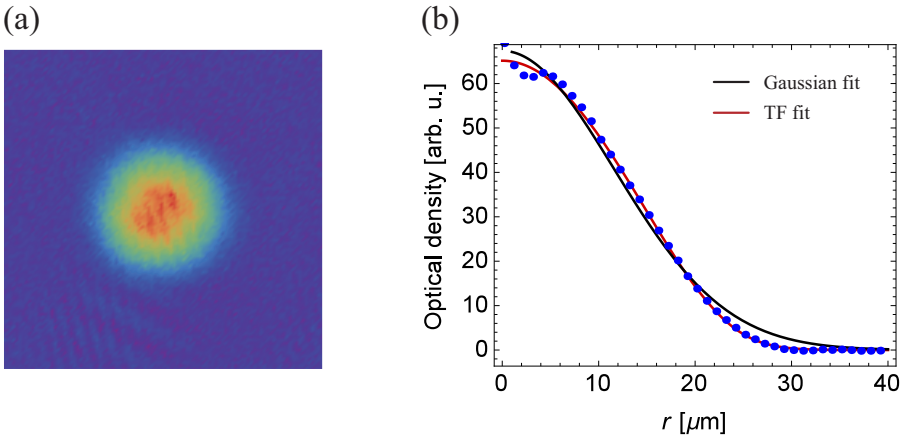

Figure 3.4.1: (a) Absorption image of a degenerate Fermi gas of 2 component ^{173}Yb. (b) Azimuthal average of optical density of the absorption image. Black and red line mean the Gaussian fit and TF fit, respectively. According to the TF fit, $T/T_{\mathrm{F}} = 0.20$.

where n_2 and n_1 denote the maximum of column and linear density, respectively. The one-dimensional fitting to the integrated optical density may give inaccurate results because the TF distribution has only slight deviation from the Gaussian distribution. Therefore, one-dimensional fitting to the azimuthally average density profile or full two-dimensional fitting is recommended. Note that it is only when the density profile is isotropic that the one-dimensional fitting to the azimuthally averaged density profile is valid. In this case, the fitting function can be transformed from the Eq.3.4.12 as

$$n(r,t) = \frac{n_2}{\mathrm{Li}_2(-z)}\mathrm{Li}_2\left[-z\,\exp\left(-\frac{r^2}{2\sigma^2(t)}\right)\right], \tag{3.4.14}$$

where $\sigma(t) = \sigma_x(t) = \sigma_y(t)$. Integrating Eq.3.4.12 and 3.4.13 over spatial coordinates, the number of atoms can be obtained:

$$N = 2\pi n_2 \sigma_x(t)\sigma_y(t)\frac{\mathrm{Li}_3(-z)}{\mathrm{Li}_2(-z)} = \sqrt{2\pi} n_1 \sigma_x(t)\frac{\mathrm{Li}_3(-z)}{\mathrm{Li}_{5/2}(-z)}. \tag{3.4.15}$$

The temperature T can be obtained from measured $\sigma_i(t)$ with using Eq.3.4.9. On the other hand, T_{F} is determined from a trap frequencies and the number of atoms. Thus, T/T_{F} is given by

$$\frac{T}{T_{\mathrm{F}}} = \frac{m\omega_i^2\sigma_i^2}{(6N/\mathcal{N})^{1/3}\hbar\bar{\omega}(1+\omega_i^2 t^2)}. \tag{3.4.16}$$

Figure 3.4.1(a) shows typical absorption image of a degenerate Fermi gas of ^{173}Yb and fig 3.4.1 is the results of TF fitting to the azimuthally averaged density. The density distribution shows clear deviation from the Gaussian function, which indicates that it is in quantum degenerate regime.

3.4.3 Bose-Einstein condensation

The density distribution of a BEC released from a harmonic trap can be derived from the time-independent GP equation such as

$$\left[-\frac{\hbar^2}{2m}\nabla^2 + V_{\rm trap}(\boldsymbol{r}) + U_0\left|\Phi(\boldsymbol{r})\right|^2\right]\Phi(\boldsymbol{r}) = \mu\Phi(\boldsymbol{r}), \tag{3.4.17}$$

where $U_0 = 4\pi\hbar^2 a/m$, a is s-wave scattering length, and μ is chemical potential of a BEC. If the number of particles N is so large that mean-field energy is much larger than kinetic energy, we can neglect the kinetic energy term in Eq.3.4.17 (Thomas-Fermi approximation):

$$\left[V_{\rm trap} + U_0\left|\Phi(\boldsymbol{r})\right|^2\right]\Phi(\boldsymbol{r}) = \mu\Phi(\boldsymbol{r}). \tag{3.4.18}$$

Since this equation must be satisfied for all the $\boldsymbol{r}$ where $\Phi(\boldsymbol{r})$ has non-zero value,

$$V_{\rm trap} + U_0\left|\Phi(\boldsymbol{r})\right|^2 = \mu. \tag{3.4.19}$$

Thus, the density distribution of a BEC under TF approximation $n_{\rm TF}(\boldsymbol{r})$ can be written as

$$n_{\rm TF}(\boldsymbol{r}) = \left|\Phi(\boldsymbol{r})\right|^2 = \max\left[\frac{\mu - V_{\rm trap}(\boldsymbol{r})}{U_0}, 0\right]. \tag{3.4.20}$$

Below, we assume anisotropic three-dimensional harmonic trap

$$V_{\rm trap}(\boldsymbol{r}) = \frac{1}{2}m\left(\omega_x^2 x^2 + \omega_y^2 y^2 + \omega_z^2 z^2\right). \tag{3.4.21}$$

From Eq.3.4.18 and 3.4.21, μ becomes

$$\mu = \frac{1}{2}\hbar\bar{\omega}\left(15Na\sqrt{\frac{m\bar{\omega}}{\hbar}}\right)^{2/5}, \tag{3.4.22}$$

where $\bar{\omega} \equiv (\omega_x\omega_y\omega_z)^{1/3}$.

Using the scaling law in Eq.3.4.4, the density distribution of a BEC after t time ballistic expansion can be represented as

$$\begin{aligned} n_{\rm TF}(\boldsymbol{r}, t) &= \frac{1}{\lambda_x(t)\lambda_y(t)\lambda_z(t)} n\left[\left(\frac{x}{\lambda_x(t)}, \frac{y}{\lambda_y(t)}, \frac{z}{\lambda_z(t)}\right), t = 0\right] \\ &= \frac{\mu}{U_0}\left[1 - \left(\frac{x^2}{d_x^2(t)} + \frac{y^2}{d_y^2(t)} + \frac{y^2}{d_y^2(t)}\right)\right], \end{aligned} \tag{3.4.23}$$

where

$$d_\nu(t) = \lambda_\nu(t)\sqrt{\frac{2\mu}{m\omega_\nu^2}}, \quad \nu = x, y, z. \tag{3.4.24}$$

With the number of coherent atoms $N_{\rm BEC}$, Eq.3.4.23 is transformed as

$$n_{\rm TF}(\boldsymbol{r}, t) = \frac{15N_{\rm BEC}}{8\pi d_x d_y d_z}\left[\max\left[1 - \left(\frac{x^2}{d_x^2(t)} + \frac{y^2}{d_y^2(t)} + \frac{y^2}{d_y^2(t)}\right), \ 0\right]\right] \tag{3.4.25}$$

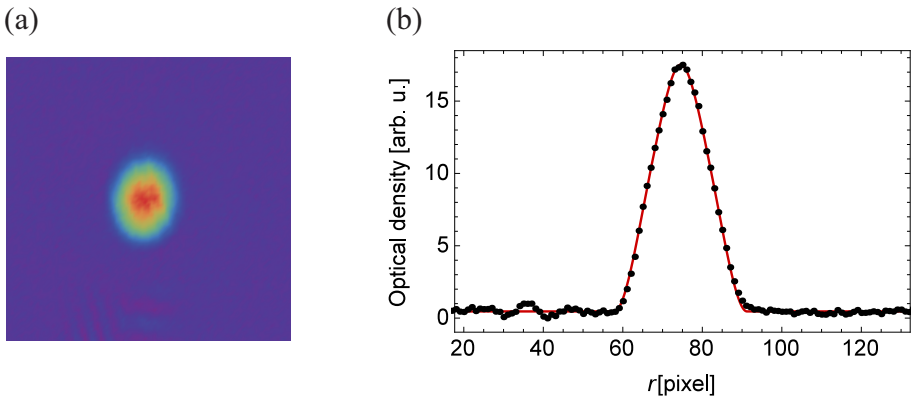

Figure 3.4.2: (a) Absorption image of ^{174}Yb BEC taken after 14 ms ballistic expansion. (b) Integrated optical density. Bimodal fitting is made. In this case, almost all of the atoms is BEC, and the fitting result is $N_{\mathrm{BEC}} = 2.0 \times 10^3$.

Integration and twice-integration give the following 2D and 1D densities

$$n_{\mathrm{TF}}(x,y,t) = \frac{5N_{\mathrm{BEC}}}{2\pi d_x d_y}\left[\max\left[1-\left(\frac{x^2}{d_x^2(t)}+\frac{y^2}{d_y^2(t)}\right),\ 0\right]\right]^{3/2}, \tag{3.4.26}$$

$$n_{\mathrm{TF}}(x,t) = \frac{15N_{\mathrm{BEC}}}{16 d_x(t)}\left[\max\left[1-\frac{x^2}{d_x^2},\ 0\right]\right]^{2}. \tag{3.4.27}$$

Figure 3.4.2(a) shows a typical absorption image of a BEC of ^{174}Yb and Fig.3.4.2 (b) is the result of bimodal fitting to the 1D optical density.

3.5 Optical lattice

In this section, we describe our experimental setup of optical lattices, including an optical Lieb lattice. Figure 3.5.1, 3.5.2, and 3.5.3 illustrate the optics setup for optical lattices.

3.5.1 Monochromatic lattice

We have three kinds of monochromatic lattices with different lattice spacing (266 nm, 532 nm, $\sqrt{2} \times 266$ nm). We call them 532 nm lattice, 1064 nm lattice, and diagonal lattice, respectively. Below, we explain the experimental setup of each lattice.

532 nm lattice

Our 532 nm lattices exist in x, y, z-axis. The 532 nm lattice in each axis is created by interference of incident laser beam and its retroreflection. As in the Fig.3.5.1(a), the 0th-order diffracted light from the AOM for intensity control of the horizontal FORT is divided to three beams, and used for 532 nm lattices. Each beam is diffracted by AOMs (Crystal Technology) for intensity stabilization and ±1st-order beam are coupled to the optical fibers. We put pinholes for mode-cleaning before fiber couplers not to cause the serious damage to the fibers. The laser intensity is stabilized by monitoring the laser power by

Before optical fiber

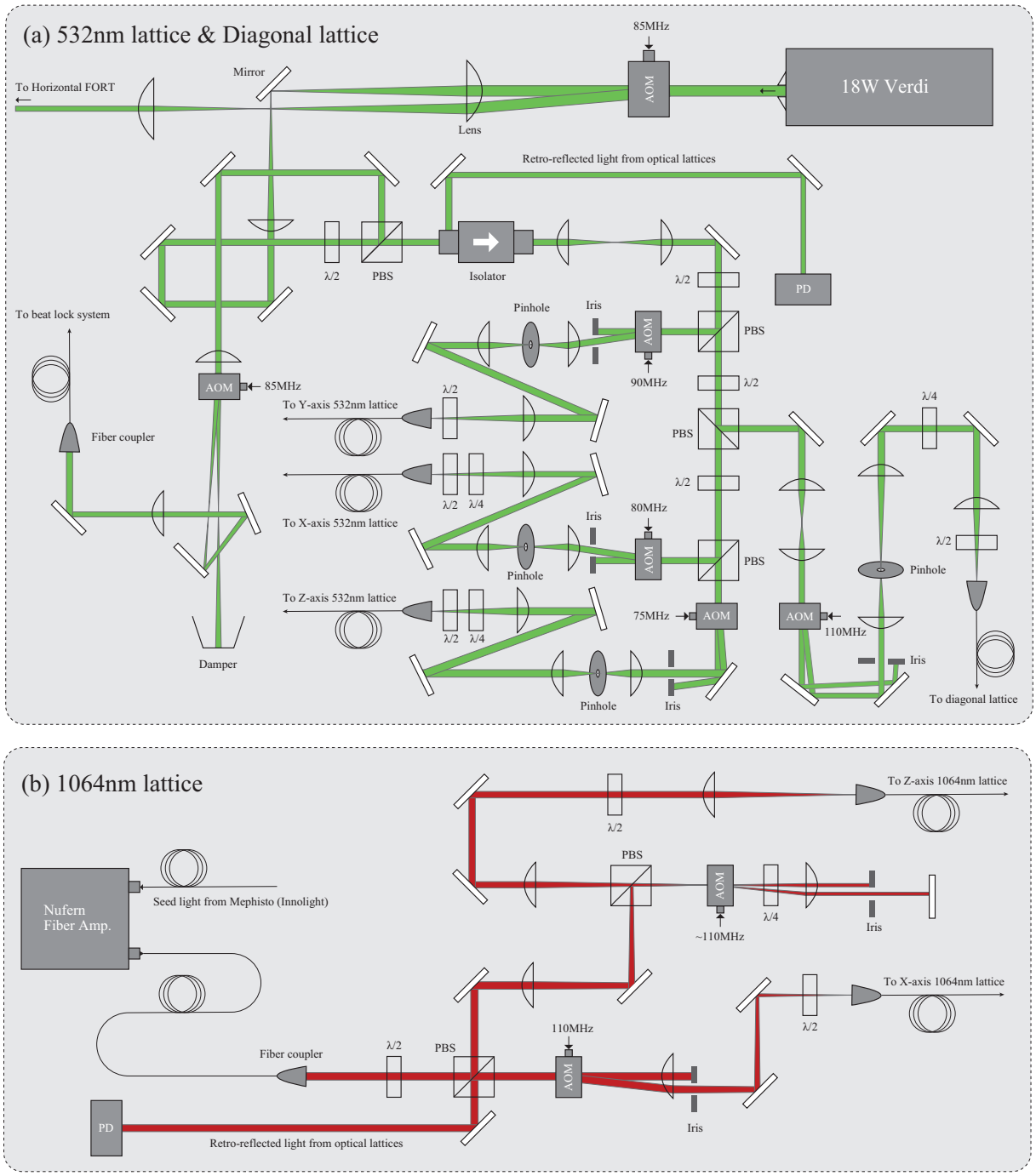

Figure 3.5.1: Optics for optical lattices before the optical fibers.

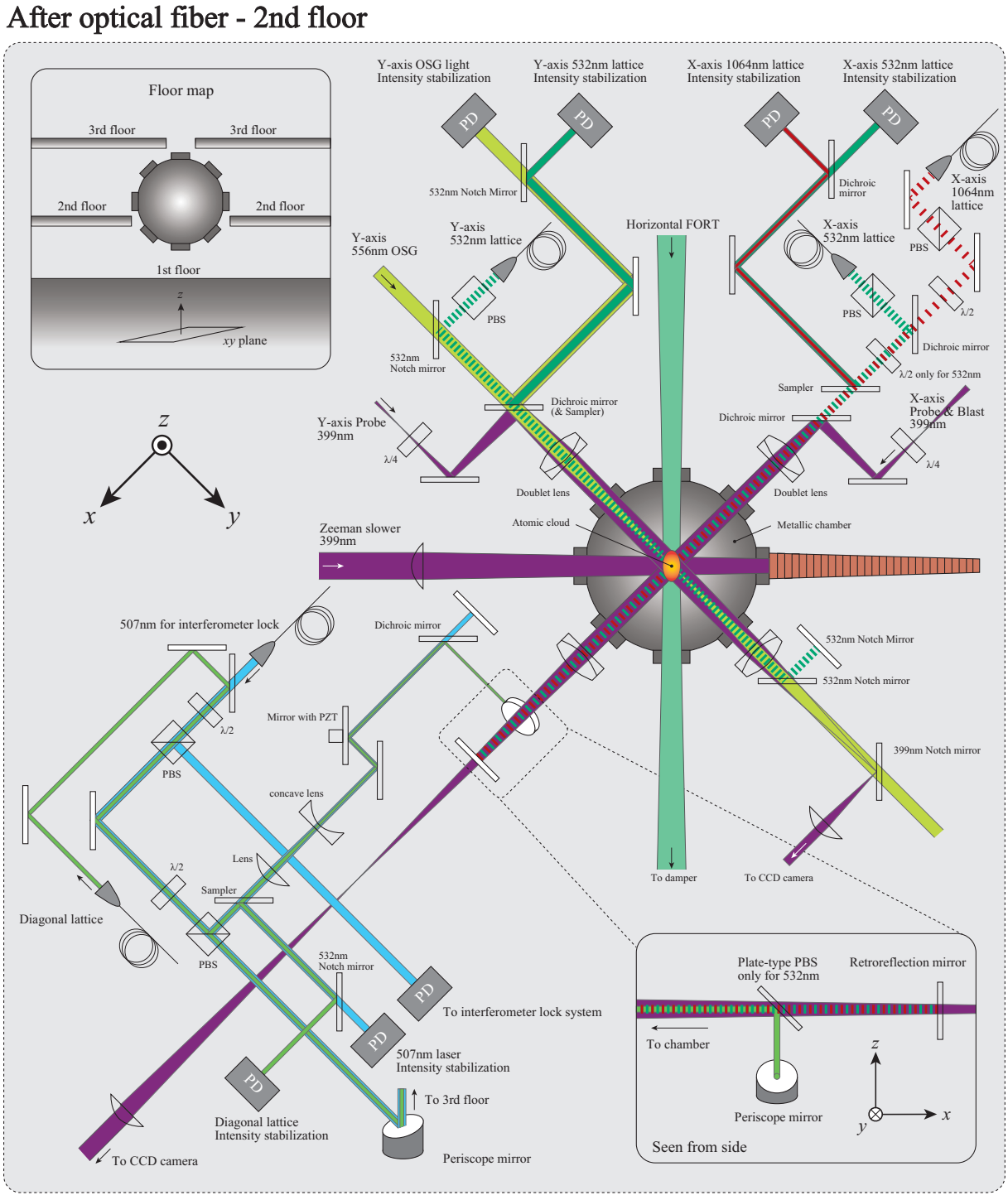

Figure 3.5.2: Optics in 2nd floor around the metallic chamber

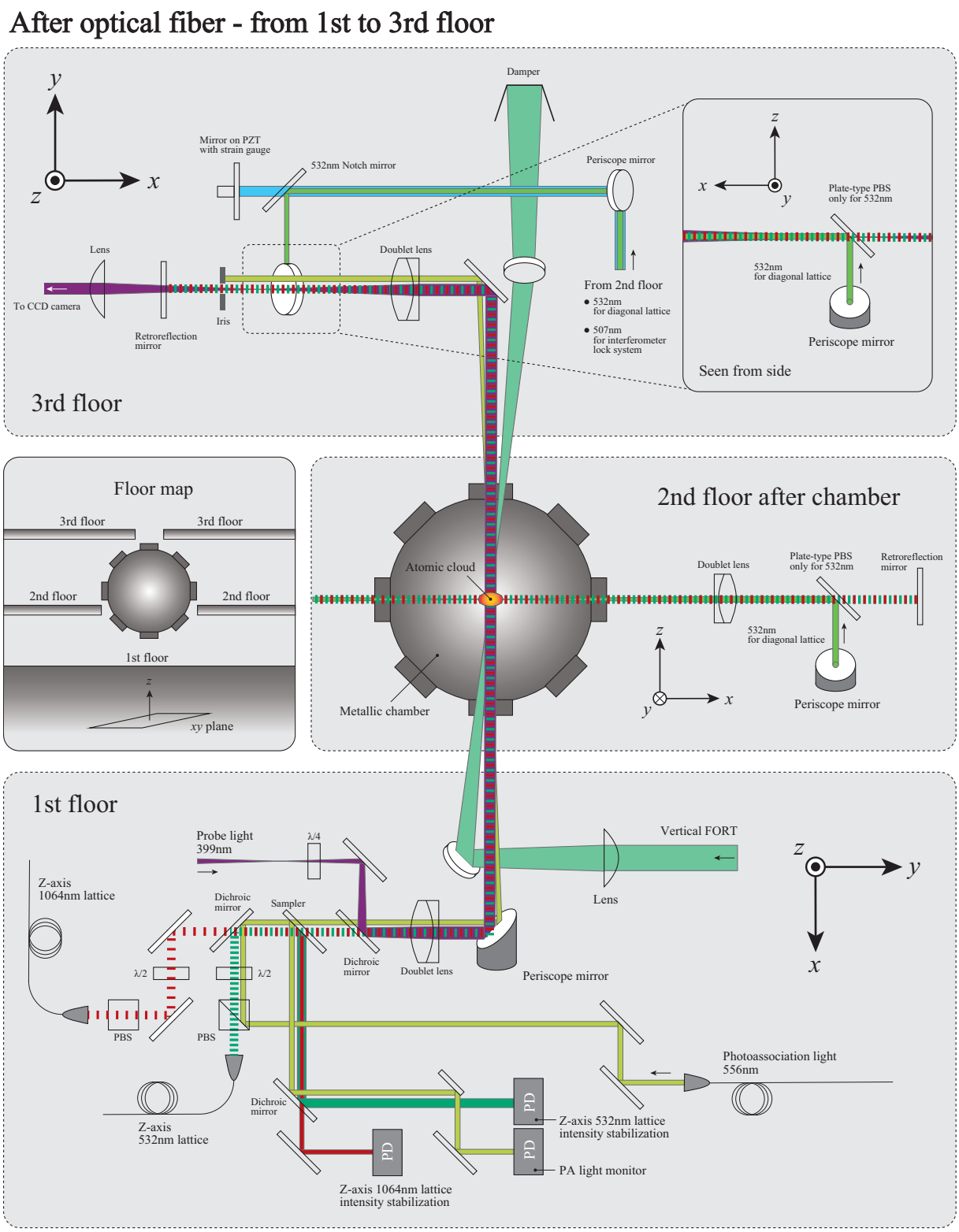

Figure 3.5.3: Optics from 1st to 3rd floor around the metallic chamber

photodiodes after the fibers (See Fig.3.5.2, 3.5.3) and sending the feedback signal to the AOMs.

To achieve enough lattice depth and avoid displacement of an atomic cloud, we have to well-align incident lattice beam and its retroreflection. The procedure is as follows. First, we align an incident lattice beam. Using a CCD camera on the same axis for an optical lattice, we record the position of atomic cloud trapped in the crossed FORT. A pulse of the incident lattice beam is shed onto the atomic cloud immediately after switching off the trapping potential. If center position of the beam is not well-aligned, atoms feel force by the field gradient of the pulse. This acceleration can be observed by measuring the position of atoms after some time-of-flight and comparing it to the case without the pulse. Typically, the pulse power is set to as high as possible and its duration is 2ms, and the time-of-flight is 14ms. Second, we align the retroreflection. We adjust the retroreflection mirror so that the retroreflected beam maximally couples to the optical fiber from which the incident lattice beam is emitted. The coupled laser light returns up to an optical isolator and is reflected by the PBS therein. The reflection is monitored by a photodiode for optimization (See Fig.3.5.1(a)).

1064 nm lattice

Our 1064 nm lattice exists in x, z-axis. 1064 nm lattice in each axis is created by interference of incident laser beam and its retroreflection. As in the Fig.3.5.1(b), output from a fiber amplifier (Nufern) is divided to two beams and used for 1064 nm lattices. Each beam is diffracted by AOMs (Crystal Technology) for intensity stabilization and $\pm$1st-order beam are coupled to the optical fibers. A double-pass AOM is used for z-axis 1064 nm lattice to adjust the difference of the relative phase of superlattices between x and z-axes (See the section 3.5.3 for details).

When we align 1064 nm lattices, we assume that x- and z-axis 532 nm lattices are already aligned. An incident beam of 1064 nm lattice and its retroreflection need fine-tuning . However, because the retroreflection mirror is already optimized for 532 nm lattice, it should not be tuned for 1064 nm lattice. Alternatively, we use two mirrors right after the fiber coupler from which the incident lattice beam is emitted and before overlapping onto 532 nm lattice (See Fig.3.5.2 and 3.5.3). The procedure is as follows. We use a video mode in a CCD camera on the same axis for a 1064 nm lattice and confirm center positions of 1064 nm lattice beam and 532 nm lattice beam. Then, we align one of the two mirrors so that these centers are overlapped. As for the retroreflection of 1064 nm lattice, we align the other mirror so that the retroreflective beam couples to the optical fiber from which the incident beam of 1064 nm lattice is emitted. We repeat the above procedure until the center position and coupling efficiency converge. Note that when aligning the input beam seeing the center on a CCD camera, its power should be as low as possible for better accuracy, on the other hand, when coupling the retroreflection to the optical fiber, its power should be as high as possible for better S/N.

Diagonal lattice

Our diagonal lattice has a lattice distance of $\sqrt{2}\times$266 nm because it is formed by interference of orthogonally propagating waves with wavelength 532 nm. Experimental setup before optical fiber is basically the same for 532 nm lattice as in Fig.3.5.1(a). After the

optical fiber, 532 nm beam is divided to x and z-axis and overlapped onto 532 nm lattices by a plate-type PBS (See Fig.3.5.2 and 3.5.3). The phase of diagonal lattice is locked and controlled by Michelson's interferometer using 507 nm laser beams, the detail of which is descried in the section 3.5.3.

When we align the diagonal lattice, we assume again that x- and z-axis 532 nm lattices are aligned. We have to overlap 532 nm laser beams constructing the diagonal lattice onto 532 nm lattice. The 532 nm laser beams of diagonal lattice come into a chamber after reflected at a PBS in front of a retroreflection mirror. At the PBS, 532 nm lattice beams are also reflected by a few percents. The reflection goes against 532 nm laser beams of diagonal lattice. If the reflection maximally couples to the optical fiber from which 532 nm laser beam of diagonal lattice is emitted, it follows that the diagonal lattice is well-aligned because the 532 nm laser beams of it propagate along the same path as 532 nm lattice.

As for alignment of the 507 nm laser beam, which is used for a Michelson's interferometer lock, it should be overlapped onto 532 nm laser beam of the diagonal lattice because the interferometer stabilizes and controls an optical path length of the diagonal lattice. We superimpose the 532 nm laser beam of the diagonal lattice onto the 507 nm laser beam. Retroreflective mirrors of 507 nm laser beams are tuned so that the interference amplitude by the retroreflection is maximized.

Calibration of the optical lattice depth

There are two ways to calibrate a lattice potential depth. One is a pulsed lattice [84], the other is parametric heating [85]. We adopt the pulsed lattice calibration using diffraction of a BEC of ^{174}Yb. Below, the principle of this method is summarized.

The initial state of an atom should be $|\Psi(t=0)\rangle = |\boldsymbol{k}=0\rangle$ since the momentum distribution of a BEC has a very sharp peak at $\boldsymbol{k}=0$. A BEC suddenly loaded into a lattice can be described as a superposition of Bloch states $|q,n\rangle$:

$$|\Psi(t=0)\rangle = \sum_{n=0}^{\infty} |q,n\rangle \langle q,n|\boldsymbol{k}=0\rangle \,. \tag{3.5.1}$$

From Eq. 2.3.6, $\langle q,n|\boldsymbol{k}=0\rangle = (A_{m=0}^{q,n})^*$. Then, while the BEC wavepacket is held in the lattice, it evolves in time according to

$$|\Psi(t)\rangle = \sum_{n=0}^{\infty} (A_{m=0}^{q,n})^* \exp\left(-i\frac{E_{q,n}}{\hbar}t\right) |q,n\rangle \,. \tag{3.5.2}$$

If the state in Eq. 3.5.2 is projected onto the plane-wave basis, we obtain the coefficients B_m^q of each $|q+mK\rangle$ in the lattice frame:

$$B_m^q(t) = \sum_{n=0}^{\infty} (A_{m=0}^{q,n})^* A_m^{q,n} \exp\left(-i\frac{E_{q,n}}{\hbar}t\right) . \tag{3.5.3}$$

The interference of the exponential factors produces oscillations in the populations of the plane-wave components as a function of t or $E_{q,n}$. Figure 3.5.4(a) shows simulated time evolution of a ^{174}Yb BEC under pulsed exposure of 532 nm lattice potential. The

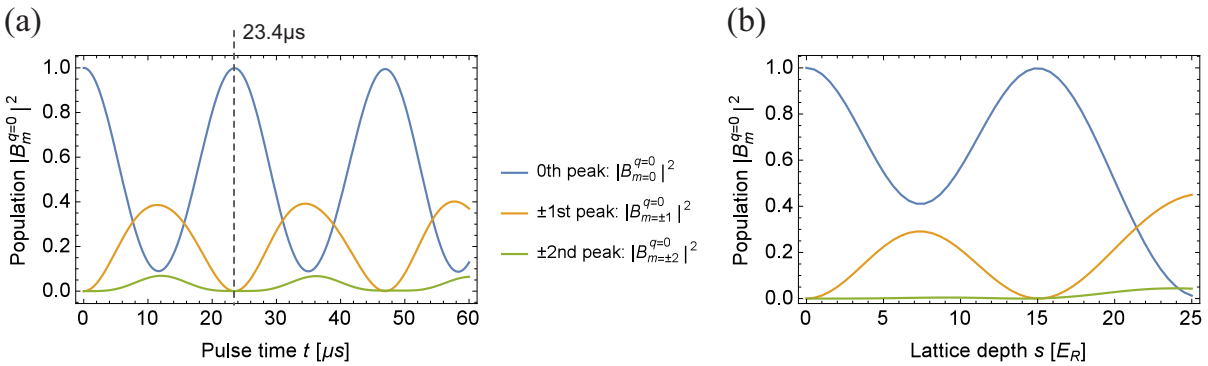

Figure 3.5.4: (a) Simulated time evolutions of a BEC in a pulsed optical lattice with the depth of 15 E_R^{532} and lattice constant of 266 nm. (b) Lattice depth versus population of each momentum component in a pulsed optical lattice with lattice constant of 266 nm after $t = 23.4\ \mu s$ time evolution.

oscillations are almost sinusoidal, and the period is about 23.4 μs. For 1064 nm lattice and diagonal lattice, the periods become $4 \times 23.4\ \mu s$ and $2 \times 23.4\ \mu s$ respectively because $E_{q,n}$ is scaled by recoil energy $E_{\mathrm{R}} = \frac{\hbar^2 k^2}{2m}$, which depends on wavelength of lasers creating the optical lattice.

In practice, we fix the pulse duration at 23.4 μs for 532 nm lattice ($4 \times 23.4\ \mu s$ for 1064 nm lattice, $2 \times 23.4\ \mu s$ for diagonal lattice, respectively), and scan the power of the lattice beam as in Fig. 3.5.4. The power where the 1st-order diffraction peaks first disappear corresponds to 15 E_{R}. Note that we irradiate the pulse of z-axis 1064 nm lattice before turning off FORT potential; otherwise gravitational force seriously distorts the momentum distribution of a BEC in the lattice during the pulse time.

3.5.2 Optical superlattice

Optical superlattice is formed by superimposing two optical lattices with different lattice spacing. One dimensional optical superlattice potential is written as

$$V(x) = V_{\mathrm{long}} \sin^2(k_{\mathrm{long}} x) + V_{\mathrm{short}} \sin^2(2k_{\mathrm{long}} x + \phi) \tag{3.5.4}$$

where ϕ is relative phase between long-lattice and short-lattice. ϕ changes the lattice configuration dynamically. Therefore, the momentum distribution also strongly depends on the relative phase. Figure 2.3.3 shows ϕ-dependence of each order diffraction peak of a BEC in the lattice. At $\phi = \pi/2$, 1st order diffraction peak disappears because the period of the lattice approximates the half of $\phi = 0$ case. This dependence can be used to determine the relative phase.

Lock and control of relative phase

First of all, we introduce the concrete form of relative phase ϕ in our experimental setup. We rewrite 1D optical superlattice as

$$\tilde{V}(x) = V_{1064} \sin^2(k_{1064} x) + V_{532} \sin^2(k_{532} x) \tag{3.5.5}$$

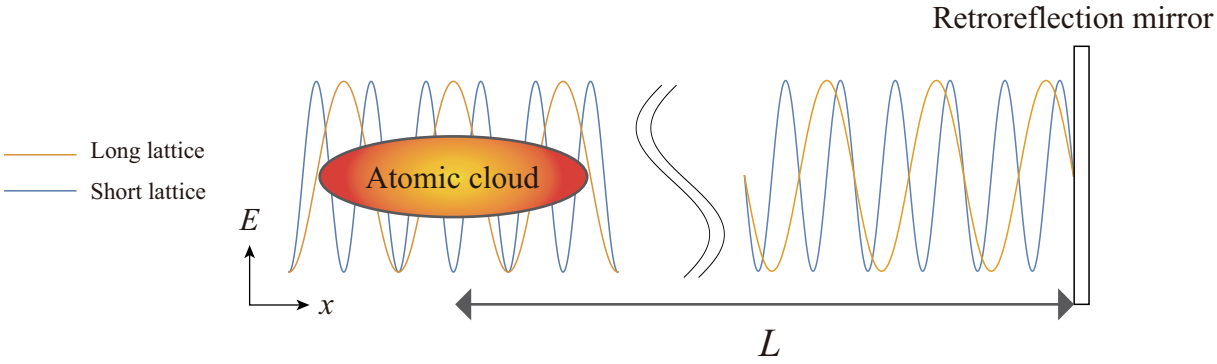

Figure 3.5.5: Schematics of relative phase of superlattice with retroreflection mirror. The relative phase is represented as $\phi = 2\pi L \Delta f_{\mathrm{beat}}/c$, where L is the optical path length from the mirror to the atomic cloud.

Note that $2k_{1064} \neq k_{532}$ in general since the laser sources of 532 nm lattice and 1064 nm lattice are different. We introduce beat frequency f_{beat} such as

$$f_{\mathrm{beat}} = f_{532} - 2f_{1064} \tag{3.5.6}$$

where $f_{532} = \frac{c}{2\pi}k_{532}$, $f_{1064} = \frac{c}{2\pi}k_{1064}$. Then, $\tilde{V}(x)$ can be transformed as

$$\tilde{V}(x) = V_{1064}\sin^2(k_{1064}x) + V_{532}\sin^2(2k_{1064}x + \frac{2\pi}{c}f_{\mathrm{beat}}x) \tag{3.5.7}$$

If we take the origin of x at the surface of retroreflective mirror, where 532 nm lattice and 1064 nm lattice are in-phase (See Fig.3.5.5), the relative phase can be written as

$$\phi = \frac{2\pi}{c}f_{\mathrm{beat}}L \tag{3.5.8}$$

where L is the distance from the surface of a retroreflective mirror to an atomic cloud. The relative phase depends on L and f_{beat}. Assuming L is passively stable, we control the relative phase ϕ by f_{beat}.

To generate a beat signal, we pick up laser lights used for 532 nm lattice and 1064 nm lattice. Laser beam of 532 nm lattice is divided by a PBS in front of an isolator (See Fig.3.5.1). After diffracted by an AOM for intensity stabilization, the signal is transported by an optical fiber to other anti-vibration table as in Fig.3.5.6, where the light source of 1064 nm lattice exists. The laser beam of 1064 nm lattice is divided by a PBS, and its frequency is doubled by a PPLN (Periodically Poled Lithium Niobate) crystal. This is the reason why there is factor 2 in front of f_{1064} in Eq.3.5.6. The SHG light is overlapped onto the sampled light of 532 nm lattice. For perfect overlap, both lights are coupled to a optical fiber, and we take a beat signal by a photo diode. The beat signal is sent to a beat lock system shown in Fig.3.5.7. First, we combine the beat signal and a signal from VCO (Voltage Controlled Oscillator) by a mixer, whose frequency is defined as f_{VCO}. Since output from the mixer has two frequency components $f_{\mathrm{beat}} \pm f_{\mathrm{VCO}}$, we extract the component with $f_{\mathrm{beat}} - f_{\mathrm{VCO}}$ by low pass filter. We rewrite this signal as $f_{\mathrm{low}} = f_{\mathrm{beat}} - f_{\mathrm{VCO}}$ just for convenience. After amplified, the signal is divided to two

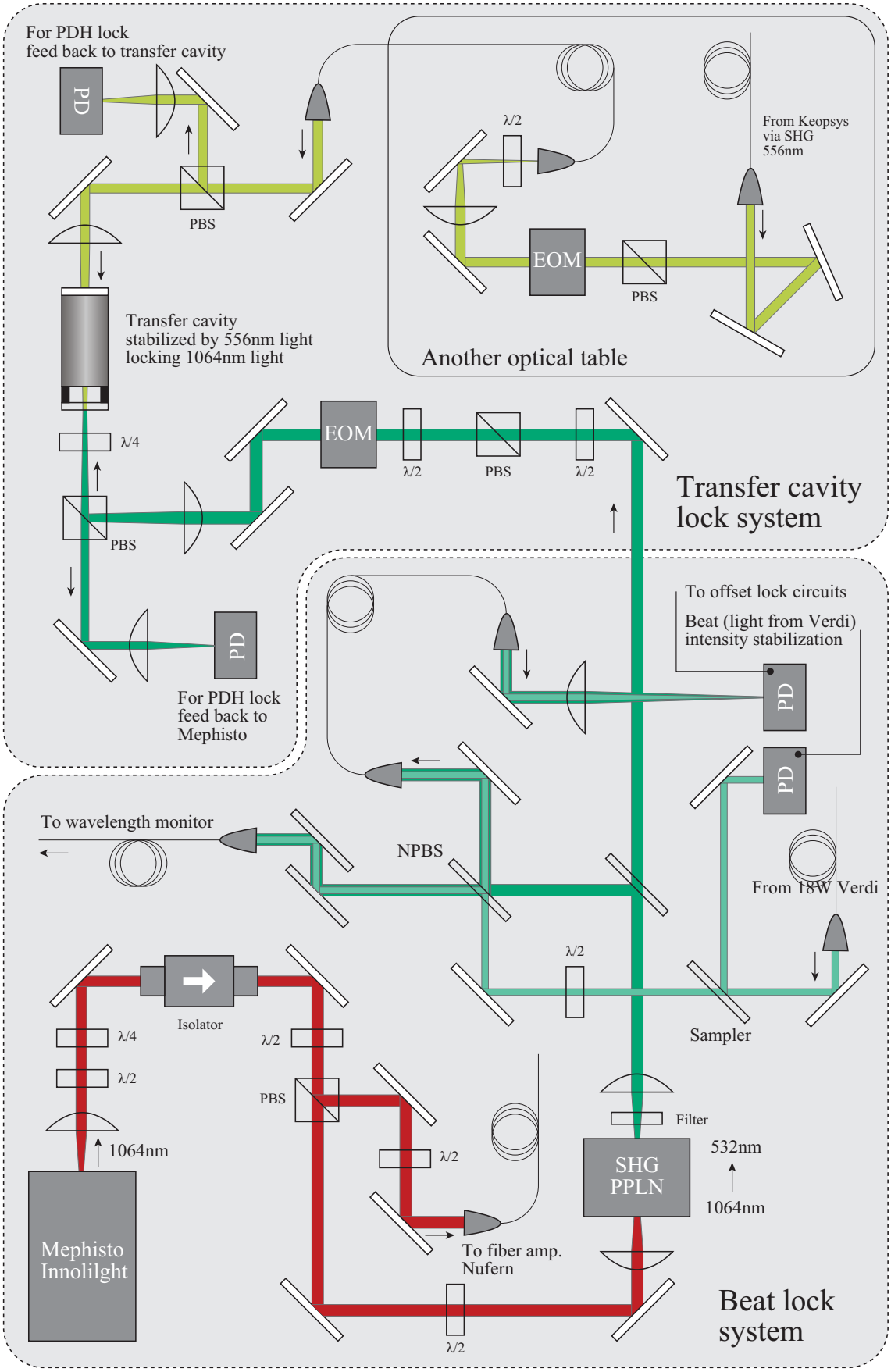

Figure 3.5.6: Optics for the beat lock and transfer-cavity lock system.

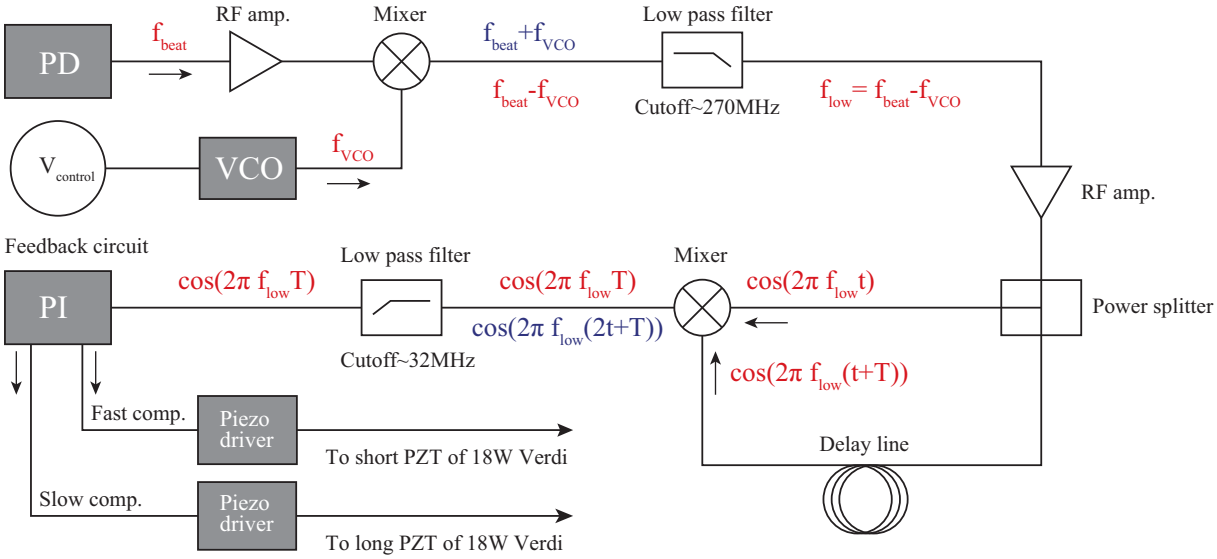

Figure 3.5.7: Schematic of the system for locking and controlling the beat signal.

signals by a power splitter. One signal propagates in a delay line, where we assume that it takes T extra time. Since inputs into a mixer are $\cos(2\pi f_{\mathrm{low}} t)$ and $\cos(2\pi f_{\mathrm{low}}(t+T))$, the output becomes $\cos(2\pi f_{\mathrm{low}} T) + \cos(2\pi f_{\mathrm{low}}(2t+T))$. We remove the AC component $\cos(2\pi f_{\mathrm{low}}(2t+T))$ by low pass filter. By using the DC signal $V_{\mathrm{DC}} \propto \cos(2\pi f_{\mathrm{low}} T)$, the offset-lock circuit feedbacks a fast signal to a short-PZT and slow signal to long-PZT in 18W Verdi via piezo drivers so that $V_{\mathrm{DC}} = 0$;

$$f_{\mathrm{low}} = f_{532} - 2f_{1064} - f_{\mathrm{VCO}} = \text{Constant}. \tag{3.5.9}$$

Thus, beat frequency f_{beat} is stabilized by the feedback, and controlled by f_{VCO}. In practice, the beat frequency is roughly adjusted by changing a lock point, and precisely adjusted by control voltage to VCO.

By TOF measurement, we observe at least two nearest f_{beat} where $\pm$1st order diffraction peak of a BEC in an optical superlattice disappears, and determine correspondence between relative phase ϕ and beat frequency f_{beat}.

3.5.3 Optical Lieb lattice

Our optical Lieb lattice is constructed by overlapping square long-lattice, square short-lattice and diagonal lattice with their phases controlled, as in Fig.3.5.8. First, we consider making 2D superlattice by overlapping square long-lattice and square short-lattice. The 2D optical superlattice potential can be written as

$$\begin{aligned} V(x,z) = V^x_{\mathrm{long}} \sin^2(k_{1064}x) + V^x_{\mathrm{short}} \sin^2(2k_{1064}x + \phi_x) \\ V^z_{\mathrm{long}} \sin^2(k_{1064}z) + V^z_{\mathrm{short}} \sin^2(2k_{1064}z + \phi_z). \end{aligned} \tag{3.5.10}$$

where $\phi_x = 2\pi L_x f_{\mathrm{beat}}/c$, $\phi_z = 2\pi L_z f_{\mathrm{beat}}/c$. To realize optical Lieb lattice, relative phases ϕ_x, ϕ_z must be zero at a certain beat frequency f_{beat}. However, generally speaking, $\phi_x \neq \phi_z$ since $L_x \neq L_z$; distances from the surface of retroflection mirror are different for the x

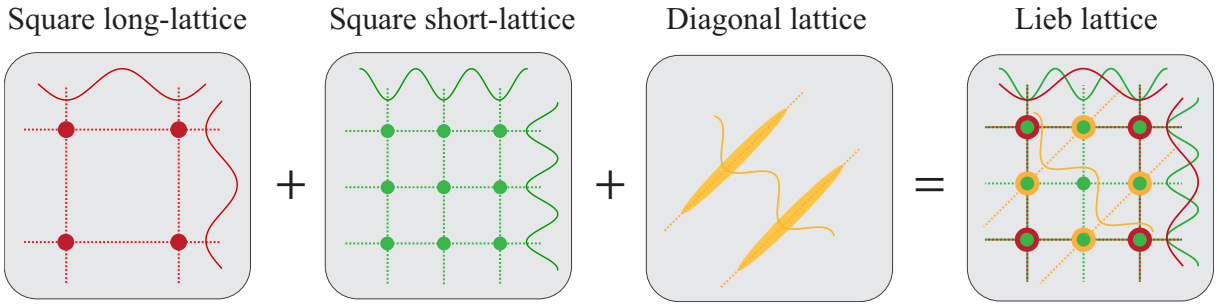

Figure 3.5.8: Construction method of our optical Lieb lattice.

and z-axis. Therefore, we compensate difference of the relative phases by adjusting RF to a double-pass AOM in z-axis 1064 nm lattice (See Fig.3.5.1(b)) so that $\phi_x = \phi_z = 0$ is satisfied.

Next, we consider superimposing a diagonal lattice onto the 2D superlattice. We have to control the relative phase between them. Since the phase of the diagonal lattice is locked by a Michelson's interferometer as described in the latter paragraph, a frequency drift of 1064 nm lattice affects the relative phase. We use a transfer cavity to stabilize the frequency of a seed light for the 1064 nm lattice (See Fig.3.5.6). 532 nm light of Mephist after SHG is coupled to a transfer cavity. The length of the cavity is stabilized by 556 nm light, frequency of which is narrow and stable since locked into a ULE cavity. The frequency of Mephist is locked to the stabilized transfer cavity. We adopt the PDH (Pound-Drever-Hall) method [86] for stabilization of the transfer cavity and Mephist.

Michelson's interferometer

Our diagonal lattice is created by interference of orthogonally propagating laser beams. Supposing that each laser beam propagates the optical path length l_1, l_2, and has electric-field $\boldsymbol{E}_1, \boldsymbol{E}_1$, laser frequency ω, and wave number k, the optical potential of diagonal lattice becomes

$$\begin{aligned} V(x,z) &\propto \overline{\left|\boldsymbol{E}_1 \cos(\omega t + k l_1) + \boldsymbol{E}_2 \cos(\omega t + k l_2)\right|^2} \\ &= \overline{\left|\boldsymbol{E}_1 \cos(\omega t + k l_1)\right|^2} + \overline{\left|\boldsymbol{E}_2 \cos(\omega t + k l_2)\right|^2} + 2\boldsymbol{E}_1 \cdot \boldsymbol{E}_2 \overline{\cos(\omega t + k l_1)\, \cos(\omega t + k l_2)} \\ &= \frac{\left|\boldsymbol{E}_1\right|^2 + \left|\boldsymbol{E}_2\right|^2}{2} + \boldsymbol{E}_1 \cdot \boldsymbol{E}_2 \cos\left(k\left(l_1 - l_2\right)\right). \end{aligned} \tag{3.5.11}$$

(3.5.12)

Thus, the phase of diagonal lattice depends on the difference of optical path lengths $l_1 - l_2$. Fluctuation of the optical path length might be caused by air flow, temperature dependence of the refractive index, mechanical instability such as vibration, and so on. Therefore, we have to stabilize the optical path length.

We construct a Michelson's interferometer by overlapping the off-resonant laser beam (507 nm light) onto 532 nm laser beam used for the diagonal lattice. Figure 3.5.9 shows the schematic of a Michelson's interferometer lock system. $l_1, l_2, l_{1\mathrm{lock}}, l_{2\mathrm{lock}}, l'_{1\mathrm{lock}}, l'_{2\mathrm{lock}}$ are the optical path length represented by each arrow. According to Eq.3.5.11, the interference

signal at PD becomes

$$V_{\mathrm{Int}}^{507} \propto \frac{|\boldsymbol{E}_1^{507}|^2 + |\boldsymbol{E}_2^{507}|^2}{2} + \boldsymbol{E}_1^{507} \cdot \boldsymbol{E}_2^{507} \cos\left(2k_{507}((l_{1\mathrm{lock}} + l'_{1\mathrm{lock}}) - (l_{2\mathrm{lock}} + l'_{2\mathrm{lock}}))\right). \tag{3.5.13}$$

We feedback to the PZT, which can change $l_{2\mathrm{lock}}$, so as to satisfy $V_{\mathrm{Int}}^{507} = 0$ by using an offset lock circuit;

$$l_{1\mathrm{lock}} - l_{2\mathrm{lock}} = -(l'_{1\mathrm{lock}} - l'_{2\mathrm{lock}}) + \mathrm{Const.}. \tag{3.5.14}$$

Then, the diagonal lattice potential at an atomic cloud becomes

$$V_{\mathrm{diag}}(x, z) \propto \boldsymbol{E}_1^{532} \cdot \boldsymbol{E}_2^{532} \cos\left(k_{532}/2(x - z) + k_{532}/2\left((l_{1\mathrm{lock}} + l_1) - (l_{2\mathrm{lock}} + l_2)\right)\right). \tag{3.5.15}$$

Here, we omit the constant term for simplicity. Substituting Eq.3.5.14, we get

$$V_{\mathrm{diag}}(x, z) \propto \boldsymbol{E}_1^{532} \cdot \boldsymbol{E}_2^{532} \cos^2\left(k_{532}/2(x - z) + k_{532}/2\left((l_1 - l_2) - (l'_{1\mathrm{lock}} - l'_{2\mathrm{lock}}) + \mathrm{Const.}\right)\right). \tag{3.5.16}$$

The phase of diagonal lattice depends on $l'_{1\mathrm{lock}}$, which can be controlled by a PZT.

Hysteresis of a PZT length against control voltage will happen when we repeatedly wiggle the length back and forth. We adopt a PZT with strain gauge to improve repeatability of phase of diagonal lattice. Strain gauge detects length of PZT therein by using Wheatstone bridge as in Fig.3.5.10(a). We use AC voltage to drive the strain gauge, amplify the readout voltage by preamplifier in Fig.3.5.10(b), and detect its peak-to-peak voltage by lock-in amplifier. We feedback the PZT by offset lock circuit so that difference between output voltage from lock-in amp. and control voltage becomes zero (See Fig.3.5.10(c)).

Calibration of diagonal phase

Through all the above process, the optical lattice potential made by superimposing square long-lattice, square short-lattice and diagonal lattice can be written as

$$\begin{aligned} V(x, y) \quad &= -V_{\mathrm{long}}(\cos^2(k_L x) + \cos^2(k_L y)) \\ &\quad -V_{\mathrm{short}}(\cos^2(2k_L x) + \cos^2(2k_L y)) \\ &\quad -V_{\mathrm{diag}} \cos^2(k_L(x - y) + \psi) \end{aligned} \tag{3.5.17}$$

where ψ is relative phase of diagonal lattice. We call it diagonal phase below. In our experiment, ψ is the last parameter that remains to be determined. We sweep the diagonal phase and find where Lieb lattice configuration is realized. In the case of bosonic isotopes, such a diagonal phase is determined by observing multi matter-wave interference patterns as in Fig.3.5.11). Because of larger hopping at a Lieb lattice configuration, the visibility gets better compared with that of the adverse phase where lattice spacing is 532 nm. As for fermionic isotopes, band mapping technique is used. In addition to the fact that the band structure in Lieb lattice has narrow total band width up to 3rd band, finite temperature and Pauli principle enforce the fermionic atoms to occupy higher bands. Therefore, higher Brillouin zones are most occupied when Lieb lattice configuration is realized.

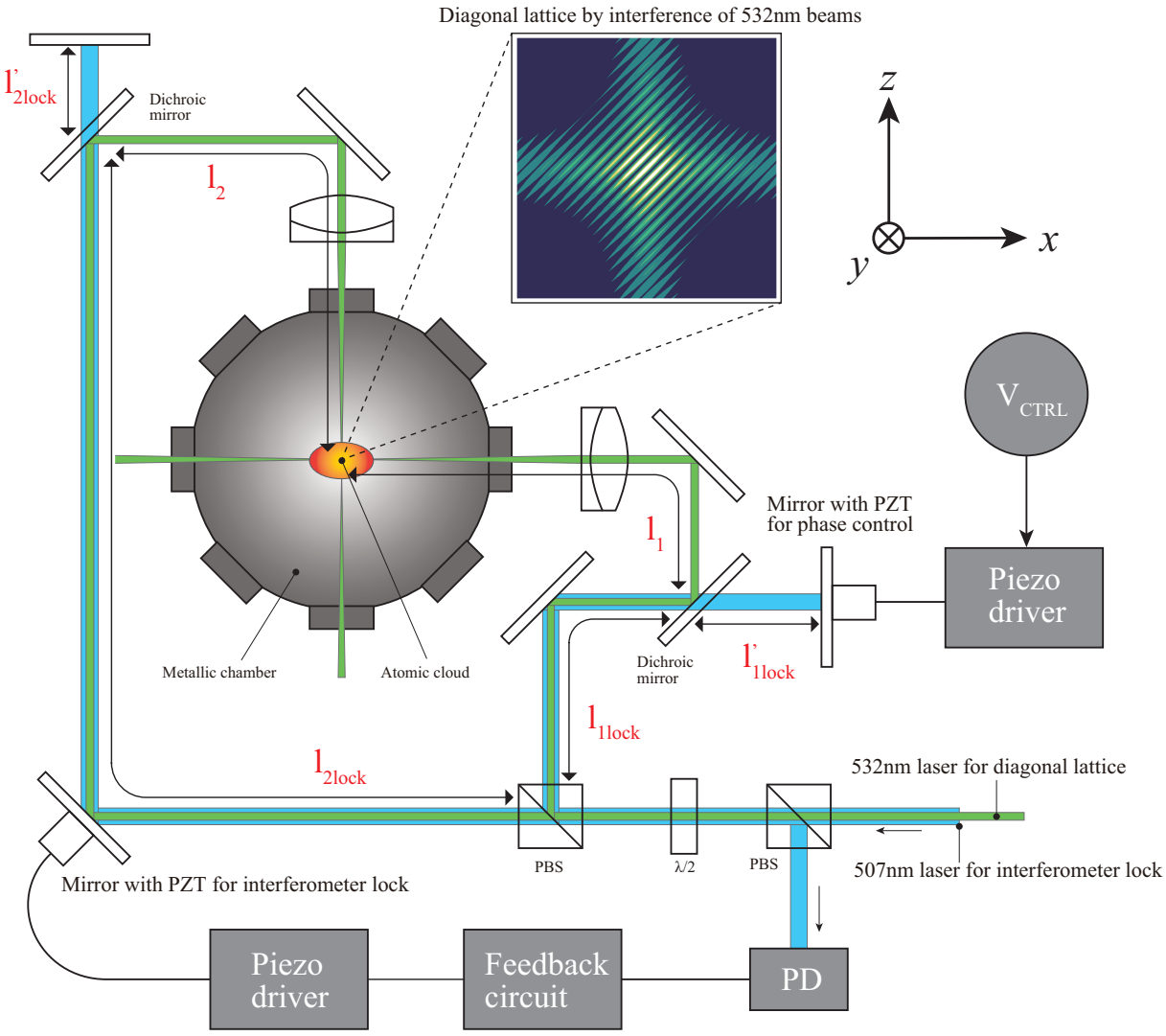

Figure 3.5.9: Schematics of a system to lock and control the relative phase of diagonal lattice. Difference of the optical path length of 507 nm light $(l_{1\mathrm{lock}}+l'_{1\mathrm{lock}})-(l_{2\mathrm{lock}}+l'_{2\mathrm{lock}})$ is locked by Michelson interferometer. Relative phase of the diagonal lattice is controlled by the retroreflection mirror with PZT. Note that actual setup is illustrated in Fig.3.5.2 and 3.5.3.

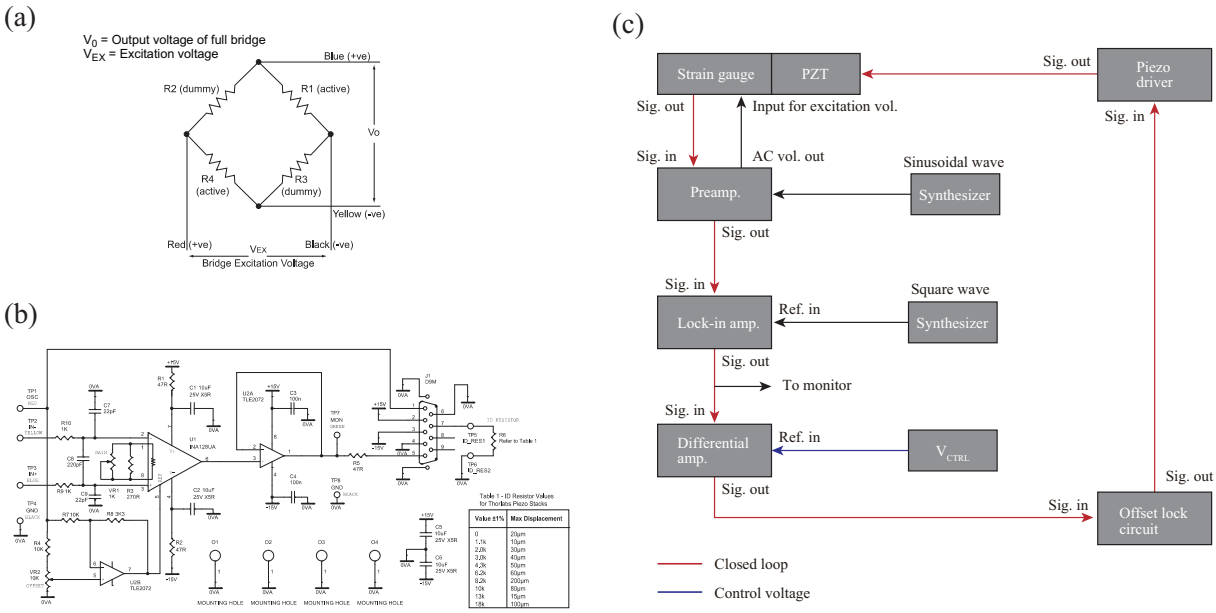

Figure 3.5.10: (a) Schematic of strain gauge. Wheatstone bridge connection is used to detect the change of resistance. (b) Preamplifier to amplify the signal from strain gauge. Figure (a) and (b) are cited from Thorlabs webpage. (c) Wiring diagram to drive the strain gauge on a PZT with feedback control.

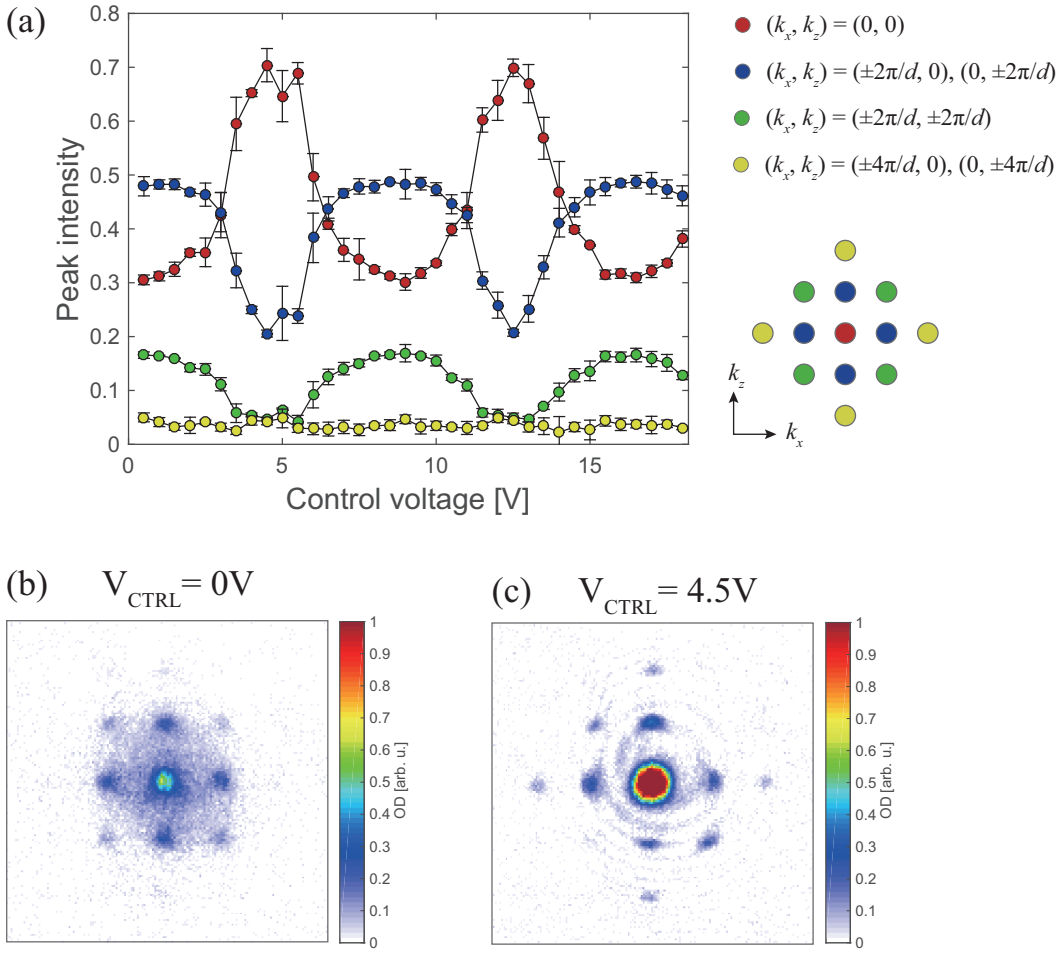

Figure 3.5.11: (a) Diagonal lattice phase versus peak intensity of interference pattern of ^{174}Yb BEC in the lattice potential 3.5.17. The horizontal axis is control voltage to a PZT. The lattice depths are $(s_{\mathrm{short}}, s_{\mathrm{long}}, s_{\mathrm{diag}}) = (8, 8, 9.5)$. Error bar means standard deviation of three-independent scan. (b), (c) Absorption image of interference pattern with $V_{\mathrm{CTRL}} = 0$ V and 4.5 V.

Chapter 4

Coherent driving and freezing of bosonic matter wave in an optical Lieb lattice

4.1 Loading a BEC into a flat band by phase imprinting

In special lattice structures such as kagome, sawtooth and Lieb lattices, the destructive interference of the tunneling induces frustration of kinetic energy and results in a flat band. For bosonic systems, a fascinating question has been considered of whether condensation is stable in a flat band (see Fig.4.1.1). It is theoretically investigated in a kagome lattice

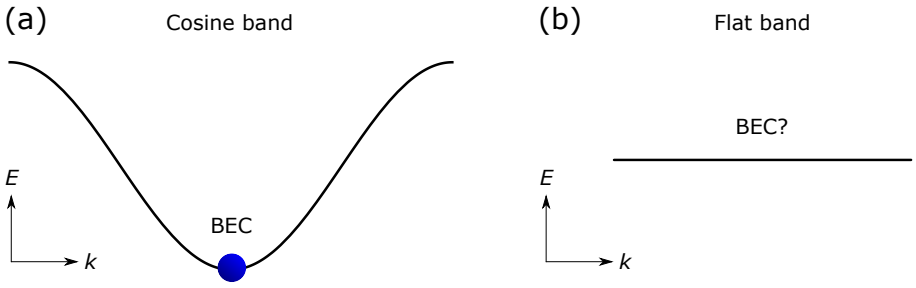

Figure 4.1.1: (a) A BEC in a typical consine band. A BEC populates at the lowest energy point of the consine band. (b) In a case of a flat band, it is not obvious where a BEC populates or whether the condensation is possible.

that an interaction makes the energy at the K point, which corresponds to the corner of the hexagonal first Brillouin zone, lowest in a flat band [87]. Yet, experimental study is hampered by the fact that the flat band in the kagome lattice exists in an excited state.

Even in a Lieb lattice, a flat band exists in the first excited band; hence, a BEC loaded adiabatically into an optical Lieb lattice is not populated in the flat band. However, our highly-tunable Lieb lattice enables us to coherently transfer the population in the lowest band into the flat band by engineering a phase between sublattices. This scheme is understood by considering tight-binding wave functions in each band (See Eq.2.1.7).

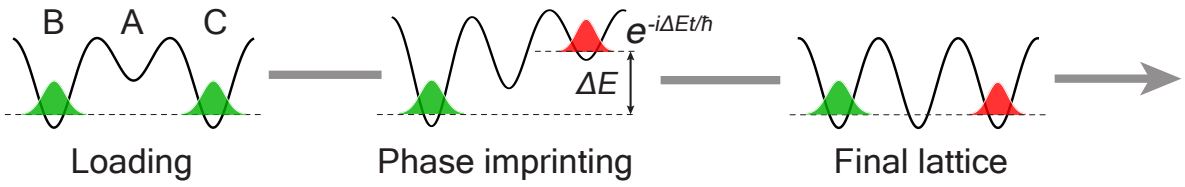

Figure 4.1.2: Sequence to coherently transfer a BEC to a flat band.

At zero quasimomentum and in the equal-offset condition $E_A = E_B = E_C$, a simple calculation gives

$$|1\text{st}\rangle \propto |A\rangle + (|B\rangle + |C\rangle)/\sqrt{2} \tag{4.1.1}$$
$$|2\text{nd}\rangle \propto |B\rangle - |C\rangle \tag{4.1.2}$$
$$|3\text{rd}\rangle \propto |A\rangle - (|B\rangle + |C\rangle)/\sqrt{2} \tag{4.1.3}$$

from the 1st to the 3rd band. We can smoothly modify these eigenstates owing to controllability in our lattice potential. With sufficiently large V_{diag}, which is equivalent to large $E_A - E_{B,C}$, the lowest Bloch state has essentially no amplitude in the A sublattice, and therefore $|B\rangle + |C\rangle$ state is realized. Next, we apply sudden change in one of the long lattice, say $V^{(z)}_{\text{long}}$. This creates energy difference between the B and C sublattices, and the relative phase of the condensate wave function starts to evolve with a period $2\pi\hbar/(E_C - E_B)$. On the basis of the initial band structure, this time evolution means a coherent oscillation between $|1\text{st}\rangle$ and $|2\text{nd}\rangle$ (See Fig.4.1.2).

The detailed procedure of loading and detecting a condensate in the flat band is as follows. We adiabatically load a pure BEC of 2×10^4 ^{174}Yb atoms into the Lieb lattice with $(s_{\text{long}}, s_{\text{short}}, s_{\text{diag}}) = (8, 8, 20)$ and apply sudden increase of $s^{(z)}_{\text{long}}$ to 26.4 for variable duration. At the same time, we ramp s_{short} up to 20 to prevent tunneling during the band transfer. After this sequence, we return the lattice depths to the initial values and perform adiabatic turning off of the lattice potential in order to map quasimomentum to free-particle; *band mapping* [88, 89].

Figure 4.1.3 shows the fraction of atoms in higher bands during phase imprinting in the absence of lattice confinement along the y axis. Inset shows the absorption images taken after 14 ms TOF, which reveal the inter-band dynamics of a condensate. At zero quasimomentum, atoms in the 2nd and 3rd band are mapped to the same point of the Brillouin zone. In addition, the finite spread of the condensate (quantum depletion) causes a mix of the population in the 2nd band with other neighboring zones. Therefore, instead of plotting the population in the 2nd Brillouin zone, we count atoms in the 1st Brillouin zone and show the fraction of atoms in other higher bands. We fit the data with the empirical function in the form

$$f(t) = a \exp(-t/\tau)\ F(t) + b\ (1 - \exp(-\mathrm{t}/\tau)), \tag{4.1.4}$$

where $F(t)$ is the numerical solution of the single-particle Schrödinger equation. In fitting the data, we adopt $s^{(z)}_{\text{long}}$ during the phase imprinting as a free parameter and obtain the

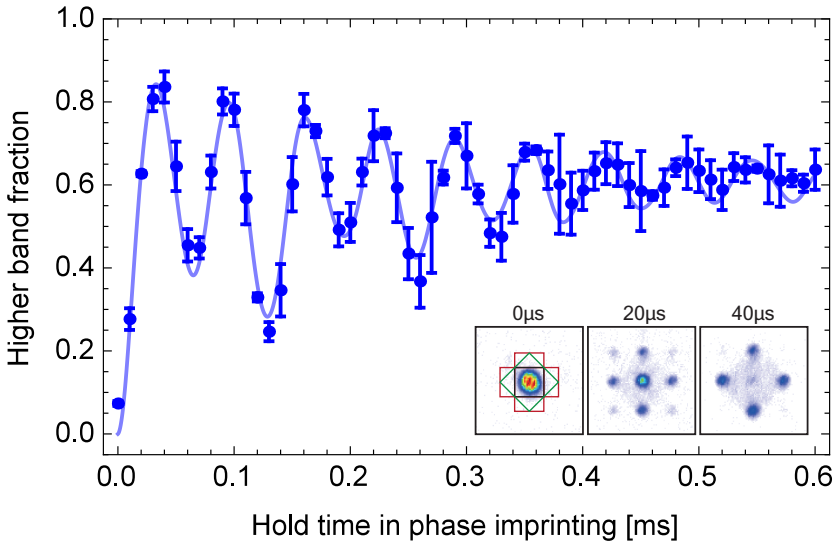

Figure 4.1.3: Inter-band oscillation during phase imprinting. Inset shows the absorption images after band mapping, along with the three Brillouin zones displayed by black, green, and red lines, respectively. Solid lines are the fit results using the single-particle solution of the Schrödinger equations. Error bars mean SD of three independent scans.

best fit with $s_{\mathrm{long}}^{(z)} = 25.5$, which is close to the expected value of 26.4. Although the inter-band oscillations involve non-negligible contributions from the bands higher than 2nd band, at the half period of the first cycle, we expect that more than 75 % of atoms are transferred to the 2nd band.

4.2 Relaxation dynamics from a flat band

We measure the lifetime of atoms in the 2nd band of the optical Lieb lattice. After transferring to the 2nd band by phase imprinting, we change the diagonal lattice depth s_{diag} to control the gap energy between the 1st band 2nd bands. As well as the band gap [75], the lifetime of a quantum gas in an excited band strongly depends on the wave-function overlap with the state in the lowest bands [90]. As we increase s_{diag}, the average gap between the 1st and 2nd bands becomes smaller and, their density profiles become more similar to each other. In the opposite limit of shallow s_{diag}, the band gap increases and the density overlap gets smaller, because the state of the lowest band mostly populates at the A sublattice. We take a variable hold time in the final lattice, followed by band mapping to count the atom number in the excited bands.

Figure 4.2.1(a) shows the decay curves, along with the typical absorption images. The lifetime of higher bands increases with large 1st-2nd band gap, as expected. In addition, increasing the gap clearly reveals that there are two processes of the decay dynamics: decay of the condensate within the 2nd band (left absorption image in (a)) and decay of atoms into the lowest band (right absorption image in (b)). We find that the curve is well fitted by a double exponential such as

$$f(t) = a_1 \exp(-t/\tau_{\mathrm{slow}}) + a_2 \exp(-t/\tau_{\mathrm{fast}}) + b. \tag{4.2.1}$$

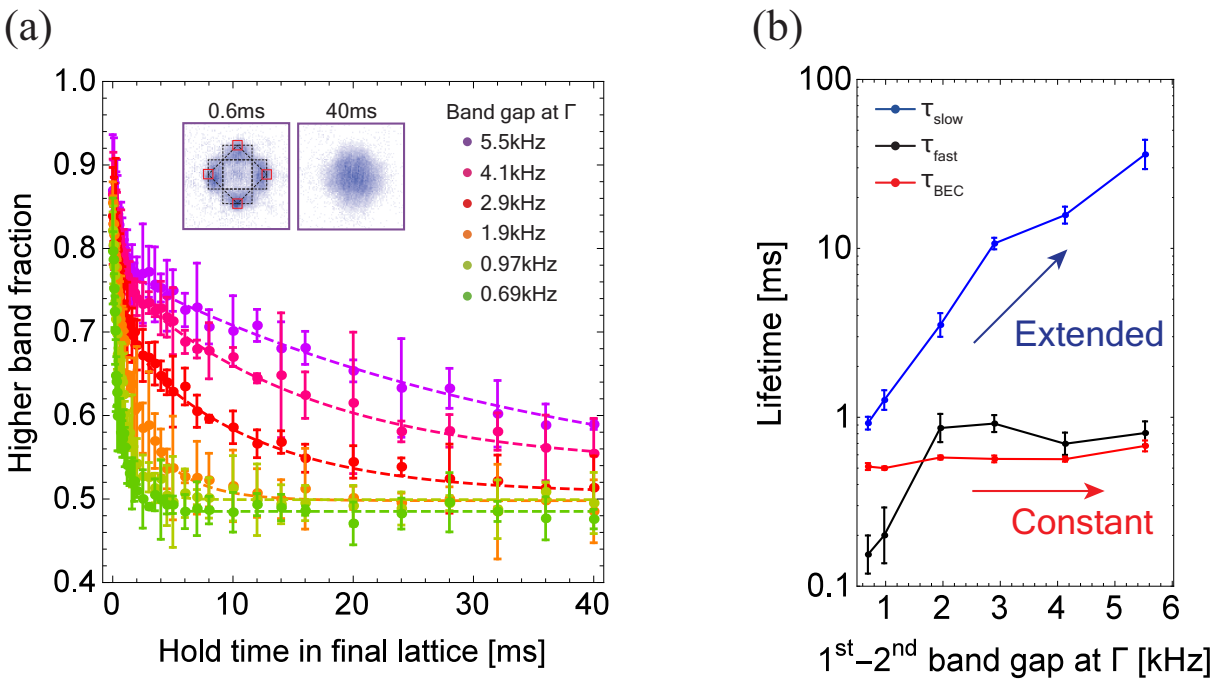

Figure 4.2.1: (a) Decay of the flat band for various 1st-2nd band gap at zero quasimomentum. Solid lines are the fit results with double-exponential curves. Error bars denote the SD of three independent scans. Inset shows the absorption images with two different hold times at the band gap of 5.5 kHz, taken after 14 ms TOF. The three Brillouin zones are indicated by the black dashed lines. The red square regions are used to evaluate the lifetime of a condensate (τ_{BEC}). (b) Measured lifetime of atoms in the flat band. $\tau_{\mathrm{slow,fast}}$ are the slow and fast decay time obtained from the data shown in (a), respectively. τ_{BEC} is the e^{-1} lifetime of a condensate. Error bar represent fitting error.

As in Fig.4.2.1(b), the fast decay component τ_{fast} shows only weak dependence on the band gap, whereas the slow decay component τ_{slow} shows more than 20-fold changes from the largest to the smallest band gap. We also extract the lifetime of the condensate in the 2nd band by counting atoms on the corner of the 2nd Brillouin zone (τ_{BEC}), and find similar behavior with τ_{fast}. This implies that the initial fast decay is related to the decay of the condensate.

4.3 Observation of a localized state in a flat band

The most intriguing property of a flat band is the localization of the wave function at certain sublattice sites. In the case of the Lieb lattice, the wave function of the flat band vanishes on the A sublattice. Here, we reveal this property by observing the tunneling dynamics of a Bose gas initially condensed at the $|B\rangle - |C\rangle$ state, and compare it to the dynamics of the state with opposite relative phase, $|B\rangle + |C\rangle$ (See Fig.4.3.1). To observe real-space dynamics of the system, we perform projection measurement of the occupation number in each sublattice, which we call *sublattice mapping*. In this method, we first suddenly change the lattice potential to $\left[\left(s^{(x)}_{\mathrm{long}}, s^{(z)}_{\mathrm{long}}\right), s_{\mathrm{short}}, s_{\mathrm{diag}}\right] = [(8, 14), 20, 0]$. In

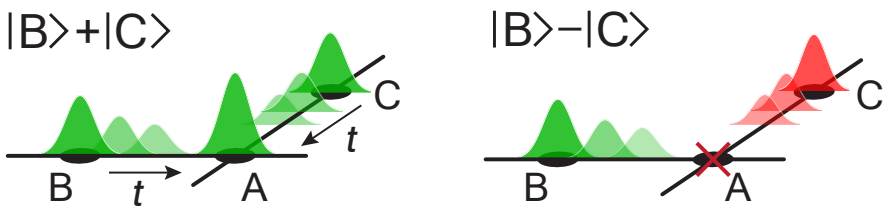

Figure 4.3.1: Difference between $|B\rangle + |C\rangle$ and $|B\rangle - |C\rangle$ states in a Lieb lattice. In $|B\rangle + |C\rangle$ state, tunneling to A sublattice is allowed, whereas the tunneling is prohibited due to destructive interference of wave function at A sublattice, which leads to the localization of the wave function at B, C sublattice and gives rise to the flat band.

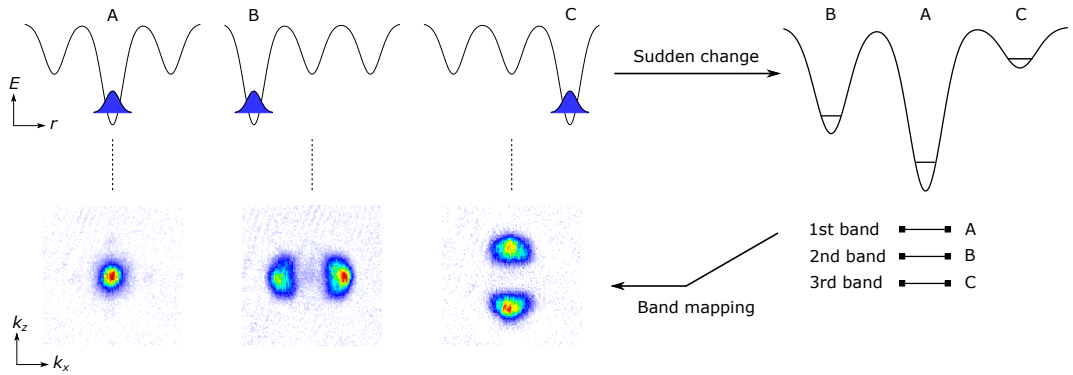

Figure 4.3.2: Demonstrating the measurement of sublattice occupancy. Sublattice mapping technique is applied to atoms loaded into (left) $\left[\left(s^{(x)}_{\text{long}}, s^{(z)}_{\text{long}}\right), s_{\text{short}}, s_{\text{diag}}\right] = [(8,8),8,0]$, (middle) $[(2,8),8,19]$, and (right) $[(8,2),8,19]$, corresponding to atoms in A, B, and C sites, respectively.

this configuration, all three sublattices are energetically well separated from each other and the lowest three bands consist of the A, B and C sublattice, respectively. This maps sublattice occupations to band occupations, which can then be measured by band mapping technique. Figure 4.3.2 shows the demonstration of this method, in cases where atoms occupy only one of the sublattices. Note that the population in the B and C sublattices are mapped to the 2nd Brillouin zones for the 1D lattice along the x and z axis, respectively. This is because the turning off the diagonal lattice decouples these two directions and the fundamental bands are labeled by the combination of band indices of 1D lattices.

We prepare the initial state $|B\rangle + |C\rangle$ by simply loading a BEC into the Lieb lattice with deep diagonal lattice. $|B\rangle - |C\rangle$ state is prepared by phase imprinting method. After manipulating the lattice depths to the equal-offset condition $E_A = E_B = E_C$, dynamics of these initial states is measured by the sublattice mapping technique. Figure 4.3.3 show the measured tunneling dynamics. This measurement reveals qualitatively different behaviors of these two states: the $|B\rangle - |C\rangle$ state shows a significant suppression of the A-sublattice

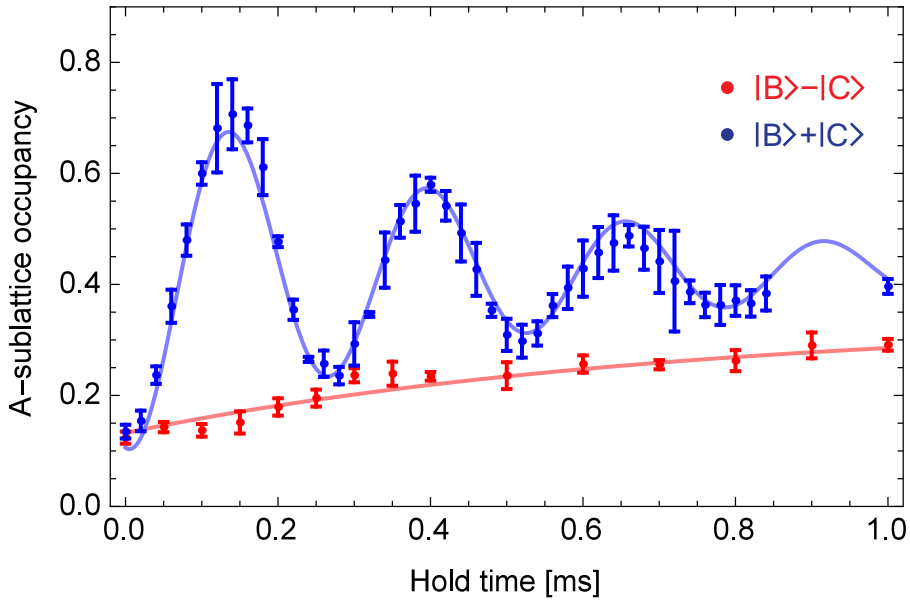

Figure 4.3.3: Measured tunneling dynamics of $|B\rangle+|C\rangle$ and $|B\rangle-|C\rangle$ initial states in the Lieb lattice of $(s_{\mathrm{long}}, s_{\mathrm{short}}, s_{\mathrm{diag}}) = (8, 8, 9.5)$. Solid lines are the fits to the experimental data with damped sinusoidal oscillation for $|B\rangle+|C\rangle$ and double exponentials for $|B\rangle-|C\rangle$. Error bars denote SD of three independent scans.

occupancy, indicating the freezing of the tunneling dynamics to the A sublattice. Note that a slowly increasing population to the A sublattice is cause by the decay of the atoms to the lowest band. $|B\rangle + |C\rangle$ state exhibits coherent oscillations between the A and BC sublattices. This is because the state $|B\rangle + |C\rangle$ is superposition of 1st and 3rd band such as $|1\mathrm{st}\rangle - |3\mathrm{rd}\rangle$ in the Bloch basis. This time evolution is driven by the 1st-3rd band gap ΔE_{1-3}, which equals $4\sqrt{2}J$ in the tight-binding model. after a half-period $\pi\hbar/\Delta E_{1-3}$, the state evolves to $|A\rangle \propto |1\mathrm{st}\rangle + |3\mathrm{rd}\rangle$, leading to coherent tunneling to the A sublattice. Similarly, it is possible to arrange the initial lattice depths so that the lowest Bloch state has the maximum overlap with a certain superposition of $|1\mathrm{st}\rangle$ and $|2\mathrm{nd}\rangle$, where coherent oscillation between the B and C sublattice is driven. We use this technique to systematically measure the band structure of the optical Lieb lattice in the latter section 5.2.

4.4 Conclusion and outlook

Here, we have successfully realized the Lieb lattice for ultracold ytterbium gases and observed the characteristic dynamics of a condensate, including the freeze of the motion in the flat band. Relatively short lifetime of atoms in the flat band was observed, although it can be made longer by increasing the band gap to the lowest band.

Chapter 5

Interaction-Driven Shift and Distortion of a Flat Band in an Optical Lieb Lattice

In ultracold atom experiments, a band structure of an optical lattice can be measured in momentum-resolved manner by Bragg spectroscopy [91] and a combination of Bloch oscillation and Stückelberg interferometry [92]. The former method requires a continuous change of the angle between the driving laser beams. In the latter method, only the gap between the 1st band and 2nd band can be measured. In this chapter, we report on the momentum-resolved measurement of the lowest three Bloch bands for an interacting array of BEC trapped in an optical Lieb lattice as in Fig.5.0.1. To investigate the dispersion relation, a BEC in the lattice transported to various quasimomenta by applying a constant force [93]. The dispersion of the lowest band is acquired by integrating group velocity measured from matter-wave interference patterns. For the higher bands, we measure the gap from the lowest band. High controllability of the optical lattice enables us to prepare the precise superposition of band eigenstates [61]. Once such a state is introduced into the Lieb lattice, the sublattice population starts oscillation, whose frequency corresponds to the band gap. Our experiment investigates the important role of the interaction in significantly modifying the Bloch band, including a flat band in the Lieb lattice.

5.1 Group-velocity measurement

We begin with describing our experimental method. to move the atoms in the reciprocal space, we utilize two kinds of external forces. One is a gravitational force acting in $\Gamma(q_x = 0, q_z = 0)$ to $\mathrm{X}(q_x = k_{\mathrm{BZ}}, q_z = 0)$ direction, which can be applied by turning off the FORT potential as in Fig.5.1.1(a). The other is a dipole force due to the potential gradient of a Gaussian beam as in Fig.5.1.1(b) with the beam waist of about 50 μm and about 1 GHz red detuning from the resonance of the $^1S_0$ - $^3P_1$ transition ($\lambda = 556$ nm) acting in Γ to $\mathrm{M}(q_x = k_{\mathrm{BZ}}, q_z = k_{\mathrm{BZ}})$ direction.

In the presence of a constant external force $\boldsymbol{F}$, which is weak enough not to induce interband transitions, a given band eigenstate $|\boldsymbol{q}(0), n\rangle$ evolves to $|\boldsymbol{q}(t), n\rangle$ according to $\boldsymbol{q}(t) = \boldsymbol{q}(0) + \boldsymbol{F}t/\hbar$ after a time t [93]. The group velocity in $|\boldsymbol{q}(t), n\rangle$ is related to the

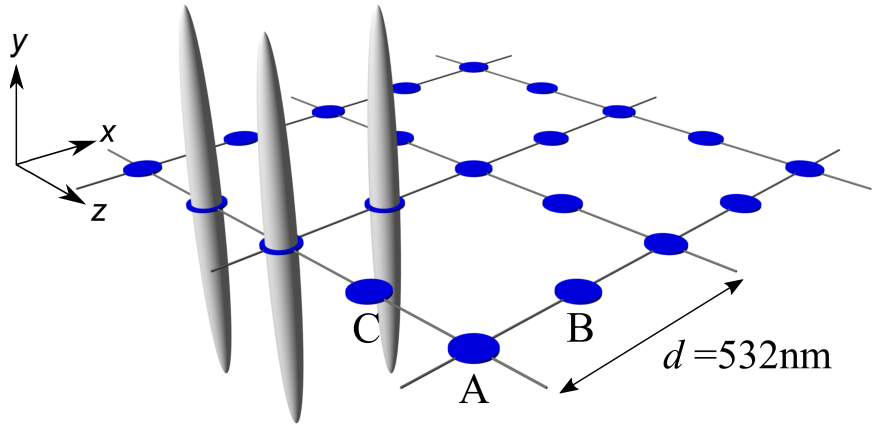

Figure 5.0.1: Schematic of the Lieb lattice. In our system. the atoms are weakly trapped along the y direction, and distribute like tubes as shown in gray in the figure. The lattice constant is $d = 532$ nm.

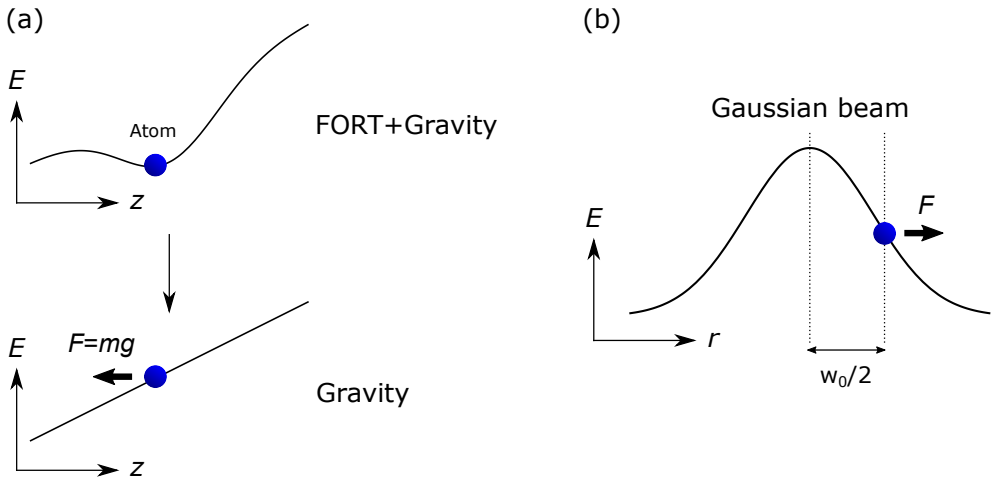

Figure 5.1.1: Schematic of external forces used in the experiment. (a) Gravitational force is applied by turning off the horizontal and vertical FORT potential. Trapping potential of optical lattices along z direction is negligibly weak with lattice depths used in the experiment. (b) Atoms are located at the shoulder of a Gaussian beam ($r = w_0/2$), where the atoms feel the steepest potential gradient.

band eigenenergy $E_n(\boldsymbol{q}(t))$ as [94]

$$\langle \boldsymbol{v} \rangle_n (\boldsymbol{q}(t)) = \frac{1}{\hbar} \frac{\mathrm{d}E_n (\boldsymbol{q}(t))}{\mathrm{d}\boldsymbol{q}}. \tag{5.1.1}$$

Note that the anomalous velocity term generally appears in the mean velocity formula under the constant force (See the appendix B), but such term is exactly zero in the Lieb

lattice since it is a topologically trivial system and the berry curvature is zero for the entire Brillouin zone (See the appendix C).

In the following, we reconstruct the dispersion of the lowest band by integrating the group velocities detected via time-of-filight (TOF) measurements [95, 2]. From a TOF image, we can observe the velocity distribution of atomic cloud $n(v_x, v_z)$, which is once integrated in the direction perpendicular to the Lieb lattice plane. Using the velocity distribution, the group velocity is given as $\langle \boldsymbol{v} \rangle = \int \mathrm{d}v_x \mathrm{d}v_z \ \boldsymbol{v} n(v_x, v_z)$. When extracting the group velocity from TOF images, we reduce the influence of the background noise in the region where the atoms are not populated by restricting the region of integration into the squares as in Fig.5.1.2(a), (b), whose centers correspond to $\hbar(q_x(t), q_z(t)), \hbar(q_x(t) \pm 2k_\mathrm{L}, q_z(t) \pm 2k_\mathrm{L}), \hbar(q_x(t), q_z(t) \pm 4k_\mathrm{L}), \hbar(q_x(t) \pm 4k_\mathrm{L}, q_z(t))$ and the width is $\simeq \hbar k_\mathrm{L}/3$. Measured group velocity at each quasimomentum is integrated in a trapezoidal approximation:

$$\begin{aligned} E(\boldsymbol{q})/\hbar &= \int_{\boldsymbol{0}}^{\boldsymbol{q}} \mathrm{d}\boldsymbol{q}' \cdot \langle \boldsymbol{v} \rangle (\boldsymbol{q}') \\ &\sim \sum_{i=0}^{q'(i)=q} \mathrm{d}q' \frac{\langle v \rangle (i+1) + \langle v \rangle (i)}{2}. \end{aligned} \tag{5.1.2}$$

When a BEC in the lowest band experiences a weak external force, the whole condensate occupies a single band at a single wave number. We compare the experimental data with Gross-Ptaievskii equation (GPE) in a tight-binding approximation, whose detail is explained in the section 2.5.

Figure 5.1.2(c) shows the dispersion of the lowest band for the lattice depth of $(s_\mathrm{long}, s_\mathrm{short}, s_\mathrm{diag}) = (13, 13, 15.5)$. At this lattice depth, the atoms are in a superfluid state and not in a Mott-insulating state. In our system, an atom density has spatial dependence due to a weak harmonic confinement by laser beams. The trap frequencies of FORT and optical lattice are $(\omega_x, \omega_y, \omega_z)/2\pi = (129, 46.2, 151)$ Hz. Assuming a local density approximation, we can calculate the density distribution of atoms $n(\mu, r)$ in the optical lattice by determining chemical potential μ from the total atom number, which is $N = 2.1(1) \times 10^4$ (See the section 2.5.3). At the trap center, the mean-field interaction amounts to $nU_A/J = 8.06$, where U_A is the interaction strength on the A-sublattice. In Fig. 5.1.2(c), band calculations for the maximum density and half of it are plotted in addition to a single-particle theory. Note that the 1st band energy at Γ (E^Γ_1st) of each interaction strength is subtracted to adjust the energy offset. The experimental data are in excellent agreement with the theoretical analysis. While the band dispersion along the Γ-M is robust against interaction, the band energy is slightly shifted up around the X point compared with the non-interacting case. This can be accounted by the concentration of the wave function on the A- and B-sites at this point.

5.2 Band-gap measurement

Next, we describe the band gap measurement. Initially, a BEC is prepared as a superposition of eigenstates for the optical Lieb lattice of $(s_\mathrm{long}, s_\mathrm{short}, s_\mathrm{diag}) = (13, 13, 15.5)$. The overlap fraction is a parameter when measuring the band gap. Figure 5.2.1 shows the measured band gaps as a function of the overlap between the prepared initial state

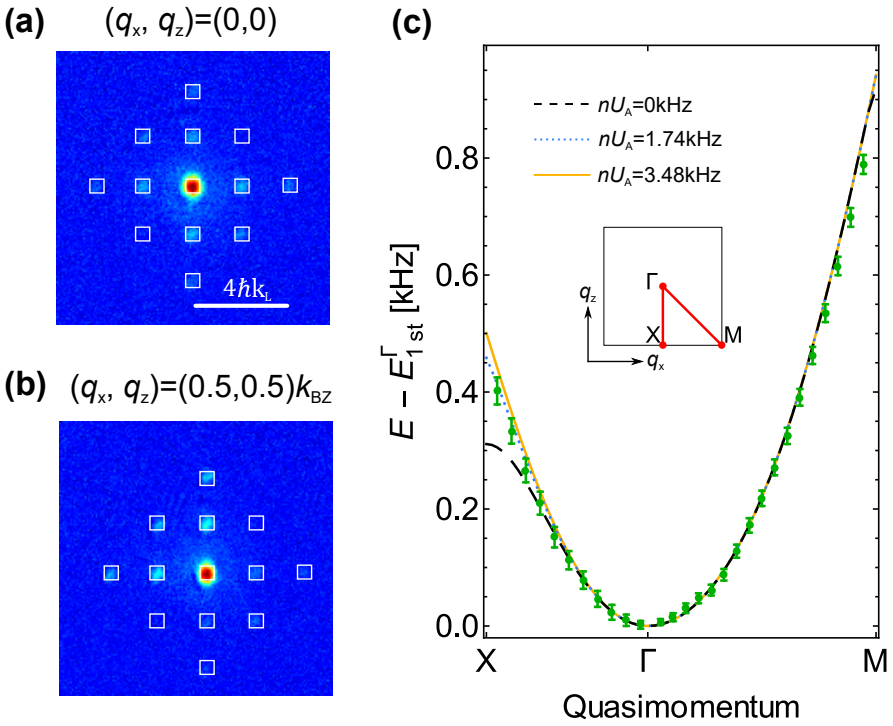

Figure 5.1.2: (a), (b) Absorption images at quasimomentum $(q_x, q_z) = (0, 0)$ and $(0.5, 0.5)k_{\mathrm{BZ}}$ respectively, where k_{BZ} corresponds to the quasimomentum at the BZ edge. The images are taken after a TOF of 14ms. We restrict the integration region within the white squares in which the atoms are mostly detected. (c) Dispersion of the 1st band of optical Lieb lattice $(s_{\mathrm{long}}, s_{\mathrm{short}}, s_{\mathrm{diag}}) = (13, 13, 15.5)$. The experimental data are denoted as green circles. The inset shows the first BZ. Dashed black line is single-particle theory. Dotted blue line is the calculation for half of the maximum number density. Solid yellow line is for the maximum number density. The vertical axis shows the energy difference from the 1st band energy at Γ for each interaction strength. Error bar means the standard deviation of three independent scans.

and higher band, determined by numerical calculation based on a single-particle theory, for the Lieb lattice of $(s^{\mathrm{long}}, s^{\mathrm{short}}, s^{\mathrm{diag}}) = (13, 13, 15.5)$. It turns out that the band gaps strongly depend on the overlap fraction if it exceeds 10 %, which is beyond our assumption of our analysis. The overlap between the initial state and the eigenstates of higher bands is set to 10 %, which is small enough for the measured band gap not to depend on the higher band fraction. The initial lattice depths are $((s^x_{\mathrm{long}}, s^z_{\mathrm{long}}), s_{\mathrm{short}}, s_{\mathrm{diag}}) = ((12.31, 14.01), 6.84, 15.24)$ for the 1st-2nd band gap (E_{2-1}) measurement and $(s_{\mathrm{long}} = s^x_{\mathrm{long}} = s^z_{\mathrm{long}}, s_{\mathrm{short}}, s_{\mathrm{diag}}) = (12.49, 13.08, 17.82)$ for the 1st-3rd band gap (E_{3-1}) measurement. After changing the lattice configuration into the Lieb lattice suddenly, we move the BEC in the reciprocal space by applying a constant force. During the subsequent holding time, the relative phase between band eigenstates evolves at the frequency of the band gap, resulting in oscillations of the sublattice populations. To observe the real-space dynamics, we perform projection measurement of the occupation number in each sublattice, which we call sublattice mapping. In this method, we change the lattice potential to $(s_{\mathrm{long}}, s_{\mathrm{short}}, s_{\mathrm{diag}}) = (8, 20, 0)$, where the lowest three bands consist

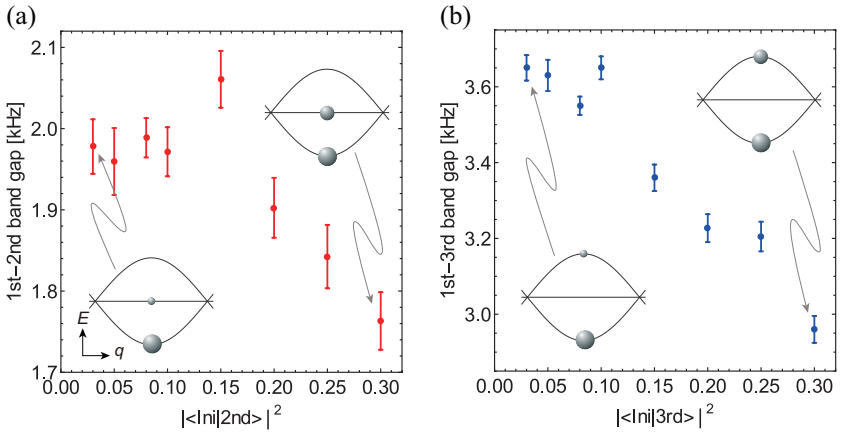

Figure 5.2.1: Overlap-fraction dependence of band gap at Γ point. Figure (a) and (b) show the 1st-2nd and 1st-3rd band gaps, respectively. Error bar means the standard deviation of three independent scans.

of the A-, B-, and C-sublattice, respectively. This maps out sublattice occupations to band occupations, which can be measured by band mapping technique (See Fig.4.3.2).

When the superposition of the 1st and 3rd bands is prepared as an initial state, all of the sublattice population oscillate because the wave functions of 1st and 3rd bands spread over all the sublattices. On the other band, since the eigenstate of the 2nd band has no amplitude on A-sublattice, only B- and C-sublattice populations oscillate in the case of the superposition of the 1st and 2nd bands as an initial state. Therefore, we extract the band gap E_{3-1} from the frequency of A-sublattice oscillation (Fig.5.2.2(a)) and E_{2-1} from the mean of frequencies of B- and C-sublattice oscillations (Fig. 5.2.2(b)). Note that the populations at B- and C-sublattices in Fig.5.2.2(a) evolve in the same way, because both of $|\Gamma, B\rangle$ and $|\Gamma, C\rangle$ always have the same coefficient in the superposed state. We fit the oscillation of sublattice population with our empirical model function

$$F(t) = a\, e^{-t/\tau} \sin(2\pi f t + b) + c \tag{5.2.1}$$

where a, b, c, f, τ are fitting parameters.

In Fig.5.2.2(c) we show the experimentally determined band energies (solid circles) in the optical Lieb lattice. The higher band energies are obtained from the combination of the energy gaps and the energy of the lowest band described above. The dashed lines are the results of the calculations based on a single particle theory. It is clear that the experimentally determined energies are significantly deviated, in particular, up-shifted and distorted, from the calculated bands, which should be ascribed as the interaction-driven effect. Note that a direct tunneling between B- and C-sublattices which exists in our Lieb lattice system distorts the flat band even in the single-particle limit. Theoretically, a Bloch state with a small fraction of higher bands is regarded as the state after the weak excitation from the lowest band. Therefore, we use the Bogoliubov-de Gennes equation (BdGE) to estimate the interaction effect on the energy gap (See the section 2.5.2). The dotted and solid curves show the results of the calculations with two different interaction strengths, respectively. Our calculation shows, in particular, that the band gaps or excitation energies around the center of BZ becomes larger as the interaction

increases. On the contrary, the gap to the 2nd band becomes closed around the BZ edge of X point, as the interaction increases. We interpret this behavior as follows. At X point, $\cos(\theta_{\mathrm{X}}) = 0$ and $\sin(\theta_{\mathrm{X}}) = 1$, and thus the Bloch wave function of the 1st band has no spatial overlap with that of the 2nd band. Therefore, the excited atoms do not interact with the atoms in the lowest band, resulting in the smaller band gap as the interaction energy increases in the lowest band. On the other hand, because the 3rd band has large spatial overlap with the 1st band, the energy necessary to excite a particle to the 3rd band gets larger as the interaction increases. Note that along the Γ-M direction, $\cos(\theta_q) = \sin(\theta_q) = 1/\sqrt{2}$, and thus the 2nd band remains flat because the sublattice distribution does not change. The experimental data certainly indicate this tendency. Note that due to decoherence caused possibly by the interaction, the oscillations of sublattice populations are damped, which makes it difficult to measure the frequency around the exact BZ edge.

5.2.1 Dependence on the mean-field interaction strength

Finally, we experimentally investigate dependence of the band gap on the interaction. The gap energies are measured with various atom numbers. Here, we focus on E_{2-1} along the Γ-X direction (see Fig.5.2.3(a)). For a uniform, weakly interacting BEC, the chemical potential has linear dependence on the atomic density, leading to $N^{2/5}$ dependence of the central density. Therefore, we plot the observed oscillation frequency as a function of $N^{2/5}$ in Fig.5.2.3(b), (c), and (d). The data are in good agreement with the calculations for the atom density with half of the maximum value. By extrapolating the experimental data to a small atom number limit, it is also confirmed that the band gap at each quasimomentum approaches the prediction of a single-particle theory.

5.3 Conclusion and outlook

Here, we have studied an interaction effect on the Bloch bands for superfluids in an optical Lieb lattice. We observed that the 2nd band, which is a flat band in a single-particle description, is significantly shifted and distorted along the Γ-X direction by the interaction. Further applications of our method include the study of an artificial gauge field, which induces the modification of an energy spectrum and a topologically nontrivial phase for fermions in a Lieb lattice [96]. In addition, our technique demonstrated for an optical Lieb lattice should be used to create and observe an interesting interaction-driven effect such as a swallow tail [97], in which the strong interaction compared with a band gap induces the loop structure in the energy band.

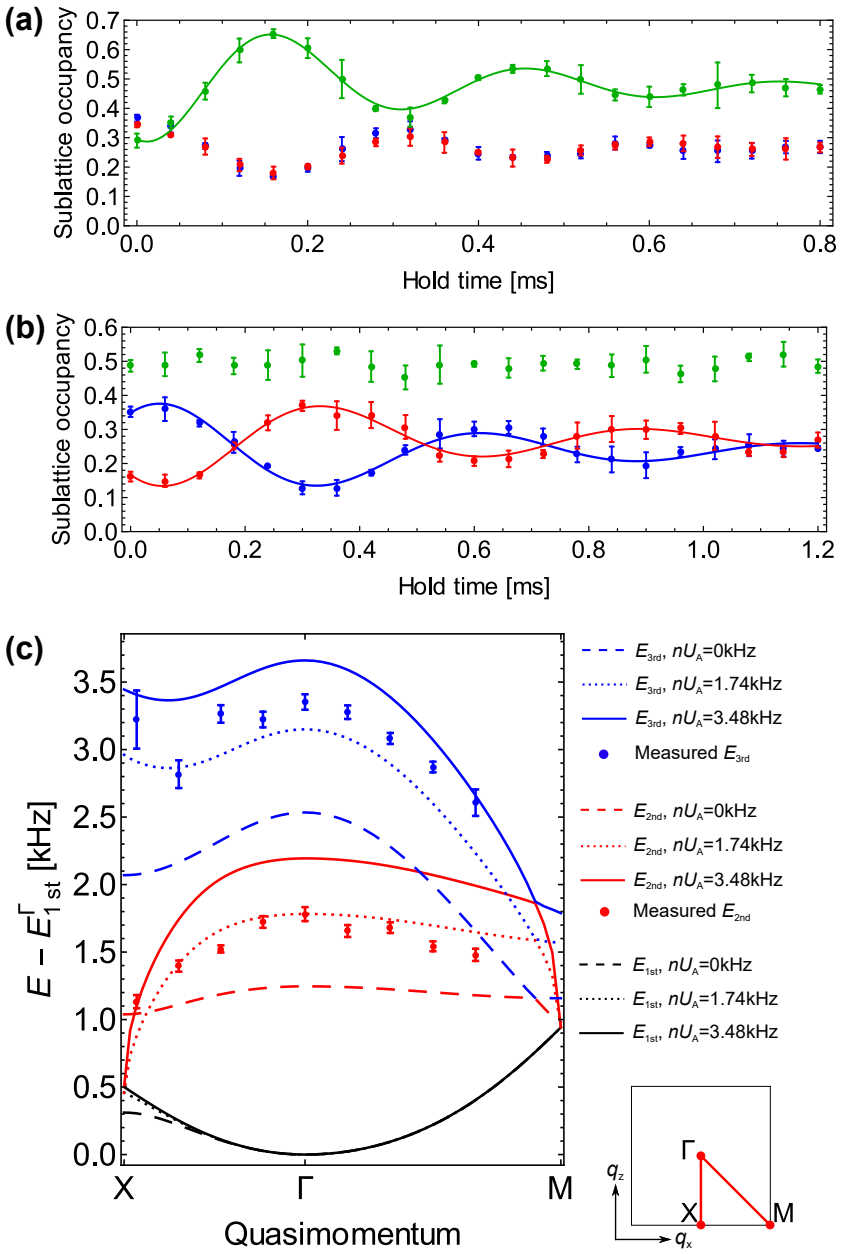

Figure 5.2.2: (a), (b) Oscillation of sublattice population at Γ point according to (a)E_{3-1} and (b) E_{2-1}, respectively. First, we load a BEC into an optical lattice the configuration of which is different from that of a Lieb lattice. In this way we create a superposition of (a) the 1st and 3rd or (b) the 1st and 2nd band eigenstates of the Lieb lattice. Next, we suddenly change the lattice configuration into the Lieb lattice, and take various hold time. We observe the temporal change of the sublattice populations obtained by the projection measurement described in the text. Each sublattice occupancy is normalized by the summation over all of the sublattice occupancy. Green, blue and red circles are A-, B-, and C-sublattice population, respectively. Error bar shows the standard deviation of three independent scans. Solid lines are fits to the data with damped sine functions(5.2.1). (c) The lowest three bands in the optical Lieb lattice of $(s_{\rm long}, s_{\rm short}, s_{\rm diag}) = (13, 13, 15.5)$. Red and blue circles are the reconstructed 2nd and 3rd band energies, respectively. Error bars mean the fitting errors. Dashed lines are the predictions based on a single-particle theory. Dotted and solid lines are the calculations including the interaction based on the BdGE with the half and maximum densities, respectively.

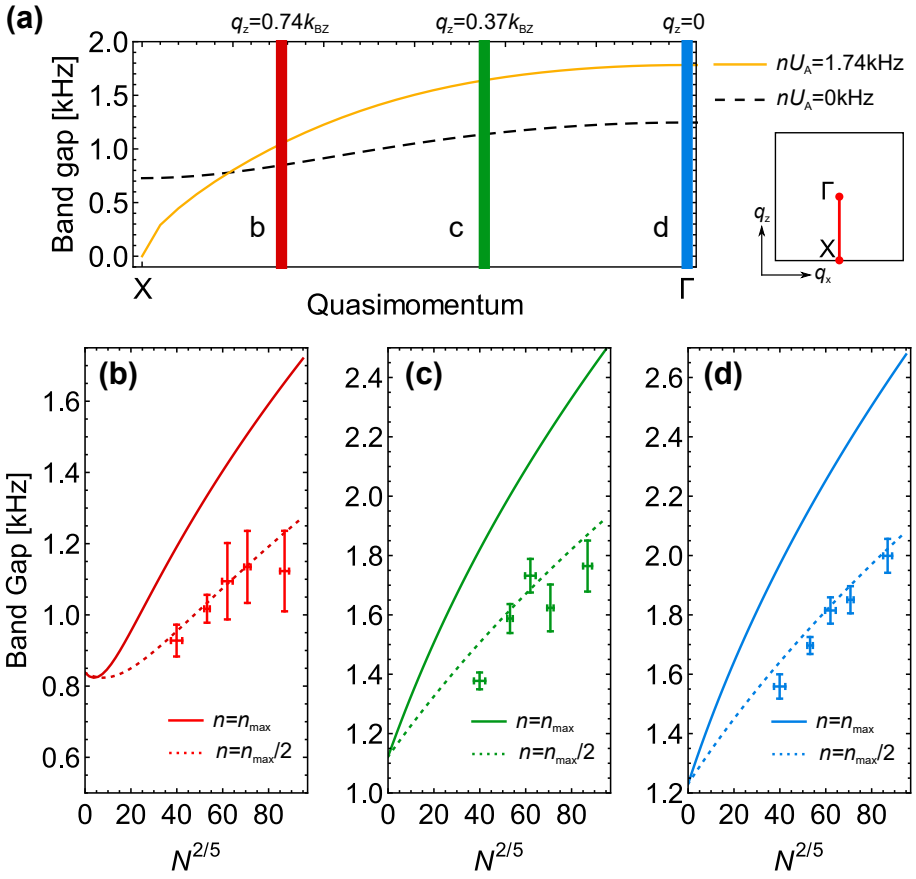

Figure 5.2.3: (a) Band gaps from the lowest band to the 2nd band. Dashed black line is the prediction on the single particle theory of the Lieb lattice potential $(s_{\mathrm{long}}, s_{\mathrm{short}}, s_{\mathrm{diag}}) = (13, 13, 15.5)$. Solid yellow line is the calculation including the interaction based on the BdGE. Thick red, green and blue lines respectively show the quasimomenta $q_z = 0.74k_{\mathrm{BZ}}, 0.37k_{\mathrm{BZ}}$, and 0 at which we have investigated the density dependence of the band gaps. (b), (c), (d) Band gap versus the atom number for $q_z = 0.74k_{\mathrm{BZ}}, 0.37k_{\mathrm{BZ}}, 0$, respectively. Solid and dotted lines show the calculations including the interaction based on the BdGE for the maximum and half densities, respectively. Error bars indicate the fitting errors.

Chapter 6

Spatial Adiabatic Passage of Massive Quantum Particles

6.1 Introduction

6.1.1 Three-level system with Λ-type transition

A three-level system is a minimal example in which quantum interference takes place. This system is considered mainly in a context of laser coupled atomic levels, and the Hamiltonian for a Λ-type system in a rotating frame is written in the form

$$H = \begin{pmatrix} 0 & \Omega_1 & \Omega_2 \\ \Omega_1 & \delta_1 & 0 \\ \Omega_2 & 0 & \delta_2 \end{pmatrix}, \tag{6.1.1}$$

where $\Omega_1(\Omega_2)$ denotes a laser-induced Rabi frequency which couples basis states $|1\rangle$ with $|2\rangle$ ($|2\rangle$ with $|3\rangle$), and $\delta_1(\delta_2)$ is the detuning of the corresponding laser 1 (2). A dark state $\cos\theta\,|1\rangle - \cos\theta\,|3\rangle$ ($\tan\theta = \Omega_1/\Omega_2$) arises as one of the eigenstate of the Hamiltonian in Eq.6.1.1 when the Raman-resonant condition $\delta_1 = \delta_2$ is satisfied. By manipulating two laser pulses in *counter-intuitive* order so that θ changes from 0 to $\pi/2$, the dark states smoothly evolve from $|B\rangle$ to $|C\rangle$. This process is well known as STImulated Raman Adiabatic Passage (STIRAP), and has been an important technique for robust population transfer between atomic and molecular states.

Electromagnetically Induced Transparency (EIT) [98] is also an important process in a three-level system. In an EIT experiment, strong optical coupling between $|2\rangle$ and $|3\rangle$ causes the splitting of the $|1\rangle \to |2\rangle$ transition by the Rabi frequency, known as Autler-Townes doublet [99]. As a result, the state B becomes transparent for laser light driving the $|1\rangle \to |2\rangle$ transition at a frequency region between the doublet.

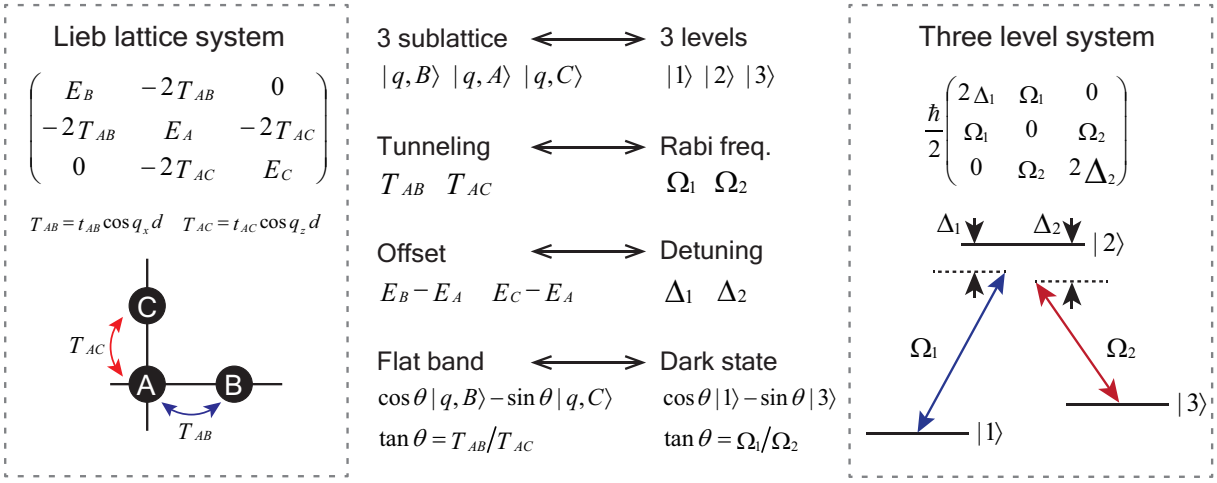

Figure 6.1.1: Correspondence between a Lieb lattice and three-level systems.

6.1.2 Correspondence between a three-level system and Lieb lattice

A Lieb lattice system has a mathematical analogy to the three level system with Λ-type transition. Figure 6.1.1 summaries the relations between two systems. Momentum-dependent couplings play a role of Rabi couplings in a three-level system, and detunings can be mimicked by energy offsets E_A, E_B and E_C of each sublattice. In our optical Lieb lattice system, these parameters can be separately controlled by changing the lattice depth along each direction, which enables us to realize a coherent scheme to transport atoms among these sublattices. In particular, by adiabatically changing the tunneling amplitudes in an counter-intuitive order, we can coherently transfer atoms from one sublattice to another without populating the intermediate sublattice, which can be regarded as a spatial analogue of STIRAP. This concept, named Spatial Adiabatic Passage (SAP), was introduced in the context of quantum dots [100, 101] and cold atoms [102], it has continuously attracted theoretical interests and various possibilities of its application have been discussed [103]. High controllability and flexibility of cold atoms system in optical lattices enables the experimental demonstration of SAP and the above applications.

6.2 Spatial adiabatic passage (SAP)

In our experiment, we use fermionic ^{171}Yb with a small scattering length of -0.14 nm to avoid interaction effects. The use of fermions causes a complexity arising from the finite momentum spread due to the Pauli principle. Adiabaticity of a process associated with a certain momentum is governed by the band gaps among the corresponding eigenstates. In the case of a Lieb lattice, adiabaticity can not be maintained on the corner of the Brillouin zone where a Dirac cone exists. To solve this problem, we slightly distort the band structure by shifting the phase of the diagonal lattice from an isotropic condition $\psi = \pi/2$. The effectiveness of this scheme can be understood from the potential landscape shown in Fig.6.2.1(b). The deformation reduces the inter-unit-cell tunneling, and therefore

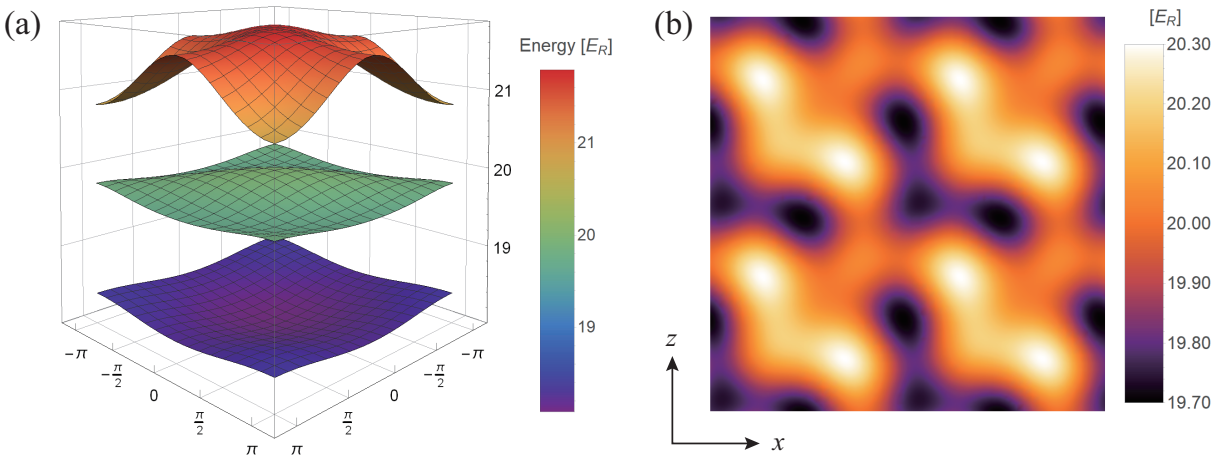

Figure 6.2.1: (a) Energy band and (b) potential landscape with distortion. If we shift the phase of the deep diagonal lattice, band gaps become large and the Dirac cone disappears. Show is the case of $\psi = (1/2 + 0.11)\pi$ and $[s_{\rm long}, s_{\rm short}, s_{\rm diag}] = [8, 8, 14]$.

each cell becomes more like an isolated triple well. As a result the momentum dependence of the energy dispersion is decreased, and the Dirac cone disappears. Mathematically, this modifies the coupling term as

$$\begin{aligned} \mathcal{T}_{AC} &\rightarrow e^{iq_z d/2}\left(J_{AC} + \delta J\right) + e^{-iq_z d/2}\left(J_{AC} - \delta J\right), \\ \mathcal{T}_{AB} &\rightarrow e^{iq_x d/2}\left(J_{AB} + \delta J\right) + e^{-iq_x d/2}\left(J_{AB} - \delta J\right), \end{aligned} \tag{6.2.1}$$

where δJ denotes the imbalance between inter- and intra-unit-cell tunnelings. For $\delta J = 0$, $\mathcal{T}_{AC}$ along the Brillouin zone boundary ($q_z d = \pi$) vanishes throughout the process. Introduction of $\delta J \neq 0$ can also suppress the breakdown of transport along this line.

SAP in the Lieb lattice is to transport atoms from B sublattice to C sublattice by a counter-intuitive manipulation of tunneling amplitudes. Throughout this process, the intermediate sublattice, say A, is not populated because the state adiabatically follows a dark state $\cos\theta_{\boldsymbol{q}} \left|\boldsymbol{q}, B\right\rangle - \sin\theta_{\boldsymbol{q}} \left|\boldsymbol{q}, C\right\rangle$, with $\tan\theta_{\boldsymbol{q}} = \mathcal{T}_{AB}(\boldsymbol{q})/\mathcal{T}_{AC}(\boldsymbol{q})$. First we load a sample of 1.2×10^4 atoms of ^{171}Yb at a temperature $T/T_{\rm F} = 0.3$ into the optical lattice of $s = [(27.7, 0), (0, 16), 14]$. In the loading stage, the potential on a B sublattice is made much deeper than those of the others in order to ensure that the initial state is populated only at B. After that, we suddenly change the lattice depths to $[(38.9, 3.8), (8, 8), 14]$ in 10 μs. This is a starting point of SAP process, where the tunneling J_{AB} is much smaller than J_{AC}. To earn a high tunneling rate, entire lattice depths are set relatively shallow, which leads to an undesired direct tunneling J_{BC}. We suppress J_{BC} by increasing the diagonal lattice depth beyond the equal-offset condition, i.e. $E_A > E_B = E_C$. As long as $E_B = E_C$ is satisfied, the dark state persists and SAP can be accomplished. We adiabatically sweep the lattice depths toward another limiting configuration $[(3.8, 38.9), (8, 8), 14]$, passing through the intermediate configuration $[8, 8, 14]$ which corresponds to the potential shown in Fig.6.2.1(b). The time evolution during this process is measured by sublattice mapping technique. The obtained TOF images suffer from the blurring of the Brillouin zone boundaries due to unavoidable non-addiabaticity of the band mapping procedure

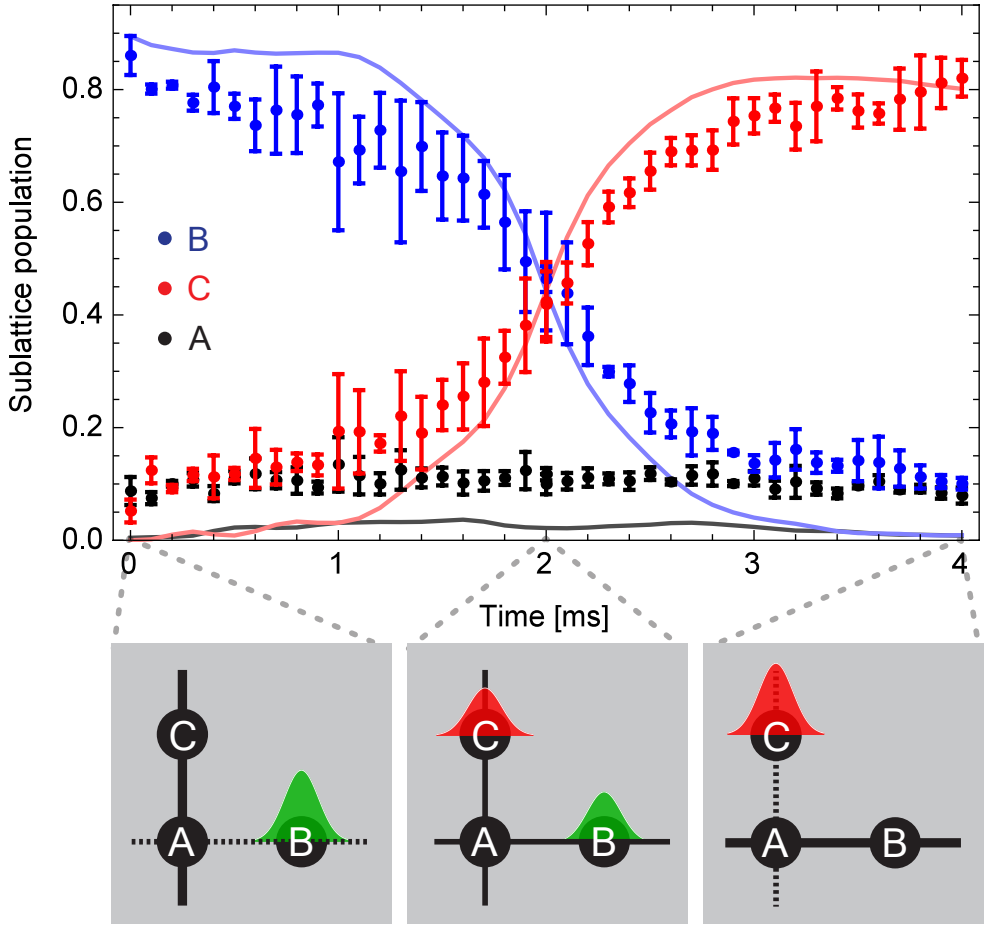

Figure 6.2.2: Time evolution of sublattice occupancies during a SAP process. Solid lines are the numerical calculation result with a single-particle Schrödinger equation.

and a harmonic confinement of the system. For a qualitative analysis of sublattice, populations, we take a set of basis images in which all atoms reside on a specific sublattice and determine sublattice occupancies by projecting images onto each basis.

Figure 6.2.2 shows the time evolution of sublattice occupancies N_A, N_B and N_C during the SAP process. Important features specific to SAP are well reproduced: initial population on the B sublattice is smoothly transfered into C sublattice, but the population on the A sublattice does not increase throughout the process. From the final population we evaluate the efficiency of the process to be $\left[N_C(T) - N_C(0)\right]/N_B(0) = 0.95(2)$, where T is the total sweep time. Furthermore, at the middle point of the SAP process, the fermionic atoms populate only in the flat band state. Usually, occupation of a certain energy band is accomplished by filling up all lower bands. The above SAP process provides an efficient way to prepare a non-equilibrium many-body state in which all fermions reside on the flat band of the Lieb lattice and the other bands are empty.

6.3 Autler-Townes doublet

To investigate a matter-wave analogue of EIT physics, we carry out a measurement similar to a pump-probe experiment. As before, we first prepare an initial state localized on B sublattice (See Fig.6.3.1(a)). Then, we introduce weak tunneling coupling J_{AB} and after a fixed time, a fraction of atoms that tunneled into A or C sublattice is measured. Figure 6.3.1(b),(c) show the characteristic tunneling spectra. In each spectrum, we scan the " detuning" via $s^{(x)}_{\mathrm{long}}$ which determines the energy difference $E_B - E_A (= E_B - E_C)$. For weak coupling J_{AC} in (b), we can observe a single dip corresponding to $B \to A$ tunneling, whereas a clear doublet structure appears for strong coupling $J_{AC} \gg J_{AB}$ in (c). The double peaks originate from tunnelings to $A + C$ and $A - C$ orbitals which are separated by the amplitude of tunneling coupling J_{AC}. The shift of the spectrum is caused by the change of the short lattice depth $s^{(z)}_{\mathrm{short}}$. While the short lattice creates the same potential curve for all sublattices, its effect on E_A, E_B and E_C slightly differs depending on the configuration of other lattices. The width of the observed resonance peaks is broadened by the band dispersion and spatial inhomogeneity due to the harmonic trap. In a typical EIT spectrum, a sharp dip can be observed even when the doublet splitting is smaller than the natural linewidth. This implies occurrence of coherent population trapping (CPT) [104] of a dark eigenstate. In the case of our system with no loss mechanism, CPT does not occur and hence a sharp EIT dip does not appear. Yet, the observed behavior exactly corresponds to a pump-probe detection of Autler-Townes doublet which is commonly observed in atom-filed systems.

6.4 Conclusion and outlook

In conclusion, we have succeeded in demonstrating coherent tunneling processes of cold fermionic atoms in an optical Lieb lattice. The three-sublattice structure of the Lieb lattice has remarkable analogy to Λ-type three level systems in quantum optics. By using this analogy and dynamical controllability of tunneling amplitudes, spatial adiabatic passage between two sublattice eigenstates was performed. We also observed an matter-wave analogue of Autler-Townes doublet in a tunneling process form a sublattice into a strongly coupled pair of sublattices. The demonstrated techniques are useful to prepare exotic many body states in optical lattices. In particular, at the half point of the SAP process in the Lieb lattice, all atoms are located on the flat band. This might be a general scheme applicable to other lattice with flat bands. Involving higher lattice orbitals is possible extension in connection with generation of angular momentum studied in Ref.[105]. In addition, recent advances in fine potential engineering [106] combined with single-site-resolved imaging of lattice gases [107] will greatly enlarge the application of SAP in cold atomic systems.

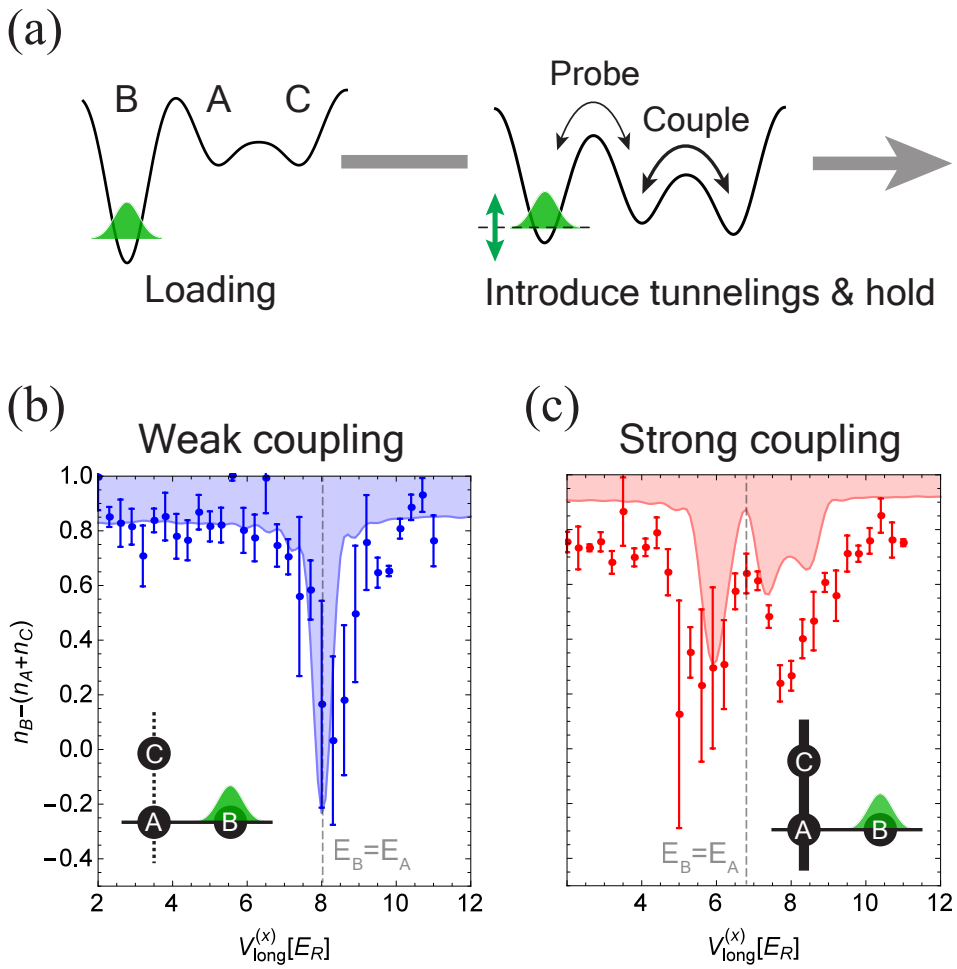

Figure 6.3.1: (a) Sequence of the experiment. (b), (c) Tunneling spectrum after a hold time of 1.8 ms, at the lattice depths of $\left[(40,40),(s^{x}_{\text{long}},8),9.5\right]$ in (b) and $\left[(40,7),(s^{(x)}_{\text{long}},8),9.5\right]$ in (c). Fraction of atoms which tunnel from the B sublattice during the hold time is shown. Filled solid lines are the theoretical curves based on the single-particle Schrödinger equation.

Chapter 7

Antiferromagnetic spin correlation of SU($\mathcal{N}$) Fermi gas in an optical dimerized lattice

7.1 Introduction

Quantum magnetism manifests itself in quantum many-body states of spins coupled by exchange or superexchange interactions and lies at the heart of many fundamental phenomena in condensed matter physics. Spin systems often tend to show long-range order at low temperature. However, the interplay of exchange interactions with geometry and quantum fluctuations can lead to quantum states characterized by their short-range magnetic order. Examples include valence-bond crystal, spin liquids in a triangular lattice [108], and possibly high-T_c superconductors [109]. Yet, the underlying many-body physics is known to be theoretically and computationally intractable, even in the simple models such as SU(2) Fermi-Hubbard model.

The controlled system of ultracold fermionic atoms in optical lattices is regarded as a promising candidate to gain novel insights into phases driven by quantum magnetism. This approach offers experimental access to a clean and highly flexible Fermi-Hubbard model. Progress toward entering the regime of quantum magnetism was hampered by the ultra-low temperatures and entropies required to observe exchange-driven spin ordering in optical lattices. To solve this problem, cooling schemes bases on the redistribution of entropy between different regions were demonstrated recently, and made a great deal of progresses in realizing the quantum magnetism for the repulsively interacting SU(2) spin systems [38, 39, 37].

In our work, we also make use of the local entropy redistribution scheme within the lattice structure to reach the regime of quantum magnetism. The atoms are prepared in a dimerized cubic lattice, where the exchange energy in a dimer is much larger than that in the other links. This setup allows us to realize the short-range quantum magnetism within th dimer at the total entropy we can currently reach. Furthermore, we introduce large-spin degree of freedom by using a fermionic isotope ^{173}Yb, which is characterized by SU($\mathcal{N} = 2I + 1$) symmetric repulsive interaction for nuclear spin $I = 5/2$. The precise control of the spin degree of freedom provided by optical pumping technique enables us a straight forward comparison between the cases of SU(2) and SU(4). We investigate the

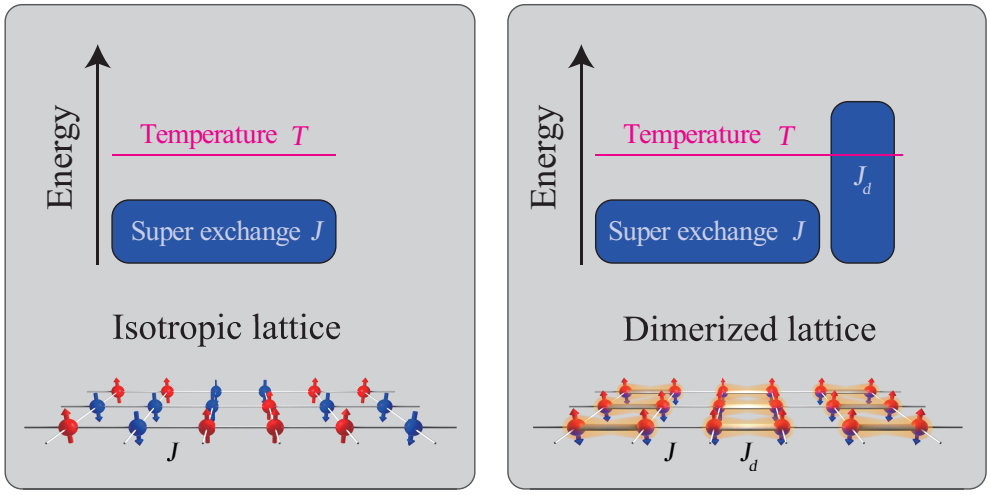

Figure 7.1.1: Local entropy redistribution scheme. The temperature in the experiment is above the exchange energy J for isotropic lattices and no magnetic spin correlations can be observed. When introducing a large exchange energy J_d on links via a dimerization, the temperature is below the large exchange energy, and magnetic spin correlations emerge within the strong links.

large-spin influence on the quantum magnetism. This work is an important step towards the realization of novel SU($\mathcal{N} > 2$) quantum magnetism.

7.2 Spin manipulation by the optical pumping

The experimental techniques that lead to the manipulation and detection of the nuclear spin degree of freedom are of central importance in the context of quantum simulation of SU($\mathcal{N}$)-symmetric models. In this section, we show how the difference nuclear spin states of ^{173}Yb can be separately imaged and how SU(4) spin mixtures can be prepared by means of optical techniques. Although removal of one or more spin states is possible by using narrow-line transitions and the Zeeman shift, associated atom losses make cooing difficult. Instead, we can make use of optical pumping which gather atoms into particular spin states.

7.2.1 Numerical simulation of the spin relaxation

First of all, we introduce the theory to simulate the spin relaxation during optical pumping. The time evolution of spin population can be described by the following rate equations:

$$\frac{dN_{F,m_F}}{dt} = -\sum_{F',m'_F} \omega_{F,m_F}^{F',m'_F} \left(N_{F,m_F} - N_{F',m'_F}\right) + \sum_{F',m'_F} \Gamma_{F,m_F}^{F',m'_F} N_{F',m'_F}, \tag{7.2.1}$$

$$\frac{dN_{F',m'_F}}{dt} = -\sum_{F,m_F} \omega_{F,m_F}^{F',m'_F} \left(N_{F',m'_F} - N_{F,m_F}\right) - \Gamma N_{F',m'_F}, \tag{7.2.2}$$

Table 7.2.1: Reduced dipole matrix elements (RMEs) for Yb [110].

Transition	RME [atomic unit]
${}^1S_0 \leftrightarrow {}^1P_1$	4.4
${}^1S_0 \leftrightarrow {}^3P_1$	0.54

where ω_{F,m_F}^{F',m'_F} and Γ_{F,m_F}^{F',m'_F} are the transition rate to the excited state and the decay rate to the ground state, respectively:

$$\omega_{F,m_F}^{F',m'_F} = \frac{e^2 I_{\text{laser}}}{\epsilon_0 \hbar^2 c} |\langle F', m'_F | r_q | F, m_F \rangle|^2 \frac{1}{\pi} \frac{\Gamma/2}{(\omega_{\text{laser}} - \omega_{F',m'_F})^2 + (\Gamma/2)^2} \tag{7.2.3}$$

$$\Gamma_{F,m_F}^{F',m'_F} = \Gamma \sum_{q=0,\pm 1} C\left[F'(J'(L'S')I'), m'_F; q; F(J(LS)I), m_F\right]^2. \tag{7.2.4}$$

$\langle F', m'_F | r_q | F, m_F \rangle$ is the dipole matrix element such as

$$\langle F', m'_F | r_q | F, m_F \rangle = C[F'(J'(L'S')I'), m'_F; q; F(J(LS)I), m_F] \frac{\langle \alpha' J' || r || \alpha J \rangle}{\sqrt{2J'+1}}. \tag{7.2.5}$$

Here, $\langle \alpha' J' || r || \alpha J \rangle$ is the reduced dipole matrix element, which is specific to the atomic species. In the case of ${}^1S_0 \leftrightarrow {}^3P_1$ of Yb, the reduced dipole matrix element amounts to $\langle \alpha' J' || r || \alpha J \rangle = 0.54 \times$ Bohr radius as shown in Tab.7.2.1.
$C[\cdots]$ is dependent on the quantum numbers for a given transition $|F(J(LS)I), m_F\rangle \leftrightarrow |F'(J'(L'S')I'), m_{F'}\rangle$, and is related to the Clebsh-Gordan coefficient [10]. This $C\left[\cdots\right]$ is given as

$$C[F'(J'(L'S')I'), m'_F; q; F(J(LS)I), m_F] = (-1)^{F'+J'+I'-m'_F+F+1} \delta_{I,I'} \sqrt{(2F'+1)(2F+1)(2J'+1)} \begin{pmatrix} F' & 1 & F \\ -m'_F & q & m_F \end{pmatrix} \begin{Bmatrix} F' & 1 & F \\ J & I' & J' \end{Bmatrix}, \tag{7.2.6}$$

where $(\cdots), \{\cdots\}$ represent Wigner's $3j$- and $6j$-symbol, respectively.

Figure 7.2.1 shows the absolute square of the normalized Clebsch-Gordan coefficients in (a) $F = 5/2 \to F' = 7/2$ and (b) $F = 5/2 \to F' = 3/2$ transition.

7.2.2 Loss spectroscopy of transition used for optical pumping

For optical pumping, we use the ${}^1S_0 \leftrightarrow {}^3P_1(F' = 3/2, 7/2)$ transition. To selectively pump the atoms in each sublevel of the ground state, we impose the B-field on them, and the sublevels split. The Zeeman shift of a sublevel $|F', m_{F'}\rangle$ is given by

$$\Delta E_{F',m_{F'}} = g_{F'} \mu_B B m_{F'}, \tag{7.2.7}$$

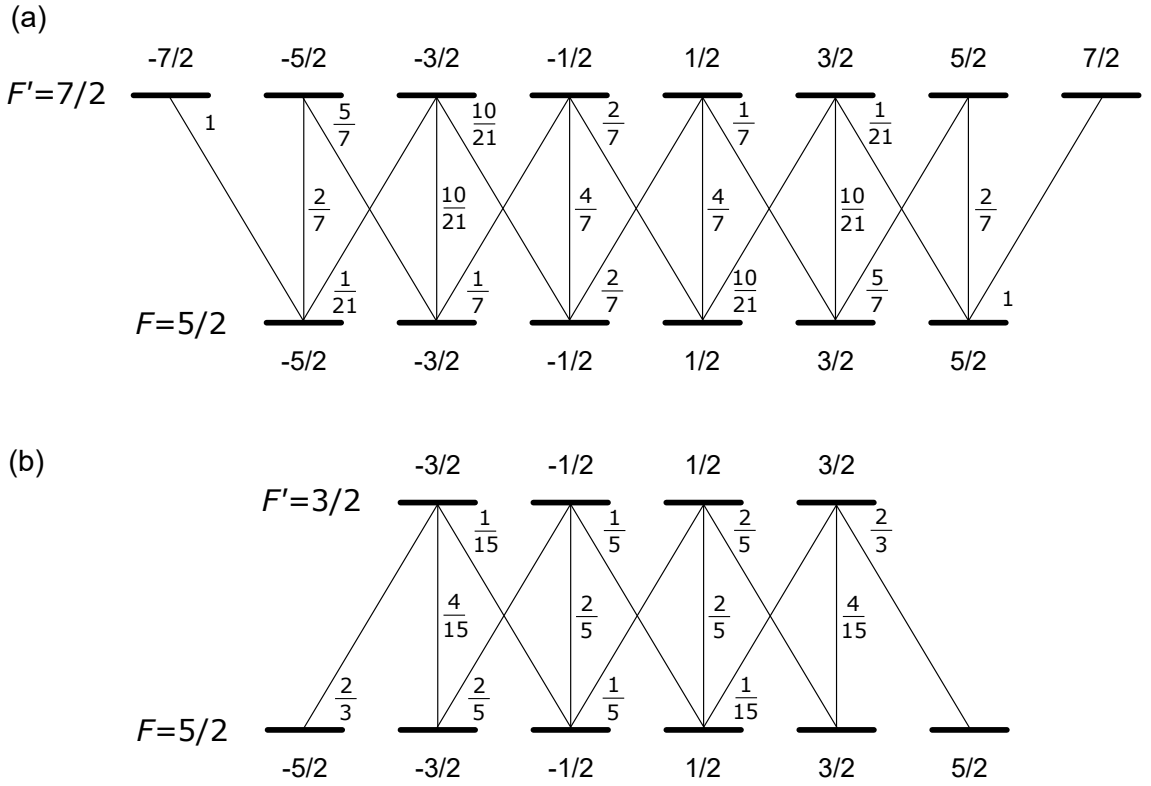

Figure 7.2.1: Squared Clebsch-Gordan coefficients in (a) $F = 5/2 \to F' = 7/2$ transition and (b) $F = 5/2 \to F' = 3/2$ of ^{173}Yb, respectively.

where g-factor is

$$g_{F'} = \frac{F'(F'+1) + J(J+1) - I(I+1)}{2F'(F'+1)} g_J \tag{7.2.8}$$

$$g_J = \frac{3}{2} + \frac{S(S+1) - L(L+1)}{2J(J+1)}. \tag{7.2.9}$$

Since $S = 1/2,\ L = 1/2,\ J = 1,\ I = 5/2$ for the $^3P_1$ state of ^{173}Yb, the g-factor for $F' = 3/2, 7.2$ becomes

$$g_{F'} = \begin{cases} -3/5 & F' = 3/2 \\ 7/3 & F' = 7/2 \end{cases}, \tag{7.2.10}$$

respectively.
We check the energy shift of sublevels in the excited state $^3P_1$ by a loss spectroscopy. Below, we show the experimental setup and results.

Spectrum of $F' = 3/2$

Figure 7.2.2(a) shows the schematic to selectively pump out a spin component in the ground state by using a transition to $F' = 3/2$ in the $^3P_1$ state. Under the high B-field,

the sublevels in $F' = 3/2$ state spread due to the Zeeman effect. With a linearly-polarized light, we can pump out $m_F = \pm 3/2, \pm 1/2$ to another. As a laser source for the pumping, we use the same light as that for the MOT, where the transition to $F' = 7/2$ is used. In order to compensate the large frequency difference between $F' = 3/2$ and $F' = 7/2$, an EOM is used as in Fig.7.2.2(b). Figure 7.2.2(c) shows the loss spectrum of $F' = 3/2$ under the high B-field $B = B_z = 16$ G. We scan the pumping light by RF to the double-pass AOM in Fig.7.2.2(b). At the loss spectroscopy, the polarization of the pumping light is not π, but the composition of σ^+ and σ^- to induce atomic loss.

Spectrum of $F' = 7/2$

Figure 7.2.3(a) shows the schematic to selectively pump out a spin component in the ground state by using the transition to $F' = 7/2$ in the $^3P_1$ state. Since the laser source for the pumping is the same as for the MOT($F' = 7/2$), where the -1st-order light of the switching AOM with 80 MHz is used, an AOM with 350 MHz is inserted to compensate the frequency shift by the switching AOM and the double-pass AOM as in Fig.7.2.3(b). Figure 7.2.3(c) is the loss spectrum of $F' = 7/2$. The offset of the atom number is slowly changing because the power of the pumping light depends on the RF to the double-pass AOM. Since the center frequency of the AOM is 110 MHz, the atomic loss gets larger around the frequency.

7.2.3 Optical Stern-Gerlach Experiment

The Stern-Gerlach technique is widely used in cold atom experiments with alkali atoms. The magnetic field gradient creates a spin-dependent force on atoms, which enables to separately observe the atoms in the different magnetic sublevels [111]. However, the same technique is not available to Yb and other alkaline-earth-like atoms since they have no electronic spin in their ground states. Alternatively, we utilize the optical Stern-Gerlach (OSG) effect [112], which originates from dependence of the light shift of the ground state on its magnetic sublevels. In this section, we describe this technique and show the result of the demonstration with ^{173}Yb atoms.

Calculation of light shifts

First, we calculate light shifts induced by a laser field detuned by a frequency on the order of the hyperfine splittings in $^3P_1$ of ^{173}Yb. The energy shift for $|F, m_F\rangle$ of the ground state is given by [113]

$$\Delta E_{F,m_F} = -\frac{e^2 I_{\text{laser}}}{\epsilon_0 \hbar c} \sum_{F',m_{F'}} \frac{\omega_{F',m_{F'}}}{\omega^2_{F',m_{F'}} - \omega^2_{\text{laser}}} \left|\langle F', m_{F'}|r_q|F, m_F\rangle\right|^2, \tag{7.2.11}$$

where I_{laser} is the intensity of laser light, ω_{laser} is the laser frequency, $\omega_{F',m_{F'}}$ is the resonant frequency between the states $|F, m_F\rangle$ and $|F', m_{F'}\rangle$, the summation is taken over all the possible F' and $m_{F'}$, and $\langle F', m_{F'}|r_q|F, m_F\rangle$ is the dipole matrix element defined in Eq.7.2.5. We use the $^1S_0 \leftrightarrow {}^3P_1$ transition for the OSG experiment. The hyperfine states of $F' = 3/2, 5/2, 7/2$ have to be taken into consideration, whose resonant frequencies are listed in Tab.3.1.3. Figure 7.2.4 shows the calculation results of light shifts for circular

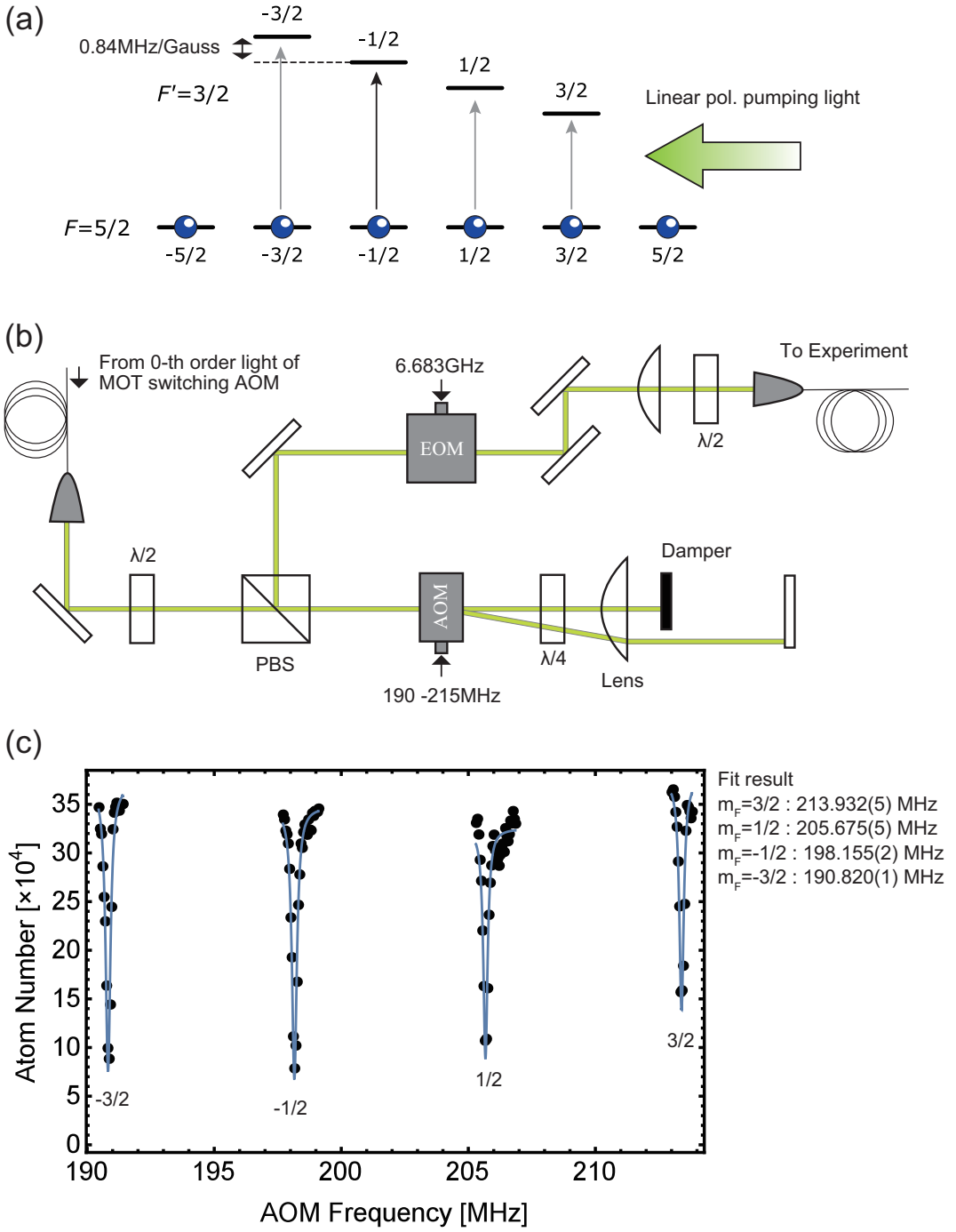

Figure 7.2.2: Schematics of the loss spectroscopy of the $F' = 3/2$ transition. (a) Energy level under the external B-field. Sublevels in $F' = 3/2$ spread according to $\Delta E = g_{F'}\mu_B B m_{F'}$. Since $g_{F'} = -3/5$ for $F' = 3/2$, the splitting amounts to $g_{F'}\mu_B = 0.84$ MHz/Gauss. (b) Experimental setup for the pumping light. We use the same laser source as that for MOT, where the $F' = 7/2$ transition is used. The frequency of the pumping laser is controlled by an RF to the double-pass AOM. (c) Loss spectrum under the B-field $B = B_z = 16$ Gauss. The horizontal axis shows the RF to the double-pass AOM. The right legend is the fit result with the Lorentzian function. The measured energy splitting is about 14.9 MHz, which is close to the theoretical estimation $0.84 \times 16 = 13.4$ MHz.

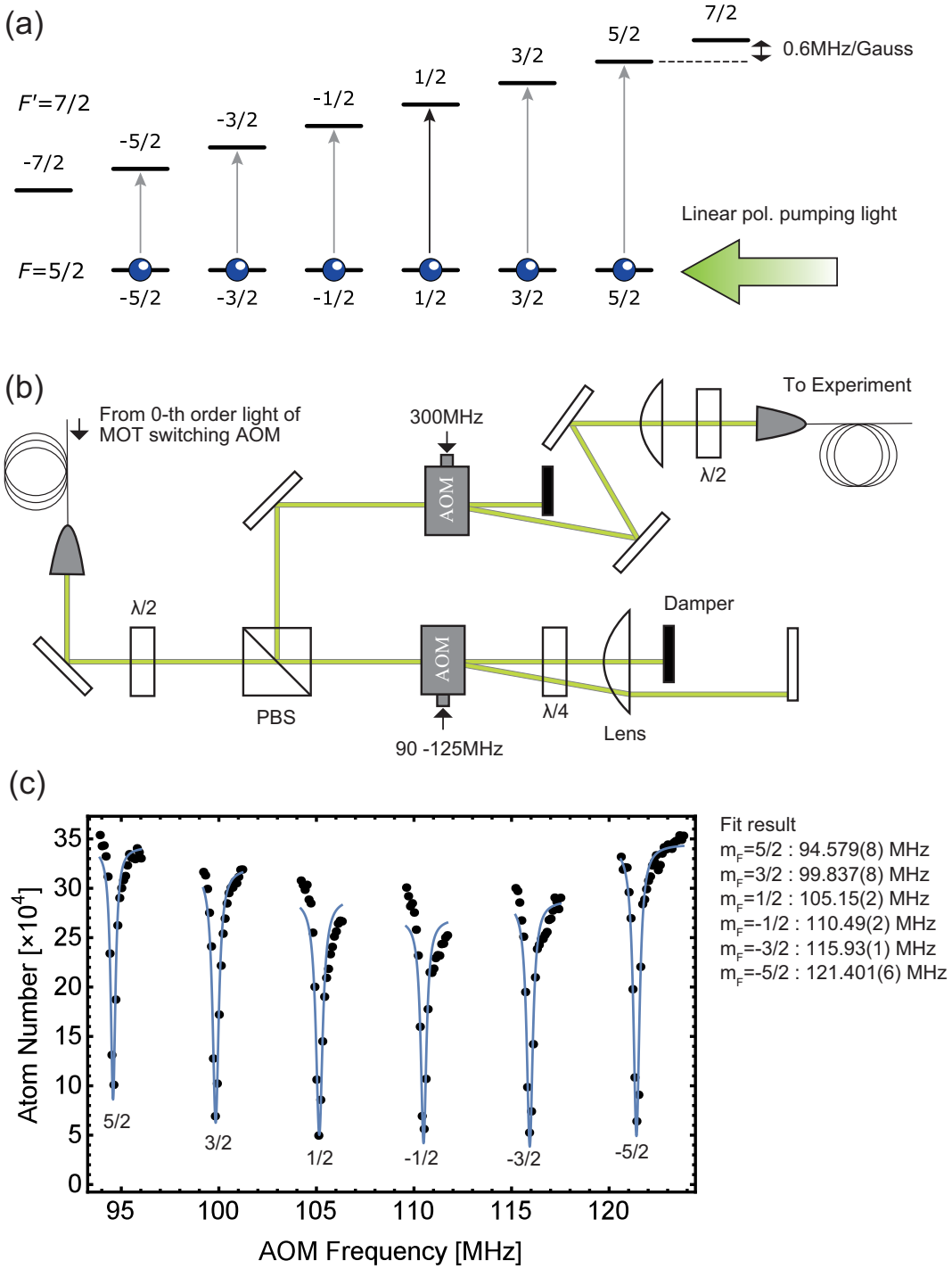

Figure 7.2.3: Schematics of the loss spectroscopy of the $F' = 7/2$ transition. (a) Energy level under the external B-field. Sublevels in $F' = 7/2$ spread according to $\Delta E = g_{F'}\mu_B B m_{F'}$. Since $g_{F'} = 3/7$ for $F' = 7/2$, the splitting amount to $g_{F'}\mu_B = 0.6$ MHz/Gauss. The transition to $\pm 7/2$ is prohibited with a linearly-polarized light. (b) Experimental setup for the pumping light. We use the same laser source as that for MOT. Frequency of the pumping laser is controlled by an RF to the double-pass AOM. (c) Loss spectrum under the B-field $B = B_z = 16$ Gauss. The horizontal axis shows the RF to the double-pass AOM. The right legend is the fit result with the Lorentzian function. The measured energy splitting is about 10 MHz, which is close to the theoretical estimation $0.6 \times 16 = 9.6$ MHz.

polarization and linear polarization. With circular polarized light, each magnetic sublevel of ^{173}Yb is well separated at around 1 GHz detuning from $F' = 7/2$ transition. On the other hand, the light shifts of sublevels with the same absolute values are degenerated in the linearly polarized light.

Experimental setup and result

Figure 7.2.5 shows the schematics of the OSG experiment. We irradiate an OSG light on an atomic cloud along the y-axis right after turning off FORT potential. The OSG light is aligned so that the atomic cloud is located at the shoulder of the Gaussian beam, where each nuclear spin feels the different gradient force according to the detuning of the OSG light as in the Fig.7.2.4. During TOF, the atomic cloud expands according to its velocity distribution, and we observe the velocity distribution of the atomic cloud by absorption imaging. Figure 7.2.6 shows the absorption images with and without the OSG light. Each spin population is separately observed with the OSG light. Since an atom in a sublevel where the large light shift is earned suffers from the large heating by photo-scattering, the width of the cloud differs depending on the sublevel.

7.2.4 Creation of balanced 4-spin mixture

Even though we can selectively pump out an arbitrary nuclear spin of ^{173}Yb by applying a B-field and splitting sublevels of the excited state, we suffer from imbalance of the spin population after the optical pumping. This is because of asymmetry of the Clebsch-Gordan coefficients in Fig.7.2.1. For example, if we pump atoms in $m_F = 3/2$ of the ground state by using $|F = 5/2, m_F = 3/2\rangle \leftrightarrow |F' = 7/2, m'_F = 3/2\rangle$ line, almost all of the atoms would be transported to $|F = 5/2, m_F = 1/2\rangle$. On the contrary, with $|F = 5/2, m_F = 3/2\rangle \leftrightarrow |F' = 3/2, m_{F'} = 3/2\rangle$ line, atoms are pumped into $|F = 5/2, m_F = 5/2\rangle$ state rather than $|F = 5/2, m_F = 1/2\rangle$ state. Then, we use both of these transition lines to compensate difference of the Clebsch-Gordan coefficients. Figure 7.2.7(a) shows the schematic of optical pumping method. We pump atoms in $m_F = \pm 3/2$ to $m_F = \pm 1/2$ and $\pm 5/2$ by using the 4-frequency light. To examine this scheme, we simulate the spin population by numerically solving the rate equations 7.2.1 and 7.2.2. Figure 7.2.7(b) shows the result of the scheme. The simulation ensures that a balanced four-component mixture can be obtained. We also find that the result is robust against the laser intensity imbalance between $F = 5/2 \rightarrow F' = 3/2$ and $F = 5/2 \rightarrow F' = 7/2$.

Figure 7.2.8 illustrates the experimental setup for the optical pumping to create a balanced 4-spin mixture. The setup before optical fibers to the experimental chamber in Fig.7.2.8(b) is merely combination of the Fig.7.2.2(b) and Fig.7.2.3(b). After optical fibers, we overlap two pumping lights on a PBS, tilt the polarization directions by 45° at a $\lambda/2$ plate, and use the lights reflected at the second PBS. These optics provide the two pumping lights with the same polarization. After passing through wave plates, notch mirrors and lens, the two lights enter the metallic chamber. When we align the optical path, we use the incident light of 532 nm y-axis lattice partially transmitted at a notch mirror for 45° angle, and adjust two mirrors so that the 532 nm light couples to the optical fibers from which the pumping lights are emitted.

Optical pumping causes some heating of atomic samples since it uses absorption and emission of photons. This is crucial for samples in the quantum degenerate regime. There-

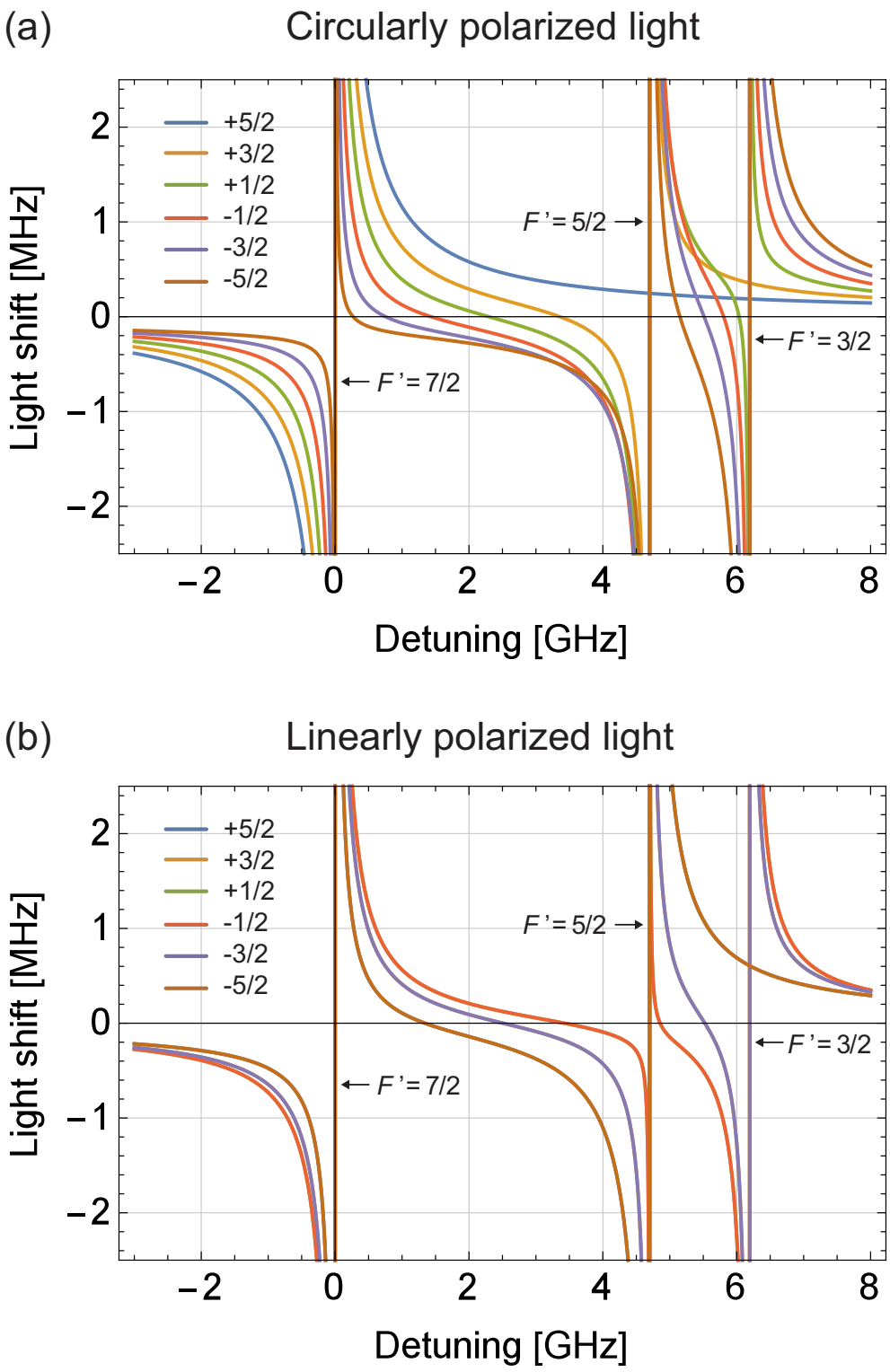

Figure 7.2.4: Calculated light shift of the OSG beam as a function of frequency detuned from the ${}^1S_0 \leftrightarrow {}^3P_1(F' = 7/2)$ transition. We assume a Gaussian beam with $w_0 = 100$ μm and an incident power of 10 mW and evaluate the laser intensity at $\rho = w_0/2$ from the beam center.

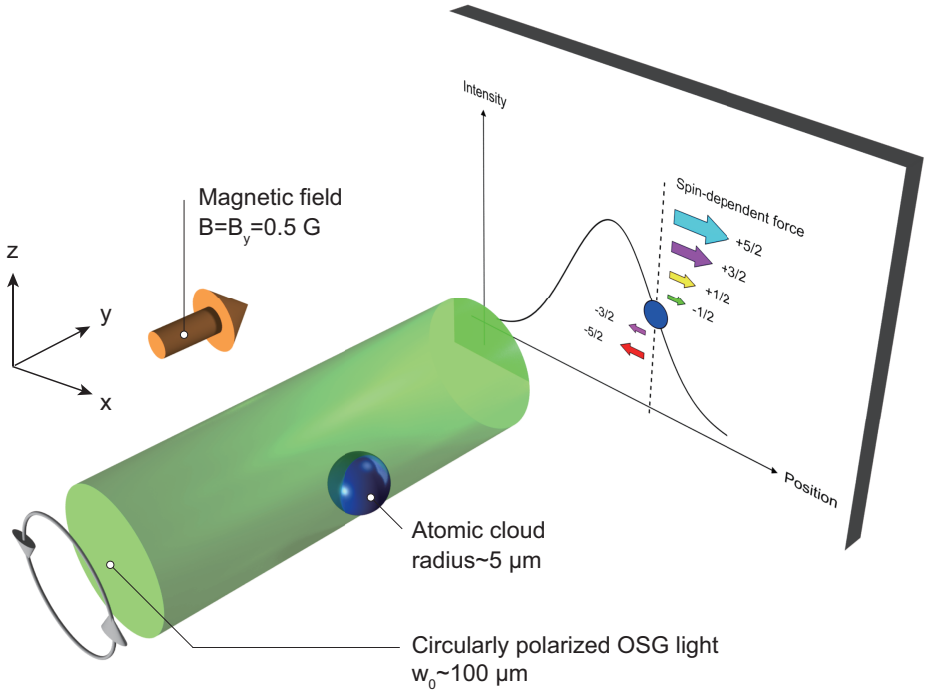

Figure 7.2.5: Schematics of the experimental setup for the OSG. The OSG light with a circular polarization propagates along the y-direction. An atomic cloud is located at the shoulder of the OSG light, where each spin feels the different gradient according to the detuning. A weak magnetic field is applied along y-direction not to cause spin precession by the fictitious magnetic field of the OSG light.

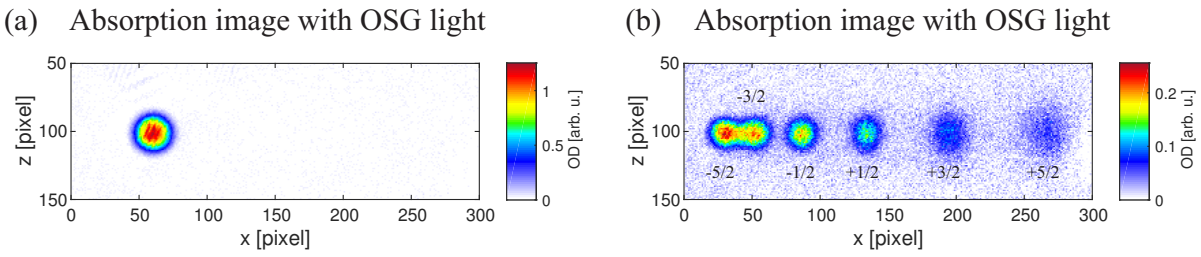

Figure 7.2.6: Absorption images (a) without and (b) with the OSG light. The OSG light is about 1 GHz blue-detuned from the resonant frequency of the $^1S_0 \leftrightarrow {}^3P_1(F' = 7/2)$ transition. The irradiation time is 0.12 ms, and incident power of the OSG light is about 40 mW. Images are taken along the y-axis after 10 ms TOF, and averaged by 5 independent shots.

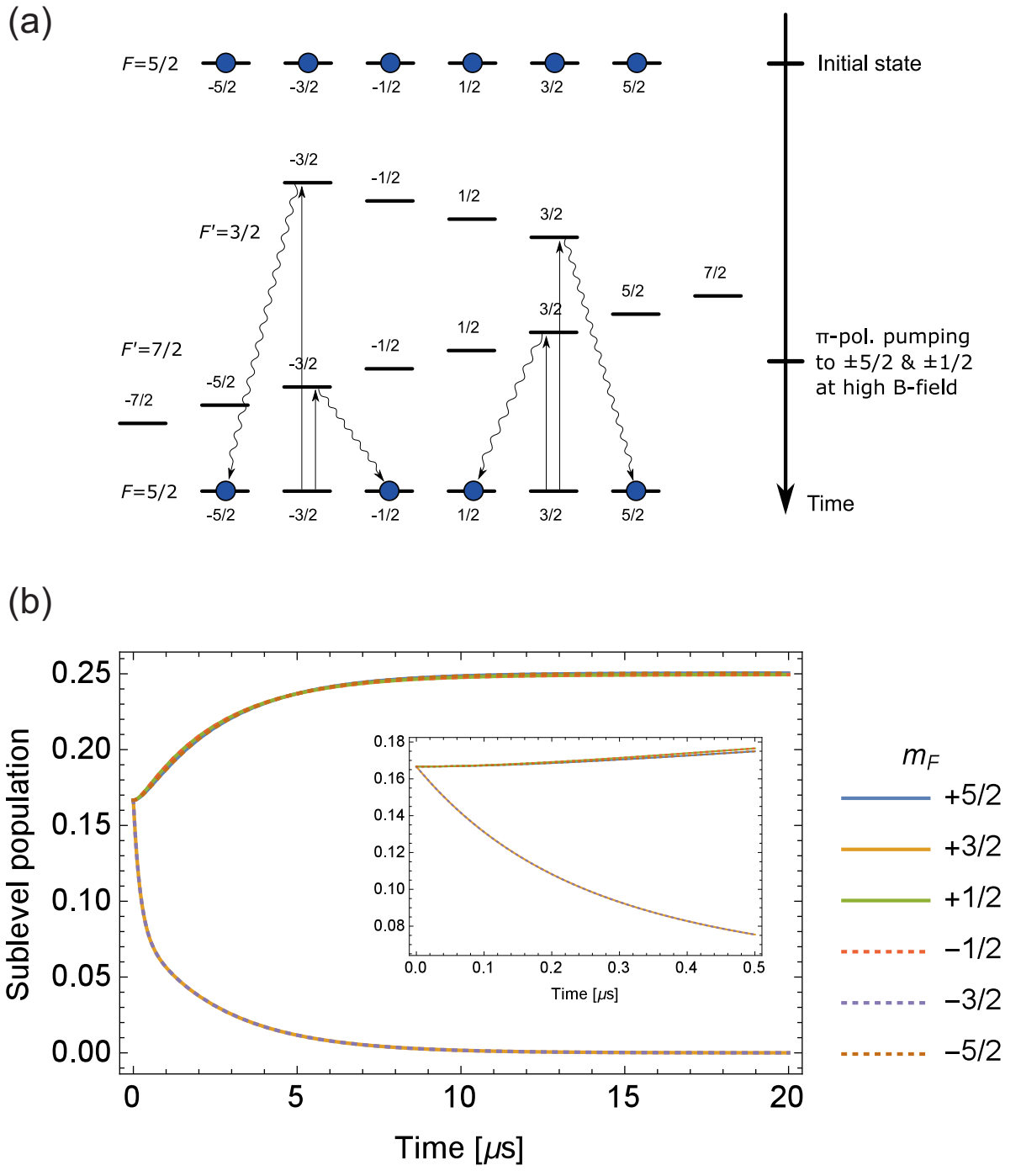

Figure 7.2.7: (a) Schematics of the optical pumping to create a balanced 4-spin mixture of ^{173}Yb. (b) Numerical simulation result of the optical pumping by rate equations.

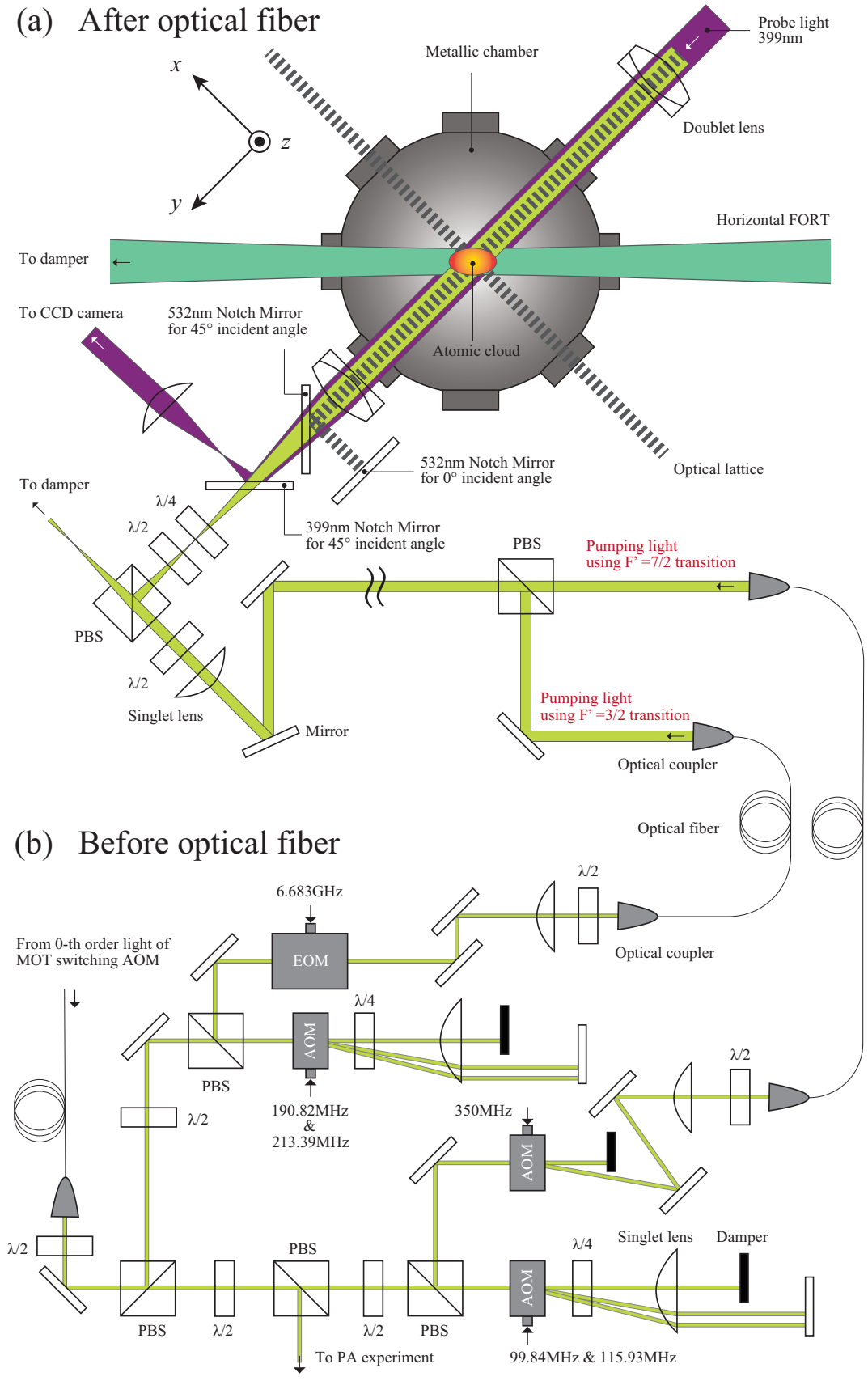

Figure 7.2.8: Experimental setup for the optical pumping (a) after and (b) before an optical fiber. Details are described in the main text.

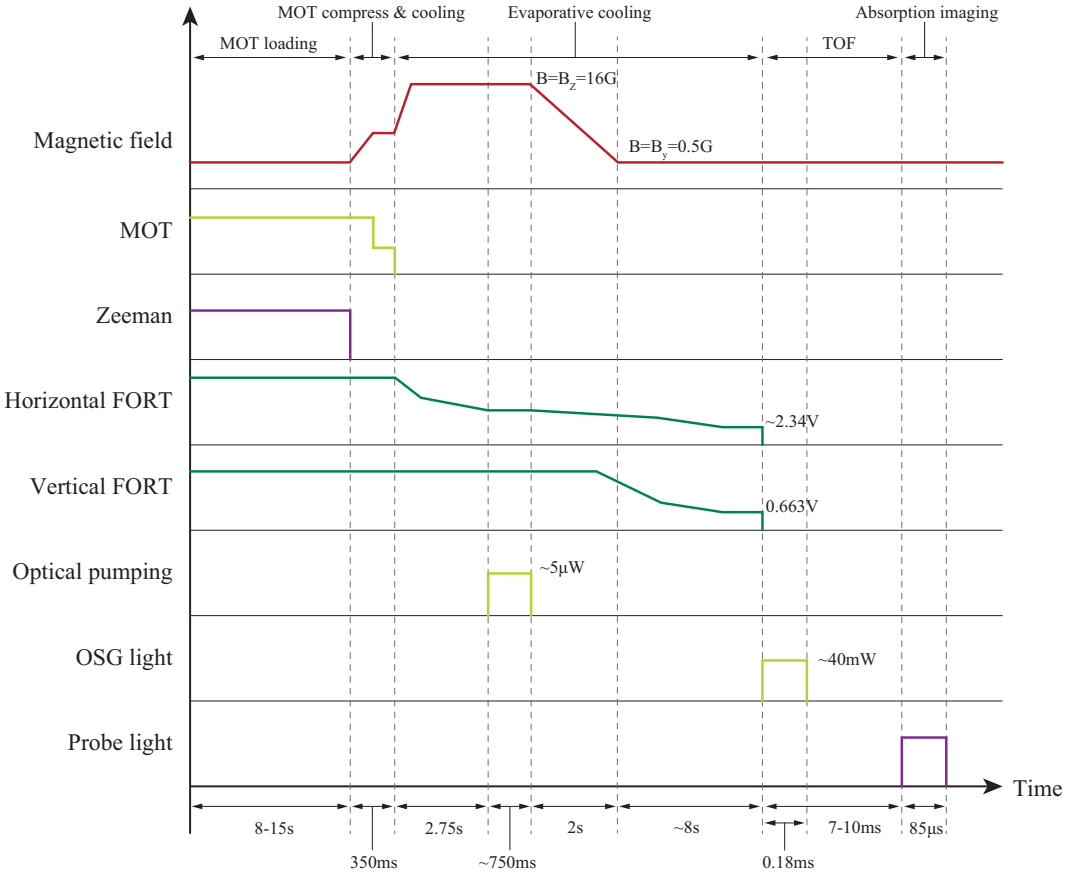

Figure 7.2.9: Typical experimental sequence for the optical pumping and OSG.

fore, we perform optical pumping at the early stage of evaporative cooling, as shown in Fig.7.2.9. Because the diameter of our pumping laser is smaller than the size of an atomic cloud immediately after loading to the FORT, we shed pumping lasers 2.75 s after the beginning of evaporative cooling. Optimization of the optical pumping is accomplished by the following OSG technique: we adjust the polarization and intensity of optical pumping lights to create a balanced 4-spin mixture.

Figure 7.2.10 shows the result of optical pumping to the 4 magnetic sublevels $m_F = \pm 1/2$ and $\pm 5/2$ of ^{173}Yb. Without optical pumping, all magnetic sublevels are equally populated, as in (a). After irradiation of pumping laser, almost all atoms are pumped into $m_F = \pm 1/2$ and $\pm 5/2$. Fitting with a multi-component Gaussian function ensures that almost balanced 4-spin mixture is achieved.

7.3 Photoassociation Experiment

Photoassociation (PA) [114, 115, 116, 117, 118] is the process in which two colliding atoms absorb a photon to form an excited molecule [119]. If PA light is applied to atoms in a deep optical lattice as in Fig.7.3.1, atoms on multiply occupied sites are converted into electronically excited molecules. The molecules can immediately decay into its electronic ground states or two free atoms. The dissociated two free atoms have large kinetic energy

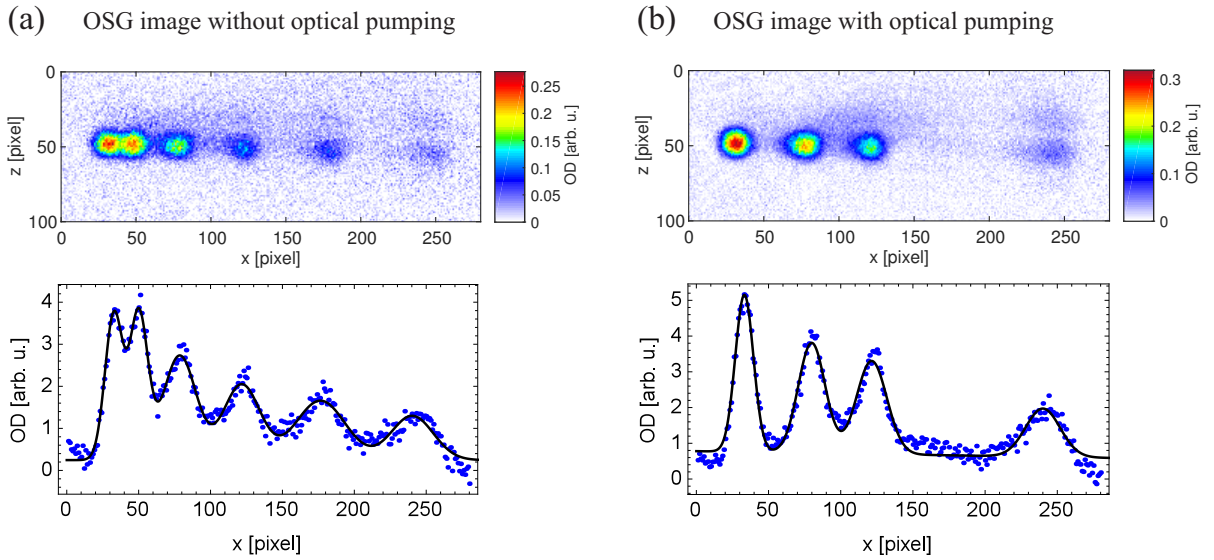

Figure 7.2.10: OSG images (a) without and (b) with the optical pumping. The lower images plot OD integrated along the z-axis. Solid lines are the fit result with a multi-component Gaussian function.

and escape from the optical trap [119]. Molecules in electronic ground states can not be detected by a standard absorption imaging.

In the experiment, we use the PA resonance around the ${}^1S_0 \leftrightarrow {}^3P_1$ atomic transition to measure the double occupancy in optical lattices. This resonance has sufficient PA rate, otherwise tunneling between neighboring lattice sites or heating due to photon scattering could occur. In this section, we describe the experiment to investigate if the PA technique uniformly works for all two spin pairs within the 4-spin mixture of $m_F = \pm 1/2$ and $\pm 5/2$.

7.3.1 Creation of arbitrary 2-spin mixture

For systematic investigation, we develop a pumping scheme to create arbitrary 2-spin mixtures. Figure 7.3.2(a) shows the schematics. As a first step, 6-spin components are pumped to $m_F = \pm 5/2$ by irradiating a π-polarization light at the low B-field $B = B_z = 0.5$ Gauss, where the splitting of sublevels in $F' = 3/2$ is negligible. As a second step, we impose the high B-field $B = B_z = 16$Gauss to split the sublevels in $F' = 7/2$, and shine the 4-frequency light, which is realized by putting RFs to a double-pass AOM via a multi-channel combiner. In the above procedure, the first step plays important role to create 2-component mixtures including $m_F = 5/2$ or $-5/2$: as can be seen from the Fig.7.2.1(a), CGC from $m_{F'} = (-)3/2$ to $m_F = (-)5/2$ is as small as 1/21. Therefore, it is not so effective to pump to $m_F = (-)5/2$ with the $F' = 7/2$ transition. This problem can be verified by the numerical simulation of the spin relaxation described in the section 7.2.1. To solve the problem, we pre-pump the atoms to $m_F = \pm 5/2$ with the $F' = 3/2$ transition, where the CGC from $m_{F'} = (-)3/2$ to $m_F = (-)5/2$ is as large as 2/3. Figure 7.3.2(b) displays the results in a matrix form. The upper triangular matrix shows the row absorption images after OSG. The lower triangular matrix shows the OD integrated along z-axis. Almost all atoms are pumped to a desired sublevel. The atoms remaining

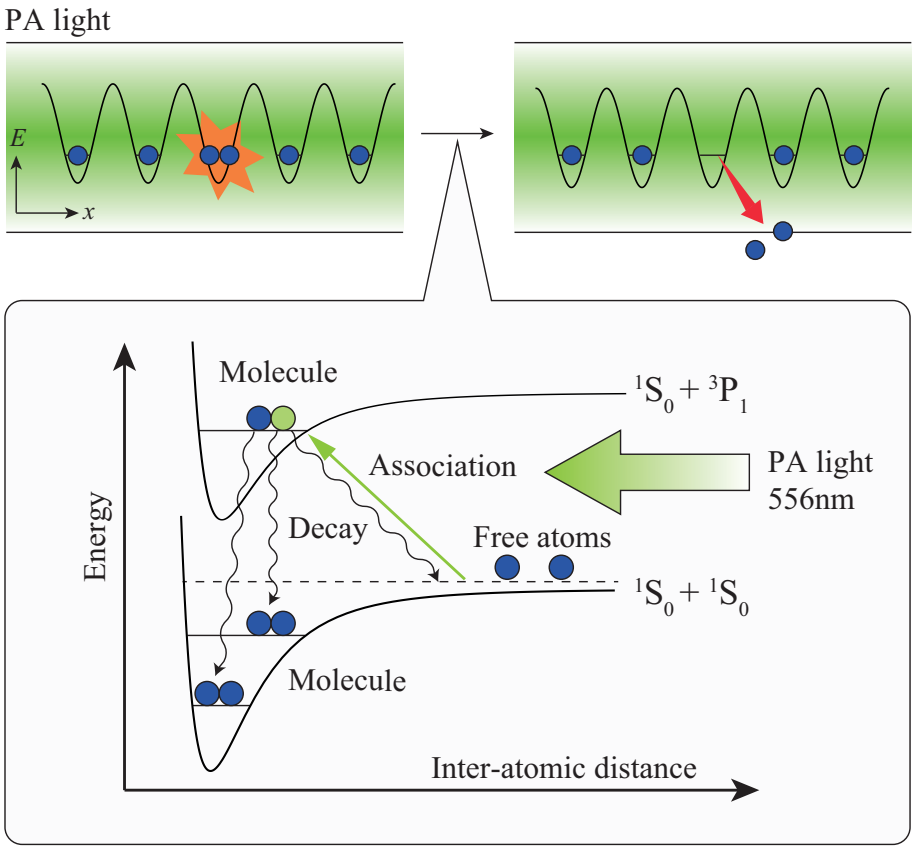

Figure 7.3.1: Schematics of the PA in an optical lattice.

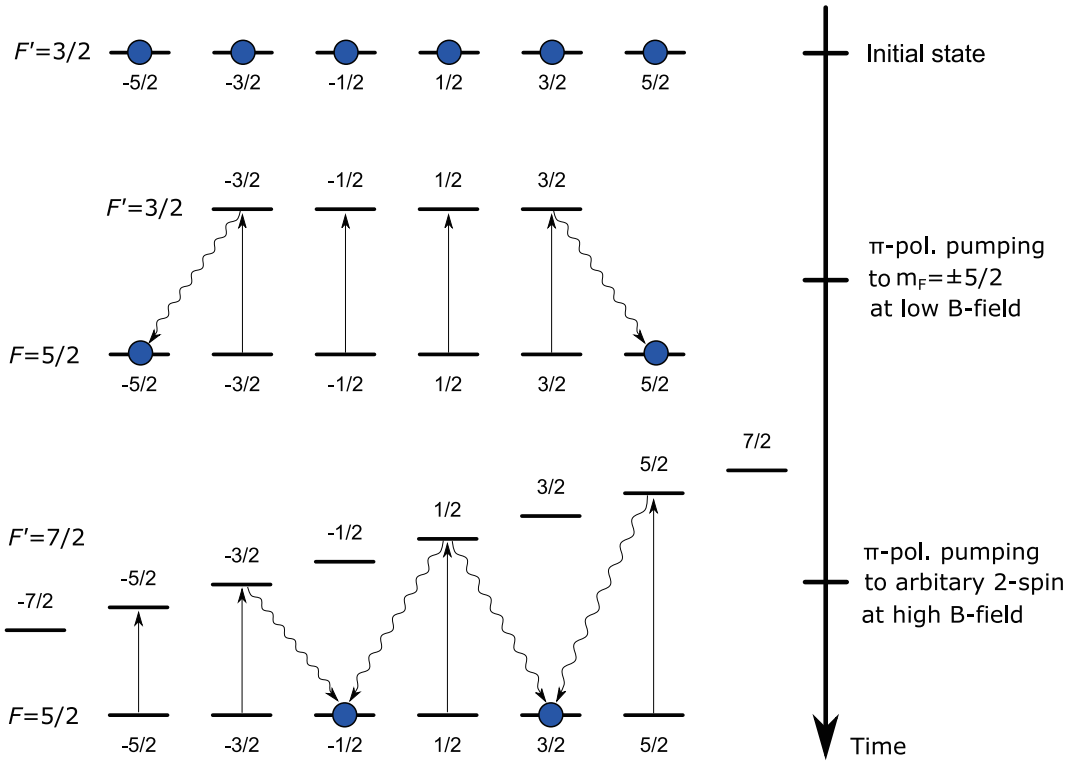

Figure 7.3.2: Schematics to create arbitrary 2-component mixtures of ^{173}Yb. The arrows mean the excitation and decay. We show the case of the optical pumping to $m_F = -1/2, 3/2$.

not to be pumped may be caused by the spatial inhomogeneity due to the trap potential.

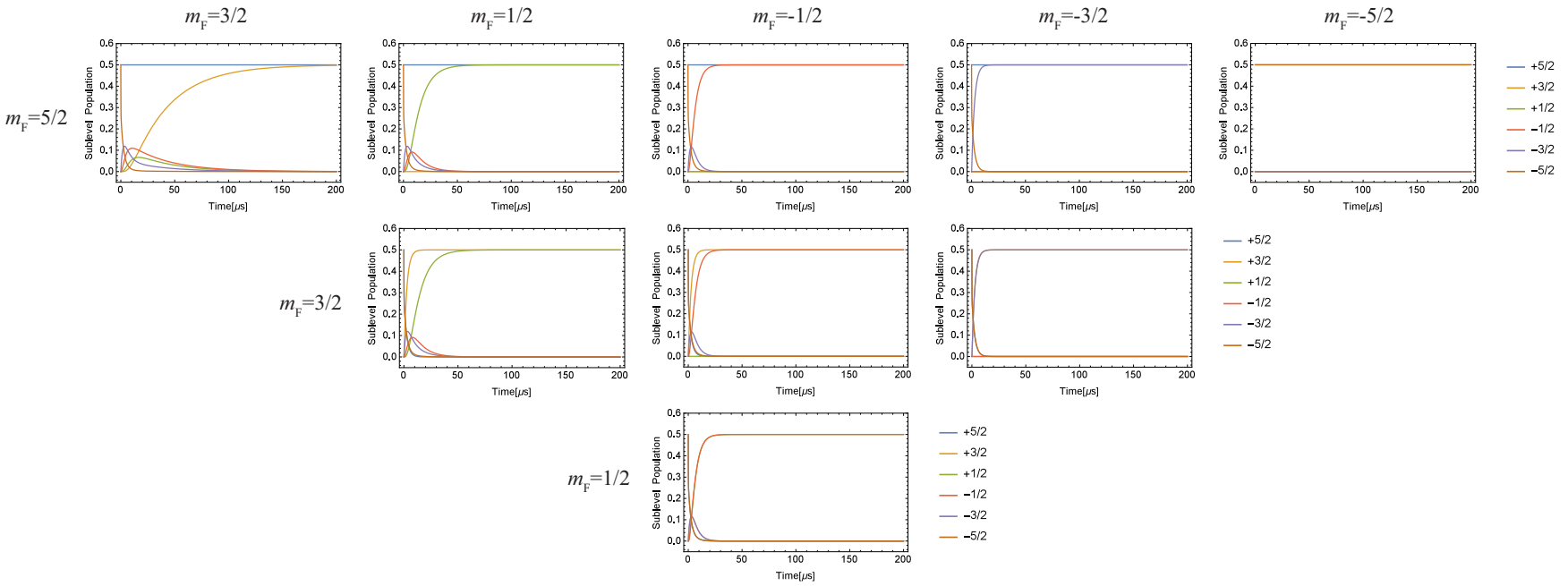

Figure 7.3.3: Numerical simulation of the optical pumping to arbitrary 2-spin mixtures. The initial state is a 2-spin mixture of $m_F = \pm 5/2$. The beam waist of the optical pumping beam is set to $w_0 = 200$ μm, and power of each 4-frequency light is 10 μW. The column and row indexes correspond to the sublevel to which a particle should be pumped. Note that the lines of $m_F = \pm s$ are overlapped in the figure of pumping to $m_F = \pm s$ ($s = 1/2, 3/2, 5/2$).

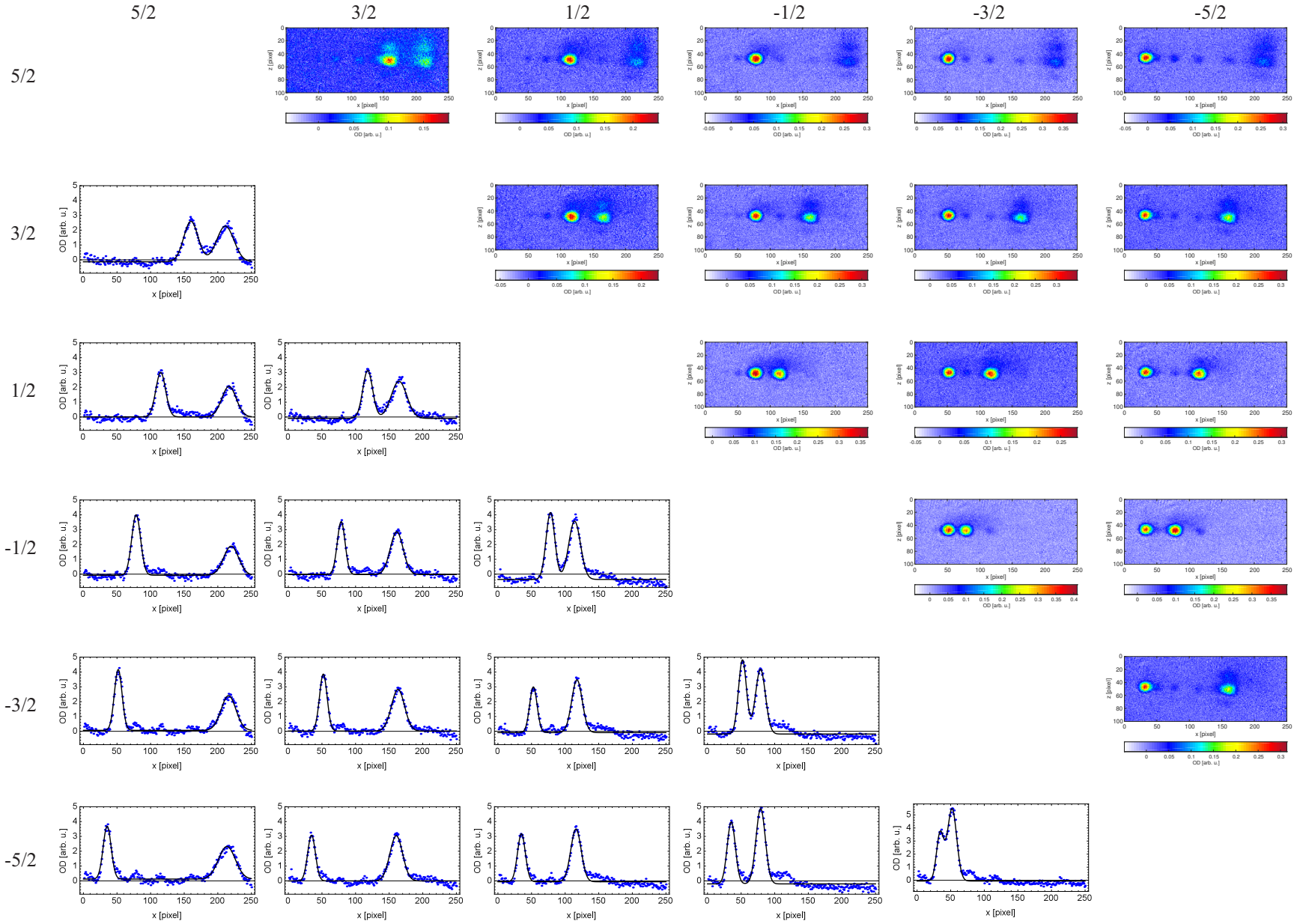

Figure 7.3.4: OSG images with the optical pumping to arbitrary 2-spin mixtures.

After creating a certain 2-component mixture of ^{173}Yb by the optical pumping, we investigate the PA rate for the spin pair. First, we describe the experimental setup for the PA (See the Fig.7.3.5). Similar to optical pumping lights, we use the 0-th order light of the switching AOM of the MOT, and detune the light by a double pass AOM. After an optical fiber, the PA light enters the metallic chamber along the z axis. To avoid retroreflection, the PA light is not overlapped with the z-axis optical lattices before the doublet lens and damped at an iris in front of the retroreflection mirror.

In the experiment, we use the PA resonance at the detuning of -812.26 MHz from the $^1S_0 \leftrightarrow ^3P_1$ atomic transition. By the following experiment procedure, we investigate if the resonance has a sufficient and uniform PA rate for all two-spin pairs within $m_F = \pm 1/2$ and $\pm 5/2$. The sample is prepared by optical pumping to a certain two-spin pair and evaporatively cooling down to the degeneracy regime. Then, we load the two-component Fermi gas of ^{173}Yb into optical lattices with an anisotropic geometry of $\left(s^{(x)}_{\mathrm{long}}, s^{(y)}_{\mathrm{short}}, s_{(\mathrm{z})}\right) = (40, 40, 15)$. At the same time as lattice loading, we ramp up the horizontal FORT potential by a few % to increase the double occupancy in the lattice. After that, we quickly ramp up the lattice depths up to $\left(s^{(x)}_{\mathrm{long}}, s^{(y)}_{\mathrm{short}}, s_{(\mathrm{z})}\right) = (100, 100, 25)$ in order to freeze the atomic motion, and irradiate the PA light for variable time. Figure 7.3.6 shows the measure atom loss curves. We fit to the data with the double exponential function as

$$f(t) = \left[a \exp\left(-t/\tau_1\right) + b\right] \exp\left(-t/\tau_2\right), \tag{7.3.1}$$

where a, b, τ_1, τ_2 are fitting parameters. The decay time shown in the inset is equivalent to τ_1, and double occupancy is defined as

$$D = \frac{a}{a+b}. \tag{7.3.2}$$

The data ensure that the PA works almost uniformly for all spin pairs and has a sufficient PA rate not to cause one-body loss during the doublon removal, as a plateau can be seen.

7.4 Singlet-triplet oscillation in dimer

In this section, the observation of antiferromagnetic spin correlations on neighboring sites in a dimerized lattice geometry is presented. After loading a low-temperature 2-component or 4-component spin mixture of fermionic atoms with repulsive interactions into the optical lattice, the spin correlations emerge as an excess number of singlets as compared to triplets, which consist of two atoms with different spins. The dependence of the singlet-triplet imbalance is studied over a wide range of entropies.

An overview of the preparation and detection scheme is given in the Fig.7.4.1. A balanced two-spin mixture of $m_F = \pm 5/2$ or four-spin mixture of $m_F = \pm 1/2$ and $\pm 5/2$ with approximately 3.2×10^4 atoms is evaporatively cooled in the FORT to degeneracy regime.

A,B The lattice potentials are turned on with a spline-shaped ramp in the first 100 ms and liner ramp in the latter 50 ms to a dimerized lattice configuration. At the same time, we linearly change the horizontal FORT potential to 2.335 V in the first 100 ms.

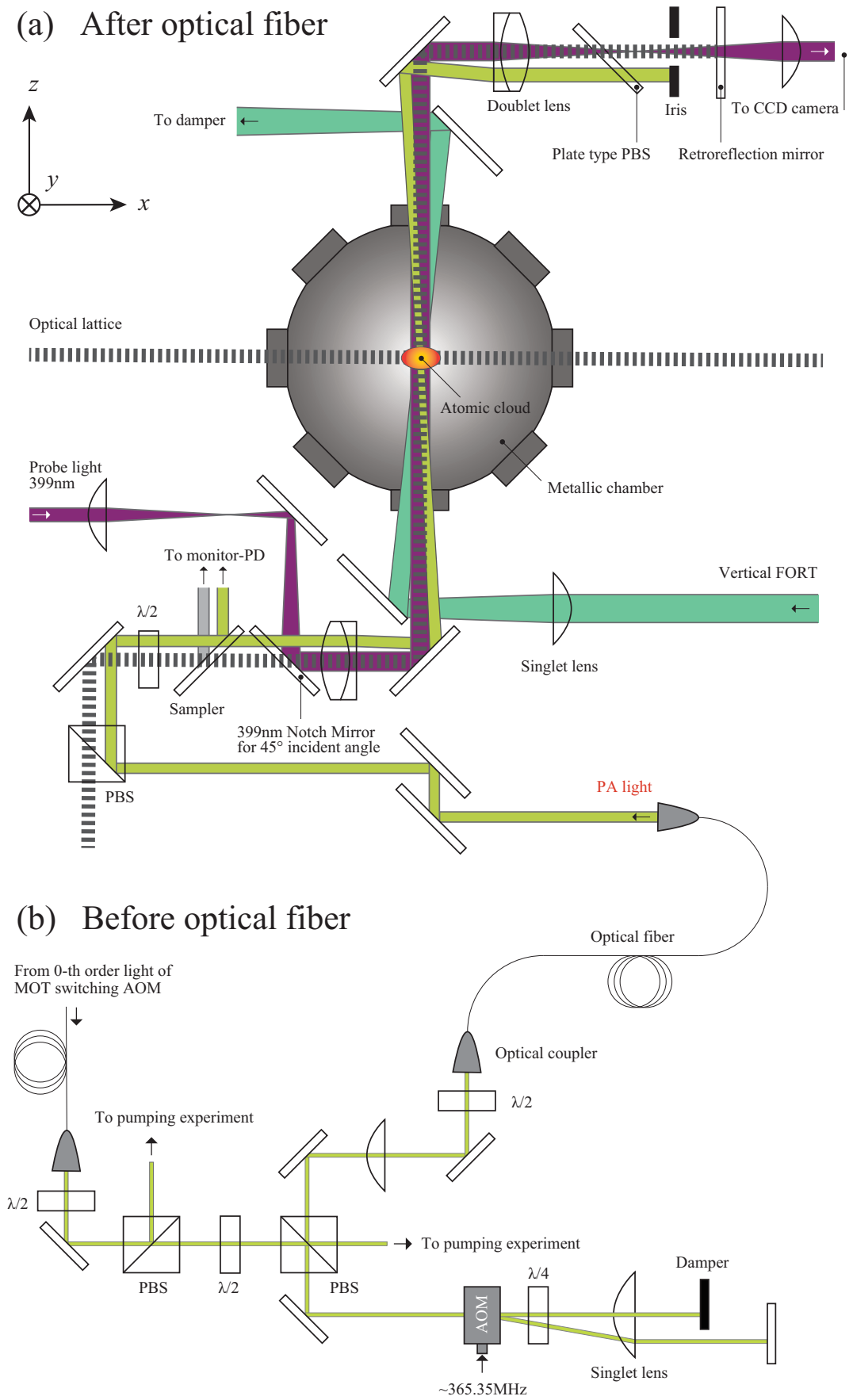

Figure 7.3.5: Experimental setup for PA (a) after and (b) before optical fiber.

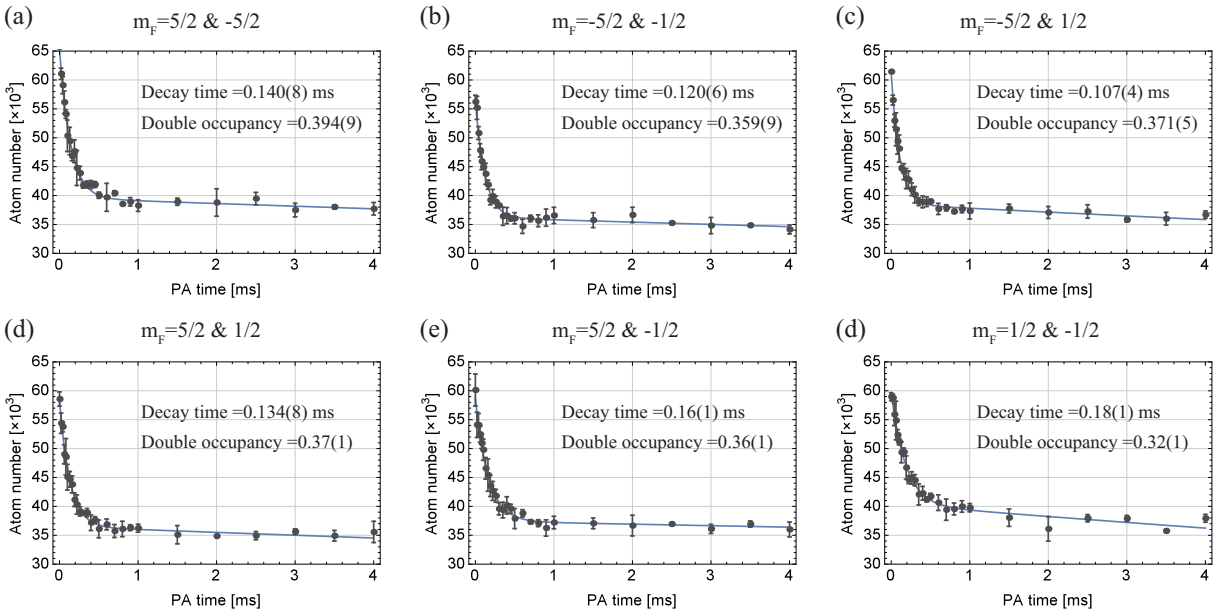

Figure 7.3.6: Atom loss curves by the PA in optical lattices for all spin pairs within $m_F = \pm 1/2$ and $\pm 5/2$.

C,D For measurements in the dimerized lattice, the lattice is ramped up in two steps. The lattice potentials are linearly increased over the course of 0.5 ms up to $\left[s^{(x)}_{\mathrm{long}}, s^{(x)}_{\mathrm{short}}, s^{(y)}_{\mathrm{short}}, s^{(z)}_{\mathrm{short}}\right] = [25, 20.8, 80, 100]$ in order to isolate each dimer. In a second linear ramp lasting 10 ms, the short x-axis lattice is increased to $s^{(x)}_{\mathrm{short}} = 100$ to freeze the atomic motion within the dimer.

E After the rapid ramp to the detection lattice, we apply the spin-dependent by the fictitious magnetic field of light, which creates a differential bias energy Δ for atoms of different spins on adjacent sites and causes coherent oscillations between the singlet $|s\rangle = (|\sigma_1, \sigma_2\rangle - |\sigma_2, \sigma_1\rangle)/\sqrt{2}$ and the triplet $|t_0\rangle = (|\sigma_1, \sigma_2\rangle + |\sigma_2, \sigma_1\rangle)/\sqrt{2}$ state at a singlet-triplet oscillation frequency $2\Delta/h$, where σ_i $(i = 1, 2)$ denote a spin component. If the initial amount of singlets and triplets is equal, no overall oscillation will be visible, as $|s\rangle$ and $|t_0\rangle$ oscillate in antiphase.

F After a certain oscillation time, we remove the gradient and merge two adjacent sites by ramping $s^{(x)}_{\mathrm{short}}$ down to zero in 1 ms. Owing to the symmetry of the two-particle wavefunction, the singlet state on neighboring sites evolves to a doubly occupied site with both atoms in the lowest band, whereas the triplet state transforms into a state with one atom in the lowest and the other atom in the first excited band.

G The fraction of atoms forming double occupancies in the lowest band of the merged lattice is detected by the PA technique, while the state with one atom in the lowest band and the other in the first excited band is note detected by the PA due to its odd partial wave functions [119].

We adjust the atom number so that the double occupancy per site does not appear at the stage of lattice loading, otherwise multiply occupied sites cause the overestimation

of the singlet fraction because the PA can remove them from the trap. The entire filling over the harmonic confinement is equal to or less than one atom per site. The optimal atom number is examined by numerical calculation using the atomic limit of the SU($\mathcal{N}$) Fermi-Hubbard model and local density approximation, details of which are described in the section 2.6. Note that the states with one atom per dimer also exist in outer region of the trap system, and the oscillation between the symmetry state= $(|\sigma_1, 0\rangle + |0, \sigma_1\rangle)/\sqrt{2}$ and antisymmetry state= $(|\sigma_1, 0\rangle - |0, \sigma_1\rangle)/\sqrt{2}$ occurs owing to the field gradient, but PA technique does not detect such states because they leads to the single occupancy after merging the dimer.

Figure 7.4.2 shows the typical singlet-triplet oscillation of the 4-spin mixture of ^{173}Yb in a strongly dimerized lattice. A clear oscillation in the atom number is visible. The damping of the oscillation is caused by the inhomogeneity of the fictitious magnetic field gradient and the heating due to photon scattering of the gradient light. We observe the STO for the 2-spin mixture. This oscillation reveals an excess number of singlets, corresponding to antiferromagnetic spin correlations on neighboring sites. We fit the data with the damped sine functions such as

$$F(t) = -a \exp(-t/\tau) \cos(2\pi f t) + b, \tag{7.4.1}$$

where a, b, τ, f are fitting parameters. Along with the data of STO, we measure the total atom number in optical lattices without applying the PA light, N. We qualify this order by the normalized imbalance A and singlet fraction p_s

$$A = \frac{2a}{N}, \tag{7.4.2}$$

$$p_s = 1 - \frac{b-a}{N}, \tag{7.4.3}$$

We note that the extracted $N - b - a$ exactly corresponds to the actual atom number in the triplet state for SU(2) spins, but that is not the case for SU(4) spins because a coherent oscillation does not occur for the spin pairs of $(m_F = 1/2, m_F = -1/2)$ and $(5/2, -5/2)$.

To analyze the effect of spin degrees of freedom on the magnetic correlations, we measure the dependence of the singlet-triplet imbalance and singlet fraction on the entropy in the harmonic trap. Figure 7.4.3 shows the result for SU(2) and SU(4) spin mixture in a dimerized cubic lattice of $\left[s^{(x)}_{\mathrm{long}}, s^{(x)}_{\mathrm{short}}, s^{(y)}_{\mathrm{short}}, s^{(z)}_{\mathrm{short}}\right] = [20, 20.8, 48, 48]$. The Hubbard parameters are $U/h = 3.0$ kHz, $t_d/h = 1.0$ kHz, $t/h = 108$ Hz, and $t_{yz}/t = 1.31$, and the geometric mean of the trap frequency amounts to $\bar{\omega} = 2\pi \times 102.9$ Hz. The normalized STO amplitude and the absolute singlet fraction p_s reduce for larger entropies, as triplet states become thermally populated. A clear and striking difference between SU(4) and SU(2) spin mixtures is visible: the antiferromagnetic spin correlation is enhanced in the SU(4)-spin system compared to SU(2) for the same initial entropy. This behavior can be understood as follows. In the case of SU(2) spins in a dimer, the lowest-lying singlet state is limited to one configuration $(|\uparrow, \downarrow\rangle - |\downarrow, \uparrow\rangle)/\sqrt{2}$. The entropy of this singlet state is $\ln(W = 1)$=0, where W denotes the number of singlet configurations in a dimer. IN the SU(4)-spin system, the larger spin degrees of freedom increase W up to 6, which makes the entropy per site of the singlet states $\ln(W = 6)/2$. This means that the initial temperature require for spins to form the singlet is significantly reduced in the SU(4)

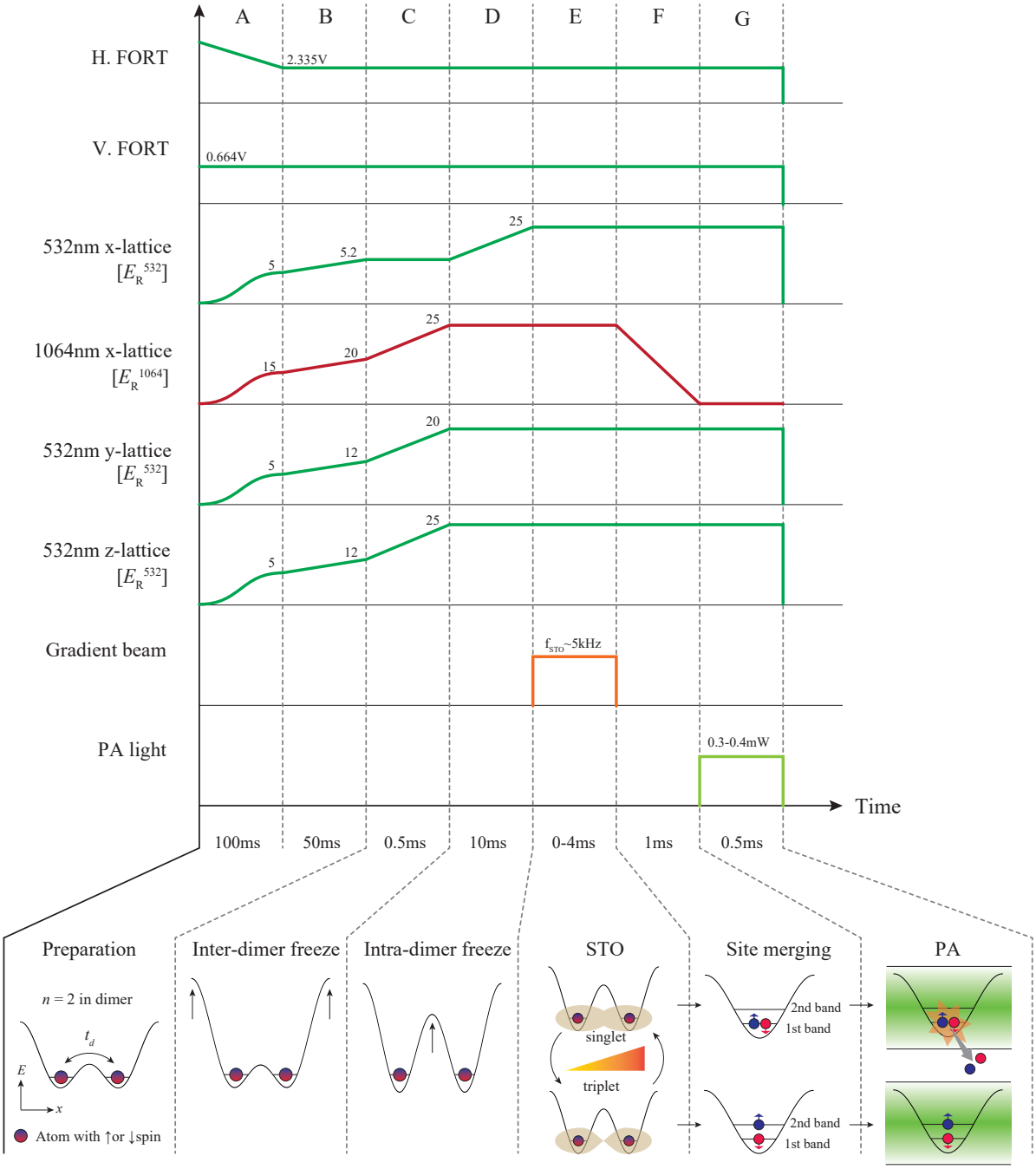

Figure 7.4.1: Typical time-sequence to observe STO in a dimerized lattice after evaporative cooling. Shown is the case of two spins (red and blue) per dimer. Depending on the STO time, the two spins form the double occupancy in the lowest band (top), or the state with one spin in the lowest band and the other in the first excited band (bottom) after merging the dimer. These states are distinguished by the PA technique.

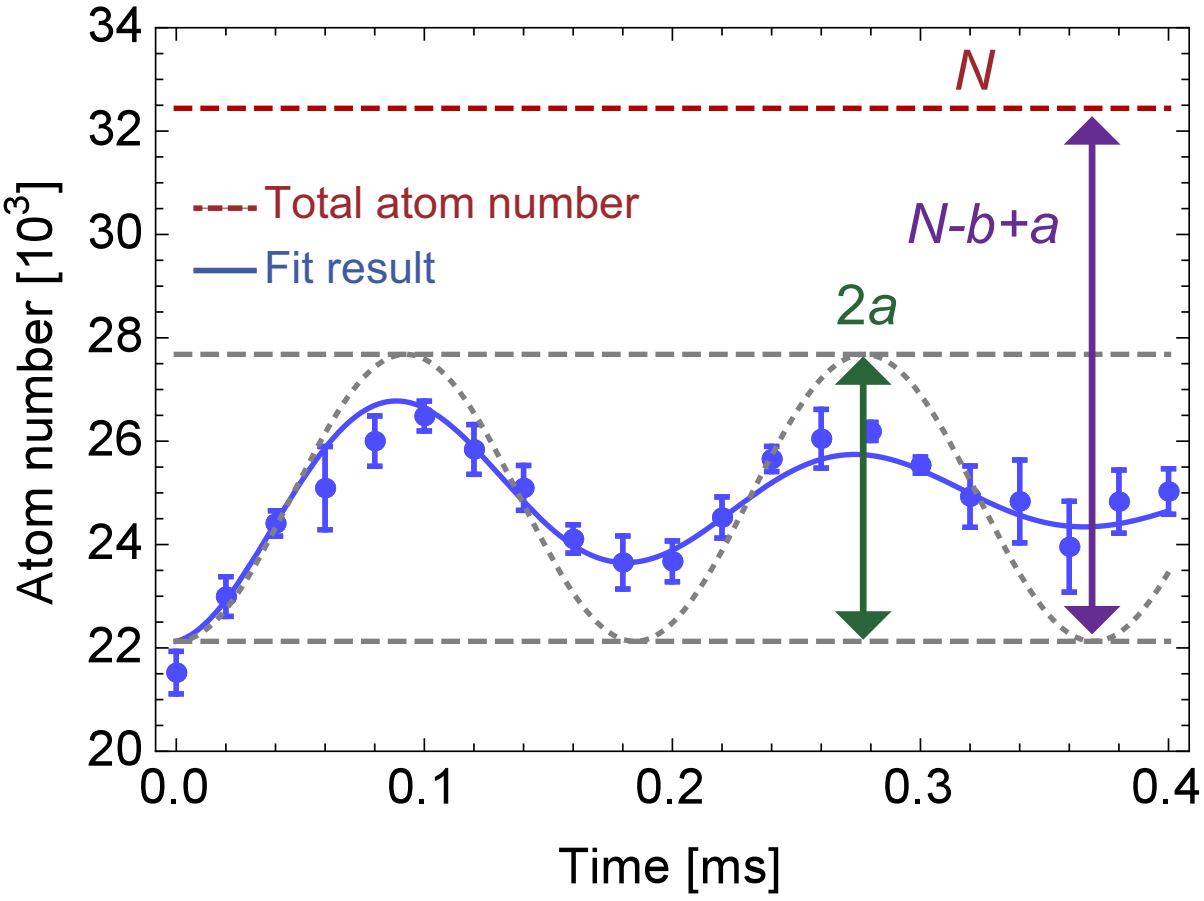

Figure 7.4.2: Singlet-triplet oscillation for SU(4) spins in a strongly dimerized lattice with $U/h = 3.02$ kHz, $t_d/h = 1.02$ kHz, $t/h = 38.0$ Hz, and $t_{yz}/t = 1.31$. The red dashed line represents the total atom number in the lattice without applying the PA. The blue solid line is the fit result with Eq.7.4.1. The gray dotted line is the STO signal assuming no damping. Error bars denote the standard deviation of four independent scans.

system. In other words, the large spin effectively cool down the system by absorbing entropy from motional degree of freedom, which is the same mechanism as Pomeranchuk cooling observed in the solid ^{3}He [120]. We note that in a trapped system, entropy is stored in a metallic state near the edge of the atomic cloud and a singlet state at the trap center survives for higher total entropy. This Pemeranchuk cooling method was already demonstrated in the SU(6) fermionic Mott-insulator, but no experimental study of this effect on the quantum magnetism was reported, which is clearly demonstrated in this work. Here we note that the data in Fig.7.4.3 (a) and (b), especially at low initial entropies, show the discrepancy with the theory. This indicates the existence of some heating effect, possibly caused by non-adiabaticity of the the lattice loading.

Finally, we investigate the dependence of the normalized STO amplitude on the intra-dimer tunneling t_d. Figure 7.4.4 shows the result with the SU(4) Fermi gas. The solid line is the theoretical curve shown only for $t_\mathrm{d}/t = 10$ and higher. Below this value the atomic limit calculation starts to be invalid. As the dimerization gets weaker, the excitation energy to the triplet state is lowered, and the STO amplitude decreases. Our experimental data show such a tendency and indicate the possibility that the nearest-neighbor antiferromagnetic correlation still remains slightly even in the isotropic cubic lattice. In terms of the entropy, the rough criterion for the onset of the nearest-neighbor spin correlation in the lattice is $s/k_\mathrm{B} = \ln(\mathcal{N})$ [121], which amounts to $\ln(\mathcal{N} = 4) = 1.38$ for the SU(4) system. Even though the average entropy in our trapped system is 1.9 in the Fig.7.4.4, the lower entropy is achieved at the trap center. The atoms around such a region are considered to contribute to the possible nearest-neighbor spin correlation in the isotropic lattice.

7.5 Conclusion and outlook

In conclusion, we have studied the important role of the spin degrees of freedom on the antiferromagnetic spin correlation in a strongly dimerized lattice by comparing the SU(2) and SU(4) systems. We observed the enhanced antiferromagnetic correlations in SU(4) due to the Pomeranchuk effect. Further cooling can be expected for a larger spin system such as SU(6), which ^{173}Yb intrinsically possesses, even though more than two frequencies arise in the STO. Another interesting direction for the experimental investigation is to develop a cooling method by engineering the shape of the confinement [36] or dynamically controlling the layered lattice potential [122].

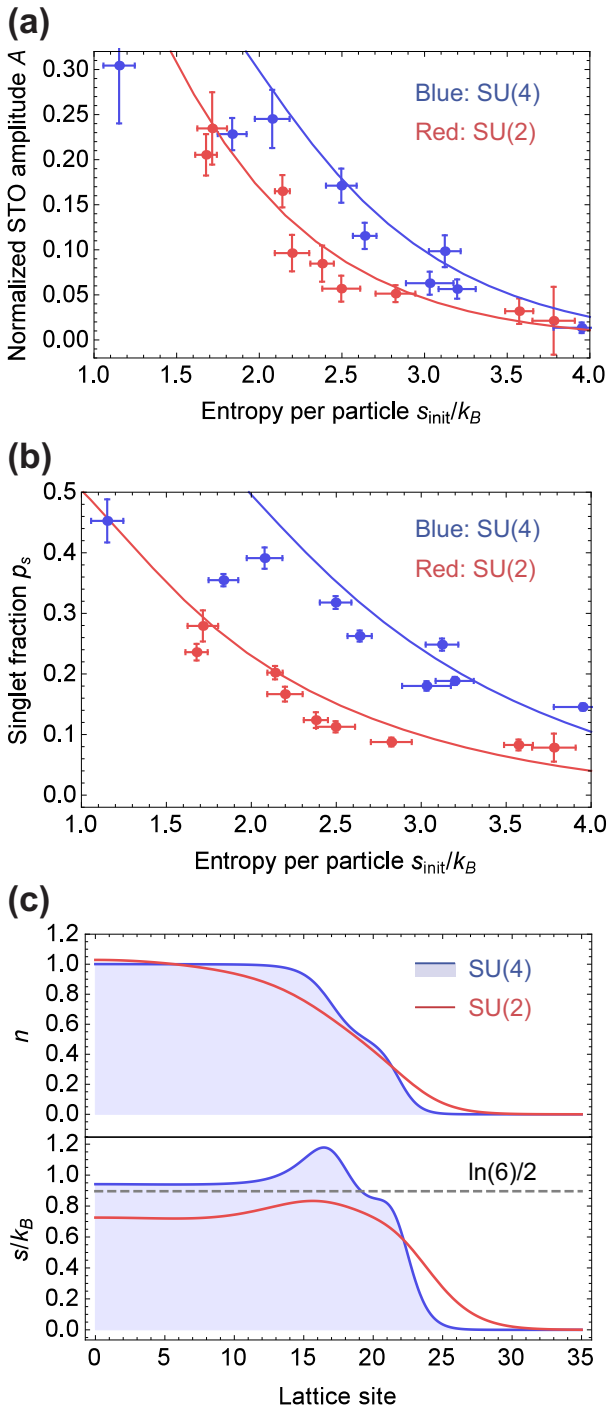

Figure 7.4.3: (a) Normalized STO amplitude and (b) singlet fraction of SU(2) and SU(4) Fermi gases in the strongly dimerized lattice. The dependence on the initial entropy in the harmonic trap is shown. The solid line is a theoretical curve that assumes adiabatic loading into the lattice. The vertical error bars include the fitting errors in the STO measurement and the standard deviation of the total atom number N. The horizontal error bars include the fitting errors. (c) Calculated density (top) and entropy distribution (bottom) at the initial entropy per particle $s_{\mathrm{init}}/k_{\mathrm{B}} = 1.5$ for SU(2) and SU(4) cases. The maximum singlet entropy per site ln(6)/2 for SU(4) is indicated by the gray dashed line.

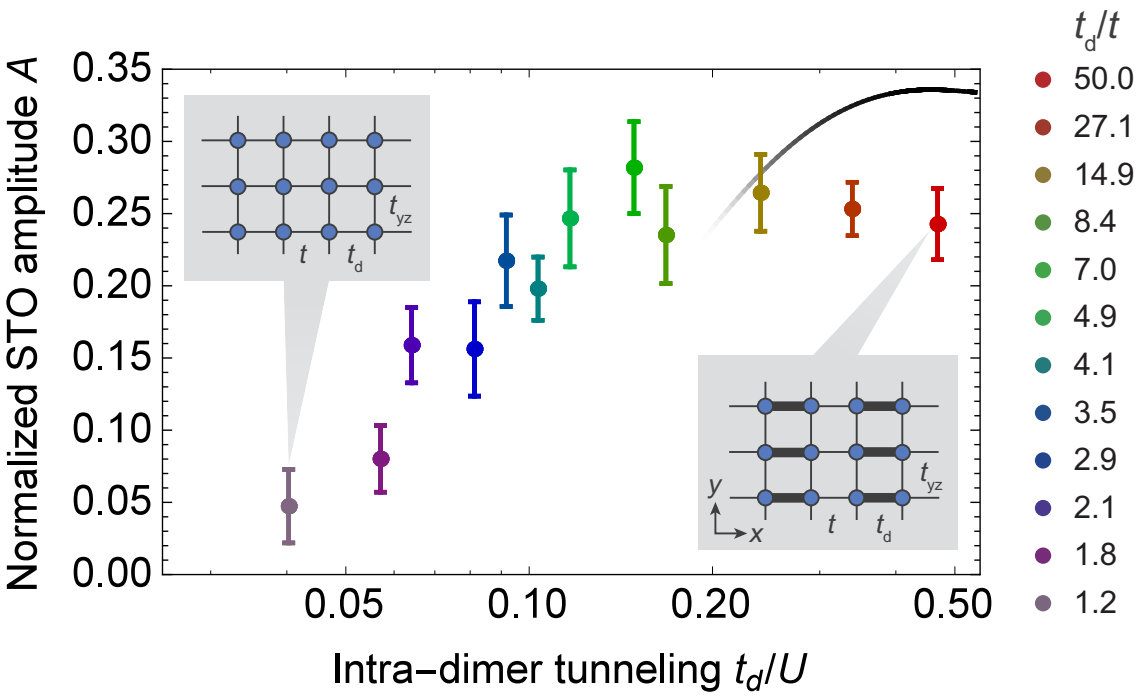

Figure 7.4.4: Normalized STO amplitude for the SU(4) Fermi gas versus the intra-dimer tunneling. The horizontal axis is shown in a logarithmic scale. The black solid curve is the prediction in the atomic limit for an entropy per particle of $s/k_{\mathrm{B}} = 1.9$ under the assumption of the adiabatic loading into the lattice, and is shown down to $t_{\mathrm{d}}/t = 10$. For the entire data, the on-site interaction is fixed to $U/h = 3.0$ kHz, while t changes form $t/h = 28.0$ Hz to 100 Hz, and t_{yz}/h form 1.7 to 1.0.

Chapter 8

Conclusion & Outlook

In this thesis, ultracold ytterbium atoms in an optical non-primitive lattice were studied. We briefly review the achievement of the work in this thesis.

- *Direct observation of a localized state in a flat band.* We succeeded in developing the phase imprinting method, which enables a coherent transportation of a BEC to the flat band of an optical Lieb lattice. Along with the inter-band dynamics of the BEC in the band, we observed the real-space dynamics of a BEC in the lattice by using the site-mapping technique. This measurement clearly shows the formation of a localized state in the flat band.

- *Measuring the interaction effect on the band structure of an optical Lieb lattice.* We performed the momentum-resolved measurement of the lowest three Bloch bands of an optical Lieb lattice for a weakly interacting BEC. Our important finding is that the second band, which should be flat in single-particle limit, is shifted and in particular distorted around the Brillouin zone edge as the interaction strength increases.

- *Demonstration of a spatial adiabatic passage in a Lieb lattice.* We reveal that a Lieb lattice system has a remarkable analogy to a three-level system with Λ-type transition. By making use of analogy and dynamical controllability of our optical Lieb lattice, we realized the spatial adiabatic passage of massive particles for the first time. This method can be used to transfer atoms into the flat band, apart from the phase imprinting method.

- *Probing the large-spin effect on the short-range quantum magnetism of a Fermi gas in a dimerized lattice.* We invented an optical pumping technique to create a balanced four-spin mixture of ^{173}Yb. By loading the four-spin mixture in a strongly dimerized optical lattice, we investigated the large-spin effect on the quantum magnetism within the dimer. Our important finding is that the antiferromagnetic order is enhanced in SU(4) compared to SU(2) as a consequence of Pomeranchuk cooling effect.

Outlook

Below, we present possible directions of the experiments with non-standard optical lattice.

Lowest-lying flat band It would be theoretically interesting to investigate in which quasimomentum a Bose gas condensate in a flat band. Although we developed methods to transfer atoms into a flat band in a Lieb lattice, further experimental study is hampered by a relatively short lifetime of atoms in the band. It would be convenient if a flat band lies at the lowest band. Lattice shaking enables engineering the band structure, as it can change the tunneling amplitude including the sign. In the kagome lattice and saw-tooth lattice, we can prepare the lowest-lying flat band by applying the lattice shaking and changing the sing of tunneling amplitude.

In a single-particle description, eigenstate of the flat band is localized at specific sublattices. On the other hand, with a strong inter-particle interaction, the flat band is distorted, and has a finite dispersion. As a result, a bose gas condensates in the lowest energy point. Furthermore, in the intermediate interaction strength, it is theoretically predicted that the novel supersolid phase, where a superfluid order and crystalline order coexist, appears. Ultracold bosonic atoms in optical lattices with the lowest lying flat band is one of the promising candidates to investigate above scenario. The supersolid phase would show a characteristic interference pattern according the density wave whose periodicity is longer than the lattice constant, which can be detected by TOF measurement. The combination with a quantum gas microscope would enable us to draw a precise phase diagram, as we could investigate the possibility of phase separation due to the harmonic confinement.

Journal Articles

Below is the list of journal articles to which I contributed during this course.

- *Antiferromagnetic spin correlation of SU($\mathcal{N}$) Fermi gas in an optical dimerized lattice.*
  H. Ozawa, S. Taie, Y. Takasu, and Y. Takahashi
  arXiv:1801.05962 (2018)

- *Spatial Adiabatic Passage of Massive Quantum Particles.*
  S. Taie, T. Ichinose, H. Ozawa, and Y. Takahashi
  arXiv:1708.01100 (2017)

- *Interaction-Driven Shift and Distortion of a Flat Band in an Optical Lieb Lattice.*
  H. Ozawa, S. Taie, T. Ichinose, and Y. Takahashi
  Phys. Rev. Lett. **118**, 175301 (2017)

- *Topological Thouless pumping of ultracold fermions.*
  S. Nakajima, T. Tomita, S. Taie, T. Ichinose, H. Ozawa, L. Wang, M. Troyer, and Y. Takahashi
  Nature Phys. **12**, 296 (2016)

- *Coherent driving and freezing of bosonic matter wave in an optical Lieb lattice.*
  S. Taie, H. Ozawa, T. Ichinose, T. Nishio, S. Nakajima, and Y. Takahashi
  Science Adv. **1**, e1500854 (2015)

Appendix A

Trap geometry

In this appendix, the detailed trap geometry of the crossed FORT and the optical lattice are presented.

A.1 Dipole force trap

First of all, we overview the basics of the Dipole Force Trap (DFT). For large detuning and small intensity compared with the saturation intensity, the dipole potential and photon scattering rate can be written as

$$V(\mathbf{r}) = -\frac{3\pi c^2}{2}\sum_\beta \frac{\Gamma_\beta}{\omega_\beta^3}\left(\frac{1}{\omega_\beta-\omega}+\frac{1}{\omega_\beta+\omega}\right) I(\mathbf{r}) \tag{A.1.1}$$

$$\simeq \frac{3\pi c^2}{2}\sum_\beta \frac{\Gamma_\beta}{\omega_\beta^3\delta_\beta} I(\mathbf{r}) \quad \text{if } |\delta_\beta| \ll \omega_\beta, \tag{A.1.2}$$

$$\gamma_{\rm sc}(\mathbf{r}) = \frac{3\pi c^2\omega^3}{2\hbar}\sum_\beta \left[\frac{\Gamma_\beta}{\omega_\beta^3}\left(\frac{1}{\omega-\omega_\beta}+\frac{1}{\omega+\omega_\beta}\right)\right]^2 I(\mathbf{r}) \tag{A.1.3}$$

$$\simeq \frac{3\pi c^2}{2\hbar}\sum_\beta \frac{\Gamma_\beta^2}{\omega_\beta^3\delta_\beta^2} I(\mathbf{r}) \quad \text{if } |\delta_\beta| \ll \omega_\beta, \tag{A.1.4}$$

respectively. Here, ω is the frequncy of the laser, β is the index for summation over the possible transitions, Γ_β and ω_β are the line width and frequency for each transition, respectively. When estimating the dipole potential and photon scattering rate for an atom in $^1S_0$ state with a 532 nm or 556 nm light, we conventionally take into account the $^1S_0 \leftrightarrow {}^1P_1$ and $^1S_0 \leftrightarrow {}^3P_1$ transitions.
The shape of a dipole force trap is determined by the following intensity distribution for a Gaussian beam:

$$I(\mathbf{r}) = \frac{2P}{\pi w(z)^2}\exp\left(-\frac{2\rho^2}{w(z)^2}\right), \tag{A.1.5}$$

$$w(z) = w_0\sqrt{1+\left(\frac{z}{z_R}\right)^2}, \tag{A.1.6}$$

$$z_{\rm R} = \frac{\pi w_0^2}{\lambda}, \tag{A.1.7}$$

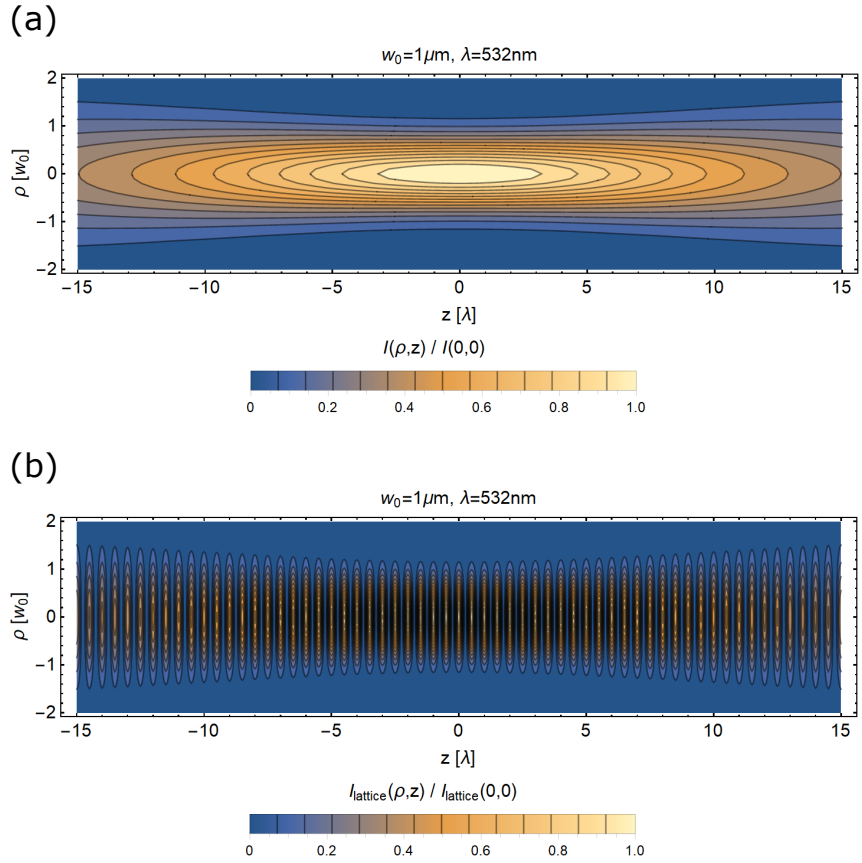

Figure A.1.1: Intensity distribution of (a) DFT and (b) otpical lattice with a Gaussian shape. Here, the beam waist and wave length of the laser beam is set to $w_0 = 1$ μm and $\lambda = 532$ nm, respectively.

where w_0 is the beam waist, λ is the wave length, P is the input power of the laser beam, and the beam is assumed to propagate along the z-axis. z_{R} is so-called Rayleigh length.

Optical lattice

An optical lattice is made by interference of two counter-propagating Gaussian beams. The intensity distribution is given by

$$I_{\mathrm{lattice}}(\mathbf{r}) = \frac{2P}{\pi w(z)^2} \exp\left(-\frac{2\rho^2}{w(z)^2}\right) 2\left[1 + \cos(2kz)\right], \tag{A.1.8}$$

where k is the wave number $k = 2\pi/\lambda$. Figure A.1.1 shows the intensity distribution calculated from Eq.A.1.5 and A.1.8.

A.2 Trap frequency

In the cold atom experiments, the inhomogeneity of the trap potential has a large influence on the result. Therefore, the trap frequency is a particularly important parameter. In

this section, we introduce some formulas for the trap frequency in the DFT and optical lattice, and the experimental method to measure the trap frequency is described.

A.2.1 FORT

The trap frequencies for atoms in a single DFT can be obtained by expanding Eq.A.1.1 around the origin:

$$V(\mathbf{r}) \simeq V(0)\left(1-\frac{2\rho^2}{w_0^2}-\frac{z^2}{z_{\mathrm{R}}^2}\right) = V(0)+\frac{1}{2}m(\omega_\rho^2\rho^2+\omega_z^2 z^2), \tag{A.2.1}$$

$$\omega_\rho = \sqrt{\frac{4|V(0)|}{mw_0^2}} \tag{A.2.2}$$

$$\omega_z = \sqrt{\frac{2|V(0)|}{mz_{\mathrm{R}}^2}}. \tag{A.2.3}$$

Since a typical value of the beam waist w_0 is on the order of 10 μm, the axial frequency ω_ρ is much smaller than the radial one as can be seen from Fig.A.1.1(a).

Trap frequency measurement in the crossed FORT

In principle, we can obtain the trap frequencies of the FORT using the Eq.A.2.2 and A.2.3 if the beam waist is known. However, the precise beam waist in the metallic chamber is difficult to measure. In addition, the trap potential could be distorted by gravity and possible misalignment of the crossed FORT. Therefore we should directly measure the the trap frequencies.

As a method, we use the dipole oscillations of a BEC of ^{174}Yb in the cross FORT. Dipole oscillation is merely the center-of-mass oscillation of the cloud and its frequency corresponds to the trap frequency along the direction of the oscillation. To induce the dipole oscillation, we need to displace the atomic cloud. The method for the displacement depends on the directions of oscillations. For the vertical direction (z-axis), we suddenly change the depth of the horizontal FORT by a few % of the original potential. This changes the gravitational sag of the trap center, and kicks the atoms along the vertical direction. Since our imaging system does not have enough resolution for observing *in situ* oscillations, we measure the position of the cloud 14 ms after the release from the trap. For the horizontal directions (x, y), the procedure to induce dipole oscillations is more complicated. We slightly shift the position of the vertical lattice beam away from the trap center. Then we gradually ramp up the lattice beam without retroreflection, which displaces the center-of-mass of the cloud. Finally we suddenly turn off the lattice beam, and the cloud starts to oscillate.

Figure A.2.1 shows the summary for measured trap frequencies in the crossed FORT.

(a)

H. FORT		V. FORT		ω / 2π [Hz]						
CTRL [V]	Power [mW]	CTRL [V]	Power [mW]	H. FORT radial	Error (2σ)	H.FORT axial	Error (2σ)	Vertical	Error (2σ)	Geometric mean
2.27	45.8	0.664	528.8	-	-	24.631	0.351	106.582	2.676	-
2.3	46.9	0.664	528.8	149.31	0.826	24.631	0.351	112.976	3.042	74.62
2.33	48	0.664	528.8	153.961	1.024	24.631	0.351	127.94	1.449	78.578
2.36	49	0.664	528.8	154.147	0.807	24.631	0.351	137.402	1.637	80.501
2.4	50.6	0.664	528.8	160.383	0.61	24.631	0.351	155.318	0.983	84.974
2.44	52.1	0.664	528.8	162.051	0.736	24.631	0.351	170.444	0.93	87.951
2.3	46.9	0.4	329.2	148.463	1.325	18.258	0.558	112.976	3.042	67.404
2.3	46.9	0.9	715.8	156.31	2.282	29.24	0.299	112.976	3.042	80.226

(b)

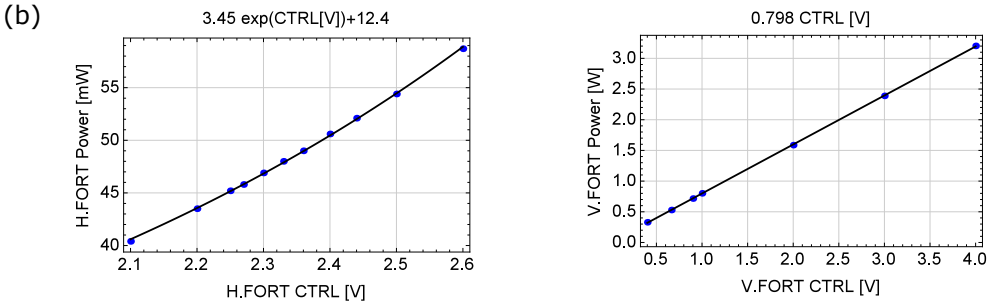

(c)

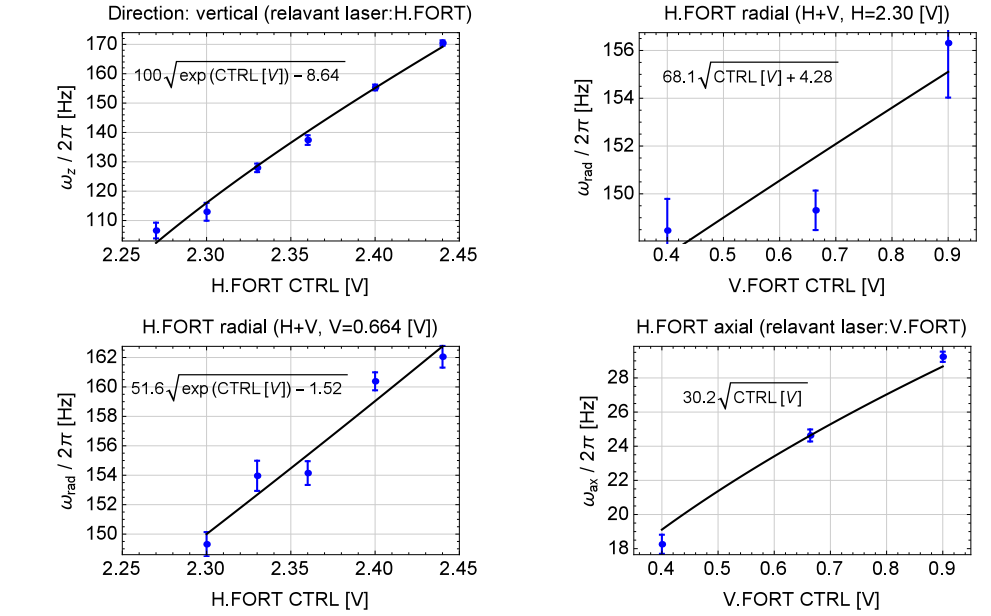

Figure A.2.1: (a) Table of the measured trap frequency in FORT. (b) FORT power versus control voltage. To monitor the horizontal FORT power, we use a logarithmic-response photo-diode with which we can earn the dynamic range. Therefore, the fitting is made with an exponential function in the case of the horizontal FORT. (c) Plots of the measured trap frequency. The black solid line is the fitting to the data, the result of which is shown in each figure.

A.2.2 Optical lattice

The trap frequencies for an optical lattice can be obtained in the same way for DFT. From Eq.A.1.8,

$$\begin{aligned} V_{\text{lattice}}(\mathbf{r}) &\simeq V_{\text{lattice}}(0)\left[1-\frac{2\rho^2}{w_0^2}-\left(\frac{1}{z_{\text{R}}^2}+k^2\right)z^2\right] \\ &= V_{\text{lattice}}(0)+\frac{1}{2}m\left(\omega_{\text{lattice},\rho}^2\rho^2+\omega_{\text{lattice},z}^2z^2\right), \qquad \text{(A.2.4)} \\ \omega_{\text{lattice},\rho} &= \sqrt{\frac{4|V_{\text{lattice}}(0)|}{mw_0^2}} \qquad \text{(A.2.5)} \\ \omega_{\text{lattice},z} &= \sqrt{\frac{2k^2|V_{\text{lattice}}(0)|}{m}} \qquad \text{(A.2.6)} \end{aligned}$$

Lattice beam waist measurement

The beam waist of an optical lattice can be evaluated from Eq.A.2.5 if the radial trap frequency at a certain lattice depth is known. We can measure the lattice depth by a lattice calibration method as described in the section 3.5.1. In principle, the radial trap frequency of an optical lattice can be measured in the same as for the crossed FORT. However, since the beam waist of our optical lattices is as large as 100 μm to suppress the inhomogeneity, it is difficult only with the optical lattice except the z-lattice to earn a trap depth enough for supporting Yb atoms against the gravitational sag. Therefore, the procedure is more complicated than for the crossed FORT.
Figure A.2.2 summarizes the procedure to measure the radial trap frequencies of optical lattices. Below, we describe each sequence:

(a) First, we gradually ramp up the 532 nm z-lattice to support atoms. At the same time, we ramp up the xy-lattice of interest. Finally, we suddenly turn off the crossed FORT to displace the cloud, and observe the dipole oscillation along z-axis, where the axial trap frequency of 532nm z-lattice is so small that the oscillation frequency is determined by the radial trap of xy-lattice.

(b) As for the 532 nm z-lattice, we turn off the crossed FORT after ramping up the lattice up to $20E_R$, which is deep enough to support atoms.

(c) Since the 1064 nm z-lattice is not able to trap the atoms only with itself, we keep the horizontal FORT and observe the dipole oscillation along the axial direction of the horizontal FORT in the z-axis imaging.

(d) Only with the z-beam for the diagonal lattice, it is difficult to displace the atomic cloud. Therefore, we ramp up the 532 nm z-lattice for displacement along the axial direction of the horizontal FORT.

Table A.2.1 shows the beam waist of our optical lattices by using the results of trap frequency measurement and Eq.A.2.5. With this table, we can evaluate the radial trap frequency for the arbitrary lattice depth.

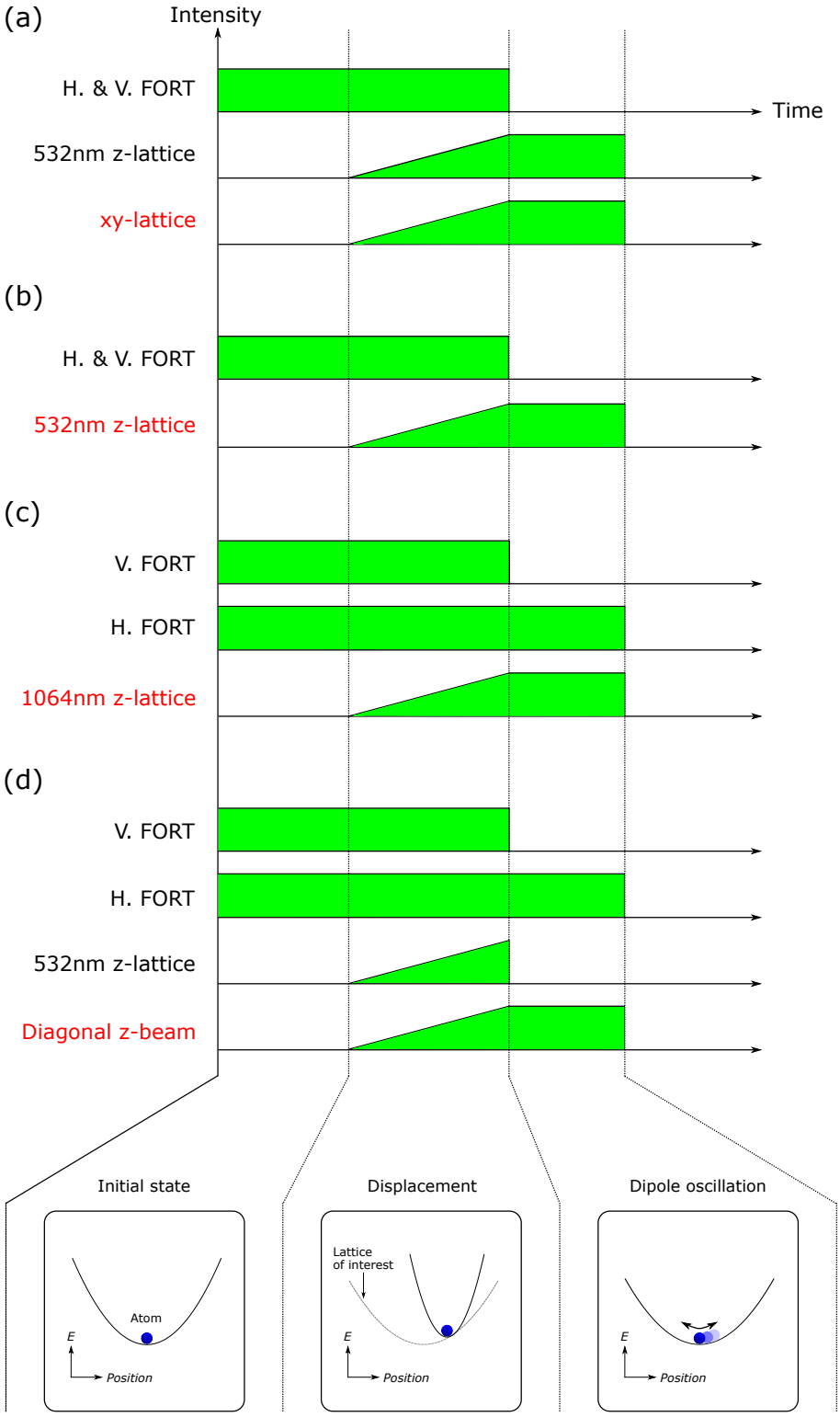

Figure A.2.2: Experimental sequence to measure the radial trap frequency for (a) 532 nm xy-lattice, 1064 nm x-lattice, and x-beam of diagonal lattice, (b) 532 nm z-lattice, (c) 1064 nm z-lattice, and (d) z-beam of diagonal lattice, respectively. The lowest figures show the atom position in a trap at each stage.

Table A.2.1: Measured beam waist of each lattice beam in the unit of μm. Note that $\omega_{0,x(z)}^{\mathrm{diagonal}}$ is the beam waist of one of two lasers creating the diagonal lattice.

$w_{0,x}^{\mathrm{short}}$	$w_{0,y}^{\mathrm{short}}$	$w_{0,z}^{\mathrm{short}}$	$w_{0,x}^{\mathrm{long}}$	$w_{0,z}^{\mathrm{long}}$	$w_{0,x}^{\mathrm{diagonal}}$	$w_{0,z}^{\mathrm{diagonal}}$
106.4	99.3	121.5	112.3	128.1	122.4	167.5

A.2.3 Trap frequency for a combined optical trap

In the experiment, we ramp up the optical lattices on an atomic cloud in FORT. Since Yb is heavy, the gravitational sag is large, and it is difficult to support Yb only with the optical lattice potential. Therefore, the FORT and optical lattice coexist.
In this case, the total optical potential in the harmonic approximation is given by

$$V_{\mathrm{trap}}(\mathbf{r}) = \frac{1}{2}m\left[\sum_{k=1}^{3}\omega_{H,k}^2(\mathbf{r}\cdot\mathbf{e}_{H,k})^2 + \sum_{k=1}^{3}\omega_{V,k}^2(\mathbf{r}\cdot\mathbf{e}_{V,k})^2 + \sum_{k=1}^{3}\omega_{L,k}^2(\mathbf{r}\cdot\mathbf{e}_{L,k})^2\right], \quad \text{(A.2.7)}$$

where $\omega_{X,k}$ $(X = H, V, L)$ is the trap frequency of the horizontal FORT (H), the vertical FORT (V), and the optical lattice (L). The subscript k represents the three principal axes of each trap, whose directions are indicated by the unit vectors $\mathbf{e}_{X,k}$. For an arbitrary basis $\{\mathbf{e}\}_{i=1}^{3}$, V_{trap} can be written as

$$V_{\mathrm{trap}}(\mathbf{r}) = \frac{1}{2}m\mathcal{V}_{ij}r_i r_j, \quad \text{(A.2.8)}$$

$$\mathcal{V}_{ij} = \mathbf{e}_i\cdot\left[\sum_{k=1}^{3}\omega_{H,k}^2\mathbf{e}_{H,k}\mathbf{e}_{H,k} + \sum_{k=1}^{3}\omega_{V,k}^2\mathbf{e}_{V,k}\mathbf{e}_{V,k} + \sum_{k=1}^{3}\omega_{L,k}^2\mathbf{e}_{L,k}\mathbf{e}_{L,k}\right]\cdot\mathbf{e}_j \quad \text{(A.2.9)}$$

where $\mathbf{a}\cdot\mathbf{bc}\cdot\mathbf{d} = (\mathbf{a}\cdot\mathbf{b})(\mathbf{c}\cdot\mathbf{d})$. By diagonalizing the matrix $\mathcal{V} = \{\mathcal{V}_{ij}\}$, we can obtain the trap frequencies $\{\omega_k\}$ of the total potential V_{trap} as the square root of the resulting eigenvalues. Here, we choose the lattice axes $\{\mathbf{e}_{L,k}\}$ as the basis. Since our horizontal FORT is slanted 45° in xy-plane of the lattice axes, the unit vectors for the horizontal and vertical FORT are represented as

$$\mathbf{e}_{H,1} = \frac{1}{\sqrt{2}}\begin{pmatrix}1\\-1\\0\end{pmatrix},\ \mathbf{e}_{H,2} = \begin{pmatrix}0\\0\\1\end{pmatrix}, \quad \text{(A.2.10)}$$

$$\mathbf{e}_{V,1} = \frac{1}{\sqrt{2}}\begin{pmatrix}1\\-1\\0\end{pmatrix},\ \mathbf{e}_{V,2} = \frac{1}{\sqrt{2}}\begin{pmatrix}1\\1\\0\end{pmatrix}. \quad \text{(A.2.11)}$$

Here, $\mathbf{e}_{H,3}$ and $\mathbf{e}_{V,3}$ are omitted since the corresponding axial trap frequencies are negligibly small compared to the radial ones.

As a result, the matrix form of $\mathcal{V}$ becomes

$$\mathcal{V} = \mathcal{V}^{(H)} + \mathcal{V}^{(V)} + \mathcal{V}^{(L)}, \tag{A.2.12}$$

$$\mathcal{V}^{(H)} = \begin{pmatrix} \frac{1}{2}\omega_{H,1}^2 & -\frac{1}{2}\omega_{H,1}^2 & 0 \\ -\frac{1}{2}\omega_{H,1}^2 & \frac{1}{2}\omega_{H,1}^2 & 0 \\ 0 & 0 & \omega_{H,2}^2 \end{pmatrix}, \tag{A.2.13}$$

$$\mathcal{V}^{(V)} = \begin{pmatrix} \frac{1}{2}(\omega_{V,1}^2 + \omega_{V,2}^2) & \frac{1}{2}(-\omega_{V,1}^2 + \omega_{V,2}^2) & 0 \\ \frac{1}{2}(-\omega_{V,1}^2 + \omega_{V,2}^2) & \frac{1}{2}(\omega_{V,1}^2 + \omega_{V,2}^2) & 0 \\ 0 & 0 & 0 \end{pmatrix}, \tag{A.2.14}$$

$$\mathcal{V}^{(L)} = \mathcal{V}_{\text{short}} + \mathcal{V}_{\text{long}} + \mathcal{V}_{\text{diag}}, \tag{A.2.15}$$

$$\mathcal{V}_{\text{short}} = \begin{pmatrix} \omega_{\text{short},y}^2 + \omega_{\text{short},z}^2 & 0 & 0 \\ 0 & \omega_{\text{short},z}^2 + \omega_{\text{short},x}^2 & 0 \\ 0 & 0 & \omega_{\text{short},x}^2 + \omega_{\text{short},y}^2 \end{pmatrix}, \tag{A.2.16}$$

$$\mathcal{V}_{\text{long}} = \begin{pmatrix} \omega_{\text{long},z}^2 & 0 & 0 \\ 0 & \omega_{\text{long},z}^2 + \omega_{\text{long},x}^2 & 0 \\ 0 & 0 & \omega_{\text{long},x}^2 \end{pmatrix}, \tag{A.2.17}$$

$$\mathcal{V}_{\text{diag}} = \begin{pmatrix} \omega_{\text{diag},z}^2 & 0 & 0 \\ 0 & \omega_{\text{diag},x}^2 + \omega_{\text{diag},z}^2 & 0 \\ 0 & 0 & \omega_{\text{diag},x}^2 \end{pmatrix}, \tag{A.2.18}$$

where $\{\omega_{\mathrm{X},i}\}$ $(\mathrm{X} = \text{short}, \text{long}, \text{diag} \quad i = x, y, z)$ are the radial trap frequencies of each lattice beam given by Eq.A.2.5 and the table A.2.1. Therefore, once the optical lattice depth is given, the resulting radial trap frequency of the lattice can be calculated. As for the FORT, figure A.2.1 shows the trap frequencies in the direction of the H.FORT radial, axial, and the V.FORT. Here, they correspond to

$$\omega_{H.FORT\ \text{radial}}^2 = \omega_{H,1}^2 + \omega_{V,1}^2, \tag{A.2.19}$$

$$\omega_{H.FORT\ \text{axial}}^2 = \omega_{V,2}^2, \tag{A.2.20}$$

$$\omega_{\text{vertical}}^2 = \omega_{H,2}^2, \tag{A.2.21}$$

respectively. From the above relations, $\mathcal{V}^{(H)} + \mathcal{V}^{(V)}$ can be known.
For typical parameters, $(\omega_{H.FORT\ \text{radial}}, \omega_{H.FORT\ \text{axial}}, \omega_{\text{vertial}})/2\pi = (146, 22.5, 124)$ Hz and $(\{s_x^{\text{short}}, s_y^{\text{short}}, s_z^{\text{short}}\}, \{s_x^{\text{long}}, s_z^{\text{long}}\}, s^{\text{diag}}) = (\{13, 13, 13\}, \{13, 13\}, 15.5)$, the trap frequencies amount to $(\omega_1, \omega_2, \omega_3)/2\pi = (152, 130, 47.5)$ Hz and the geometric mean is $\bar{\omega}/2\pi = 98.1$ Hz.

Appendix B

Mean velocity in a periodic potential

In this appendix, we introduce the expressions for the mean velocity of a particle in a periodic potential, based on the perturbation theory. We also consider the case with the influence of the external field except the periodic potential.

B.1 The case without external field

Here, we prove that the differential coefficient of the band dispersion corresponds to the mean velocity of a particle [94].

The differential coefficients $\frac{\partial \epsilon_n(\mathbf{k})}{\partial k_i}$ ($i = x, y, z$ n : band index $\mathbf{k}$: momentum) can be achieved as the 1st-order expansion coefficients of the band dispersion ϵ_n around $\mathbf{k}$:

$$\epsilon_n(\mathbf{k}+\mathbf{q}) = \epsilon_n(\mathbf{k}) + \sum_{i=x,y,z} \frac{\partial \epsilon_n(\mathbf{k})}{\partial k_i} q_i + O\left(q^2\right). \tag{B.1.1}$$

Using a periodic function $|u_n(\mathbf{k})\rangle$, the eigenstate of a single-particle Hamiltonian in the periodic potential can be expressed as

$$|\psi_n(\mathbf{k})\rangle = \mathrm{e}^{i\mathbf{k}\cdot\mathbf{r}} |u_n(\mathbf{k})\rangle \tag{B.1.2}$$

$|u_n(\mathbf{k})\rangle$ satisfies the equation

$$\begin{aligned} H(\mathbf{k})|u_n(\mathbf{k})\rangle &= \left[\frac{\hbar^2}{2m}\left(\frac{1}{i}\nabla + \mathbf{k}\right)^2 + V(\mathbf{r})\right]|u_n(\mathbf{k})\rangle \\ &= \epsilon_n(\mathbf{k})|u_n(\mathbf{k})\rangle, \end{aligned} \tag{B.1.3}$$

where $V(\mathbf{r})$ is the periodic potential. From the definition of the Hamiltonian,

$$H(\mathbf{k}+\mathbf{q}) = H(\mathbf{k}) + \frac{\hbar^2}{m}\mathbf{q}\cdot\left(\frac{1}{i}\nabla + \mathbf{k}\right) + \frac{\hbar^2}{2m}q^2. \tag{B.1.4}$$

Regarding the 2nd term as perturbation, we get $\frac{\partial \epsilon_n(\mathbf{k})}{\partial \mathbf{k}}$. According to the perturbation theory, the eigenvalue ϵ_n for $H = H_0 + H_1$, where H_1 is the perturbation term, can be written as

$$\epsilon_n = \epsilon_n^0 + \langle\psi_n| H_1 |\psi_n\rangle + \cdots, \tag{B.1.5}$$

where ϵ_n^0 and $|\psi_n\rangle$ satisfy $H_0 |\psi_n\rangle = \epsilon_n^0 |\psi_n\rangle$. Therefore, taking into consideration the 1st order of the perturbation, the eigenvalue is

$$\epsilon_n (\mathbf{k}+\mathbf{q}) = \epsilon_n (\mathbf{k}) + \langle u_n (\mathbf{k})| \sum_j \frac{\hbar^2}{m} \left(\frac{1}{i}\nabla + \mathbf{k}\right)_j q_j |u_n (\mathbf{k})\rangle + \cdots . \tag{B.1.6}$$

Comparing with the Eq.B.1.1, we get

$$\frac{\partial \epsilon_n (\mathbf{k})}{\partial \mathbf{k}} = \langle u_n (\mathbf{k})| \frac{\hbar^2}{m} \left(\frac{1}{i}\nabla + \mathbf{k}\right) |u_n (\mathbf{k})\rangle . \tag{B.1.7}$$

Since the Bloch function is $|\psi_n (\mathbf{k})\rangle = \mathrm{e}^{i\mathbf{k}\cdot\mathbf{r}} |u_n (\mathbf{k})\rangle$, Eq.B.1.7 can be expressed as

$$\frac{\partial \epsilon_n (\mathbf{k})}{\partial \mathbf{k}} = \frac{\hbar^2}{m} \langle \psi_n (\mathbf{k})| \frac{1}{i}\nabla |\psi_n (\mathbf{k})\rangle . \tag{B.1.8}$$

Since $\frac{1}{m}\frac{\hbar}{i}\nabla$ is the velocity operator [1] , Eq.B.1.8 means that the band dispersion $\frac{\partial \epsilon_n (\mathbf{k})}{\partial \mathbf{k}}$ corresponds to the mean velocity of a particle in an energy level $n, \mathbf{k}$.

B.2 The case with external field

In this section, we consider the case where a certain parameter, a momentum for example, is adiabatically changing due to an external field, and introduce the expression for the mean velocity of a particle under such a circumstance.

B.2.1 Adiabatic evolution [1]

We assume that the Hamiltonian $H[\mathbf{R}(t)]$ is dependent on a certain parameter $\mathbf{R}(t)$ in the system, and the parameter $\mathbf{R}(t)$ is adiabatically changing. Time evolution of the state obeys the Schrödinger equation:

$$i\hbar \frac{d}{dt} |\psi(t)\rangle = H(t) |\psi(t)\rangle . \tag{B.2.1}$$

We expand the state$|\psi(t)\rangle$ in terms of the eigenvector $|n(t)\rangle$ of $H(t)$:

$$|\psi(t)\rangle = \sum_n \exp\left(-\frac{i}{\hbar}\int_0^t dt'\, E_n (t')\right) a_n(t) |n(t)\rangle . \tag{B.2.2}$$

Since $|\psi(t)\rangle$ satisfies the Schrödinger equation, the expansion coefficient $a_n(t)$ satisfies

$$\dot{a}_n(t) = -\sum_l a_l(t) \langle n(t)| \frac{d}{dt} |l(t)\rangle \times \exp\left(-\frac{i}{\hbar}\int_0^t dt'\, [E_l(t') - E_n(t')]\right) . \tag{B.2.3}$$

[1] The velocity operator is defined as

$$\mathbf{v} = \dot{\mathbf{r}} = \frac{i}{\hbar}[H, \mathbf{r}] = \frac{\mathbf{p}}{m} = \frac{\hbar\nabla}{im}. \tag{B.1.9}$$

In order to make the calculation simple, we impose the following assumption (parallel transport) on the eigenstate $|n(t)\rangle$ in a energy level n of the instantaneous Hamiltonian:

$$\langle n(t)| \frac{d}{dt} |n(t)\rangle = \dot{\mathbf{R}}(t) \langle n(t)| \frac{\partial}{\partial \mathbf{R}} |n(t)\rangle = 0 \text{ for } {}^{\exists}n. \tag{B.2.4}$$

Taking into consideration up to the 0th-order in terms of the time differentiation, namely in the limit of $\dot{\mathbf{R}} \to 0$,

$$\dot{a}_n(t) = 0 \text{ for } {}^{\forall}n. \tag{B.2.5}$$

This means that the state keep staying in the n-th energy level if the initial state is in the n-th energy level $|n\rangle$, which is so-called the "Quantum Adiabatic Theorem".

Below, we deal with up to the 1st order in terms of the time differentiation. As an initial state, we choose $a_n(0) = 1,\ a_m = 0$ for $m \neq n$. The formal integration of Eq.B.2.3 reads

$$\begin{aligned} a_n(t) &= 1 - \int_0^t dt' \sum_l a_l(t') \langle n(t')| \frac{d}{dt'} |l(t')\rangle \\ &\quad \times \exp\left(-\frac{i}{\hbar} \int_0^{t'} dt'' \ [E_l(t'') - E_n(t'')] \right) \end{aligned} \tag{B.2.6}$$

$$\begin{aligned} a_m(t) &= -\int_0^t dt' \sum_l a_l(t') \langle m(t')| \frac{d}{dt'} |l(t')\rangle \\ &\quad \times \exp\left(-\frac{i}{\hbar} \int_0^{t'} dt'' \ [E_l(t'') - E_m(t'')] \right) \text{ for } m \neq n. \end{aligned} \tag{B.2.7}$$

We successively substitute the above equations in $a_l(t')$ appearing in the summation of the right-hand side. First, $a_n(t)$ can be written as

$$\begin{aligned} a_n(t) &= 1 - \int_0^t dt' \left\{ \sum_{l \neq n} \left[-\int_0^{t'} dt'' \sum_k a_k(t'') \langle l(t'')| \frac{d}{dt''} |k(t'')\rangle \right. \right. \\ &\quad \left. \times \exp\left(-\frac{i}{\hbar} \int_0^{t''} dt''' \ [E_k(t''') - E_l(t'')] \right) \right] \\ &\quad \times \langle n(t')| \frac{d}{dt'} |l(t')\rangle \times \exp\left(-\frac{i}{\hbar} \int_0^{t'} dt'' \ [E_l(t'') - E_n(t'')] \right) \\ &\quad + \left[1 - \int_0^{t'} dt'' \sum_k a_k(t'') \langle n(t'')| \frac{d}{dt''} |k(t'')\rangle \right. \\ &\quad \left. \times \exp\left(-\frac{i}{\hbar} \int_0^{t''} dt''' \ [E_k(t''') - E_n(t''')] \right) \right] \\ &\quad \left. \times \langle n(t')| \frac{d}{dt'} |n(t')\rangle \right\}. \end{aligned} \tag{B.2.8}$$

Taking up to the 1st order and using Eq.B.2.4,

$$a_n(t) \simeq 1 - \int_0^t dt' \ \langle n(t')| \frac{d}{dt'} |n(t')\rangle \tag{B.2.9}$$

$$= 1. \tag{B.2.10}$$

We can similarly calculate $a_m(t)$ for $m \neq n$:

$$\begin{aligned} a_m(t) &= -\int_0^t dt' \ \left\{ \sum_{l\neq n} \left[-\int_0^{t'} dt'' \ \sum_k a_k(t'') \langle l(t'')| \frac{d}{dt''} |k(t'')\rangle \right.\right. \\ &\quad \left. \times \exp\left(-\frac{i}{\hbar} \int_0^{t''} dt''' \ [E_k(t''') - E_l(t'')] \right) \right] \\ &\quad \times \langle n(t')| \frac{d}{dt'} |l(t')\rangle \times \exp\left(-\frac{i}{\hbar} \int_0^{t'} dt'' \ [E_l(t'') - E_n(t'')] \right) \\ &\quad + \left[1 - \int_0^{t'} dt'' \ \sum_k a_k(t'') \langle n(t'')| \frac{d}{dt''} |k(t'')\rangle \right. \\ &\quad \left. \times \exp\left(-\frac{i}{\hbar} \int_0^{t''} dt''' \ [E_k(t''') - E_n(t''')] \right) \right] \\ &\quad \left. \times \langle m(t')| \frac{d}{dt'} |n(t')\rangle \times \exp\left(-\frac{i}{\hbar} \int_0^{t'} dt'' \ [E_n(t'') - E_m(t'')] \right) \right\} \end{aligned} \tag{B.2.11}$$

$$\begin{aligned} &\simeq -\int_0^t dt' \ \langle m(t')| \frac{d}{dt'} |n(t')\rangle \\ &\qquad \times \exp\left(-\frac{i}{\hbar} \int_0^{t'} dt'' \ [E_n(t'') - E_m(t'')] \right) \end{aligned} \tag{B.2.12}$$

Below, we assume the adiabatic condition: if the Hamiltonian is not strongly dependent on the time, we can neglect the time dependence of the inner product $\langle m(t)| \frac{d}{dt} |n\rangle$ and $E_m(t) - E_n(t)$. Under this assumption, we can execute the integration, and the result is

$$a_m(t) = -i\hbar \frac{\langle m(t)| \frac{d}{dt} |n(t)\rangle}{E_n - E_m} \times \exp\left(-\frac{i}{\hbar} \int_0^t dt' \ [E_n(t') - E_m(t')] \right). \tag{B.2.13}$$

Therefore, the time evolution of the state up to the 1st order can be written as

$$|\psi(t)\rangle = \exp\left(-\frac{i}{\hbar} \int_0^t dt' \ E_n(t') \right) \times \left[|n(t)\rangle - i\hbar \sum_{l\neq n} |l(t)\rangle \frac{\langle l(t)| \frac{d}{dt} |n(t)\rangle}{E_n(t) - E_l(t)} \right]. \tag{B.2.14}$$

B.2.2 The case where the momentum is adiabatically changing [2]

When the momentum $\mathbf{k}$ is adiabatically changing due to an external field, the time evolution of the state $|\tilde{u}_n(\mathbf{k})\rangle$ except the dynamical phase factor [2] is

$$|\tilde{u}_n(\mathbf{k})\rangle = |u_n(\mathbf{k})\rangle - i\hbar \sum_{n' \neq n} \frac{|u_{n'}(\mathbf{k})\rangle \langle u_{n'}(\mathbf{k})|\dot{u}_n(\mathbf{k})\rangle}{\epsilon_n(\mathbf{k}) - \epsilon_{n'}(\mathbf{k})} \tag{B.2.15}$$

$$\dot{\mathbf{k}} = \mathbf{F}/\hbar. \tag{B.2.16}$$

Here, $\epsilon_n(\mathbf{k})$ is the eigenenergy: $H(\mathbf{k})|u_n(\mathbf{k})\rangle = \epsilon_n(\mathbf{k})|u_n(\mathbf{k})\rangle$. Since the velocity operator is defined as $\mathbf{v} = \dot{\mathbf{r}} = (i/\hbar)[H, \mathbf{r}]$, in the q-representation, it becomes

$$\mathbf{v}(\mathbf{k}) = e^{-i\mathbf{k}\cdot\mathbf{r}}(i/\hbar)[\mathbf{r}, H]e^{i\mathbf{k}\cdot\mathbf{r}} \tag{B.2.17}$$

$$= \frac{\partial H(\mathbf{k}, t)}{\partial \hbar \mathbf{k}}. \tag{B.2.18}$$

The mean velocity is

$$\hbar\mathbf{v} = \langle \tilde{u}_n(\mathbf{k})| \frac{\partial H}{\partial \mathbf{k}} |\tilde{u}_n(\mathbf{k})\rangle \tag{B.2.19}$$

$$= \left[\langle u_n(\mathbf{k})| + i\hbar \sum_{n' \neq n} \frac{\langle \dot{u}_n(\mathbf{k})|u_{n'}(\mathbf{k})\rangle \langle u_{n'}(\mathbf{k})|}{\epsilon_n(\mathbf{k}) - \epsilon_{n'}(\mathbf{k})}\right] \frac{\partial H}{\partial \mathbf{k}} \left[|u_n(\mathbf{k})\rangle - i\hbar \sum_{n' \neq n} \frac{|u_{n'}(\mathbf{k})\rangle \langle u_{n'}(\mathbf{k})|\dot{u}_n(\mathbf{k})\rangle}{\epsilon_n(\mathbf{k}) - \epsilon_{n'}(\mathbf{k})}\right] \tag{B.2.20}$$

$$\simeq \langle u_n(\mathbf{k})| \frac{\partial H}{\partial \mathbf{k}} |u_n(\mathbf{k})\rangle - \hbar \sum_{n' \neq n} \left[i \langle u_n(\mathbf{k})| \frac{\partial H}{\partial \mathbf{k}} |u_{n'}(\mathbf{k})\rangle \frac{\langle u_{n'}(\mathbf{k})|\dot{u}_n(\mathbf{k})\rangle}{\epsilon_n(\mathbf{k}) - \epsilon_{n'}(\mathbf{k})} + \text{c.c}\right], \tag{B.2.21}$$

where c.c in the square bracket means the complex conjugate of the 1st term.

[2] The time-evolution including the dynamical phase factor is expressed as

$$|\tilde{u}_n(\mathbf{k})\rangle = \exp\left[-\frac{i}{\hbar}\int^t \epsilon_n(\mathbf{k}(t'))\,dt'\right]\left(|u_n(\mathbf{k})\rangle - i\hbar \sum_{n' \neq n} \frac{|u_{n'}(\mathbf{k})\rangle \langle u_{n'}(\mathbf{k})|\dot{u}_n(\mathbf{k})\rangle}{\epsilon_n(\mathbf{k}) - \epsilon_{n'}(\mathbf{k})}\right).$$

Since the phase factor disappears when calculating the mean velocity, we begin without considering it for simplicity.

Using the equations [3] [4]

$$\langle u_n(\mathbf{k})| \frac{\partial H(\mathbf{k})}{\partial \mathbf{k}} |u_n(\mathbf{k})\rangle = \frac{\partial \epsilon_n(\mathbf{k})}{\partial \mathbf{k}}, \tag{B.2.22}$$

$$\langle u_{n'}(\mathbf{k})| \frac{\partial H(\mathbf{k})}{\partial \mathbf{k}} |u_n(\mathbf{k})\rangle = (\epsilon_{n'} - \epsilon_n) \langle u_{n'}(\mathbf{k}) | \frac{\partial u_n(\mathbf{k})}{\partial \mathbf{k}} \rangle, \tag{B.2.23}$$

$$\langle u_n(\mathbf{k})| \frac{\partial u_n(\mathbf{k})}{\partial \mathbf{k}} \rangle = -\langle \frac{\partial u_n(\mathbf{k})}{\partial \mathbf{k}} | u_n(\mathbf{k}) \rangle, \tag{B.2.24}$$

the mean velocity becomes

$$\begin{aligned}
\hbar \mathbf{v} &\simeq \frac{\partial \epsilon_n(\mathbf{k})}{\partial \mathbf{k}} - i\hbar \sum_{n' \neq n} \Big[\langle \frac{\partial u_n(\mathbf{k})}{\partial \mathbf{k}} | u_{n'}(\mathbf{k}) \rangle \langle u_{n'}(\mathbf{k}) | \dot{u}_n(\mathbf{k}) \rangle \\
&\qquad - \langle \dot{u}_n(\mathbf{k}) | u_{n'}(\mathbf{k}) \rangle \langle u_{n'}(\mathbf{k}) | \frac{\partial u_n(\mathbf{k})}{\partial \mathbf{k}} \rangle \Big] \qquad \text{(B.2.25)} \\
&= \frac{\partial \epsilon_n(\mathbf{k})}{\partial \mathbf{k}} - i\hbar \Big[\sum_{n'} \langle \frac{\partial u_n(\mathbf{k})}{\partial \mathbf{k}} | u_{n'}(\mathbf{k}) \rangle \langle u_{n'}(\mathbf{k}) | \dot{u}_n(\mathbf{k}) \rangle \\
&\qquad - \langle \frac{\partial u_n(\mathbf{k})}{\partial \mathbf{k}} | u_n(\mathbf{k}) \rangle \langle u_n(\mathbf{k}) | \dot{u}_n(\mathbf{k}) \rangle \\
&\qquad - \sum_{n'} \langle \dot{u}_n(\mathbf{k}) | u_{n'}(\mathbf{k}) \rangle \langle u_{n'}(\mathbf{k}) | \frac{\partial u_n(\mathbf{k})}{\partial \mathbf{k}} \rangle \\
&\qquad + \langle \dot{u}_n(\mathbf{k}) | u_n(\mathbf{k}) \rangle \langle u_n(\mathbf{k}) | \frac{\partial u_n(\mathbf{k})}{\partial \mathbf{k}} \rangle \Big] \qquad \text{(B.2.26)} \\
&= \frac{\partial \epsilon_n(\mathbf{k})}{\partial \mathbf{k}} - i\hbar \Big[\langle \frac{\partial u_n(\mathbf{k})}{\partial \mathbf{k}} | \dot{u}_n(\mathbf{k}) \rangle - \langle \dot{u}_n(\mathbf{k}) | \frac{\partial u_n(\mathbf{k})}{\partial \mathbf{k}} \rangle \Big]. \qquad \text{(B.2.27)}
\end{aligned}$$

[3] Partially differentiating the equation $H(\mathbf{k}) |u_n(\mathbf{k})\rangle = \epsilon_n(\mathbf{k}) |u_n(\mathbf{k})\rangle$ in terms of $\mathbf{k}$, we get

$$\frac{\partial H(\mathbf{k})}{\partial \mathbf{k}} |u_n(\mathbf{k})\rangle + H(\mathbf{k}) |\frac{\partial u_n(\mathbf{k})}{\partial \mathbf{k}} \rangle = \frac{\partial \epsilon_n(\mathbf{k})}{\partial \mathbf{k}} |u_n(\mathbf{k})\rangle + \epsilon_n(\mathbf{k}) |\frac{\partial u_n(\mathbf{k})}{\partial \mathbf{k}} \rangle .$$

Applying $\langle u_n(\mathbf{k})|, \langle u_{n'}(\mathbf{k})|$ to the above equation, the result is

$$\begin{aligned}
\langle u_n(\mathbf{k})| \frac{\partial H(\mathbf{k})}{\partial \mathbf{k}} |u_n(\mathbf{k})\rangle &= \frac{\partial \epsilon_n(\mathbf{k})}{\partial \mathbf{k}} \\
\langle u_{n'}(\mathbf{k})| \frac{\partial H(\mathbf{k})}{\partial \mathbf{k}} |u_n(\mathbf{k})\rangle &= (\epsilon_n(\mathbf{k}) - \epsilon_{n'}(\mathbf{k})) \langle u_{n'}(\mathbf{k}) | \frac{\partial u_n(\mathbf{k})}{\partial \mathbf{k}} \rangle
\end{aligned}$$

, respectively.

[4] Partial differentiation of the normalization condition $\langle u_n(\mathbf{k}) | u_n(\mathbf{k}) \rangle = 1$ in terms of $\mathbf{k}$.

Calculating the x component in the square bracket with $|\dot{u}_n(\mathbf{k})\rangle = \sum_{i=x,y,z} \frac{dk_i}{dt} |\frac{\partial u_n(\mathbf{k})}{\partial k_i}\rangle$,

$$\begin{aligned}
\Big[\cdots\Big] &= \sum_{i=x,y,z} \frac{dk_i}{dt}\left[\langle\frac{\partial u_n(\mathbf{k})}{\partial k_x}|\frac{\partial u_n(\mathbf{k})}{\partial k_i}\rangle - \langle\frac{\partial u_n(\mathbf{k})}{\partial k_i}|\frac{\partial u_n(\mathbf{k})}{\partial k_x}\rangle\right] && \text{(B.2.28)}\\
&= \frac{dk_y}{dt}\left(\langle\frac{\partial u_n(\mathbf{k})}{\partial k_x}|\frac{\partial u_n(\mathbf{k})}{\partial k_y}\rangle - \langle\frac{\partial u_n(\mathbf{k})}{\partial k_y}|\frac{\partial u_n(\mathbf{k})}{\partial k_x}\rangle\right)\\
&\quad + \frac{dk_z}{dt}\left(\langle\frac{\partial u_n(\mathbf{k})}{\partial k_x}|\frac{\partial u_n(\mathbf{k})}{\partial k_z}\rangle - \langle\frac{\partial u_n(\mathbf{k})}{\partial k_z}|\frac{\partial u_n(\mathbf{k})}{\partial k_x}\rangle\right) && \text{(B.2.29)}\\
&= \frac{1}{i}\left(\frac{dk_y}{dt}\Omega_{xy}(\mathbf{k}) + \frac{dk_z}{dt}\Omega_{xz}(\mathbf{k})\right), && \text{(B.2.30)}
\end{aligned}$$

where $\Omega_{ij}(\mathbf{k}) \equiv i\left(\langle\frac{\partial u_n(\mathbf{k})}{\partial k_i}|\frac{\partial u_n(\mathbf{k})}{\partial k_j}\rangle - \langle\frac{\partial u_n(\mathbf{k})}{\partial k_j}|\frac{\partial u_n(\mathbf{k})}{\partial k_i}\rangle\right)$ is the Berry curvature defined in (k_i, k_j)-Brillouin zone. The y, z components can be similarly calculated. If the periodic potential is created in xy plane and the system is uniform along z axis, $\Omega_{zi} = 0$ $(i = x, y)$ since $\frac{\partial u_n(\mathbf{k})}{\partial k_z} = \mathbf{0}$.
Therefore,

$$\begin{aligned}
i\langle\frac{\partial u_n(\mathbf{k})}{\partial \mathbf{k}}|\dot{u}_n(\mathbf{k})\rangle - \langle\dot{u}_n(\mathbf{k})|\frac{\partial u_n(\mathbf{k})}{\partial \mathbf{k}}\rangle &= \Big(\dot{k}_y\Omega_{xy}(\mathbf{k}) + \dot{k}_z\Omega_{xz}(\mathbf{k}),\\
&\quad \dot{k}_x\Omega_{yx}(\mathbf{k}) + \dot{k}_z\Omega_{yz}(\mathbf{k}),\\
&\quad \dot{k}_x\Omega_{zx}(\mathbf{k}) + \dot{k}_y\Omega_{zy}(\mathbf{k})\Big) && \text{(B.2.31)}\\
&= \Big(\dot{k}_y\Omega_{xy}(\mathbf{k}),\ -\dot{k}_x\Omega_{xy}(\mathbf{k}),\ 0\Big) && \text{(B.2.32)}\\
&= \dot{\mathbf{k}}\times\hat{\mathbf{z}}\,\Omega_{xy}(\mathbf{k}), && \text{(B.2.33)}
\end{aligned}$$

where $\hat{\mathbf{z}}$ is the unit vector along z axis.
As a result, the semi-classical equation of motion of a particle can be written as

$$\begin{aligned}
\mathbf{v} &= \frac{\partial\epsilon_n(\mathbf{k})}{\partial\hbar\mathbf{k}} - \dot{\mathbf{k}}\times\hat{\mathbf{z}}\,\Omega_{xy}(\mathbf{k}) && \text{(B.2.34)}\\
\dot{\mathbf{k}} &= \frac{\mathbf{F}}{\hbar}. && \text{(B.2.35)}
\end{aligned}$$

Appendix C

Berry curvature in an optical lattice

In this appendix, the numerical calculation method of the Berry curvature in an optical lattice is described according to the Ref.[123]. We apply the method to the optical Lieb lattice and the 1D superlattice, and calculate the Berry curvature in the discretized Brillouin zone.

C.1 Chern number and Berry curvature

The Chern number assigned to the nth band is defined as

$$c_n = -\frac{1}{2\pi}\int_{T^2} \mathrm{d}^2k\, \Omega_n(k), \tag{C.1.1}$$

where T^2 means the two-dimensional torus, and $\Omega_n(k)$ is the Berry curvature given by

$$\Omega_n(k) = \partial_1 A_2(k) - \partial_2 A_1(k) \tag{C.1.2}$$

$$A_\mu = i\langle n(k)|\,\partial_\mu\,|n(k)\rangle \tag{C.1.3}$$

with $|n(k)\rangle$ being a normalized wave function of the nth Bloch band such that $H(k)\,|n(k)\rangle = E_n(k)\,|n(k)\rangle$, and $A_\mu(k)$ $(\mu = 1, 2)$ is the Berry connection. In the above expressions, the derivative ∂_μ stands for $\partial/\partial k_\mu$. We assume that there is no degeneracy for the nth state. In the context of the quantum Hall effect, the Chern number associated with the Berry curvature plays a crucial role in characterizing the Hall conductance [124]: when the Fermi energy lies in a gap, the Hall conductance is given by

$$\sigma_{xy} = -\frac{e^2}{h}\sum_n c_n. \tag{C.1.4}$$

C.2 Calculation method without specifying any gauge

The Chern number and the Berry curvature are given in the two-dimensional surfaces such as the Brillouin zone. In practical numerical calculations, we diagonalize the Hamiltonians on a set of discrete points within the surfaces. In these calculations, a phase ambiguity of the wave function $|n(k)\rangle$ causes a gauge ambiguity of the Berry connection $A_\mu(k)$. As can

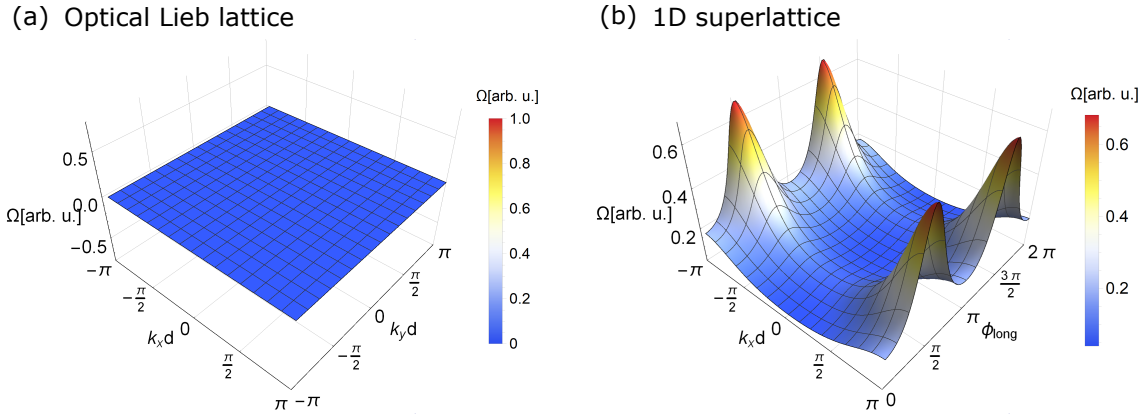

Figure C.2.1: Berry curvature in (a) optical Lieb lattice and (b) 1D superlattice in k-t Brillouin zone. The Berry curvature is calculated using the U(1) link variable. (a) The Berry curvature is zero over the entire Brillouin zone. (b) The Berry curvature is positive over the entire k-t Brillouin zone, and the Chern number amounts to 1.

be seen from the Eq.C.1.2, the Berry curvature is defined by the derivative of the Berry connection, and the local-gauge invariant. Therefore, in the straightforward calculations, one must appropriately choose a local gauge with which the Bloch wave function $|n(k)\rangle$ is smoothly differentiable near k. However, this direct procedure can be costly, and we must choose the appropriate local gauge case-by-case.

To avoid such a problem, it is very convenient to introduce the U(1) link variable [123]. It is defined as

$$U_\mu(k_l) = \frac{\langle n(k_l)|n(k_l+\hat{\mu})\rangle}{|\,\langle n(k_l)|n(k_l+\hat{\mu})\rangle\,|}, \tag{C.2.1}$$

where $\hat{\mu} = \hat{1}, \hat{2}$ is a vector from k_l to the neighboring points in the two-dimensional discretized Brillouin zone. The link variables are well defined as long as $|\,\langle n(k_l)|n(k_l+\hat{\mu})\rangle\,| \neq 0$, which can be always assumed to be the case.
With the link variable, the Berry curvature is given by

$$\tilde{\Omega}_n(k_l) \;=\; \ln\left[U_1(k_l)U_2(k_l+\hat{1})U_1(k_l+\hat{2})^{-1}U_2(k_l)^{-1}\right], \quad -\pi < \tilde{\Omega}_n(k_l) \leq \pi \tag{C.2.2}$$

It is obvious that this Berry curvature is gauge invariant. This implies that we do not need to determine which gauge is adopted: any choice of gauge gives an ideal Berry curvature. Moreover, the Chern number

$$\tilde{c}_n = -\frac{1}{2\pi}\sum_l \tilde{\Omega}_n(k_l) \tag{C.2.3}$$

is strictly an integer for arbitrary spacings of the grid. Therefore, with this method, we can decrease the cost for the numerical calculation compared to the straightforward method.

Figure C.2.1 shows the calculation result of the Berry curvature in the optical Lieb lattice and 1D superlattice. For the optical Lieb lattice, the lattice depth is set to $(V_{\text{short}}, V_{\text{long}}, V_{\text{diag}}) = (8, 8, 9.5)E_R^{\text{long}}$. For the 1D superlattice, $(V_{\text{short}}, V_{\text{long}}) = (4, 4)E_R^{\text{long}}$. In the optical Lieb lattice, the Berry curvature is zero over the entire Brillouin zone, and the Chern number is zero. This is because the Lieb lattice is a topologically trivial

system. In the 1D superlattice system, the Berry curvature is positive over the entire k-t Brillouin zone, and the Chern number amounts to 1 since this system realizes the topological pumping [125, 126] proposed by Thouless [127].

Bibliography

[1] Di Xiao, Ming-Che Chang, and Qian Niu. Berry phase effects on electronic properties. *Reviews of Modern Physics*, 82(3):1959–2007, jul 2010.

[2] H M Price and N R Cooper. Mapping the Berry curvature from semiclassical dynamics in optical lattices. *Physical Review A*, 85(3):033620, mar 2012.

[3] Grégoire Misguich and Claire Lhuillier. *TWO-DIMENSIONAL QUANTUM ANTIFERROMAGNETS*, pages 229–306.

[4] J G Bednorz and K A Müller. Possible high Tc superconductivity in the Ba-La-Cu-O system. *Zeitschrift für Physik B Condensed Matter*, 64(2):189–193, 1986.

[5] John Hubbard. Electron correlations in narrow energy bands. *Proceedings of the Royal Society of London. Series A. Mathematical and Physical Sciences*, 276(1365):238 LP – 257, nov 1963.

[6] R Staudt, M Dzierzawa, and A Muramatsu. Phase diagram of the three-dimensional Hubbard model at half filling. *The European Physical Journal B - Condensed Matter and Complex Systems*, 17(3):411–415, 2000.

[7] Immanuel Bloch, Jean Dalibard, and Sylvain Nascimbene. Quantum simulations with ultracold quantum gases. *Nature Phys*, 8(4):267–276, apr 2012.

[8] Immanuel Bloch, Jean Dalibard, and Wilhelm Zwerger. Many-body physics with ultracold gases. *Rev. Mod. Phys.*, 80(3):885–964, 2008.

[9] Richard P. Feynman. Simulating physics with computers. *International Journal of Theoretical Physics*, 21(6-7):467–488, 1982.

[10] Harold J. Metcalf and Peter van der Straten. *Laser Cooling and Trapping*, volume 13. 1999.

[11] K B Davis, M O. Mewes, M R Andrews, N J van Druten, D S Durfee, D M Kurn, and W Ketterle. Bose-Einstein Condensation in a Gas of Sodium Atoms. *Phys. Rev. Lett.*, 75(22):3969–3973, 1995.

[12] M H Anderson, J R Ensher, M R Matthews, C E Wieman, and E A Cornell. Observation of Bose-Einstein Condensation in a Dilute Atomic Vapor. *Science*, 269(5221):198–201, 1995.

[13] B DeMarco and D S Jin. Onset of Fermi degeneracy in a trapped atomic gas. *Science*, 285(5434):1703–1706, 1999.

[14] C A Regal, M Greiner, and D S Jin. Observation of Resonance Condensation of Fermionic Atom Pairs. *Phys. Rev. Lett.*, 92(4):40403, 2004.

[15] M W Zwierlein, C A Stan, C H Schunck, S M F Raupach, A J Kerman, and W Ketterle. Condensation of Pairs of Fermionic Atoms near a Feshbach Resonance. *Phys. Rev. Lett.*, 92(12):120403, 2004.

[16] M W Zwierlein, J R Abo-Shaeer, A Schirotzek, C H Schunck, and W Ketterle. Vortices and superfluidity in a strongly interacting Fermi gas. *Nature*, 435:1047, jun 2005.

[17] Markus Greiner, Olaf Mandel, Tilman Esslinger, Theodor W Hänsch, and Immanuel Bloch. Quantum phase transition from a superfluid to a Mott insulator in a gas of ultracold atoms. *Nature*, 415(6867):39–44, jan 2002.

[18] Markus Greiner, Olaf Mandel, Theodor W Hänsch, and Immanuel Bloch. Collapse and revival of the matter wave field of a Bose-Einstein condensate. *Nature*, 419(6902):51–54, sep 2002.

[19] S Trotzky, L Pollet, F Gerbier, U Schnorrberger, I Bloch, N V Prokof/'ev, B Svistunov, and M Troyer. Suppression of the critical temperature for superfluidity near the Mott transition. *Nat Phys*, 6(12):998–1004, dec 2010.

[20] Chen-Lung Hung, Xibo Zhang, Nathan Gemelke, and Cheng Chin. Observation of scale invariance and universality in two-dimensional Bose gases. *Nature*, 470:236, jan 2011.

[21] Xibo Zhang, Chen-Lung Hung, Shih-Kuang Tung, and Cheng Chin. Observation of Quantum Criticality with Ultracold Atoms in Optical Lattices. *Science*, 335(6072):1070–1072, 2012.

[22] Jacob F Sherson, Christof Weitenberg, Manuel Endres, Marc Cheneau, Immanuel Bloch, and Stefan Kuhr. Single-atom-resolved fluorescence imaging of an atomic Mott insulator. *Nature*, 467:68, aug 2010.

[23] W S Bakr, A Peng, M E Tai, R Ma, J Simon, J I Gillen, S Fölling, L Pollet, and M Greiner. Probing the Superfluid-to-Mott Insulator Transition at the Single-Atom Level. *Science*, 329(5991):547 LP – 550, jul 2010.

[24] Martin Miranda, Ryotaro Inoue, Naoki Tambo, and Mikio Kozuma. Site-resolved imaging of a bosonic Mott insulator using ytterbium atoms. *Phys. Rev. A*, 96(4):43626, 2017.

[25] Th. Best, S Will, U Schneider, L Hackermüller, D van Oosten, I Bloch, and D.-S. Lühmann. Role of Interactions in 87Rb-40K Bose-Fermi Mixtures in a 3D Optical Lattice. *Phys. Rev. Lett.*, 102(3):30408, 2009.

[26] S Ospelkaus, C Ospelkaus, O Wille, M Succo, P Ernst, K Sengstock, and K Bongs. Localization of Bosonic Atoms by Fermionic Impurities in a Three-Dimensional Optical Lattice. *Phys. Rev. Lett.*, 96(18):180403, 2006.

[27] Kenneth Günter, Thilo Stöferle, Henning Moritz, Michael Köhl, and Tilman Esslinger. Bose-Fermi Mixtures in a Three-Dimensional Optical Lattice. *Phys. Rev. Lett.*, 96(18):180402, 2006.

[28] Seiji Sugawa, Kensuke Inaba, Shintaro Taie, Rekishu Yamazaki, Makoto Yamashita, and Yoshiro Takahashi. Interaction and filling-induced quantum phases of dual Mott insulators of bosons and fermions. *Nature Phys.*, 7(8):642–648, aug 2011.

[29] T Rom, Th. Best, D van Oosten, U Schneider, S Fölling, B Paredes, and I Bloch. Free fermion antibunching in a degenerate atomic Fermi gas released from an optical lattice. *Nature*, 444:733, dec 2006.

[30] S S Kondov, W R McGehee, J J Zirbel, and B DeMarco. Three-Dimensional Anderson Localization of Ultracold Matter. *Science*, 334(6052):66 LP – 68, oct 2011.

[31] Ulrich Schneider, Lucia Hackermuller, Jens Philipp Ronzheimer, Sebastian Will, Simon Braun, Thorsten Best, Immanuel Bloch, Eugene Demler, Stephan Mandt, David Rasch, and Achim Rosch. Fermionic transport and out-of-equilibrium dynamics in a homogeneous Hubbard model with ultracold atoms. *Nat Phys*, 8(3):213–218, mar 2012.

[32] U Schneider, L Hackermüller, S Will, Th. Best, I Bloch, T A Costi, R W Helmes, D Rasch, and A Rosch. Metallic and Insulating Phases of Repulsively Interacting Fermions in a 3D Optical Lattice. *Science*, 322(5907):1520–1525, 2008.

[33] Robert Jördens, Niels Strohmaier, Kenneth Günter, Henning Moritz, and Tilman Esslinger. A Mott insulator of fermionic atoms in an optical lattice. *Nature*, 455:204, sep 2008.

[34] Michael Lubasch, Valentin Murg, Ulrich Schneider, J Ignacio Cirac, and Mari-Carmen Bañuls. Adiabatic Preparation of a Heisenberg Antiferromagnet Using an Optical Superlattice. *Phys. Rev. Lett.*, 107(16):165301, 2011.

[35] Tin-Lun Ho and Qi Zhou. Squeezing out the entropy of fermions in optical lattices. *Proceedings of the National Academy of Sciences of the United States of America*, 106(17):6916–20, apr 2009.

[36] Jean-Sébastien Bernier, Corinna Kollath, Antoine Georges, Lorenzo De Leo, Fabrice Gerbier, Christophe Salomon, and Michael Köhl. Cooling fermionic atoms in optical lattices by shaping the confinement. *Phys. Rev. A*, 79(6):061601, 2009.

[37] Daniel Greif, Thomas Uehlinger, Gregor Jotzu, Leticia Tarruell, and Tilman Esslinger. Short-Range Quantum Magnetism of Ultracold Fermions in an Optical Lattice. *Science*, 340(6138):1307–1310, 2013.

[38] Russell A Hart, Pedro M Duarte, Tsung-Lin Yang, Xinxing Liu, Thereza Paiva, Ehsan Khatami, Richard T Scalettar, Nandini Trivedi, David A Huse, and Randall G Hulet. Observation of antiferromagnetic correlations in the Hubbard model with ultracold atoms. *Nature*, 519(7542):211–214, mar 2015.

[39] Anton Mazurenko, Christie S Chiu, Geoffrey Ji, Maxwell F Parsons, Márton Kanász-Nagy, Richard Schmidt, Fabian Grusdt, Eugene Demler, Daniel Greif, and Markus Greiner. A cold-atom Fermi-Hubbard antiferromagnet. *Nature*, 545(7655):462–466, may 2017.

[40] Masao Takamoto, Feng-Lei Hong, Ryoichi Higashi, and Hidetoshi Katori. An optical lattice clock. *Nature*, 435:321, may 2005.

[41] N Hinkley, J A Sherman, N B Phillips, M Schioppo, N D Lemke, K Beloy, M Pizzocaro, C W Oates, and A D Ludlow. An Atomic Clock with 10-18 Instability. *Science*, 341(6151):1215 LP – 1218, sep 2013.

[42] B J Bloom, T L Nicholson, J R Williams, S L Campbell, M Bishof, X Zhang, W Zhang, S L Bromley, and J Ye. An optical lattice clock with accuracy and stability at the 10 − 18 level. *Nature*, 506:71, jan 2014.

[43] Yosuke Takasu, Kenichi Maki, Kaduki Komori, Tetsushi Takano, Kazuhito Honda, Mitsutaka Kumakura, Tsutomu Yabuzaki, and Yoshiro Takahashi. Spin-Singlet Bose-Einstein Condensation of Two-Electron Atoms. *Phys. Rev. Lett.*, 91(4):40404, 2003.

[44] Takeshi Fukuhara, Yosuke Takasu, Mitsutaka Kumakura, and Yoshiro Takahashi. Degenerate Fermi Gases of Ytterbium. *Phys. Rev. Lett.*, 98(3):030401, 2007.

[45] Takeshi Fukuhara, Seiji Sugawa, Yosuke Takasu, and Yoshiro Takahashi. All-optical formation of quantum degenerate mixtures. *Phys. Rev. A*, 79(2):21601, 2009.

[46] Sebastian Kraft, Felix Vogt, Oliver Appel, Fritz Riehle, and Uwe Sterr. Bose-Einstein Condensation of Alkaline Earth Atoms: 40Ca. *Phys. Rev. Lett.*, 103(13):130401, 2009.

[47] Y N Martinez de Escobar, P G Mickelson, M Yan, B J DeSalvo, S B Nagel, and T C Killian. Bose-Einstein Condensation of 84Sr. *Phys. Rev. Lett.*, 103(20):200402, 2009.

[48] B J DeSalvo, M Yan, P G Mickelson, Y N Martinez de Escobar, and T C Killian. Degenerate Fermi Gas of 87Sr. *Phys. Rev. Lett.*, 105(3):030402, 2010.

[49] Shintaro Taie, Yosuke Takasu, Seiji Sugawa, Rekishu Yamazaki, Takuya Tsujimoto, Ryo Murakami, and Yoshiro Takahashi. Realization of a SU(2) × SU(6) System of Fermions in a Cold Atomic Gas. *Phys. Rev. Lett.*, 105(19):190401, 2010.

[50] Shintaro Taie, Rekishu Yamazaki, Seiji Sugawa, and Yoshiro Takahashi. An SU(6) Mott insulator of an atomic Fermi gas realized by large-spin Pomeranchuk cooling. *Nature Physics*, 8(11):825–830, sep 2012.

[51] Masaaki Kitagawa, Katsunari Enomoto, Kentaro Kasa, Yoshiro Takahashi, Roman Ciury\lo, Pascal Naidon, and Paul S Julienne. Two-color photoassociation spectroscopy of ytterbium atoms and the precise determinations of s-wave scattering lengths. *Phys. Rev. A*, 77(1):12719, 2008.

[52] Y N de Escobar, P G Mickelson, P Pellegrini, S B Nagel, A Traverso, M Yan, R Côté, and T C Killian. Two-photon photoassociative spectroscopy of ultracold 88Sr. *Phys. Rev. A*, 78(6):62708, 2008.

[53] M A Cazalilla, A F Ho, and M Ueda. Ultracold gases of ytterbium: ferromagnetism and Mott states in an SU(6) Fermi system. *New Journal of Physics*, 11(10):103033, 2009.

[54] A V Gorshkov, M Hermele, V Gurarie, C Xu, P S Julienne, J Ye, P Zoller, E Demler, M D Lukin, and A M Rey. Two-orbital SU(N) magnetism with ultracold alkaline-earth atoms. *Nature Physics*, 6:289, feb 2010.

[55] S Trotzky, P Cheinet, S Fölling, M Feld, U Schnorrberger, A M Rey, A Polkovnikov, E A Demler, M D Lukin, and I Bloch. Time-Resolved Observation and Control of Superexchange Interactions with Ultracold Atoms in Optical Lattices. *Science*, 319(5861):295–299, 2008.

[56] Leticia Tarruell, Daniel Greif, Thomas Uehlinger, Gregor Jotzu, and Tilman Esslinger. Creating, moving and merging Dirac points with a Fermi gas in a tunable honeycomb lattice. *Nature*, 483(7389):302–305, mar 2012.

[57] J Struck, C Ölschläger, R Le Targat, P Soltan-Panahi, A Eckardt, M Lewenstein, P Windpassinger, and K Sengstock. Quantum Simulation of Frustrated Classical Magnetism in Triangular Optical Lattices. *Science*, 333(6045):996–999, 2011.

[58] Georg Wirth, Matthias Ölschläger, Andreas Hemmerich, Mätthias Ölschlager, and Andreas Hemmerich. Evidence for orbital superfluidity in the P-band of a bipartite optical square lattice. *Nature Physics*, 7(2):147–153, feb 2011.

[59] Gyu-Boong Jo, Jennie Guzman, Claire K Thomas, Pavan Hosur, Ashvin Vishwanath, and Dan M Stamper-Kurn. Ultracold Atoms in a Tunable Optical Kagome Lattice. *Phys. Rev. Lett.*, 108(4):045305, 2012.

[60] Sebastian D Huber and Ehud Altman. Bose condensation in flat bands. *Phys. Rev. B*, 82(18):184502, 2010.

[61] Shintaro Taie, Hideki Ozawa, Tomohiro Ichinose, Takuei Nishio, Shuta Nakajima, and Yoshiro Takahashi. Coherent driving and freezing of bosonic matter wave in an optical Lieb lattice. *Science Advances*, 1(10):e1500854–e1500854, nov 2015.

[62] R Shen, L B Shao, Baigeng Wang, and D Y Xing. Single Dirac cone with a flat band touching on line-centered-square optical lattices. *Phys. Rev. B*, 81(4):41410, 2010.

[63] V J Emery. Theory of high-Tc superconductivity in oxides. *Phys. Rev. Lett.*, 58(26):2794–2797, 1987.

[64] C M Varma, S Schmitt-Rink, and Elihu Abrahams. Charge transfer excitations and superconductivity in "ionic" metals. *Solid State Communications*, 62(10):681–685, 1987.

[65] V I Iglovikov, F Hébert, B Grémaud, G G Batrouni, and R T Scalettar. Superconducting transitions in flat-band systems. *Phys. Rev. B*, 90(9):94506, 2014.

[66] Elliott H Lieb. Two theorems on the Hubbard model. *Phys. Rev. Lett.*, 62(10):1201–1204, 1989.

[67] D Guzmán-Silva, C Mejía-Cortés, M A Bandres, M C Rechtsman, S Weimann, S Nolte, M Segev, A Szameit, and R A Vicencio. Experimental observation of bulk and edge transport in photonic Lieb lattices. *New Journal of Physics*, 16(6):63061, 2014.

[68] Rodrigo A Vicencio, Camilo Cantillano, Luis Morales-Inostroza, Bastián Real, Cristian Mejía-Cortés, Steffen Weimann, Alexander Szameit, and Mario I Molina. Observation of Localized States in Lieb Photonic Lattices. *Phys. Rev. Lett.*, 114(24):245503, 2015.

[69] Sebabrata Mukherjee, Alexander Spracklen, Debaditya Choudhury, Nathan Goldman, Patrik Öhberg, Erika Andersson, and Robert R Thomson. Observation of a Localized Flat-Band State in a Photonic Lieb Lattice. *Phys. Rev. Lett.*, 114(24):245504, 2015.

[70] F Baboux, L Ge, Thibault Jacqmin, M Biondi, E. Galopin, A. Lemaître, L. Le Gratiet, I. Sagnes, S Schmidt, H. E. Türeci, Alberto Amo, and Jacqueline Bloch. Bosonic Condensation and Disorder-Induced Localization in a Flat Band. *Physical Review Letters*, 116(6):066402, feb 2016.

[71] Hideki Ozawa, Shintaro Taie, Tomohiro Ichinose, and Yoshiro Takahashi. Interaction-Driven Shift and Distortion of a Flat Band in an Optical Lieb Lattice. *Phys. Rev. Lett.*, 118(17):175301, 2017.

[72] Shintaro Taie, Tomohiro Ichinose, Hideki Ozawa, and Yoshiro Takahashi. Spatial Adiabatic Passage of Massive Quantum Particles. 8502:1–6, 2017.

[73] J R Kuklinski, U Gaubatz, F T Hioe, and K Bergmann. Adiabatic population transfer in a three-level system driven by delayed laser pulses. *Phys. Rev. A*, 40(11):6741–6744, 1989.

[74] U Gaubatz, P Rudecki, S Schiemann, and K Bergmann. Population transfer between molecular vibrational levels by stimulated Raman scattering with partially overlapping laser fields. A new concept and experimental results. *The Journal of Chemical Physics*, 92(9):5363–5376, 1990.

[75] K Bergmann, H Theuer, and B W Shore. Coherent population transfer among quantum states of atoms and molecules. *Rev. Mod. Phys.*, 70(3):1003–1025, 1998.

[76] Nicola Marzari and David Vanderbilt. Maximally localized generalized Wannier functions for composite energy bands. *Phys. Rev. B*, 56(20):12847–12865, 1997.

[77] Dirk-Sören Lühmann, Ole Jürgensen, Malte Weinberg, Juliette Simonet, Parvis Soltan-Panahi, and Klaus Sengstock. Quantum phases in tunable state-dependent hexagonal optical lattices. *Phys. Rev. A*, 90(1):13614, 2014.

[78] Christopher Pethick and Henrik Smith. *Bose-Einstein condensation in dilute gases*. Cambridge University Press, Cambridge, U.K., 2002.

[79] Andrea Trombettoni and Augusto Smerzi. Discrete Solitons and Breathers with Dilute Bose-Einstein Condensates. *Phys. Rev. Lett.*, 86(11):2353–2356, 2001.

[80] Takeshi Fukuhara, Seiji Sugawa, and Yoshiro Takahashi. Bose-Einstein condensation of an ytterbium isotope. *Phys. Rev. A*, 76(5):51604, 2007.

[81] Seiji Sugawa, Rekishu Yamazaki, Shintaro Taie, and Yoshiro Takahashi. Bose-Einstein condensate in gases of rare atomic species. *Phys. Rev. A*, 84(1):11610, 2011.

[82] Dipankar Das, Sachin Barthwal, Ayan Banerjee, and Vasant Natarajan. Absolute frequency measurements in Yb with 0.08 ppb uncertainty: Isotope shifts and hyperfine structure in the 399-nm 1S0 → 1P1 line. *Phys. Rev. A*, 72(3):32506, 2005.

[83] Kanhaiya Pandey, Alok K Singh, P V Kiran Kumar, M V Suryanarayana, and Vasant Natarajan. Isotope shifts and hyperfine structure in the 555.8-nm 1S0-3P1 line of Yb. *Phys. Rev. A*, 80(2):22518, 2009.

[84] J Hecker Denschlag, J E Simsarian, H Häffner, C McKenzie, A Browaeys, D Cho, K Helmerson, S L Rolston, and W D Phillips. A Bose-Einstein condensate in an optical lattice. *Journal of Physics B: Atomic, Molecular and Optical Physics*, 35(14):3095, 2002.

[85] T A Savard, K M O'Hara, and J E Thomas. Laser-noise-induced heating in far-off resonance optical traps. *Phys. Rev. A*, 56(2):R1095—-R1098, 1997.

[86] Eric D Black. An introduction to Pound-Drever-Hall laser frequency stabilization. *American Journal of Physics*, 69(1):79–87, 2001.

[87] Yi-Zhuang You, Zhu Chen, Xiao-Qi Sun, and Hui Zhai. Superfluidity of Bosons in Kagome Lattices with Frustration. *Phys. Rev. Lett.*, 109(26):265302, 2012.

[88] Markus Greiner, Immanuel Bloch, Olaf Mandel, Theodor W Hänsch, and Tilman Esslinger. Exploring Phase Coherence in a 2D Lattice of Bose-Einstein Condensates. *Phys. Rev. Lett.*, 87(16):160405, 2001.

[89] Michael Köhl, Henning Moritz, Thilo Stöferle, Kenneth Günter, and Tilman Esslinger. Fermionic Atoms in a Three Dimensional Optical Lattice: Observing Fermi Surfaces, Dynamics, and Interactions. *Phys. Rev. Lett.*, 94(8):80403, 2005.

[90] Torben Müller, Simon Fölling, Artur Widera, and Immanuel Bloch. State Preparation and Dynamics of Ultracold Atoms in Higher Lattice Orbitals. *Phys. Rev. Lett.*, 99(20):200405, 2007.

[91] Philipp T. Ernst, Sören Götze, Jasper S. Krauser, Karsten Pyka, Dirk-Sören Lühmann, Daniela Pfannkuche, and Klaus Sengstock. Probing superfluids in optical lattices by momentum-resolved Bragg spectroscopy. *Nature Phys.*, 6(1):56–61, 2010.

[92] Sebastian Kling, Tobias Salger, Christopher Grossert, and Martin Weitz. Atomic Bloch-Zener Oscillations and Stückelberg Interferometry in Optical Lattices. *Phys. Rev. Lett.*, 105(21):215301, 2010.

[93] Maxime Ben Dahan, Ekkehard Peik, Jakob Reichel, Yvan Castin, and Christophe Salomon. Bloch Oscillations of Atoms in an Optical Potential. *Phys. Rev. Lett.*, 76(24):4508–4511, 1996.

[94] N W. Ashcroft and Neil D. Mermin. *Solid State Physics*. W. B. Saunders Co., Philadelphia, 1976.

[95] Giulio Pettini and Michele Modugno. Anomalous Bloch oscillations in one-dimensional parity-breaking periodic potentials. *Physical Review A*, 83(1):013619, jan 2011.

[96] N Goldman, D F Urban, and D Bercioux. Topological phases for fermionic cold atoms on the Lieb lattice. *Phys. Rev. A*, 83(6):063601, 2011.

[97] M Machholm, C J Pethick, and H Smith. Band structure, elementary excitations, and stability of a Bose-Einstein condensate in a periodic potential. *Phys. Rev. A*, 67(5):053613, 2003.

[98] K.-J. Boller, A Imamolu, and S E Harris. Observation of electromagnetically induced transparency. *Phys. Rev. Lett.*, 66(20):2593–2596, 1991.

[99] S H Autler and C H Townes. Stark Effect in Rapidly Varying Fields. *Phys. Rev.*, 100(2):703–722, 1955.

[100] F Renzoni and T Brandes. Charge transport through quantum dots via time-varying tunnel coupling. *Phys. Rev. B*, 64(24):245301, 2001.

[101] Andrew D Greentree, Jared H Cole, A R Hamilton, and Lloyd C L Hollenberg. Coherent electronic transfer in quantum dot systems using adiabatic passage. *Phys. Rev. B*, 70(23):235317, 2004.

[102] K Eckert, M Lewenstein, R Corbalán, G Birkl, W Ertmer, and J Mompart. Three-level atom optics via the tunneling interaction. *Phys. Rev. A*, 70(2):23606, 2004.

[103] R Menchon-Enrich, A Benseny, V Ahufinger, A D Greentree, Th Busch, and J Mompart. Spatial adiabatic passage: a review of recent progress. *Reports on Progress in Physics*, 79(7):74401, 2016.

[104] E Arimondo. V Coherent Population Trapping in Laser Spectroscopy. volume 35 of *Progress in Optics*, pages 257–354. Elsevier, 1996.

[105] R Menchon-Enrich, S McEndoo, J Mompart, V Ahufinger, and Th. Busch. Tunneling-induced angular momentum for single cold atoms. *Phys. Rev. A*, 89(1):13626, 2014.

[106] Jinyang Liang, Jr. Rudolph N. Kohn, Michael F Becker, and Daniel J Heinzen. High-precision laser beam shaping using a binary-amplitude spatial light modulator. *Appl. Opt.*, 49(8):1323–1330, 2010.

[107] Waseem S Bakr, Jonathon I Gillen, Amy Peng, Simon Fölling, and Markus Greiner. A quantum gas microscope for detecting single atoms in a Hubbard-regime optical lattice. *Nature*, 462:74, nov 2009.

[108] Leon Balents. Spin liquids in frustrated magnets. *Nature*, 464(7286):199–208, mar 2010.

[109] P W Anderson, P A Lee, M Randeria, T M Rice, N Trivedi, and F C Zhang. The physics behind high-temperature superconducting cuprates: the 'plain vanilla' version of RVB. *Journal of Physics: Condensed Matter*, 16(24):R755, 2004.

[110] S G Porsev, Yu. G Rakhlina, and M G Kozlov. Electric-dipole amplitudes, lifetimes, and polarizabilities of the low-lying levels of atomic ytterbium. *Phys. Rev. A*, 60(4):2781–2785, 1999.

[111] D M Stamper-Kurn, M R Andrews, A P Chikkatur, S Inouye, H.-J. Miesner, J Stenger, and W Ketterle. Optical Confinement of a Bose-Einstein Condensate. *Phys. Rev. Lett.*, 80(10):2027–2030, 1998.

[112] T Sleator, T Pfau, V Balykin, O Carnal, and J Mlynek. Experimental demonstration of the optical Stern-Gerlach effect. *Phys. Rev. Lett.*, 68(13):1996–1999, 1992.

[113] Claude Cohen-Tannoudji. Atom-Photon Interactions: Basic Processes and Applications, 1993.

[114] J D Miller, R A Cline, and D J Heinzen. Photoassociation spectrum of ultracold Rb atoms. *Phys. Rev. Lett.*, 71(14):2204–2207, 1993.

[115] P D Lett, K Helmerson, W D Phillips, L P Ratliff, S L Rolston, and M E Wagshul. Spectroscopy of Na_2 by photoassociation of laser-cooled Na. *Phys. Rev. Lett.*, 71(14):2200–2203, 1993.

[116] E R I Abraham, W I McAlexander, C A Sackett, and Randall G Hulet. Spectroscopic Determination of the s-Wave Scattering Length of Lithium. *Phys. Rev. Lett.*, 74(8):1315–1318, 1995.

[117] Y B Band and P S Julienne. Ultracold-molecule production by laser-cooled atom photoassociation. *Phys. Rev. A*, 51(6):R4317—-R4320, 1995.

[118] Tim Rom, Thorsten Best, Olaf Mandel, Artur Widera, Markus Greiner, Theodor W Hänsch, and Immanuel Bloch. State Selective Production of Molecules in Optical Lattices. *Phys. Rev. Lett.*, 93(7):073002, 2004.

[119] Kevin M Jones, Eite Tiesinga, Paul D Lett, and Paul S Julienne. Ultracold photoassociation spectroscopy: Long-range molecules and atomic scattering. *Rev. Mod. Phys.*, 78(2):483–535, 2006.

[120] Robert C Richardson. The Pomeranchuk effect. *Rev. Mod. Phys.*, 69(3):683–690, 1997.

[121] Laura Messio and Frédéric Mila. Entropy Dependence of Correlations in One-Dimensional SU(N) Antiferromagnets. *Phys. Rev. Lett.*, 109(20):205306, 2012.

[122] Shimpei Goto and Ippei Danshita. Cooling schemes for two-component fermions in layered optical lattices. *Phys. Rev. A*, 96(6):063602, 2017.

[123] Takahiro Fukui, Yasuhiro Hatsugai, and Hiroshi Suzuki. Chern Numbers in Discretized Brillouin Zone: Efficient Method of Computing (Spin) Hall Conductances. *Journal of the Physical Society of Japan*, 74(6):1674–1677, jun 2005.

[124] D J Thouless, M Kohmoto, M P Nightingale, and M den Nijs. Quantized Hall Conductance in a Two-Dimensional Periodic Potential. *Phys. Rev. Lett.*, 49(6):405–408, 1982.

[125] Shuta Nakajima, Takafumi Tomita, Shintaro Taie, Tomohiro Ichinose, Hideki Ozawa, Lei Wang, Matthias Troyer, and Yoshiro Takahashi. Topological Thouless pumping of ultracold fermions. *Nature Physics*, 12(4):296–300, jan 2016.

[126] M Lohse, C Schweizer, O Zilberberg, M Aidelsburger, and I Bloch. A Thouless quantum pump with ultracold bosonic atoms in an optical superlattice. *Nature Physics*, 12(4):350–354, apr 2016.

[127] D. J. Thouless. Quantization of particle transport. *Physical Review B*, 27(10):6083–6087, may 1983.

Acknowledgements

本論文は、京都大学量子光学研究室において行った研究をまとめたものです。この場を借りて、本研究に携わってこられた方々に厚く御礼申し上げます。

高橋義朗教授には、学部 4 回生の頃から 6 年間にわたり指導していただきました。自由な研究環境と非常に魅力的な研究テーマを用意していただき、伸び伸びと研究を進めることができました。また、投稿論文の執筆や口頭発表練習の際にはきめ細やかなご指導をしていただきました。重ねて御礼申し上げます。

研究室内で私が所属した光格子グループでは、個性豊かなメンバーに恵まれました。
田家慎太郎特定助教とは、私が M 1 の時から D3 までの 5 年もの間、一緒に実験を行い、研究生活のあらゆる面においてお世話になりました。お世話になりすぎて、感謝の一言で済ますことができません。オプティクスの使い方、ミラーの拭き方などの基本的な実験技術から、数値計算の手法や論文の書き方に至るまで、研究を投稿論文にするまでの一通りのプロセスを非常に丁寧かつ明快に教えていただきました。私が頼りないばかりに幾度となく徹夜で実験に付き合わせてしまって申し訳ありませんでした。本論文での成果は、田家さんの存在なくしては成しえなかったでしょう。あらゆるシーンで常に問題の核心をついた言動や研究に対する真摯な姿勢は、研究をする上での模範としてこれからも見習っていきたいと思います。
既に卒業して就職されていますが、一ノ瀬友宏君とは、Lieb 格子の実験を一緒に進めました。物理学だけでなく様々な学問についての教養があり、鋭い質問をする姿勢に感心させられるだけでなく、実りある議論を交わすことで研究に深みを増すことができました。
高須洋介助教は、本研究のみならず量子光学研究室の実験装置の支柱となっていました。実験装置の日々のメンテナンスをしていただいたり、急なトラブルの際には迅速に対応していただき、実験をスムーズに進めることができました。
後輩の塩津博章君とは、一緒に実験した期間は短かったものの居室の席が隣りだったということもあり、研究のことからプライベートのことまで色々と話しました。“魅せる”ことに全てをつぎ込む姿勢には楽しませていただきました。その姿勢を貫いていくことを期待しています。
その他にも歴代の光格子グループのメンバーには実験装置を共有している都合上、色々とお世話になりました。ありがとうございました。

秘書の寺川公美子さんには、物品購入や学会への出張にともなう事務手続きをしていただきました。複雑な手続きも丁寧に説明していただいたおかげで、研究を円滑に進めることができました。事務だけではなく、折に触れて研究室内でのイベントを積極的に企画していただいたことで、日々の研究生活にハリがでました。
後輩の富田隆文君には、研究室の計算機係として色々と作業を手伝っていただき、大変助かりました。著しい研究成果を上げる姿勢に刺激を受けただけでなく、映画や本、展示会

についての素敵に面白い話を聞くのは、研究生活の良い息抜きになっていました。
その他にも小野滉貴君をはじめとした研究室のメンバーとは、研究の合間を縫って、自転車で琵琶湖を一周したり、フットサル大会に出たりと、忙しい研究生活の中でも楽しいひと時を過ごすことができました。ありがとうございました。

また、博士課程在学中、日本学術振興会から経済的な援助を頂き、集中して研究に取り組むことができたことを深く感謝致します。

最後に、博士課程修了まで私を見守ってくれた家族と友人たちに心より感謝いたします。